
DOCTORAL THESIS

**ULTRA-SHORT NON-AGING CREEP BEHAVIOR
OF HYDRATES, CEMENT PASTES, MORTARS,
AND CONCRETES: A COMBINED
EXPERIMENTAL-COMPUTATIONAL MULTISCALE
APPROACH**

DISSERTATION

**ULTRA-KURZES ALTERUNGSFREIES
KRIECHVERHALTEN VON HYDRATEN,
ZEMENTSTEINEN, MÖRTELN UND BETONEN:
EIN KOMBINIERTER
EXPERIMENTELL-RECHNERISCHER
MEHRSKALEN-ANSATZ**

ausgeführt zum Zwecke der Erlangung des akademischen Grades eines
Doktors der technischen Wissenschaften

eingereicht an der Technischen Universität Wien
Fakultät für Bauingenieurwesen

von

Engr. M.Sc. Muhammad Irfan-ul-Hassan

Matrikelnummer: 1229766

Schellhamnergasse 10/2/14, 1160 Wien, Österreich

- Referent: Univ.-Prof. Dipl.-Ing. Dr. techn. Christian Hellmich
Institut für Mechanik der Werkstoffe und Strukturen
Technische Universität Wien
Karlsplatz 13, 1040 Wien, Österreich
- Referent: Assoc. Prof. Priv.-Doz. Dipl.-Ing. Dr. techn. Bernhard Pichler
Institut für Mechanik der Werkstoffe und Strukturen
Technische Universität Wien
Karlsplatz 13, 1040 Wien, Österreich
- Koreferent: Assoc. Prof. Dr. Stéphanie Staquet
Unit of Construction and Architecture
Université Libre de Bruxelles
Brussels, Belgium

Wien, im Juli 2016

.....

Acknowledgment

The research study reported in this dissertation has been performed at Vienna University of Technology, Institute for Mechanics of Materials and Structures (IMWS), Civil Engineering Department, at the Laboratory for Macroscopic Material Testing, Vienna, Austria.

I would like to express my sincere gratitude to Prof. Dr. Christian Hellmich. It has been a great privilege to work under the supervision of Prof. Hellmich. I am really thankful to him for his intellectual ideas, knowledge in the subject, competent guidance, dealing with challenges, and broad vision about the research. During my stay at Vienna, Prof. Hellmich shared a valuable knowledge and experience with me to conclude my PhD thesis. I am also thankful to him for giving me the opportunity to work at TU Wien in an excellent working environment.

I am highly indebted to my co-supervisor Assoc. Prof. Dr. Bernhard Pichler for his excellent guidance, suggestions, encouragement, and advice throughout my PhD work. I really appreciate the way Prof. Pichler helped me and guided me thoroughly during my testing work at the laboratory, evaluation, and writing. He indeed cared a lot about my research work and devoted a lot of time. His exceptional knowledge to the subject was indeed helpful.

I would like to express my gratitude to the external member of the thesis defense committee, Prof. Dr. Stéphanie Staquet, Université Libre de Bruxelles, Belgium for her interest in my research work and the time and effort she put into reading this dissertation.

I greatly appreciate and thankful to the the scientific and technical staff of the Laboratory for Macroscopic Material Testing at IMWS, TU Wien, specially Dr. Roland Reihnsner and Wolfgang Dörner for their excellent cooperation during testing and devoted assistance throughout the experimental part of this study.

Special thanks to Dipl.-Ing. Markus Königsberger for his support and help in working together to accomplish our research work. I would like to thank all of my colleagues Michal, Jiaolong, Hui, Olaf, Thomas, Eva, and Johannes for sharing a good working environment and the fruitful discussions we had during my time at IMWS, TU Wien. Thanks to Dr. Scheiner for write-up guidance. Martina Pöll, Gabriele Ostrowski, and Astrid Schuh deserve a huge appreciation for dealing with official matters. I am so thankful to David for his prompt help whenever required. Thanks to all colleagues of the institute(IMWS) for the good time I have spent here with them.

The Higher Education Commission (HEC), Pakistan and Civil Engineering Department, University of Engineering and Technology, Pakistan, are gratefully acknowledged for their financial support to this research study. In addition, OeAD (Austrian Agency for International Cooperation in Education and Research) is also acknowledged for dealing with all administrative issues. I would like to take this opportunity to thank all of my teachers who taught me at one

or the other stage of my studies and brought me to the lights of knowledge. I appreciate all my friends and colleagues of Civil Engineering Department, UET Lahore, Pakistan, for their encouragement. Thanks to all HEC scholars, from Pakistan studying here at Austria, for the time we have shared. Now, as my PhD is going to be finished, I will try to fulfill my promise to serve my country with full of my potential.

Personally, I want to especially thank my father and mother for everything they have done, to help me reach this point. I am so much thankful to my wife Amna for standing beside me throughout and showing a great patience with every single moment during my research work. A special thanks to my wonderful children: Muahid and Fabeeha, for always making me smile, and for understanding while I am busy. I would like also to express my sincere gratitude to my brothers Zia-ul-Hassan, Saqib, my sisters, my in-laws, in Pakistan, for their prayers and continuous support.

Finally, and above all, all praises to *Allah* Almighty, for His countless blessings and for giving me the strength to complete this dissertation.

Abstract

Cementitious materials – such as cement pastes, mortars, and concretes – are not only highly creep active at early ages, but also their microstructure is continuously changing because of the ongoing chemical reaction between cement clinker and water, and the correspondingly increasing amount of so-called hydration products. The central idea of the present thesis is to decouple the phenomena of early age creep and hydration, in the context of a combined experimental-theoretical approach.

The goal of the experimental activities is to characterize early-age evolutions of Young's elastic modulus and of non-aging creep properties of ordinary Portland cement pastes, mortars, and concretes conditioned at 20 °C. Using an innovative early-age creep testing protocol, we perform a series of 168 three minute-long uniaxial macroscopic creep tests on the aging materials, with one such test per hour and with corresponding material ages spanning from 21 hours to approximately eight days. In this way, it is guaranteed that the material microstructure remains virtually unaltered during each individual creep test, while subsequent creep tests refer to different microstructures. In order to minimize possible material damage, the compressive loads are restricted to at most 15% of the uniaxial compressive strength reached at the time of testing. The loading protocol consists of quasi-instantaneous compressive loading and unloading steps as well as a three minutes long holding period in between.

As for experiments on cement pastes, three different material compositions are investigated, defined in terms of initial water-to-cement mass ratios amounting to 0.42, 0.45, and 0.50, respectively. Precise representation of the measured compliances by means of a power-law expression including elastic and creep moduli, as well as a creep exponent, while requiring the elastic and creep strains to be compressive at all times, yields concavely increasing time evolutions of elastic and creep moduli, as well as slightly decreasing or quasi-constant evolutions of the creep exponent. Combination of these results with calorimetry-based evolutions of the degree of hydration yields linear elasticity-hydration degree and over-linear creep modulus-hydration degree relations, while the creep exponents slightly decrease with ongoing hydration. Notably, the herein quasi-statically determined elastic moduli agree very well with those determined ultrasonically on the same cement pastes. This impressively underlines the fundamental characteristics of the elastic properties being related to an energy potential, independently of loading paths and corresponding strain rates. Conclusively, Young's moduli which are either determined from loading or unloading paths only, may not exclusively refer to elastic material behavior, but also to dissipative phenomena.

The measured creep properties of cement pastes result from the viscoelastic behavior of the hydration products. We here identify a corresponding single isochoric creep function characterizing well-saturated Portland cement hydrates, through downscaling of 500 different non-aging creep functions obtained from

the aforementioned three minute-long tests on differently old cement pastes with three different initial water-to-cement mass ratios. A two-scale micromechanics representation of cement paste is used for downscaling. At a scale of 700 microns, spherical clinker inclusions are embedded in a continuous hydrate foam matrix. The latter is resolved, at the smaller scale of 20 microns, as a highly disordered arrangement of isotropically oriented hydrate needles, which are interacting with spherical water and air pores. Homogenization of viscoelastic properties is based on the correspondence principle, involving transformation of the time-dependent multiscale problem to Laplace-Carson space, followed by quasi-elastic upscaling and numerical back-transformation. With water, air, and clinker behaving elastically according to well accepted published data, the hydrates indeed show one single power law-type creep behavior with a creep exponent being surprisingly close to those found for the different cement pastes tested. The general validity of the identified hydrate creep properties is further corroborated by using them for predicting the creep performance of a 30 years old cement paste in a 30 days long creep test: the respective model predictions agree very well with results from creep experiments published in the open literature.

Focusing finally on predicting the mechanical properties of mortars and concretes, it is important to note that customary micromechanics models for the poroelasticity, creep, and strength of concrete restrict the domain affected by the hydration reaction, to the cement paste volume; considering the latter as thermodynamically closed system with respect to the chemically inert aggregates. Accordingly, such micromechanical models typically rely on the famous Powers hydration model, in order to quantify volume fractions of clinker, cement, water, and aggregates, as functions of the hydration degree. The situation changes once internal curing occurs, i.e. once part of the present water is absorbed initially by the aggregates, and then soaked “back” to the cement paste during the hydration reaction. For this case, we here develop an extended hydration model, introducing water uptake capacity of the aggregates on the one hand, and paste void filling extent on the other, as additional quantities. Based on constant values for just these two new quantities, and on experimentally determined creep properties of cement pastes as functions of an effective water-to-cement mass ratio (i.e. that associated to the cement paste domain, rather than to the entire concrete volume), a series of three minute creep tests on different mortars and concretes can indeed be very satisfactorily predicted by a standard micro-viscoelastic two-scale model. This further extends the applicability range of micromechanics modeling in cement and concrete research, and it concludes the present thesis which combines innovative macroscopic material testing and state-of-the-art multiscale modeling from sub-micrometric hydrate needles to decimeter-sized specimens of mortars and concretes.

Contents

1	Introduction	1
1.1	Motivation	1
1.2	Objectives and scope of the research	4
1.3	Methodology and key results	6
1.3.1	Chapter 2	6
1.3.2	Chapter 3	7
1.3.3	Chapter 4	8
1.3.4	Chapter 5	9
2	Elastic and creep properties of young cement paste, as determined from hourly repeated minutes-long quasi-static tests	10
2.1	Introduction	10
2.2	Materials and Experimental Methods	11
2.2.1	Test Preparation	12
2.2.2	Creep Testing	13
2.3	Test Evaluation	16
2.3.1	Quantification of Young's Modulus	16
2.3.2	Quantification of Creep Properties	19
2.4	Results	21
2.4.1	Elastic Young's modulus	21
2.4.2	Temporal evolution of creep modulus and power-law exponent	22
2.4.3	Evolution of Young's modulus, creep modulus, and power-law exponent as functions of degree of hydration	24
2.5	Discussion	27
2.5.1	Non-aging, non-damaging creep tests	27

2.5.2	Self-desiccation and reduction of internal relative humidity	28
2.5.3	Test evaluation strategy	29
2.5.4	Static versus dynamic stiffness	31
2.5.5	Macroscopic testing versus microindentation testing: Power-law creep versus logarithmic creep?	32
2.5.6	Extrapolation from three-minutes non-aging creep tests to two-days aging creep tests	33
2.5.7	Future outlook to microstructurally-designed materials	35
2.6	Conclusions	36
3	Downscaling-based identification of non-aging power-law creep of cement hydrates	39
3.1	Introduction	39
3.2	Micromechanics of creeping cement pastes	41
3.2.1	Micromechanical representation of cement pastes	41
3.2.2	Homogenization of hydrate foam properties	41
3.2.3	Homogenization of cement paste properties	46
3.3	Identification of power-law creep properties of well-saturated cement hydrates	47
3.3.1	Downscaling minute-long creep test data from cement paste to hydrate level	47
3.3.2	Confirmation of hydrate creep properties by data from weeks-long creep test on 30 year-old cement paste	49
3.4	General characteristics of the creep of well-saturated hydrates	51
3.5	Discussion and conclusion	52
4	How water-aggregate interactions affect concrete creep: a multiscale analysis	59
4.1	Introduction	59
4.2	Modeling hydration-dependent water migration to and from the aggregates	61
4.3	Creep homogenization of mortars and concretes	64
4.4	Comparison of ultrashort creep experiments and corresponding micromechanics predictions - identification of water absorption capacities of quartz aggregates and of paste void filling extent	69
4.5	Conclusions	80
4.6	Acknowledgment	83

5	Creep testing database: results from hourly-repeated three-minute creep tests on cement pastes, mortars, and concretes	87
5.1	Results from characterization of cement pastes at different temperatures	89
5.1.1	Water-cement ratio = 0.42, Temperature = 20 °C	90
5.1.2	Water-cement ratio = 0.45, Temperature = 20 °C	98
5.1.3	Water-cement ratio = 0.50, Temperature = 20 °C	106
5.1.4	Water-cement ratio = 0.42, Temperature = 30 °C	114
5.1.5	Water-cement ratio = 0.42, Temperature = 10 °C	122
5.2	Identified elastic and creep properties of cement pastes	130
5.3	Results from characterization of mortars and concretes at 20 °C	131
5.3.1	Mortar: w/c = 0.42, a/c = 2.70	132
5.3.2	Mortar: w/c = 0.45, a/c = 2.80	140
5.3.3	Mortar: w/c = 0.50, a/c = 3.0	148
5.3.4	Mortar: w/c = 0.42, a/c = 1.35	156
5.3.5	Mortar: w/c = 0.50, a/c = 1.50	164
5.3.6	Concrete: w/c = 0.42, a/c = 2.70	172
5.3.7	Concrete: w/c = 0.50, a/c = 3.0	180
6	Conclusions	188
	Appendix-A1	192
	Appendix-B1	195
	Appendix-B2	200
	Appendix-C	205
	Bibliography	215
	List of Figures	231
	List of Tables	252

Chapter 1

Introduction

1.1 Motivation

Concrete is the most used man-made material in the world. More than 20 billion tons of concrete are produced every year, and this corresponds to nearly three tons per capita and year. The benefits of concrete provided to our societies are immense, considering that concrete is used to build our schools, hospitals, apartment blocks, bridges, tunnels, dams, sewerage systems, pavements, runways, roads, and more. Concrete is produced by mixing cement, water, and aggregates. Therefore, concrete is an environmentally friendly material, making it a natural choice for sustainable construction. The effectiveness, price, and performance, of concrete is much better compared to other materials. Twice as much concrete is used around the world than the total of all other building materials, including wood, steel, plastic, and aluminum. None of these other materials can replace concrete, rendering concrete indispensable for construction ([WBCSD 2013](#)). The Cement Sustainability Index (CSI) recognizes that in an increasingly urbanized population, concrete and cement will keep playing a vital part in our daily lives, through many diverse applications and usages. At the same time, the CSI believes that it is essential to properly measure the externalities of cement and concrete. This enables a better understanding of general impacts and helps in appropriate decision making. Due to the extensive use of concrete, there has been always the need to get more detailed insight into its behavior. Even nowadays, many areas need to be explored using innovative experimental techniques and new modeling approaches, especially multiscale material modeling and poromechanics.

Concrete exhibits creep, i.e. the material deforms progressively under, and induced by, a constant sustained load ([Neville 1971](#)). In material science,

creep is more generally understood as the tendency of a solid material to move slowly or deform permanently under the influence of mechanical stresses. Since the first publication on the creep of reinforced concrete in 1907 ([Hatt 1907](#)), the subject has been studied intensively, but the fundamental mechanisms of creep is still not fully understood, for several reasons. Firstly, due to the fact that cement and concrete are multi-scale heterogeneous materials. Creep can be observed at different scales ranging from that of concrete down to the one of individual hydration products. Secondly, creep is sensitive to a variety of parameters: moisture, temperature, stress level, curing conditions, and mix design (i.e. water-to-cement ratio, admixtures, aggregates), see [Neville \(1971\)](#). Thirdly, cementitious materials, such as cement pastes, mortars, and concretes, are obtained by hydration of binders, and the hydration lasts months to decades. As a consequence, the microstructures of cementitious materials evolve with time and the creep properties depend on the maturity at which a given material is tested. Therefore, the phenomenon of creep is still far from being fully understood ([Bažant 2001](#); [Bazant and Li 2008](#)).

State-of-the-art testing and modeling of concrete creep are typically of macroscopic and of phenomenological nature ([Hanson and Laboratories 1953](#); [Keeton 1965](#); [Brooks and Neville 1975](#); [Bažant et al. 1976](#); [Bažant and Panula 1978](#); [Bažant and Chern 1985](#); [Sakata and Shimomura 2004](#); [Tamtsia et al. 2004](#)). Results from many creep experiments were collected and tabulated in large databases ([Bazant and Li 2008](#)), like the RILEM database ([RILEM 1995](#)), and the one of the Japanese society of civil engineering ([JSCE 2000](#)). These databases helped to develop a number of creep models for codes, e.g. ACI-209 ([ACI 1992](#)), including models for different types of concrete like (i) normal strength concrete by [Bažant \(2001\)](#) and [Baweja et al. \(1998\)](#), and (ii) high performance concrete by [Le Roy et al. \(1996\)](#) as well as by [Dilger and Wang \(1995\)](#). Researchers have particularly focused on creep properties for hardened concrete ([Mazloom 2008](#); [Shariq et al. 2016](#)), and nowadays there is plenty of evidence that long term creep of concrete finally becomes linear at logarithmic time-scale ([Bažant et al. 2011](#); [Zhang et al. 2014](#)). Few researchers have performed tests at load levels up to 80% of the compressive strength which may induce damage in the material resulting in non-linear creep ([Rossi et al. 1994, 2011](#)). Many researchers reported challenges in performing and standardizing creep experiments, e.g. creep compliances found in different databases exhibit significant dispersion, underlining that the problem is not yet solved in a satisfactory fashion. Additionally, in order to gain reliable insight into long-term creep, creep testing on concrete is recommended to be carried out over hundreds of days ([Le Roy et al. 1996](#); [Havláek and Jirásek 2012](#)), and this requires not only the availability of testing facilities over long periods of time, but it is also difficult to control experimental parameters as temperature, applied load, and moisture distribution within the sample.

Creep of concrete significantly influences the performance and durability of civil engineering infrastructure, both at early ages and during long-term ser-

vice. Therefore, in addition to mechanical properties such as modulus of elasticity, as well as tensile and compressive strength, the time dependent properties of concrete must be considered for evaluating the performance of structures (Schutter and Taerwe 1996; Bažant 2001; Atrushi 2003; Nehdi and Soliman 2011). The creep contribution to differential axial shortening of high-rise buildings, for instance, is becoming significant with increasing stresses on the structural elements. It is also well known that time-dependent deformations cause loss of prestress (Youakim 2006) and increase of deformations (Ghali et al. 2006), reducing the durability of structures. At the same time, time-dependent deformations can be beneficial in the form of redistribution of stresses caused by imposed deformations or loads, and also the reduction of undesirable stresses, particularly in early age concrete (Neville 1971; Bažant 2001; Atrushi 2003) and in shotcrete tunneling (Hellmich et al. 2000, 2001; Ullah et al. 2010, 2012, 2013). However, stress redistribution might increase the probability of cracking in new structures, and even overstressing that might lead to structural collapse of old structures (Binda et al. 1992; Bažant 2001; Shrive et al. 2001). Furthermore, creep can produce permanent displacements in large and thin arch dams up to 30 or 40 years after dam completion (Hachem and Schleiss 2011; Erpicum et al. 2013). Turning finally to early ages, cement-based construction materials exhibit significant developments of heat of hydration and autogenous deformation (Bažant et al. 1976; Tamtsia et al. 2004; Nehdi and Soliman 2011; Briffaut et al. 2012; Boulay et al. 2014; Jiang et al. 2014; Sellier et al. 2016). This results in generation of internal stresses, because internal and external restraints nearly always prevail in structural concrete elements. While the viscoelastic behavior of young concrete reduces these stresses to lower magnitudes (Schutter and Taerwe 1996; Voigt et al. 2003; Gu et al. 2006), the risk of larger internal stresses is larger in case of mass concreting like in dams, barrage floors, silos, and concrete domes around nuclear reactors (Smith 1991; Hilaire et al. 2014; Shariq et al. 2016; Bažant and Chern 1985; Kovler 1994; Boumiz et al. 1996; Delsaute et al. 2011). Improving the properties of concrete at early-ages contributes to improving its long term durability.

Focusing on early-age creep of cementitious materials, it turns out that testing and modeling are very challenging tasks because of the coupling between creep and hydration. The typical duration of a macroscopic creep experiment ranges from hours to several days (Bažant et al. 1976; Tamtsia et al. 2004; Rossi et al. 2011), weeks (Laplante 2003; Tamtsia and Beaudoin 2000; Atrushi 2003; Briffaut et al. 2012), months (Rossi et al. 1994; Zhang et al. 2014), or even years (Bažant et al. 2011, 2012; Zhang et al. 2014), and this is of the same order of magnitude or even larger than the characteristic time of the chemical hydration reaction at early ages. Consequently, early-age creep tests as referred to above, do not refer to one and the same microstructure which would stay unaltered during such as test. This qualifies standardly performed early-age experiments as aging creep tests. The described lack of separated time-scales renders also the mathematical description of early-age

creep as very challenging. In particular in the context of multiscale modeling approaches (Scheiner and Hellmich 2009; Sanahuja 2013b), the time-dependent behavior of the elementary constituents needs to be quantified, *together with* the temporal evolution of microstructures built up by these constituents (Pichler and Lackner 2008; Scheiner and Hellmich 2009; Sanahuja and Dormieux 2010; Jiang et al. 2014; Hilaire et al. 2014). At the same time shrinkage strains and thermal strains are also developed in the materials starting at the level of hydrates (Němeček 2009; Nguyen et al. 2014; Vandamme and Ulm 2013; Königsberger et al. 2016). These microstructural processes are responsible for the macroscopically observed behavior. Summarizing, separation of different microstructural processes and phenomena is challenging but desirable, see e.g. (Zhao 1990; Smith 1991; Kovler 1994; Schutter and Taerwe 1996; Yuan and Wan 2002). As for decoupling creep from hydration at early-ages, short term non-aging creep testing is well suited and already used, see the work of Vandamme and Ulm (2009); Boulay et al. (2012); Vandamme and Ulm (2013); Delsaute et al. (2011); Delsaute and Staquet (2011); Zhang et al. (2014). Decoupling creep from the hydration is also the key idea of the present thesis.

1.2 Objectives and scope of the research

This thesis is devoted to early-age stiffness characterization of cementitious materials, such as cement pastes, mortars, and concretes. Experimental activities aim at decoupling creep from hydration. The corresponding test evaluation strategy aims at separating instantaneous elastic deformation from time-dependent creep deformation. Subsequent multiscale exploitation of experimental results aims at (i) identification of “universal” creep properties of (sub)micron-sized cement hydrates, and (ii) prediction of non-aging creep properties of mortars and concretes. These overall objectives are sub-structured into the following points.

- Decoupling the time-dependent phenomena creep and hydration is achieved by performing ultra short creep experiments. Three-minute creep tests, namely, are so short that the hydration reaction does not make significant progress, i.e. that the tested microstructure is practically the same throughout the test. This qualifies ultra short creep experiments as *non-aging* tests.
- Deformation histories measured during an ultra short creep test are decomposed very carefully into (i) the instantaneous elastic part and (ii) the time-dependent creep part. This allows for quantifying the *elastic* material stiffness in terms of the *instantaneous* Young’s modulus, and the time-dependent material compliance in terms of the uniaxial creep function.

- In order to quantify the early-age *evolutions* of elastic stiffness and *non-aging* creep properties, ultra short creep experiment are performed once every hour, starting 21 hours after production and continuing up to material ages of eight days.
- The described testing and evaluation strategies are applied to macroscopic specimens of cement pastes, mortars, and concretes. The tested materials differ in composition, i.e. in terms of the initial water-to-cement mass ratio, the initial aggregate-to-cement mass ratio, the aggregate size distribution, and the aggregate type, resulting in a comprehensive database of experimental results.
- Multiscale exploitation of experimental results starts with top-down identification of universal creep properties of (sub)micron-sized cement hydrates. This aims at explaining the deformation histories measured in more than 500 ultra short creep tests on cement pastes based on only 1 set of universal creep properties of (sub)micron-sized and needle-shaped hydrates.
- The universality of the identified hydrate creep properties is validated by (i) predicting the evolution of creep deformations for a 30 days lasting creep test on a cement paste that cured for 30 years under water, and (ii) by comparing model predictions with experimental data taken from the literature.
- Multiscale exploitation of experimental results continues with bottom-up prediction of creep of mortars and concretes. This aims at showing that “internal curing” does not only happen with light-weight aggregates, but also with oven-dried regular aggregates, because (i) aggregates take up a certain mass of water during mixing of raw materials, and (ii) this water mass is soaked “back” into the hydrating cement paste matrix, driven by autogeneous shrinkage.
- The analysis of “internal curing” results in the development of a new hydration model which considers hydrating cement paste to be a thermodynamically open system relative to the surface porosity of the aggregates. The effective water-to-cement ratio of the cement paste matrix is shown to increase linearly with increasing hydration degree. This result could be achieved, only because of the comprehensive test database from hourly testing of cement pastes, mortars, and concretes levels.

1.3 Methodology and key results

1.3.1 Chapter 2

This chapter is based on the joint publication of Muhammad Irfan-ul-Hassan, Roland Reihnsner, Bernhard Pichler, and Christian Hellmich published in the Elsevier Journal of Cement and Concrete Research (CCR), 2016, vol. 80, pp. 36–49.

Bernhard Pichler and Christian Hellmich set up the overall strategies for experimental testing and evaluation of measurements, using (i) the principle of separation of time scales to decouple creep from hydration and (ii) the physical requirement that time-dependent deformation under uniaxial compression must result in a shortening of the tested specimen. They supervised the research progress, checked key results, and supported the documentation process. Muhammad Irfan-ul-Hassan produced the cement paste specimens and carried out hourly-repeated three-minute creep experiments, supported by the technical staff of the laboratory. He developed Matlab codes for the evaluation of test data and documented the research results. Roland Reihnsner contributed to the discussion processes and operated the testing machine as well as the deformation measurement equipment.

DIGEST:

Cement pastes are highly creep active materials at early ages. We here characterize both the elastic stiffness and the creep properties of ordinary Portland cement pastes conditioned at 20 degrees Celsius. Three different compositions are investigated, defined in terms of initial water-to-cement mass ratios amounting to 0.42, 0.45, and 0.50, respectively. Implementing a new early-age creep testing protocol, we perform a series of 168 three minutes long uniaxial macroscopic creep tests on the aging materials, with one such test per hour and corresponding material ages spanning from 21 hours to approximately eight days. In this way, it is guaranteed that the material microstructure remains virtually unaltered during each individual creep test, while subsequent creep tests refer to clearly different microstructures. In order to minimize material damage, the compressive loads are restricted to at most 15 percent of the uniaxial compressive strength reached at the time of testing. The loading protocol consists of quasi-instantaneous compressive loading and unloading steps as well as a three minutes long holding period in between. Representing the measured compliances very precisely by means of a power-law expression including elastic and creep moduli, as well as a creep exponent, while requiring the elastic and creep strains to be compressive at all times, yields concavely increasing time evolutions of elastic and creep moduli, as well as slightly decreasing or quasi-constant evolutions of the creep exponent. Combination of these results with

calorimetry-based evolutions of the degree of hydration yields linear elasticity-hydration degree and over-linear creep modulus-hydration degree relations, while the creep exponents (slightly) decrease with ongoing hydration. The herein quasi-statically determined elastic moduli agree very well with those determined ultrasonically on the same cement pastes. This impressively underlines the fundamental characteristics of elastic properties being related to an energy potential, independently of loading paths and corresponding strain rates.

1.3.2 Chapter 3

This chapter is based on the joint publication of Markus Königsberger, Muhammad Irfan-ul-Hassan, Christian Hellmich, and Bernhard Pichler accepted for publication in the Journal of Engineering Mechanics (ASCE).

Christian Hellmich and Bernhard Pichler set up the overall strategy for top-down identification of hydrate creep properties by means of three-scale creep homogenization of cement pastes. They supervised the research progress, checked key results, and supported the documentation process. Markus Königsberger developed a Maple code for three-scale creep homogenization of cement pastes, identified universal creep properties of (sub)micron-sized needle-shaped cement hydrates, carried out model validation based on data he found in the open literature, and documented the research results. Muhammad Irfan-ul-Hassan provided his experimental data in suitable numerical formats, contributed to the discussion processes, and helped proof reading the paper.

DIGEST:

Creep of cementitious materials results from the viscoelastic behavior of the reaction products of cement and water, called hydrates. In the present paper, a single isochoric creep function characterizing well-saturated Portland cement hydrates is identified through downscaling of 500 different non-aging creep functions derived from three minute-long tests on differently old cement pastes with three different initial water-to-cement mass ratios. A two-scale micromechanics representation of cement paste is used for downscaling. At a scale of 700 microns, spherical clinker inclusions are embedded in a continuous hydrate foam matrix. The latter is resolved, at the smaller scale of 20 microns, as a highly disordered arrangement of isotropically oriented hydrate needles, which are interacting with spherical water and air pores. Homogenization of viscoelastic properties is based on the correspondence principle, involving transformation of the time-dependent multiscale problem to Laplace-Carson space, followed by quasi-elastic upscaling and numerical back-transformation. With water, air, and clinker behaving elastically according to well-accepted

published data, the hydrates indeed show one single power law-type creep behavior with a creep exponent being surprisingly close to those found for the different cement pastes tested. The general validity of the identified hydrate creep properties is further corroborated by using them for predicting the creep performance of a 30 years old cement paste in a 30 day-lasting creep test: the respective model predictions agree very well with results from creep experiments published in the open literature.

1.3.3 Chapter 4

This chapter is based on the joint publication of Muhammad Irfan-ul-Hassan, Markus Königsberger, Roland Reihnsner, Christian Hellmich, and Bernhard Pichler submitted to the Journal of Nanomechanics and Micromechanics (ASCE).

Bernhard Pichler and Christian Hellmich set up the overall strategy for bottom-up prediction of creep properties of mortars and concretes, based on a new hydration model considering (i) initial water uptake by aggregates and (ii) autogeneous shrinkage-driven suction of water “back” to the cement paste matrix. They supervised the research progress, checked key results, and supported the documentation process. Muhammad Irfan-ul-Hassan produced the mortar and concrete specimens and carried out hourly-repeated three-minute creep experiments supported by the technical staff of the laboratory. He incorporated the new hydration model into a Maple code for two-scale creep homogenization of mortars and concretes. He used the code for identification (i) of the water uptake capacity of the used aggregates, and (ii) of the filling extent of shrinkage-induced voids by water. He carried out model validation and documented the research results. Markus Königsberger developed the Maple code for creep homogenization, contributed to both the discussion processes and the documentation of research results, and helped proof reading the paper. Roland Reihnsner operated the testing machine and the deformation measurement equipment.

DIGEST:

Customary micromechanics models for the poroelasticity, creep, and strength of concrete restrict the domain affected by the hydration reaction, to the cement paste volume; considering the latter as thermodynamically closed system with respect to the (chemically inert) aggregates. Accordingly, the famous Powers hydration model appears as a natural choice for the determination of clinker, cement, water, and aggregates volume fractions entering such micromechanical models. The situation changes once internal curing occurs, i.e. once part of the present water is absorbed initially by the aggregates, and then soaked “back” to the cement paste during the hydration reaction. For

this case, we here develop an extended hydration model, introducing water uptake capacity of the aggregates on the one hand, and paste void filling extent on the other, as additional quantities. Based on constant values for just these two new quantities, and on previously determined creep properties of cement pastes as functions of an effective water-to-cement mass ratio (i.e. that associated to the cement paste domain, rather than to the entire concrete volume), a series of ultrashort-term creep tests on different mortars and concretes can indeed be very satisfactorily predicted by a standard micro-viscoelastic mathematical model. This further extends the applicability range of micromechanics modeling in cement and concrete research.

1.3.4 Chapter 5

This chapter illustrates the comprehensive databases obtained from early-age non-aging short term creep testing of cement pastes, mortars, and concretes, summing up to some four thousand five hundred quasi-static creep tests. As for displaying the results, measured creep histories are normalized by the plateau stress, and the resulting quantities are plotted over the duration of the three-minute tests.

Chapter 2

Elastic and creep properties of young cement paste, as determined from hourly repeated minutes-long quasi-static tests

2.1 Introduction

Creep characterization of cementitious materials poses great challenges at early-ages, because the typical duration of a macroscopic creep experiment ranges from hours to several days (Tamtsia et al. 2004; Bažant et al. 1976; Rossi et al. 2011), weeks (Tamtsia and Beaudoin 2000; Briffaut et al. 2012; Atrushi 2003; Laplante 2003), months (Zhang et al. 2014; Rossi et al. 1994), or even years (Zhang et al. 2014; Bažant et al. 2011, 2012), and this is of the same order of magnitude or even larger than the characteristic time of the chemical hydration reaction at early ages. Consequently, early-age creep tests as referred to above, do not refer to one and the same microstructure which would stay unaltered during such as test. The described lack of separated time-scales renders the mathematical description of early-age creep as very challenging. In particular in the context of multiscale modeling approaches (Sanahuja 2013b; Scheiner and Hellmich 2009), the time-dependent behavior of the elementary constituents needs to be quantified, *together with* the temporal evolution of

microstructures built up by these constituents (Scheiner and Hellmich 2009; Sanahuja and Dormieux 2010; Jiang et al. 2014; Hilaire et al. 2014; Pichler and Lackner 2008). This calls for development of novel, improved experimental protocols for cement pastes and concretes, and the present contribution is devoted to exactly such developments.

More precisely, we here provide insight into early-age creep properties of cement pastes, separating the effect of the time-dependent deformation behavior of the hydrates, from the evolution of the overall microstructure due to ongoing chemical hydration. In more detail, we report on minutes-long creep tests on cement pastes carried out during the second, third, fourth, fifth, sixth, seventh, and eighth day after production. The duration of our tests is so short that the microstructure of the tested materials remains practically the same throughout each individual creep test. On the other hand, since one creep test is performed every hour and given that the investigated cement pastes are younger than one week, two subsequent tests already refer to different microstructures. This allows us to characterize the evolution of creep properties of specific cement pastes, throughout the first week after their production.

It is very important for our repeated testing approach that the characterized cement pastes remain undamaged during the individual creep tests. Therefore, we subject the specimens to maximum compressive forces amounting to only 15 percent of the compressive strength at the time instant of testing. In this context, we quantify the temporal evolution of the compressive strength of cement pastes by means of a validated multiscale strength model (Pichler et al. 2013; Pichler and Hellmich 2011) combined with results from isothermal differential calorimetry (Karte et al. 2015).

This paper is organized as follows. At first, we describe (i) the chosen test setup which is inspired by the one previously developed for quantification of unloading moduli (Karte et al. 2015), and (ii) the creep test protocol, see Section 2. Test evaluation includes a new approach for the identification of (elastic) Young's modulus and for quantification of power-law creep properties, see Section 3. Results are presented both as functions of material age and as functions of hydration degree, obtained from the calorimetry, see Section 4. Finally, the results are discussed in the light of existing early-age test data from cement paste, and of the fundamentals of elasticity theory and material thermodynamics.

2.2 Materials and Experimental Methods

Herein, we characterize early-age elastic stiffness and creep of three cement pastes made from a commercial cement of type CEM I 42.5 N and distilled water. They differ in compositions, as defined in terms of initial water-to-cement ratios w/c amounting to 0.42, 0.45, and 0.50, respectively.

2.2.1 Test Preparation

Cylindrical specimens with a diameter of 70 mm and a height of 300 mm are produced, through a specific hollow cylindrical plastic mold. After mixing, placement, and compaction, the opening of the mold is sealed by several layers of food preservation foil, in order to avoid water evaporation. Bleeding was not observed. The specimens are stored in a climate chamber at 20 degrees Celsius. The core temperature of the specimens increased during the first 10 hours up to $\approx 26^\circ\text{C}$, followed by a smooth reduction down to 20°C , reached after 45 hours. Such temperature differences at very early ages are expected to leave the samples undamaged. At an age of 20 hours, the specimens are demolded, and both circular end faces are shaved with a Stanley knife, in order to minimize possible inhomogeneities resulting from production and/or storage, and to achieve coplanarity of the two faces (Fischer et al. 2014; Karte et al. 2015; Pichler et al. 2014). Preliminary samples were crushed for inspection of the fracture surfaces. This allowed for a successful visual check of the homogeneity of the samples.

The used test setup for uniaxial compression is very similar to the one recently developed for early-age stiffness characterization of cement pastes (Karte et al. 2015). As for achieving a central load application, we use a serial arrangement of the specimen with two metal cylinders. The latter were equipped by so-called cylindrical bottlenecks, see Fig. A.1. The bottlenecks exhibit diameters of 30 mm, and this is by a factor of 2.3 smaller than the diameter of the sample.

Also during testing, the samples are kept at 20 degrees Celsius. To this end, the described test setup is placed inside an insulated temperature chamber, equipped with a temperature control unit Lauda RK8 KP. In addition, the specimens are covered by several layers of food preservation foil, in order to minimize loss of water via evaporation.

Deformations of the samples are quantified by means of five Linear Variable Differential Transducers (LVDTs) of type “Solartron”. The latter give access to the relative displacements between two aluminum rings, which are fixed to the specimens by means of three screws each. Thereby, the rings are positioned at a mutual distance of 164 mm, each of them 70 mm distant from the interfaces between specimen and metal cylinders; see Fig. A.1. In this way, the top and bottom 70 mm of the specimens are part of the load application system, and this is very effective in achieving shear-free stress and strain states in the central measurement region. Undesired shear stresses, resulting from inevitable discrepancies of Poisson’s ratio of the specimen and the attached metal cylinders, namely, decay with increasing distance from the specimen metal interface, such that they are practically negligible in a distance being equal to the diameter of the sample (Karte et al. 2015). The five LVDTs are evenly distributed around the perimeter of the specimen, i.e. at a spacing of 72° . Using five rather than the minimum of three required LVDTs, increases the measurement accuracy by 29% (Karte et al. 2015).

The described setup is installed in an electromechanical universal testing machine of type Walter and Bai LFM 150. Before the actual testing, the position of the specimen is iteratively improved in order to come close to a central load application. This is done based on the LVDT readings obtained in short-term preliminary loading-unloading tests with a load of 3 kN. The position of the specimen is accepted, once the largest of the LVDT readings is not larger than twice the smallest reading.

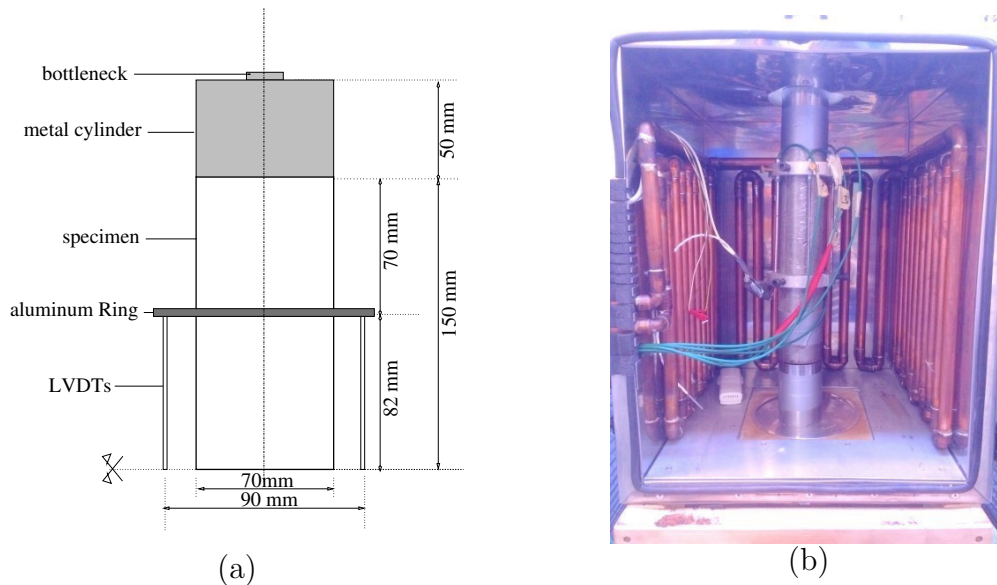


Figure 2.1: Test setup consisting of the cement paste specimen, metal cylinders with bottleneck, and two aluminum rings holding five LVDTs (a) schematic illustration of symmetric upper half of the test setup, (b) actual test setup inside climate chamber containing two temperature sensors and copper pipes filled with conditioning fluid

2.2.2 Creep Testing

One specific loading-unloading test with a characteristic creep duration of three minutes is performed every hour. During the remaining 57 minutes of every hour, a permanent compressive force amounting to 0.2 kN ensures that the whole setup (including the sample and the bottlenecks) stays in an upright position without tipping over. The creep strain rates resulting from this small loading decay quickly, such that they can be neglected with respect to the significantly larger creep strain rates measured during the following three-minutes creep tests.

Infinitely fast loading would be desirable for a creep test, but this is impossible in a real experiment. Herein, loading is carried out under force control, with a

prescribed force-rate amounting to 7.697 kN/s, corresponding to a specimen-related stress rate amounting to 2 MPa/s, see Fig. A.2. This fast loading speed ensures that the duration of the loading phase is by two orders of magnitude smaller compared to the following creep test, where the load was held constant for 180 seconds. Unloading is again carried out under load control with a force-rate amounting to 3.849 kN/s which is equivalent to a specimen-related stress rate amounting to 1 MPa/s. This ensures that the prescribed loading speed is reliably reached after an initial acceleration and before the final deceleration of the piston.

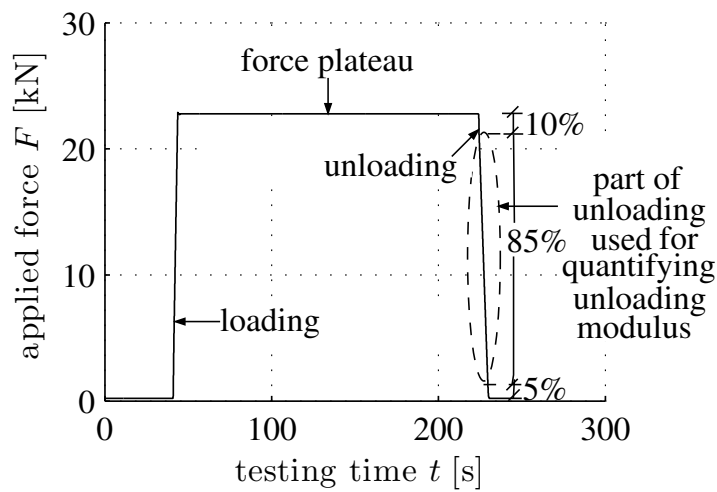


Figure 2.2: Typical force readings captured during a three-minutes creep test

Moreover, a trade-off between non-destructive testing and reliable deformation measurements needed to be found. On the one hand, load levels smaller than or equal to 15 % of the compressive strength are believed to stay within the elastic limit of the material, because they stay out of the so called non-linear creep regime (Ruiz et al. 2007) which would result in damage of the material (Rossi et al. 2011; Fischer et al. 2014). On the other hand, such load levels turned out to result in creep deformations which are large enough for obtaining reliable LVDT readings. Still, this approach requires knowledge on the compressive strength of cement paste which increases significantly during the first week after production.

A validated continuum micromechanics model (Pichler et al. 2013; Pichler and Hellmich 2011) is used to quantify the composition-specific evolution of compressive strength as a function of hydration degree, see Fig. A.3(a). Quasi-isothermal calorimetry carried out at 20 degrees Celsius (for all three types of cement pastes $w/c = 0.42$, $w/c = 0.45$, and $w/c = 0.50$, respectively) allows us to establish a relation between age of the material and the hydration degree ξ , see Fig. A.3(b). Hydration degree ξ is determined as the ratio of the

accumulated specific heat release $Q(t)$ and the latent heat of ordinary Portland cement amounting to 500 J/g : $\xi(t) = \frac{Q(t)}{500 \text{ J/g}}$. Combining the relationship between the compressive strength and hydration degree, with the relationship between hydration degree and age of the materials, and multiplying the resulting temporal evolution of compressive strength by 15 percent, delivers maximum load levels for our creep testing campaigns, see Fig. A.4.

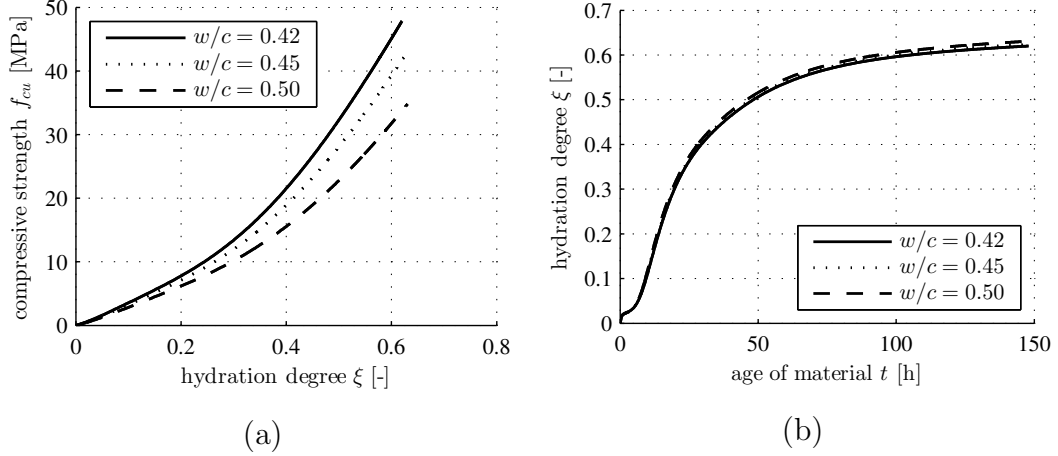


Figure 2.3: (a) Prediction of compressive strength based on validated multi-scale model (Pichler and Hellmich 2011; Pichler et al. 2013) as a function of hydration degree, (b) evolution of hydration degree as a function of material age, derived from quasi-isothermal calorimetry at 20 degrees Celsius

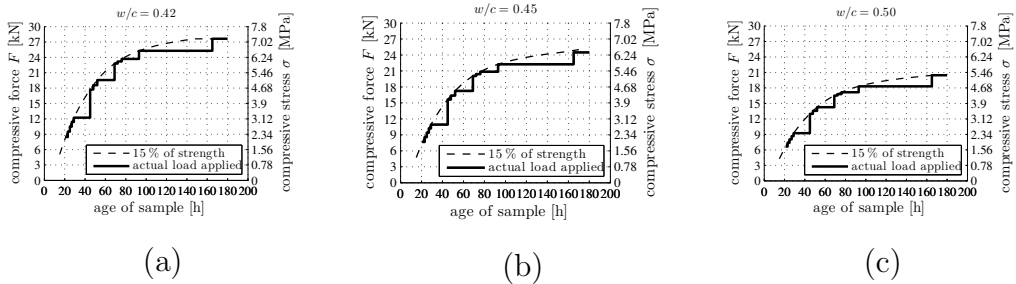


Figure 2.4: Load plateau values prescribed during creep testing of cement pastes with (a) $w/c = 0.42$, (b) $w/c = 0.45$, and (c) $w/c = 0.50$

During the second, third, and fourth day after specimen production, the maximum load applied in our test was repeatedly updated during regular working hours, such that the specimens were kept at a load level related to 15% of the model-predicted strength, see Fig. A.4. During the night and over the weekend, in turn, the load levels remained invariant, for safety reasons. In this way, the effectively applied loads always ranged between 10% and 15% of the compressive strength.

The digital measurement equipment Orbit of Solartron Metrology is used for storing the measured data in terms of Excel sheets. This includes displacement

measurement signals of the five LVDTs, the signal from the force measurement unit of the universal testing machine, and the signals of two quality assuring temperature sensors. A Visual BASIC script automatically controls the measurement frequency: The maximum data acquisition rate is used during the creep test, resulting in approximately 75 individual readings per second; and between two successive creep tests, when the specimen is subjected to the permanent load level, the measurement frequency is reduced to one reading every two seconds. Displacement readings measured from five LVDTs, as well as the mean of these readings, are exemplarily shown in the Fig. A.5.

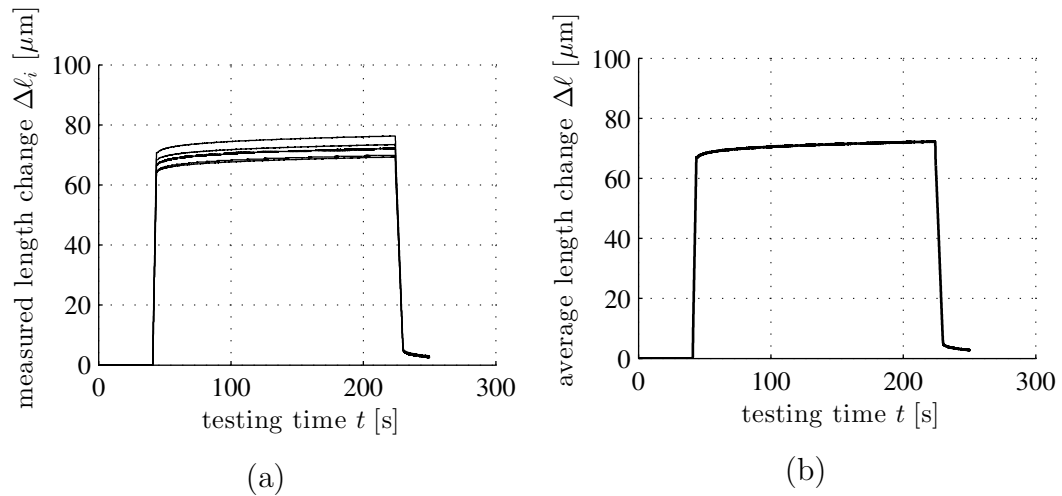


Figure 2.5: Length-changes measured during a creep test on a cement paste specimen with $w/c = 0.42$, subjected at an age of 70 h to a force amounting to 22.79 kN: (a) five individual LVDT readings, (b) mean of five LVDT readings

2.3 Test Evaluation

From each three-minutes creep test, the (elastic) Young's modulus and the creep properties were derived. This is based on force readings, see Fig. A.2, and averaged LVDT readings, see Fig. A.5(b).

2.3.1 Quantification of Young's Modulus

Unloading modulus is determined from point-wisely defined stress-strain diagrams (Karte et al. 2015). They are derived from the central parts of the unloading events, where the desired unloading speed of 1.0 MPa/s was actually realized. To this end, the top 10 % and bottom 5 % of the unloading paths are cut away, see Fig. A.2. Stress ordinates are calculated by dividing the remaining force readings by the crosssectional area of cylindrical specimens, which is equal to $A = 3848.5 \text{ mm}^2$. Corresponding strain ordinates follow

from dividing the averaged LVDT readings by the measurement length, i.e. by 164 mm, being equal to the distance of the two aluminum rings holding the LVDTs. Each point-wisely defined stress-strain diagram is very reliably approximated by a straight line, as quantified by quadratic correlation coefficients typically amounting to $r^2 = 99.7\%$. The slope of the straight line represents the sought unloading modulus, see Fig. A.6.

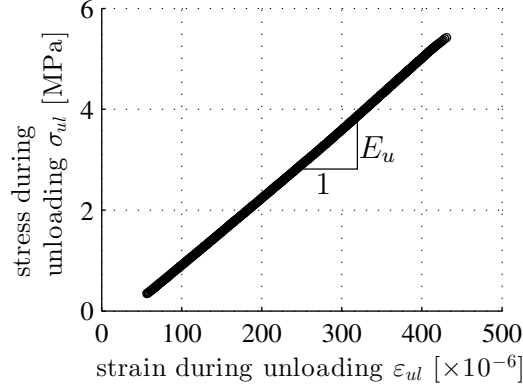


Figure 2.6: Stress-strain diagrams referring to unloading at the end of three-minutes creep test: the slope of best linear fit represents the sought unloading modulus E_u

The unloading modulus is an estimate for the (elastic) Young's modulus because unloading allows for efficient mechanical recovery of energy which was previously stored in the compressed material sample (Coussy 2004; Salençon 2001; Luczynski et al. 2013, 2015). However, since the material creeps, two addition effects need to be considered: (i) the strain response measured during unloading may be partially due to delayed deformations resulting from the load level prescribed before the unloading process; (ii) also during unloading, the strain response may include viscoelastic phenomena with characteristic times in the range of seconds. This calls for an improved estimate for the elastic Young's modulus, as described next: From the total strains (= averaged LVDT readings divided by measured length 164 mm) the elastic strains are subtracted in order to extract the creep strains. Thereby, the elastic strains are computed as the stress (= force readings divided by the crosssectional area $A = 3848.5 \text{ mm}^2$) divided by the estimated elastic Young's modulus:

$$\varepsilon_{creep}(t) = \varepsilon_{total}(t) - \varepsilon_{elastic}(t) = \frac{1}{5 \ell_o} \sum_{i=1}^5 \Delta \ell_i(t) - \frac{\sigma(t)}{E}$$

When computing the creep strain evolution (62) based on the unloading modulus $E = E_u$, the result does not comply with the expectation that creep strains are *compressive* throughout both the loading phase and the subsequent three-minutes creep test. Instead, *tensile* creep strains are obtained at the very

beginning of the loading phase, see Fig. A.7(a), and this nonphysical result is a consequence of the fact that unloading modulus slightly underestimates the Young's modulus. Increasing the Young's modulus value which is used to evaluate Eq. (1), namely, reduces the described tensile strains. This provides a possibility to determine an improved estimate of Young's modulus.

Starting with unloading modulus, progressively larger estimates of Young's modulus are inserted into Eq. (1), until the computed creep strains exhibit the expected property of being compressive everywhere. In more detail, progressive increase of Young's modulus values has converged towards an improved value of Young's modulus, once the creep strain evolution does no longer undershoot the measurement noise-related scatter-bandwidth of creep strains observed in the last seconds *before* the loading event, see Fig. A.7(b). This correction procedure delivers improved estimates of the (elastic) Young's moduli, which are typically by 3% to 4% larger than the unloading moduli.

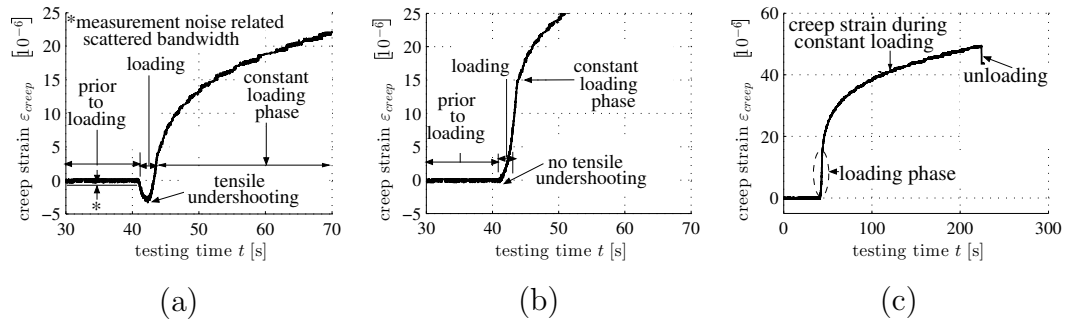


Figure 2.7: Creep strains evolutions computed according to Eq. (1) for cement paste with $w/c = 0.42$ subjected at an age of 70 h to a force amounting to 22.79 kN: (a) unloading modulus (13.633 GPa) results in nonphysical tensile undershooting, (b) improved estimate of Young's modulus (13.995 GPa) delivers a qualitatively plausible creep strain evolution without tensile undershooting, and (c) overall creep strain evolution obtained with the improved estimate of the (elastic) Young's modulus

2.3.2 Quantification of Creep Properties

As for the quantification of the creep properties from the derived creep strain evolution is concerned, we follow Tamtsia and Beaudoin (Tamtsia et al. 2004) and use a power-law type creep function. This choice is appealing because it limits the number of fitting parameters to two only. Tamtsia and Beaudoin introduced the creep compliance rate as (Tamtsia et al. 2004)

$$\frac{dJ(t)}{dt} = C \left(\frac{t - t_0}{t_{ref}} \right)^\gamma \quad (2.1)$$

where $t_{ref} = 1 \text{ d} = 86400 \text{ s}$ is a constant, t_0 denotes the time instant of sudden loading, C the creep compliance rate at time $t = t_0 + t_{ref}$, as follows from specification of Eq. (63) for $t - t_0 = t_{ref}$, and γ represents a dimensionless power-law exponent.

The elementary creep answer for sudden loading at time instant t_0 up to stress level σ_0 which is kept constant thereafter follows as

$$\varepsilon_{total}^{mod}(t) = \frac{\sigma_0}{E} + \int_{t_0}^t \sigma_0 C \left(\frac{\tau - t_0}{t_{ref}} \right)^\gamma d\tau \quad t \geq t_0 \quad (2.2)$$

where σ_0/E denotes the elastic answer of the material at time t_0 . The solution of Eq. (2) reads as

$$\varepsilon_{total}^{mod}(t) = \frac{\sigma_0}{E} + \frac{\sigma_0}{E_c} \left(\frac{t - t_0}{t_{ref}} \right)^\beta \quad t \geq t_0 \quad (2.3)$$

where $E_c = (\gamma + 1)/(C t_{ref})$ denotes the creep modulus at time $t = t_0 + t_{ref}$, as follows from specification of Eq. (65) for $t - t_0 = t_{ref}$, and $\beta = \gamma + 1$ stands, by analogy to γ in Eq. (63), for a dimensionless power-law exponent.

The creep evolution derived from our experiments indicates a significant development of creep strains already during the loading phase. Therefore, the force history is subdivided into a sequence of many small load steps, and Eq. (65) is considered in the framework of Boltzmann's superposition principle (Boltzmann 1878):

$$\varepsilon_{total}^{mod}(t) = \sum_{i=1}^n \frac{F(t_i) - F(t_{i-1})}{A} \left[\frac{1}{E} + \frac{1}{E_c} \left(\frac{t - t_i}{t_{ref}} \right)^\beta \right] \quad t_n \leq t \leq t_{n+1} \quad (2.4)$$

with $F(t_0) = 0.2 \text{ kN}$ representing the permanent load level. Notably, t in Eq. (66) resolves the three-minutes duration of our creep tests. During such a short period of time, the material properties E , E_c , and β in Eq. (66) are virtually constant. Namely, they are functions of the microstructure of cement

paste, the changes of which are driven by the hydration process, and the characteristic time of the latter largely exceeds three minutes. Creep strains follow from the total strains (66) when the elastic contribution is removed, i.e.

$$\varepsilon_{creep}^{mod}(t) = \sum_{i=1}^n \frac{F(t_i) - F(t_{i-1})}{A} \frac{1}{E_c} \left(\frac{t - t_i}{t_{ref}} \right)^\beta \quad t_n \leq t \leq t_{n+1} \quad (2.5)$$

For each test, creep modulus E_c and power-law exponent β are identified such that the square root of sum of squares error, \mathcal{E}_{SRSS} , quantifying the difference between creep strains evolution $\varepsilon_{creep}(t)$ derived from the experiments, see Eq. (62), and modeled creep strains evolution $\varepsilon_{creep}^{mod}(t)$, see Eq. (2.5), attains a minimum:

$$\mathcal{E}_{SRSS}(E_c, \beta) = \sqrt{\frac{1}{N} \sum_{i=1}^N \left[\varepsilon_{creep}(t_i) - \varepsilon_{creep}^{mod}(t_i) \right]^2} \rightarrow \min \quad (2.6)$$

where N is the total number of experimental readings considered for test evaluation during loading and the subsequent load plateau, typically amounting to $N \approx 5400$.

Optimization problem (2.6) is solved iteratively. At first, intervals are defined for the creep modulus E_c and power-law exponent β . These intervals are subdivided such that 7 equidistant values are obtained for both variables to be optimized. For all $7 \times 7 = 49$ combinations, representing a “testing grid” as shown in Fig. 2.8(a), the error function (2.6) is evaluated, see Fig. 2.8(a). The combination of values for E_c and β , which results in the smallest error value, is treated as a first estimate of the optimum solution. It represents the basis for defining improved optimization intervals and corresponding testing grids, as described next.

- If the variable estimate lies on the boundary of the corresponding optimization interval (as is the case for the creep modulus in Fig. 2.8(a)), the interval is shifted by moving its center to the aforementioned variable estimate (as is seen for the creep modulus in Fig. 2.8(b)).
- If the variable does not lie on the boundary of the corresponding optimization interval (as is the case for the power-law exponent in Fig. 2.8(a)), the latter is again shifted so as to take the aforementioned variable estimate as center, but at the same time, the interval is also shrunk to half of its original size, thereby refining its internal “resolution” (see Fig. 2.8(b) for the testing grid shrunk in ordinate direction with respect to its original size seen in Fig. 2.8(a)).

As before, the new optimization intervals are subdivided so as to define 7 equidistant values, and the error function \mathcal{E}_{SRSS} is evaluated for all 49 parameter combinations. After 15 rounds of shifting and refining the optimization

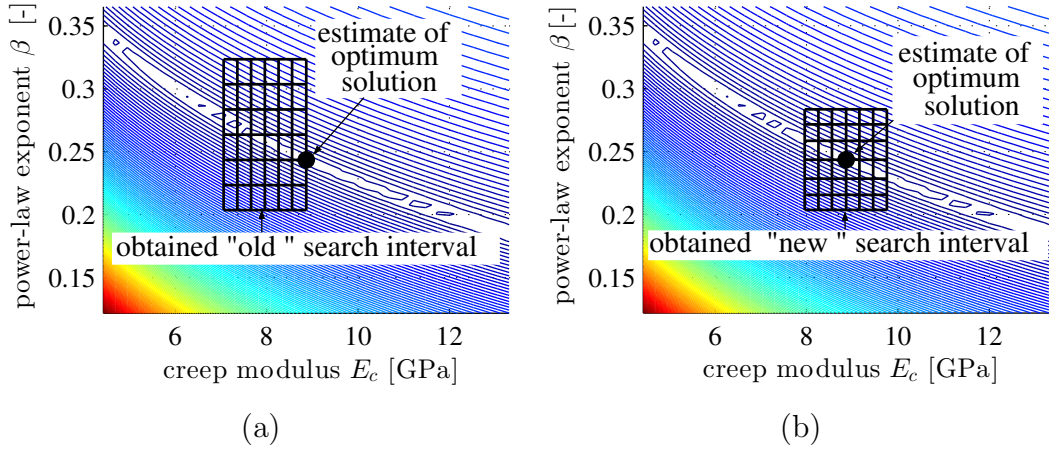


Figure 2.8: Contour plot of the error function (2.6) showing shifting and refinement of search intervals: (a) “old” testing grid with corresponding estimate for optimum solution, in terms of variable combination for E_c and power-law exponent β ; and (b) “new” testing grid for the next iteration of the optimization procedure

intervals, the optimized values are determined up to a precision of 4 significant digits, and the optimization process is stopped. In order to reduce the time required for this optimization procedure to a reasonable minimum, we consider only every fifth data point. This results in an effective measurement frequency of 15 Hz, such that 180 seconds are covered by some 2700 equally spaced readings.

2.4 Results

Evaluation of our test data allows for quantifying the temporal evolution of elastic stiffness and creep properties of cement pastes with $w/c = 0.42$, $w/c = 0.45$, and $w/c = 0.50$, respectively. For each of these compositions, we have tested two different specimens, resulting in virtually the same evaluation results. This underlines the repeatability of the test protocol and the significance of the results discussed next.

2.4.1 Elastic Young’s modulus

The temporal evolution of the (elastic) Young’s modulus increases monotonously and under-linearly with increasing age of the materials. In addition the elastic stiffness is the larger the smaller the initial water-to-cement mass ratio w/c , see Fig. 2.9.

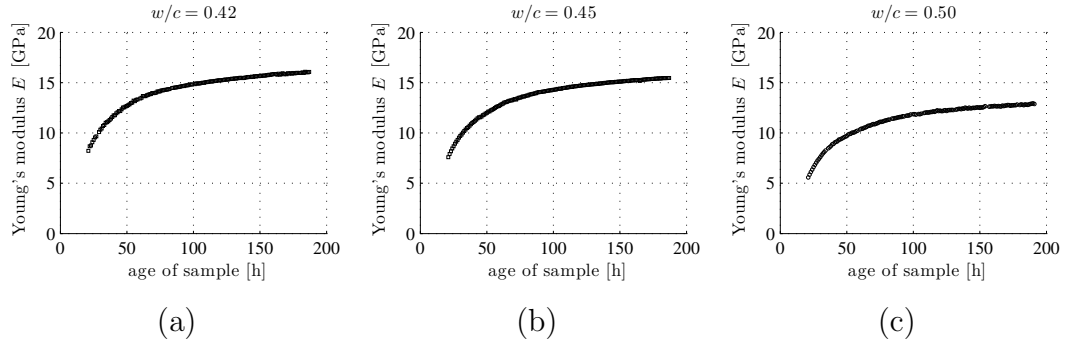


Figure 2.9: Evolution of elastic Young's modulus for cement paste with (a) $w/c = 0.42$, (b) $w/c = 0.45$, and (c) $w/c = 0.50$

The smooth evolution of Young's modulus strongly supports the evaluation strategy described in Section 3.1. Unloading modulus, namely, does not increase monotonously with increasing age of the materials, but it drops slightly every time the load level is updated, i.e. increased, for being kept close to 15% of the compressive strength, see Fig. 2.10.

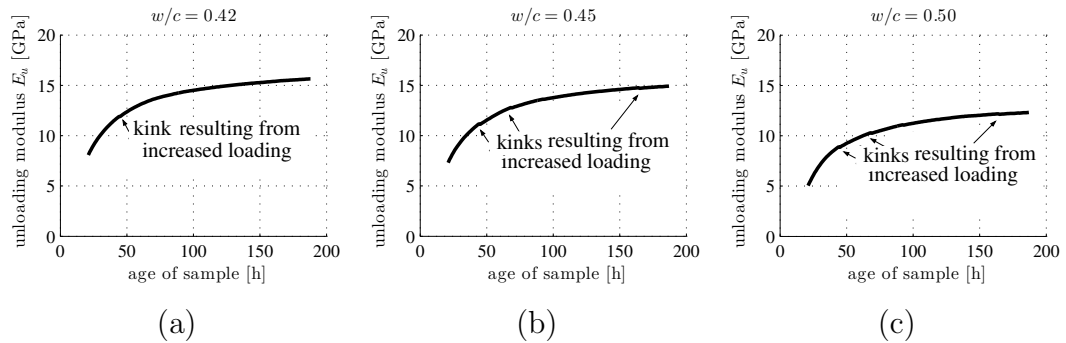


Figure 2.10: Evolution of unloading modulus for cement paste with (a) $w/c = 0.42$, (b) $w/c = 0.45$, and (c) $w/c = 0.50$

2.4.2 Temporal evolution of creep modulus and power-law exponent

The modeled creep strain history (66) allows for an almost perfect fit (see Fig. 2.11) of our measured data in the sense that the strains derived from our experiments fluctuate only slightly around the model predicted strains, and these fluctuations stem practically speaking from the measurement noise, as

quantified by the relative prediction error

$$\mathcal{E}_{rel}(E_c, \beta) = \frac{\frac{1}{N} \sum_{i=1}^N \left[\left| \varepsilon_{creep}^{mod}(t_i) \right| - \left| \varepsilon_{creep}(t_i) \right| \right]}{\frac{1}{N} \sum_{i=1}^N \left| \varepsilon_{creep}(t_i) \right|} \quad (2.7)$$

which is typically as small as 1%. In addition, the determined optimal values of creep modulus E_c and power-law exponent β represent unique solutions, as can be seen from the evaluation of error value (2.6) ($\mathcal{E}_{SRSS} \leq 0.1\mu\text{m}$) over wide intervals of the two optimization variables, see Fig. 2.11 and Fig. 2.12.

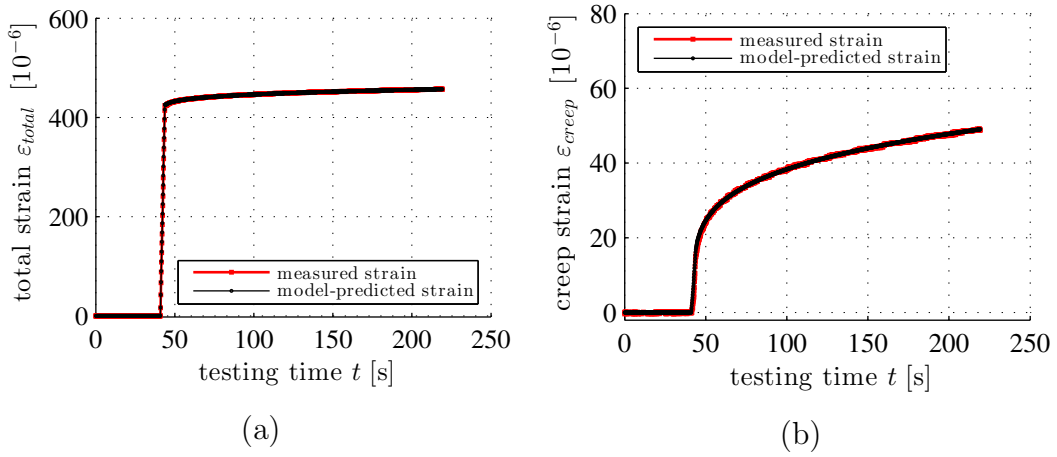


Figure 2.11: Comparison of model predicted strain evolution, see Eq. (66), and measured strain evolution for cement paste with $w/c = 0.42$ subjected at an age of 70 h to a force amounting to 22.79 kN: (a) comparison of total strains, (b) comparison of creep strains; optimal values of E_c and β read as $E_c = 29.94$ GPa and $\beta = 0.22$

Creep moduli increase monotonously and under-linearly with increasing age of materials. In addition, creep moduli are the larger the smaller the initial water-to-cement mass ratio w/c , see Fig. 2.13. Notably, creep moduli E_c are by a factor of 2 to 3 larger than the corresponding (elastic) Young's moduli; compare Fig. 2.9 with Fig. 2.13. As the creep modulus E_c refers to $t_{ref} = 1$ day, the aforementioned comparison implies that after a 1-day constant loading of an invariant microstructure, the creep strains would be by a factor of 2 to 3 smaller than the elastic strains.

Power-law exponent β decreases monotonously and over-linearly with increasing age of the materials, see Fig. 2.14. In contrast to the (elastic) Young's moduli and creep moduli, power-law exponent shows only a minor sensitivity with respect to the composition of the cement paste, in the investigated w/c interval from 0.42 to 0.50.

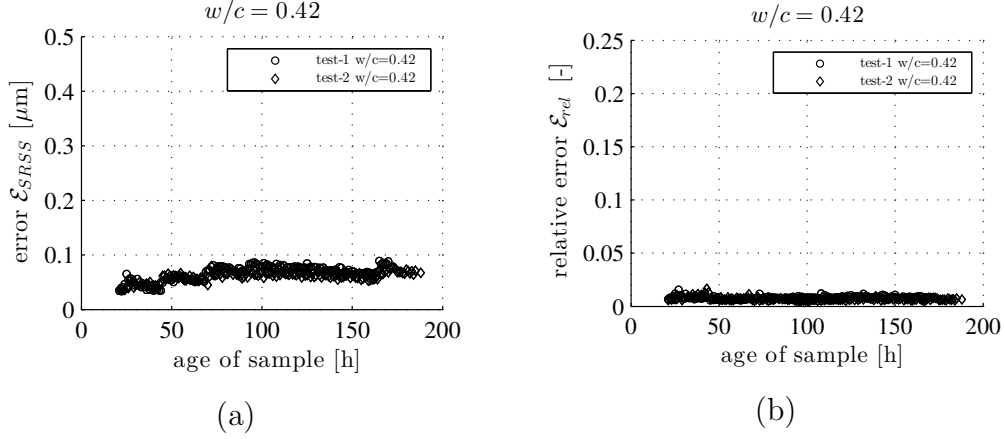


Figure 2.12: Computed error between measured and modeled strain for $w/c = 0.42$: (a) absolute error \mathcal{E}_{SRSS} according to Eq. (2.6), (b) relative error \mathcal{E}_{rel} according to Eq. (2.7)

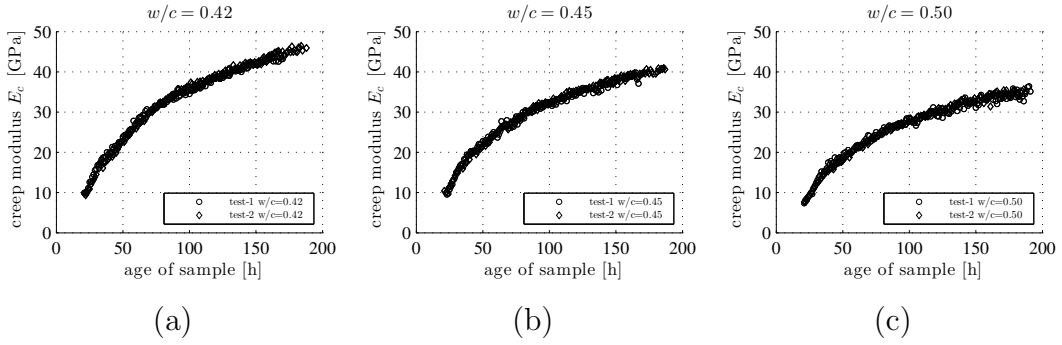


Figure 2.13: Evolution of creep modulus E_c for cement paste with (a) $w/c = 0.42$, (b) $w/c = 0.45$, and (c) $w/c = 0.50$

2.4.3 Evolution of Young's modulus, creep modulus, and power-law exponent as functions of degree of hydration

“Degree of hydration” is clearly preferable over “age of the material” when it comes to selecting a suitable maturity parameter (Ulm and Coussy 1995), because the speed of the chemical reaction between cement clinker and water increases with increasing temperature. This is the motivation for illustrating the evolutions of elastic and creep properties as functions of hydration degree, simply by combining the temporal evolutions of the identified mechanical properties (Young’s modulus, see Fig. 2.9, creep modulus, see Fig. 2.13, and power-law exponent, see Fig. 2.14) with the relationships between hydration degree and age of the tested cement pastes, see Fig. A.3(b).

The (elastic) Young’s modulus increases in very good approximation linearly

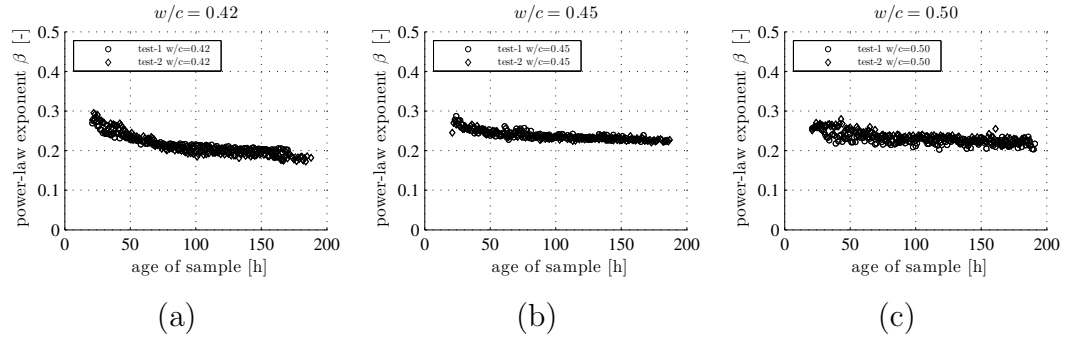


Figure 2.14: Evolution of power-law exponent β in standard optimization over Tamtsia model for cement paste with (a) $w/c = 0.42$, (b) $w/c = 0.45$, and (c) $w/c = 0.50$

with increasing hydration degree in the studied interval ranging from 30% to 65%, see Fig. 2.15. For a given hydration degree, Young's modulus is the larger, the smaller the initial water-to-cement mass ratio. Creep modulus increases over-linearly with increasing hydration degree, see Fig. 2.16. For a given hydration degree, creep modulus is the larger, the smaller the initial water-to-cement mass ratio. The power-law exponent slightly decreases – in an apparently linear fashion – with increasing hydration degree, see Fig. 2.17. Interestingly, different compositions in terms of different initial water-to-cement mass ratios do not exhibit a significant influence of the absolute values of the power-law exponent, at least in the investigated composition interval ranging from $w/c = 0.42$ to $w/c = 0.50$.

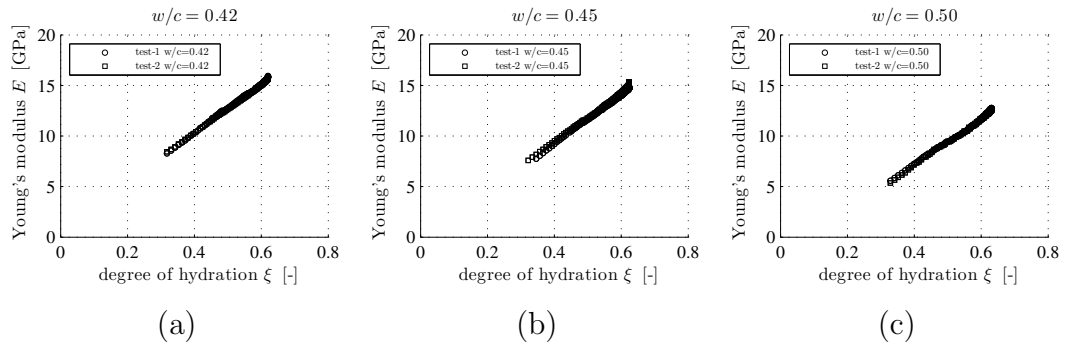


Figure 2.15: Elastic Young's modulus E as a function of hydration degree, for cement paste with (a) $w/c = 0.42$, (b) $w/c = 0.45$, and (c) $w/c = 0.50$

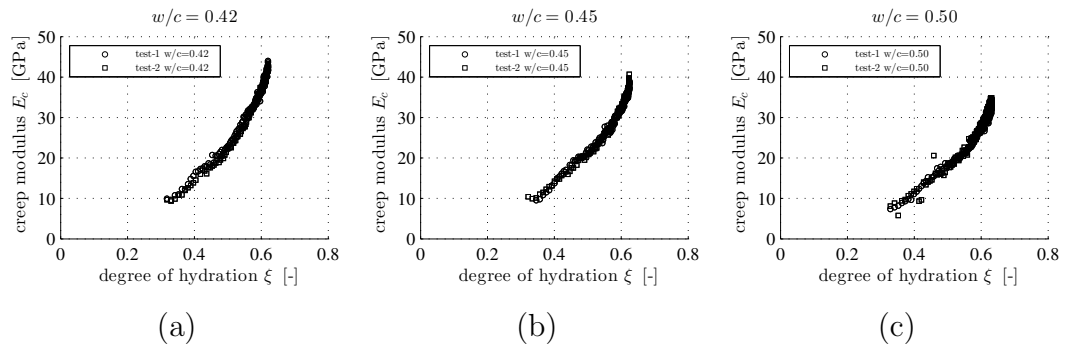


Figure 2.16: Creep modulus E_c as a function of hydration degree, for cement paste with (a) $w/c = 0.42$, (b) $w/c = 0.45$, and (c) $w/c = 0.50$

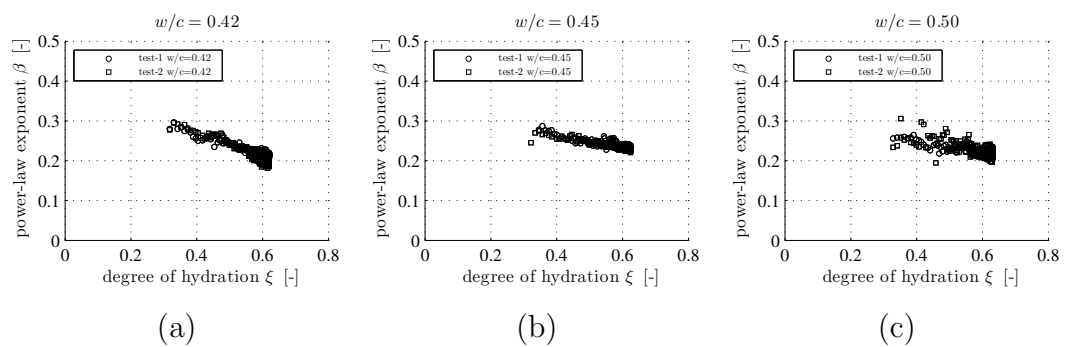


Figure 2.17: Power law exponent β as a function of hydration degree, for cement paste with (a) $w/c = 0.42$, (b) $w/c = 0.45$, and (c) $w/c = 0.50$

2.5 Discussion

We here discuss the non-aging and non-damaging aspects of the new creep testing protocol (Subsection 2.5.1), the role of self-desiccation and the associated reduction of internal relative humidity (Subsection 2.5.2), alternatives to the here-used test evaluation strategy (Subsection 2.5.3), we address the question regarding the difference between static and dynamic elastic stiffness by comparing the statically obtained Young's moduli with results from ultrasonics testing on the same materials (Subsection 2.5.4), we discuss the transition from initially power law-type creep to logarithmic creep (Subsection 2.5.5), we check extrapolation of creep properties from three-minutes non-aging creep tests to two-days aging creep tests (Subsection 2.5.6), and we close with a future outlook regarding testing of microstructurally-designed materials (Subsection 2.5.7).

2.5.1 Non-aging, non-damaging creep tests

Our individual creep tests last for three minutes, and this is so short that the microstructure of cement paste remains in very good approximation the same, although hydration continues during each creep test. Two subsequent creep tests, in turn, are separated by a characteristic duration of one hour. This time span is large enough that two subsequent tests provide access to properties of two already different microstructures.

The prescribed creep loads are smaller than or equal to 15% of the uniaxial compressive strength predicted by a validated multiscale strength model for cement pastes (Pichler et al. 2013; Pichler and Hellmich 2011). These load levels are small enough for allowing damage-free mechanical testing of the investigated specimens. At the same time, they are large enough for provoking length changes within the measurement region of the tested specimens, which are large enough as to ensure reliable readings of the used displacement sensors. Deformation readings taken within the first few minutes right *after* the completion of the creep test provide valuable experimental insight into the two aspects discussed above. Notably, our specimens return to the configuration *before* the creep test (Fig. 2.18), up to resolution being equal to the measurement accuracy of our displacement sensors, which amounts to approximately $0.1\ \mu\text{m}$, (Karte et al. 2015). This practically complete recovery of spontaneous elastic and delayed creep deformation underlines (i) the effectiveness of the chosen strategy in preventing damage of the tested materials, and (ii) that the microstructure has practically not changed during the test.

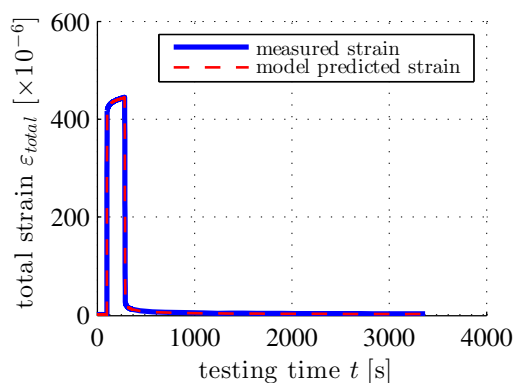


Figure 2.18: Strain evolution of a specimen loaded, at an age of 70 h, to a force of 22.79 kN for three minutes; and being without load thereafter: measurements and predictions according to Eq. (66)

2.5.2 Self-desiccation and reduction of internal relative humidity

Hourly repeated creep tests on young cement pastes provide access to hydration-induced evolutions (i) of elastic properties in terms of Young's modulus E and (ii) of creep properties in terms of creep modulus E_c and power-law exponent β . The significant increase of creep modulus during the observed interval of material age can be explained from a microstructural viewpoint. At microstructural scales, hydration consumes water and cement clinker for the production of cement hydrates. This implies, on the one hand, that capillary porosity decreases with increasing hydration, reducing the stress concentration into the creeping hydrates and, hence, reducing the overall creep activity. On the other hand, the water content of cement paste decreases because of hydration, and this self-desiccation process (Chen et al. 2013) is also known to reduce the creep activity of the material (Jiang et al. 2014; Bažant and Chern 1985). In order to avoid loss of water through drying, our specimens were sealed against the ambient air, from right after production until the end of the testing activity. In this context, it is interesting to note that measurements of relative humidity on sealed cement pastes with initial water-to-cement ratios ranging from 0.22 to 0.35, revealed a humidity decrease from initially 100% down to about 90%, see Wyrzykowski and Lura (Wyrzykowski and Lura 2014). While humidity was not monitored in the present study, similar evolutions will have probably taken place inside the specimens investigated here.

In order to provide more insight into the question whether (i) stress concentration into hydrates or (ii) self-desiccation and decrease of relative humidity is more important for early-age creep of cement paste, we study the evolution of the creep compliance $1/E_c$ as a function of the gel-space ratio γ_g (Freysinet 1933). This maturity parameter combines both composition in terms of the initial water-to-cement mass ratio w/c and the hydration degree ξ , see, e.g. (Pich-

ler et al. 2013)

$$\gamma_g = \frac{43.15 \xi}{20 \xi + 63 w/c} \quad (2.8)$$

Creep compliance values identified based on six tested specimens (two for each of the considered compositions in terms of $w/c = 0.42$, $w/c = 0.45$, and $w/c = 0.50$, respectively; see Fig. 2.16) form a quite dense data cloud, when plotted as a function of gel-space ratio, see Fig. 2.19. Notably, also early-age uniaxial compressive strength of cement pastes with different compositions is – in good approximation – a universal function of gel-space ratio (Pichler et al. 2013), and this opens the door to the following interpretation of similarities between compressive strength and creep compliance. As regards strength, hydrates hold together cement paste microstructures, such that the microscopic load carrying capacity of hydrates triggers the macroscopic strength of cement paste. A universal relationship between strength and gel-space ratio indicates that *differently composed* cement pastes exhibiting *the same* gel-space ratio show *the same* stress concentration from macroscopic loading imposed on a cement paste specimen down to stresses of microscopic hydrates. Therefore, the “pseudo-universal” relationship between creep compliance and gel-space ratio (Fig. 2.19) suggests that also creep of young cement pastes is mainly triggered by stress concentration from macro-loading down to stresses in microscopic hydrates, at least in the investigated range of gel-space ratios ranging from 35 to more than 60 %. This motivates further investment into multiscale creep modeling of cement pastes (Sanahuja 2013b; Scheiner and Hellmich 2009; Sanahuja and Dormieux 2010).

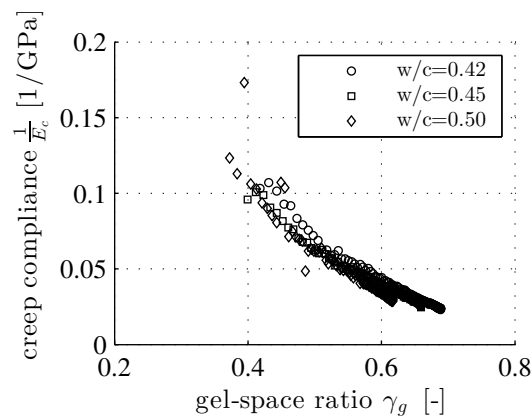


Figure 2.19: Creep compliance $\frac{1}{E_c}$ as a function of gel space ratio γ_g for cement pastes with different w/c ratios

2.5.3 Test evaluation strategy

Identification of elastic and creep properties represents an optimization problem, and this raises the question regarding a suitable solution method. No-

tably, the error surface defined through (2.6) exhibits several local minima resulting from the measurement noise (see Fig. 2.8). Gradient descend methods, such as, e.g., the Levenberg-Marquardt method, would identify a local minimum, rather than the sought global minimum. This raises the need for an optimization algorithm checking the error surface also in the vicinity of a detected near-optimum solution. The optimization approach used here provides a satisfactory solution to this problem. Namely, several numerical tests provided evidence that this approach indeed identifies the global minimum of the underlying error surfaces.

We here identified elastic and creep properties by means of a two-step strategy. At first, we identified the elastic Young's modulus from a stress strain relation obtained via unloading (see Fig. A.6), while forbidding tensile creep strains during a compressive creep test. After that, the identification of creep modulus and power-law exponent requires the solution of a two-dimensional optimization problem. An alternative strategy would have been to identify all three quantities simultaneously. Notably, this three-dimensional optimization problem is challenging because the sensitivity of modeled strains with respect to changes in Young's modulus is, by orders of magnitude, larger than the sensitivity with respect to changes in creep modulus and power-law exponent. This would imply that the "optimal Young's modulus" were even smaller than the unloading modulus, and that the "optimal creep strains" would again imply non-physical tensile creep strains under compressive loading. Hence, the proposed mechanics-based, staggered, identification strategy is clearly preferable over identification strategies which are merely motivated by mathematical formalisms alone.

The idea that, due to viscoelastic deformations, the unloading modulus is not necessarily equal to the elastic modulus, is not new. E. g. in the context of indentation experiments, Feng and Ngan (Feng and Ngan 2002) have proposed to determine the elastic modulus from the indentation rate right before *before* initiation of unloading and the force rate right at the *beginning* of the unloading phase. Translated into the present context of macroscopic material testing, the aforementioned "correction strategy" would read as

$$\frac{1}{E} = \frac{1}{E_u} - \frac{\dot{\epsilon}(t_u^-)}{\dot{\sigma}(t_u^+)} \quad \text{with} \quad \dot{\epsilon}(t_u^-) = \lim_{\epsilon \rightarrow 0^+} \dot{\epsilon}(t_u - \epsilon) \quad \text{and} \quad \dot{\sigma}(t_u^+) = \lim_{\epsilon \rightarrow 0^+} \dot{\sigma}(t_u + \epsilon) \quad (2.9)$$

where t_u denotes the time instant when unloading starts. In Eq. (2.9), $\dot{\epsilon}(t_u^-)$ and $\dot{\sigma}(t_u^+)$, respectively, denote the strain rate right before unloading and the stress rate right at the beginning of the unloading phase. However, the "correction strategy" (2.9) cannot be implemented in the present context of macroscopic experiments, because the acceleration capabilities of the piston of a spindle-based electromechanical testing machine are much more limited than those of a nanoindentation tip. While nanoindentation devices typically allow for quasi-immediate prescription of a desired unloading force rate, macroscopic mechanical test devices do not allow for such an option: Strictly speaking, the

macroscopic unloading stress rate vanishes at the beginning of the unloading phase. As a remedy, one could evaluate Eq. (2.9) based on the *average* stress rate during unloading rather than based on the stress rate right at the *beginning* of the unloading phase, but this would result in an “improved” value for Young’s modulus, which would still be related to significant tensile creep strains at the beginning of the loading phase. Hence, we conclude that the approach of Feng and Ngan cannot be straightforwardly adapted for our present experimental set-up.

2.5.4 Static versus dynamic stiffness

It is interesting to compare the elastic Young’s moduli, as they were herein determined from a quasi-static test protocol, with ultrasonic experimental results of (Karte et al. 2015) on the same cement pastes (identical raw materials and compositions $w/c = 0.42$ and $w/c = 0.50$); i.e. with Young’s moduli derived from a dynamic test protocol. Remarkably, they are essentially the same, see Fig. 2.20. While this somewhat contradicts the tale of the “difference between quasi-static and dynamic Young’s moduli” (Kolias and Williams 1980), it is perfectly in line with the energetic and thermodynamic definition of elasticity (Coussy 2004; Salençon 2001): Elasticity is path-independent, and therefore, also independent on the velocities and rates experienced along the evolution of whatever path. Accordingly, any “moduli” derived from stress-strain protocols exhibiting strain rate-dependencies, relate (at least partially) to dissipative phenomena: This concerns potentially visco-elasto-viscoplastic loading moduli (often, but still confusingly, termed “quasi-static Young’s moduli” (Kolias and Williams 1980)) as well as potentially visco-elastic unloading moduli (as recently documented by Karte et al (Karte et al. 2015)), which in light of the present results, would also reflect delayed dissipation-related phenomena.

It is also interesting to discuss the possible activation of loading-induced pore pressures. Macroscopic compressive loading of cement paste leads to a reduction of the macroscopic specimen volume, and this manifests itself at the microscale in a volume reduction of the solid constituents and of the pore space. The reduction of porosity is a driving force for water transport from water-filled into air-filled pores. Water transport counteracts the build-up of pore water pressure, but is limited by the size of the channels which connect neighboring pores. Therefore, the faster the macroscopic loading is increased, the less effective can transport processes counteract the build-up of pore water pressure. The latter, in turn, increases the macroscopic apparent stiffness of the material. Hence, one would expect that the apparent macroscopic stiffness of a porous material increases with increasing loading speed. In this context, it is noteworthy that ultrasonics (exhibiting extremely fast loading speed) and the present quasi-static experiments delivered virtually identical elastic stiffnesses. This result strongly suggests that both types of tests activate the same

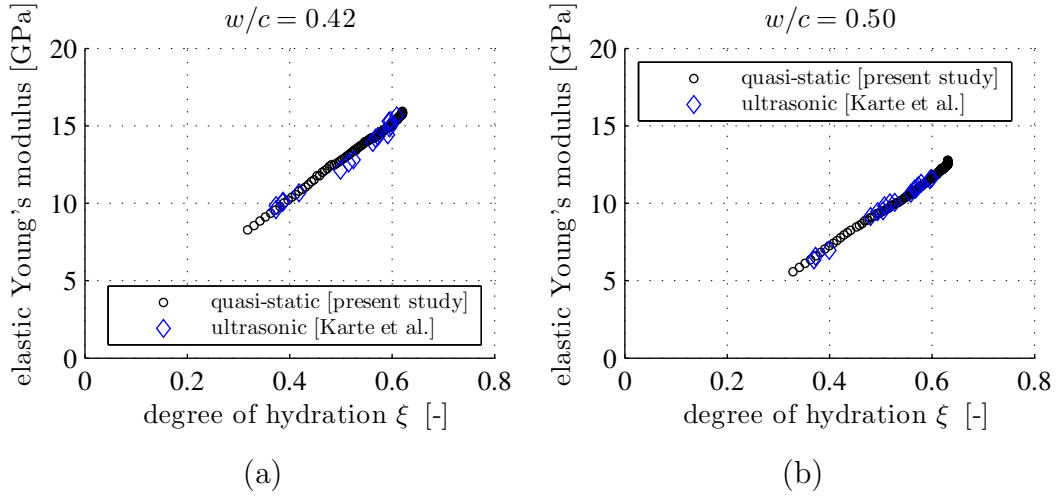


Figure 2.20: Comparison between the static Young's modulus identified herein, with the dynamic Young's modulus reported by Karte et al. (Karte et al. 2015). Very remarkably they turn out to be essentially the same, (a) $w/c = 0.42$, and (b) $w/c = 0.50$

types of pore pressures. One could speculate that significant pore pressures are activated in isolated (non-connected) gel pores, while no significant pore pressures are activated in well-connected capillary pores. Clarification requires future research combining experiments with microporomechanical theories, as the ones described by Dormieux et al. (Dormieux et al. 2006).

2.5.5 Macroscopic testing versus microindentation testing: Power-law creep versus logarithmic creep?

It is interesting to compare our minutes-long *macroscopic* creep tests with minutes-long *microindentation* creep tests into cement paste (Vandamme and Ulm 2013; Jones and Grasley 2011; Zhang 2014) and with minutes-long *nanoinindentation* creep tests into low-density C-S-H (Vandamme and Ulm 2013). The three methods deliver similar results in the sense that they all indicate *non-asymptotic* creep behavior. However, there are also significant qualitative differences. Nano- and microindentation yield – after an initial transition phase – so-called logarithmic creep, which is expressed by a *linear* relation between creep deformation and the logarithm of time, i.e. an *underlinear* relation between the logarithm of creep deformation and the logarithm of time. Our macroscopic tests, in turn, yield power law-type creep, which is expressed by an *overlinear* relation between creep deformation and the logarithm of time, i.e. by a *linear* relation between the logarithm of creep deformation and the logarithm of time. Together, these two observations suggest that creep of cement paste starts with power-law creep rates and ends, after an intermediate

transition phase, with logarithmic creep rates. This is underlined by non-aging macroscopic creep tests on mature cement pastes with characteristic durations of more than 75 days, see Zhang et al. (Zhang et al. 2014). The initial part of the measured creep functions can be represented very reliably by means of power laws (Fig. 2.21). The final part of the measured creep functions, in turn, can be represented very reliably by means of a logarithmic function of the form $J(t) = (1/C) \times \ln(t/\tau + 1)$, with C and τ as fitting parameters. This suggests that the transition from initial power law-type creep to subsequent logarithmic creep takes place between 20 and 45 days after the start of the creep test. Also, it may be possible, in the future, to perform two three-minutes creep tests – one macroscopic test such as described herein, and one microindentation test such as described in (Zhang et al. 2014) –, in order to characterize the complete creep function of a non-aging cement paste.

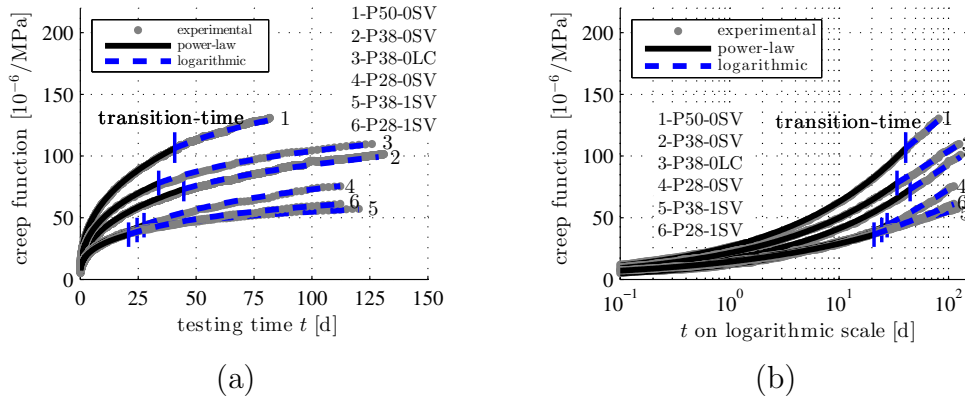


Figure 2.21: Transition from power law-type to logarithmic creep behavior, shown by example of creep experiments reported by Zhang et al. (Zhang et al. 2014) for mature cement pastes which were tested longer than 75 days: creep functions plotted over (a) linear and (b) logarithmic time scale

2.5.6 Extrapolation from three-minutes non-aging creep tests to two-days aging creep tests

Next, we discuss potential and limitation regarding the estimation of the aging creep strain development over two days, from data obtained during a three minute non-aging creep test. To this end, we subjected cement paste with $w/c = 0.42$, at an age of 24 hours, to a load of 9.5 kN, and we kept this load constant for the following 48 hours, see Fig. 2.22 for the measured strain evolution. In this context, we note that significant autogenous shrinkage develops during the second and third day after production. Therefore, we consider the measured strains to be a superposition of elastic strains, creep

strains, and autogeneous shrinkage strains

$$\varepsilon_{total}(t) = \varepsilon_{elastic}(t) + \varepsilon_{creep}(t) + \varepsilon_{shrinkage}(t) \quad (2.10)$$

Autogeneous shrinkage strains are discussed next.

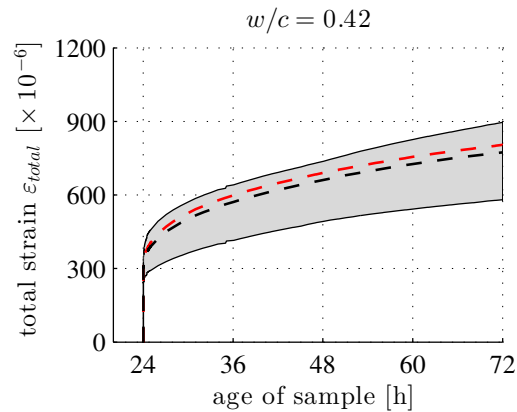


Figure 2.22: Extrapolation from three-minutes non-aging creep tests to two-days aging creep tests of cement paste with $w/c = 0.42$: measured creep strains during two-days creep tests starting at 24 hours age, see dashed curves; and 99 % confidence interval of extrapolated creep strain evolution, see shaded domain; corresponding material properties are collected in Table 2.1

Hydration of cement pastes is associated with autogeneous shrinkage. During a three-minutes creep test, hydration progresses only insignificantly, such that newly developing autogeneous shrinkage strains are negligibly small with respect to the (by order of magnitude larger) elastic and creep strains induced by the mechanical loading. Therefore, it is sufficient to focus on strain *changes* when it comes to identification of elastic and creep properties from three-minutes creep tests, and this is facilitated when setting the strains at the beginning of each three-minutes creep test formally equal to zero. During a time span of hours and days, however, the hydration process does exhibit a significant progress, and this leads to considerable autogeneous shrinkage. In this context, (i) we emphasize that the herein reported quasi-static (elastic) Young's moduli agree extremely well with the ultrasonics results of Karte et al. (Karte et al. 2015), and (ii) we note that ultrasound is well-known to leave specimens undamaged. This suggests that repeated creep testing left our specimens undamaged, and that creep strains are completely recovered after each test, see, e.g., Fig. 2.18. Therefore, the small difference of absolute strains measured right *before* two successive creep tests can be used to quantify the evolution of autogeneous shrinkage strains, see Fig. 2.23. These evolutions are considered in Eq. (2.10).

As for the comparison of creep strains extrapolated, from a three-minutes test, to a two-days test, we note that three-minutes tests provide virtually *non-aging*

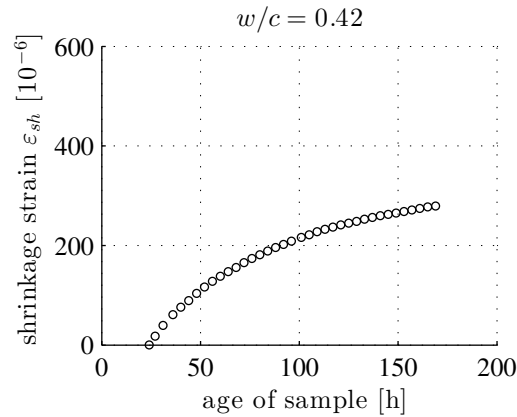


Figure 2.23: Shrinkage strain evolution quantified as the difference of absolute strains measured right *before* two successive creep tests, for $w/c = 0.42$

properties, while two-days tests refer to an *aging* microstructure (because of ongoing hydration). Still, we check the potential relevance of such an extrapolation, by means of the following statistical exercise. We consider (elastic) Young’s modulus E , creep modulus E_c , and power-law exponent β to be random variables characterized by a lognormal distribution, and we determine 99% confidence intervals of the corresponding expected values, for mathematical details see, e.g., (Pichler et al. 2005). The confidence intervals consider the rather small statistical sample size amounting to $n = 4$. Namely, two specimens were tested and evaluated as described in Sections 2.2 and 2.3, and another two specimens were subjected to two-days creep tests, whereby the first three minutes can be evaluated as described in Section 2.3, see Table 2.1. The determined confidence intervals of E , E_c , and β are related to a confidence interval of extrapolated creep strains, see Fig. 2.22. Albeit the large extrapolation distance – two days are by a factor of 960 larger than three minutes –, the confidence interval of extrapolated creep strains encloses the two measured aging strain evolutions. This further corroborates the significance of the herein reported test results. We also conclude that the microstructure which is present at the time instant of loading, plays also an important role for aging creep tests; and this is consistent with recent modeling approaches, see (Sanahuja 2013a,c).

2.5.7 Future outlook to microstructurally-designed materials

In the future, it will be interesting to combine the herein described creep testing protocol with “microstructurally designed” cement pastes. As for their production, a certain part of the clinker is replaced by chemically inert particles of similar size and stiffness, see (Termkhajornkit et al. 2015; Di Bella

Table 2.1: (Elastic) Young’s modulus, creep modulus, and power-law exponent of four samples with $w/c = 0.42$, subjected to three-minutes creep tests, 24 hours after their production; and 99 % confidence intervals of expected values of lognormal distributions

	E	E_c	β
properties of sample #1	9.21 GPa	10.9 GPa	0.282
properties of sample #2	9.28 GPa	12.9 GPa	0.240
properties of sample #3	8.90 GPa	9.93 GPa	0.280
properties of sample #4	8.82 GPa	8.99 GPa	0.286
upper limit of 99 % confidence interval of expected value	9.74 GPa	16.7 GPa	0.344
lower limit of 99 % confidence interval of expected value	8.41 GPa	6.74 GPa	0.214

et al. 2015). Complete hydration results in a material which is representative of an early-age microstructure, because the inert particles take over the role of unhydrated clinker. Thanks to the chemically inert nature of such “microstructurally designed” cement pastes, they may provide insights which are not accessible through test campaigns on hydrating materials, e.g. (i) repeated tests in order to gain very detailed insight into strain recovery, and (ii) test series with increasing load levels, in order to study the transition from linear creep to non-linear creep.

2.6 Conclusions

The following conclusions are drawn:

- The new testing protocol consisting of hourly repeated three-minutes creep tests, with compressive force levels smaller or equal to 15 % of the compressive strength of the material, provides valuable insight into the evolution of elastic and creep properties of hydrating cement pastes.
- Ensuring that creep strains are *compressive* throughout the entire creep test, and this includes in particular the initial phase of loading, allows for identifying a static Young’s modulus which is in very good approximation equal to the dynamic Young’s modulus identified from ultrasonics.
- Any “moduli” derived from stress-strain protocols exhibiting strain rate-dependencies, relate (at least partially) to dissipative phenomena: This concerns potentially visco-elasto-viscoplastic loading moduli (often, but still confusingly, termed “quasi-static Young’s moduli” (Kolias and Williams 1980)) as well as potentially visco-elastic unloading moduli (as

recently documented by Karte et al (Karte et al. 2015)), which in light of the present results, would also reflect delayed dissipation-related phenomena.

Acknowledgment

We cordially thank for valuable help of the laboratory staff of Vienna University of Technology at the Institute of Mechanics of Materials and Structures. The first author also wishes to thank HEC (Higher Education Commission) Pakistan and University of Engineering and Technology, Lahore, Pakistan, for their support.

Nomenclature

Nomenclature

A	—	cross-sectional area of sample
C-S-H	—	Calcium Silicate Hydrates
C	—	creep compliance
E	—	Young's modulus
E_c	—	creep modulus
E_u	—	unloading modulus
F	—	compressive force
ℓ_o	—	measurement length
LVDTs	—	Linear Variable Differential Transducers
Q	—	specific heat release
t	—	time
t_0	—	time instant at start of loading
t_{ref}	—	reference time
w/c	—	initial water-to-cement mass ratio
β	—	power-law exponent
$\Delta\ell_i$	—	length change measured by i -th LVDT
$\Delta\ell_{model}$	—	change of length computed by creep model
$\Delta\ell_{total}$	—	total change of measurement length
$\Delta\ell_{creep}$	—	creep contribution to $\Delta\ell_{total}$
$\Delta\ell_{elastic}$	—	elastic contribution to $\Delta\ell_{total}$
$\Delta\sigma$	—	incremental stress change (positive if compressive)
\mathcal{E}_{SRSS}	—	“square root of sum of squares”- error
\mathcal{E}_{rel}	—	relative prediction error
γ	—	dimensionless power-law exponent
γ_g	—	gel-space ratio
ε	—	strain

ε_{total}	—	total strain
$\varepsilon_{elastic}$	—	elastic strain
ε_{creep}	—	creep strain
$\varepsilon_{creep}^{mod}$	—	modeled creep strain
ε_{ul}	—	strain during unloading
σ	—	compressive stress
σ_0	—	stress at time t_0
σ_{ul}	—	stress during unloading
τ	—	characteristic creep time
ξ	—	degree of hydration

Chapter 3

Downscaling-based identification of non-aging power-law creep of cement hydrates

3.1 Introduction

It is well accepted in the cement and concrete research community that the creep properties of cementitious materials stem from the viscoelastic nature of the reaction products between cement and water, called hydrates; while the remaining solid material constituents, namely unhydrated clinker grains and aggregates, do not exhibit delayed deformations under time-invariant stresses (Neville 1964; Bažant and Prasannan 1989a,b; Acker 2001). It is also a widely acknowledged idea that the aging, i.e. time variant, creep properties of concrete are due to the hydration process, i.e. the subsequent formation of increasingly many hydrates, while the hydrates themselves may actually exhibit non-aging, i.e. time-invariant, creep properties (Bažant and Prasannan 1989a,b; Scheiner and Hellmich 2009). However, quantification of such non-aging hydrate creep properties, both short and long term, remains an unsettled challenge – and this challenge is tackled in the present contribution. In this context, ultra-short term creep tests are of interest (Delsaute et al. 2012, 2016), and we here build upon a very recent experimental campaign consisting of three minute-long creep tests on ordinary Portland cement pastes with different water-to-cement ratios and different maturity degrees (Irfan-ul-Hassan et al. 2016). Over this short creep measuring time, the pastes virtually do not age at all, and their creep behavior is almost perfectly represented (see Fig. 3.1) by a uniaxial

power-law creep function of the form

$$J_{cp}^{exp}(t - \tau) = J_{e,cp}^{exp} + J_{v,cp}^{exp}(t - \tau) = \frac{1}{E_{cp}^{exp}} + \frac{1}{E_{c,cp}^{exp}} \left(\frac{t - \tau}{t_{ref}} \right)^{\beta_{cp}^{exp}}, \quad (3.1)$$

with t as chronological time, τ as time instant of loading, and $t_{ref} = 1 \text{ d} = 86400 \text{ s}$ as a fixed reference time (Irfan-ul-Hassan et al. 2016); with E_{cp}^{exp} denoting the Young's elastic modulus, $E_{c,cp}^{exp}$ denoting the Young's creep modulus, and β_{cp}^{exp} representing a dimensionless power-law exponent. Notably, the latter three quantities depend on the microstructural composition of the cement paste encountered at the time instant of loading, τ .

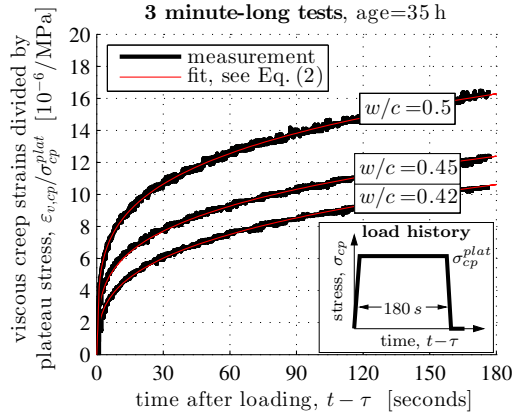


Figure 3.1: Experimentally measured temporal evolutions of viscous creep strains (divided by the applied stress at the loading plateau) and corresponding power-law fits according to Eq. (3.1) for 35h old cement paste with $w/c \in \{0.42, 0.45, 0.50\}$; quadratic correlation coefficients amount to $R^2 = \{99.7\%, 99.6\%, 99.5\%\}$; see (Irfan-ul-Hassan et al. 2016) for details

In the remainder of the present paper, we will test whether the maturity- and composition-dependent parameters $E_{c,cp}^{exp}$ and β_{cp}^{exp} reported by Irfan-ul-Hassan et al. (2016) may actually be traced back to only one “universal” Portland cement-related, isochoric hydrate creep tensor function

$$\mathbb{J}_{hyd}(t - \tau) = \frac{1}{3k_{hyd}} \mathbb{I}_{vol} + \frac{1}{2} \left[\frac{1}{\mu_{hyd}} + \frac{1}{\mu_{c,hyd}} \left(\frac{t - \tau}{t_{ref}} \right)^{\beta_{hyd}} \right] \mathbb{I}_{dev}, \quad (3.2)$$

with the (elastic) bulk and shear modulus of the hydrates denoted as k_{hyd} and μ_{hyd} , and with the shear creep modulus and the power-law creep exponent of hydrates denoted as $\mu_{c,hyd}$ and β_{hyd} . \mathbb{I}_{vol} and \mathbb{I}_{dev} are the volumetric and deviatoric parts of the fourth-order identity tensor \mathbb{I} , defined as $I_{ijkl} = 1/2(\delta_{ik}\delta_{jl} + \delta_{il}\delta_{jk})$, $\mathbb{I}_{vol} = 1/3(\mathbf{1} \otimes \mathbf{1})$, and $\mathbb{I}_{dev} = \mathbb{I} - \mathbb{I}_{vol}$, respectively, whereby $\mathbf{1}$ denotes the second-order identity tensor with components equal to the Kronecker delta δ_{ij} , namely $\delta_{ij} = 1$ for $i=j$, and 0 otherwise. For

“downscaling” from the cement paste to the hydrate level, we use the micromechanical representation of cement paste as developed by [Pichler and Hellmich \(2011\)](#), in combination with the theory of viscoelastic homogenization ([Laws and McLaughlin 1978](#); [Scheiner and Hellmich 2009](#); [Sanahuja and Dormieux 2010](#)).

The present paper is organized as follows: after a review of micromechanics and viscoelastic scale transitions, mixture-independent hydrate creep is back-analyzed from the aforementioned three minute test campaign over various mixtures. The resulting hydrate creep function is then further validated through Tamtsia and Beaudoin’s classical test on very old cement paste ([Tamtsia and Beaudoin 2000](#)). Corresponding results are carefully discussed thereafter, followed by concluding remarks.

3.2 Micromechanics of creeping cement pastes

3.2.1 Micromechanical representation of cement pastes

Cement pastes are microheterogeneous materials exhibiting a scale-separated hierarchical organization. In agreement with our focus on creep of cement paste, we here account for four quasi-homogeneous constituents (or material phases), namely for cement clinker, water, hydration products, and air. Their characteristic sizes, their characteristic phase shapes, and their specific modes of mutual interaction motivate the two-scale representation of cement pastes according to [Pichler and Hellmich \(2011\)](#), sketched in Fig. 3.2.

- At the scale of a few tens of microns, we envision a representative volume element (RVE) of *hydrate foam*, consisting of single micron-sized or even smaller spherical water and air phases, as well as of similarly thick hydrate needles oriented uniformly in all space directions. All three material phases are in direct mutual interaction, i.e. they are arranged in a polycrystalline fashion.
- At the significantly larger scale of several hundreds of microns, we envision a representative volume element of *cement paste*, consisting of a quasi-homogeneous hydrate foam matrix and a spherical cement clinker phase. Their interaction is the one typically encountered in matrix-inclusion composites.

3.2.2 Homogenization of hydrate foam properties

The RVE of Fig. 3.2(b) is subjected to homogeneous (“macroscopic”) strains $\boldsymbol{\varepsilon}_{hf}$, in terms of “microscopic” displacements $\underline{\xi}(\underline{x}, t)$ fulfilling

$$\underline{\xi}(\underline{x}, t) = \boldsymbol{\varepsilon}_{hf}(t) \cdot \underline{x}, \quad (3.3)$$

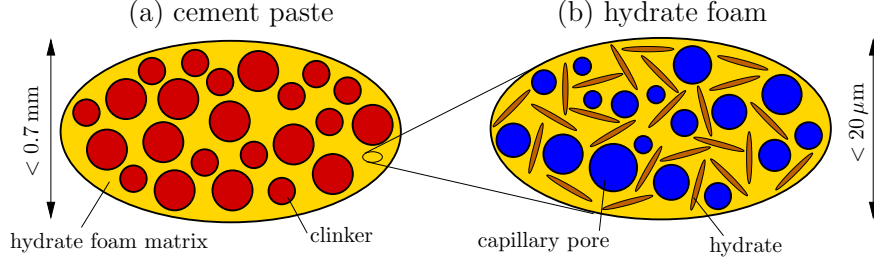


Figure 3.2: Micromechanical representation of cement paste by means of the two-step homogenization scheme of Pichler and Hellmich (2011): (a) RVE of matrix-inclusion composite “cement paste” where a spherical clinker phase is embedded in a hydrate foam matrix [modeled by means of a Mori-Tanaka scheme (Mori and Tanaka 1973; Benveniste 1987; Bernard et al. 2003b)]; (b) polycrystalline RVE of “hydrate foam” built up of spherical capillary porosity (water and air phases), as well as of needle-shaped hydrate phases oriented uniformly in all space directions [modeled by means of a self-consistent scheme (Hershey 1954; Hill 1965; Fritsch et al. 2006)]; all schematic 2D sketches refer to 3D volume elements

with \underline{x} labeling positions inside as well as at the boundary of the RVE. Boundary condition (3.3) and compatibility of the microstrains inside the RVE, reading as

$$\underline{\varepsilon}(\underline{x}, t) = \frac{1}{2} [\nabla \underline{\xi}(\underline{x}, t) + \nabla^T \underline{\xi}(\underline{x}, t)] , \quad (3.4)$$

imply the so-called strain average rule (Hashin 1983; Zaoui 2002)

$$\underline{\varepsilon}_{hf}(t) = \frac{1}{V_{hf}} \int_{V_{hf}} \underline{\varepsilon}(\underline{x}, t) dV , \quad (3.5)$$

with V_{hf} as the volume of the RVE. Moreover, these deformations provoke traction forces \underline{T} at the boundary ∂V_{hf} of the RVE, and equilibrated microstresses $\underline{\sigma}$ throughout the RVE. They fulfill

$$\underline{T}(\underline{x}, t) = \underline{\sigma}(\underline{x}, t) \cdot \underline{n}(\underline{x}) \quad \text{and} \quad \text{div} \underline{\sigma}(\underline{x}, t) = 0 , \quad (3.6)$$

with \underline{n} as the normal to the surface ∂V_{hf} of the RVE. The (external) work density done by these traction forces reads as

$$\begin{aligned} W_{hf}^{ext}(t) &= \frac{1}{V_{hf}} \int_{\partial V_{hf}} \underline{T}(\underline{x}, t) \cdot \underline{\xi}(\underline{x}, t) dS \\ &= \frac{1}{V_{hf}} \int_{\partial V_{hf}} [\underline{\varepsilon}_{hf}(\underline{x}, t) \cdot \underline{x}] \cdot [\underline{\sigma}(\underline{x}, t) \cdot \underline{n}(\underline{x})] dS = \underline{\varepsilon}_{hf}(t) : \frac{1}{V_{hf}} \int_{V_{hf}} \underline{\sigma}(\underline{x}, t) dV . \end{aligned} \quad (3.7)$$

Hence, the force quantity doing work on the macroscopic strains $\underline{\varepsilon}_{hf}$ is the spatial average over the microscopic stresses. Thus, this average qualifies as

the macroscopic stress, i.e. here as the stress tensor $\boldsymbol{\sigma}_{hf}$ related to the hydrate foam,

$$\boldsymbol{\sigma}_{hf}(t) = \frac{1}{V_{hf}} \int_{V_{hf}} \boldsymbol{\sigma}(\underline{x}, t) dV. \quad (3.8)$$

Given the morphological representation of the hydrate foam RVE [see Fig. 3.2 (b)], the strain average rule (3.5) takes the particular form

$$\boldsymbol{\varepsilon}_{hf}(t) = f_{por}^{hf} \boldsymbol{\varepsilon}_{por}(t) + f_{hyd}^{hf} \int_0^{2\pi} \int_0^{\pi} \boldsymbol{\varepsilon}_{hyd}(\varphi, \vartheta, t) \frac{\sin \vartheta}{4\pi} d\vartheta d\varphi. \quad (3.9)$$

In Eq. (3.9), f_{por}^{hf} , and f_{hyd}^{hf} denote the volume fractions of capillary pores and of the hydrates, within the RVE of hydrate foam. $\boldsymbol{\varepsilon}_{por}$ is the microstrain averaged over the RVE-subvolume $V_{por} = V_{air} + V_{H_2O}$, occupied by the capillary pores, namely

$$\boldsymbol{\varepsilon}_{por}(t) = \frac{1}{V_{por}} \int_{V_{por}} \boldsymbol{\varepsilon}(\underline{x}, t) dV, \quad (3.10)$$

and $\boldsymbol{\varepsilon}_{hyd}(\varphi, \vartheta)$ relates to the average strains in the needle-shaped hydrate phase oriented in φ, ϑ -direction,

$$\boldsymbol{\varepsilon}_{hyd}(\varphi, \vartheta, t) = \frac{1}{\ell(\varphi, \vartheta)} \int_{\ell(\varphi, \vartheta)} \boldsymbol{\varepsilon}(\underline{x}, t) ds, \quad (3.11)$$

with $\ell(\varphi, \vartheta)$ as the length of all needle-shaped hydrates oriented in φ, ϑ -direction. Analogously, the stress average rule (3.8) specifies to

$$\boldsymbol{\sigma}_{hf}(t) = f_{por}^{hf} \boldsymbol{\sigma}_{por}(t) + f_{hyd}^{hf} \int_0^{2\pi} \int_0^{\pi} \boldsymbol{\sigma}_{hyd}(\varphi, \vartheta, t) \frac{\sin \vartheta}{4\pi} d\vartheta d\varphi. \quad (3.12)$$

The hydrates exhibit viscoelastic behavior (Acker 2001),

$$\boldsymbol{\sigma}_{hyd}(t) = \int_{-\infty}^t \mathbb{R}_{hyd}(t-\tau) : \frac{\partial \boldsymbol{\varepsilon}_{hyd}(\tau)}{\partial \tau} d\tau, \quad \boldsymbol{\varepsilon}_{hyd}(t) = \int_{-\infty}^t \mathbb{J}_{hyd}(t-\tau) : \frac{\partial \boldsymbol{\sigma}_{hyd}(\tau)}{\partial \tau} d\tau, \quad (3.13)$$

where the creep and relaxation tensor functions, \mathbb{J}_{hyd} and \mathbb{R}_{hyd} , fulfill the convolution condition (Schwarzl and Struik 1968)

$$\int_{-\infty}^t \mathbb{J}_{hyd}(t-\tau) : \mathbb{R}_{hyd}(\tau) d\tau = \int_{-\infty}^t \mathbb{R}_{hyd}(t-\tau) : \mathbb{J}_{hyd}(\tau) d\tau = t \mathbb{I}, \quad (3.14)$$

and where the hydrate creep function has the format of Eq. (3.2). On the other hand, the capillary pore phase behaves elastically,

$$\boldsymbol{\sigma}_{por}(t) = \mathbb{C}_{por} : \boldsymbol{\varepsilon}_{por}(t), \quad (3.15)$$

with the stiffness tensors \mathbb{C}_{por} playing the role of time-invariant (constant) relaxation “functions”,

$$\mathbb{C}_{por} = \mathbb{R}_{por}(t - \tau) = 3 k_{por} \mathbb{I}_{vol} + 2 \mu_{por} \mathbb{I}_{dev} \quad (3.16)$$

whereby $k_{por} = 0$ and $\mu_{por} = 0$ denote the vanishing (elastic) bulk and shear modulus of the pores, i.e. we consider, from a poromechanical viewpoint, drained pores.

Upscaling of this material behavior, up to the level of the hydrate foam, is particularly easily done in the Laplace-Carson (rather than the time) domain. The Laplace-Carson (LC) transform $f^*(p)$ of any time-dependent function $f(t)$ is defined as

$$f^*(p) = p \hat{f}(p) = p \int_0^{\infty} f(t) e^{-pt} dt, \quad (3.17)$$

where p is the complex variable in the Laplace-Carson domain, and $\hat{f}(p)$ is the Laplace transform of $f(t)$. Applying the transformation rule (47) to the viscoelastic behavior of the hydrates (3.13) as well as to the elastic behavior of air and water (46) yields algebraic constitutive equations in the LC space, reading as (Gurtin and Sternberg 1962)

$$\boldsymbol{\varepsilon}_j^*(p) = \mathbb{J}_j^*(p) : \boldsymbol{\sigma}_j^*(p), \quad \boldsymbol{\sigma}_j^*(p) = \mathbb{R}_j^*(p) : \boldsymbol{\varepsilon}_j^*(p) \quad \forall j \in \{por, hyd\}, \quad (3.18)$$

whereby, interestingly, the convolution condition (43) is transformed into a simple inversion rule,

$$\mathbb{R}_j^*(p) = [\mathbb{J}_j^*(p)]^{-1}. \quad (3.19)$$

Hence, LC transformation (47) of the creep function (3.2), followed by insertion of the respective result for $\mathbb{J}_{hyd}^*(p)$ into (49), yields the LC-transformed relaxation function of the hydrates as

$$\begin{aligned} \mathbb{R}_{hyd}^*(p) &= 3 k_{hyd} \mathbb{I}^{vol} + 2 \mu_{hyd}^*(p) \mathbb{I}^{vol} \\ &= 3 k_{hyd} \mathbb{I}^{vol} + 2 \left[\frac{1}{\mu_{hyd}} + \frac{1}{\mu_{c,hyd}} \left(\frac{1}{t_{ref}} \right)^{\beta_{hyd}} \Gamma(\beta_{hyd} + 1) p^{-\beta_{hyd}} \right]^{-1} \mathbb{I}_{dev}. \end{aligned} \quad (3.20)$$

Note that Eqs. (48) are formally identical to the relations encountered with linear elasticity homogenization. Thus, upscaling of viscoelastic properties to the hydrate foam can be done as quasi-elastic homogenization in the LC space [this is referred to as the correspondence principle (Read 1950, 1951; Laws and McLaughlin 1978; Beurthey and Zaoui 2000)]. This process is based on the LC-transformed average rules (3.9) and (3.12) reading as

$$\boldsymbol{\varepsilon}_{hf}^*(p) = f_{por}^{hf} \boldsymbol{\varepsilon}_{por}^*(p) + f_{hyd}^{hf} \int_0^{2\pi} \int_0^{\pi} \boldsymbol{\varepsilon}_{hyd}^*(\varphi, \vartheta, p) \frac{\sin \vartheta}{4\pi} d\vartheta d\varphi, \quad (3.21)$$

$$\boldsymbol{\sigma}_{hf}^*(p) = f_{por}^{hf} \boldsymbol{\sigma}_{por}^*(p) + f_{hyd}^{hf} \int_0^{2\pi} \int_0^{\pi} \boldsymbol{\sigma}_{hyd}^*(\varphi, \vartheta, p) \frac{\sin \vartheta}{4\pi} d\vartheta d\varphi. \quad (3.22)$$

Linearity of the problem defined by (11), (3.6), and (48) implies a *linear* strain concentration rule from the LC-transformed macrostrains to the LC-transformed microstrains in phase j , reading as

$$\boldsymbol{\varepsilon}_j^*(p) = \mathbb{A}_j^*(p) : \boldsymbol{\varepsilon}_{hf}^*(p) \quad \forall j \in \{por, hyd\}, \quad (3.23)$$

where \mathbb{A}_j^* denotes the LC-transformed phase strain concentration tensor, which can be accessed from classical Eshelby-type matrix inclusion problems (Eshelby 1957; Laws 1977; Benveniste 1987; Zaoui 2002), while considering the polycrystalline morphology of the hydrate foam by means of the self-consistent scheme (Hershey 1954; Kröner 1958). This results in

$$\begin{aligned} \mathbb{A}_j^*(p) = & \left\{ \mathbb{I} + \mathbb{P}_j^{hf,*}(p) : [\mathbb{R}_j^*(p) - \mathbb{R}_{hf}^*(p)] \right\}^{-1} : \\ & \left(\begin{aligned} & f_{por}^{hf} \left\{ \mathbb{I} + \mathbb{P}_{sph}^{hf,*}(p) : [\mathbb{R}_{por}^*(p) - \mathbb{R}_{hf}^*(p)] \right\}^{-1} \\ & + f_{hyd}^{hf} \int_0^{2\pi} \int_0^\pi \left\{ \mathbb{I} + \mathbb{P}_{cyl}^{hf,*}(p, \varphi, \vartheta) : [\mathbb{R}_{hyd}^*(p) - \mathbb{R}_{hf}^*(p)] \right\}^{-1} \frac{\sin \vartheta}{4\pi} d\vartheta d\varphi \end{aligned} \right)^{-1} \\ & \forall j \in \{por, hyd\}. \end{aligned} \quad (3.24)$$

In Eq. (54), $\mathbb{P}_j^{hf,*}$ denotes the LC transform of the fourth-order Hill tensor, which accounts for the shape of phase j embedded in a fictitious matrix with “stiffness” \mathbb{R}_{hf}^* . Pores are considered to be spherical inclusions, hydrates are cylindrical (needle-shaped), see Fig. 3.2, and the corresponding LC-transformed Hill tensors read as $\mathbb{P}_{sph}^{hf,*}$, and $\mathbb{P}_{cyl}^{hf,*}$, see the Appendix for corresponding mathematical details. Insertion of the macro-to-micro strain concentration relation (53) and of the constitutive behavior (48)₂, into the LC-transformed stress average rule (52) leads, after comparison to the LC-transformed constitutive law at hydrate foam level, $\boldsymbol{\sigma}_{hf}^*(p) = \mathbb{R}_{hf}^*(p) : \boldsymbol{\varepsilon}_{hf}^*(p)$, to an implicit expression for the LC-transformed homogenized relaxation ten-

sor of the hydrate foam, \mathbb{R}_{hf}^* , reading as

$$\begin{aligned}
\mathbb{R}_{hf}^*(p) &= \sum_j f_j \mathbb{R}_j^*(p) : \mathbb{A}_j^*(p) \\
&= \left(f_{por}^{hf} \mathbb{R}_{por}^*(p) : \left\{ \mathbb{I} + \mathbb{P}_{sph}^{hf,*}(p) : [\mathbb{R}_{por}^*(p) - \mathbb{R}_{hf}^*(p)] \right\}^{-1} \right. \\
&\quad \left. + f_{hyd}^{hf} \mathbb{R}_{hyd}^*(p) : \int_0^{2\pi} \int_0^\pi \left\{ \mathbb{I} + \mathbb{P}_{cyl}^{hf,*}(p, \varphi, \vartheta) : [\mathbb{R}_{hyd}^*(p) - \mathbb{R}_{hf}^*(p)] \right\}^{-1} \frac{\sin \vartheta}{4\pi} d\vartheta d\varphi \right) : \\
&\quad \left(f_{por}^{hf} \left\{ \mathbb{I} + \mathbb{P}_{sph}^{hf,*}(p) : [\mathbb{R}_{por}^*(p) - \mathbb{R}_{hf}^*(p)] \right\}^{-1} \right. \\
&\quad \left. + f_{hyd}^{hf} \int_0^{2\pi} \int_0^\pi \left\{ \mathbb{I} + \mathbb{P}_{cyl}^{hf,*}(p, \varphi, \vartheta) : [\mathbb{R}_{hyd}^*(p) - \mathbb{R}_{hf}^*(p)] \right\}^{-1} \frac{\sin \vartheta}{4\pi} d\vartheta d\varphi \right)^{-1}. \tag{3.25}
\end{aligned}$$

3.2.3 Homogenization of cement paste properties

We are left with homogenization of the RVE of cement paste. Given the matrix-inclusion type morphology of the RVE, the Mori-Tanaka scheme (Mori and Tanaka 1973; Benveniste 1987) is appropriate to account for phase interactions. Accordingly, the LC-transformed relaxation function of the infinite matrix in the corresponding matrix-inclusion problems is set equal to the LC-transformed homogenized relaxation function of the hydrate foam. This results in an explicit expression for the LC-transformed relaxation function of cement paste, \mathbb{R}_{cp}^* , reading, by analogy to (55), as

$$\begin{aligned}
\mathbb{R}_{cp}^*(p) &= \left(\{1 - f_{clin}^{cp}\} \mathbb{R}_{hf}^*(p) + f_{clin}^{cp} \mathbb{R}_{clin}^*(p) : \left\{ \mathbb{I} + \mathbb{P}_{sph}^{hf,*}(p) : [\mathbb{R}_{clin}^*(p) - \mathbb{R}_{hf}^*(p)] \right\}^{-1} \right) : \\
&\quad \left(\{1 - f_{clin}^{cp}\} \mathbb{I} + f_{clin}^{cp} \left\{ \mathbb{I} + \mathbb{P}_{sph}^{hf,*}(p) : [\mathbb{R}_{clin}^*(p) - \mathbb{R}_{hf}^*(p)] \right\}^{-1} \right)^{-1}. \tag{3.26}
\end{aligned}$$

This relaxation function, as well as its creep analogue, $\mathbb{J}_{cp}^*(p) = [\mathbb{R}_{cp}^*(p)]^{-1}$, is then back-transformed from the LC domain, back to the time domain. This is done by means of the Gaver-Wynn-Rho algorithm (Abate and Valkó 2004; Valkó and Abate 2004), which allows for reliable numerical back-transformation, provided that the quantities in the LC space are available in a multiprecision number format. In more detail, the approximation accuracy of the back-transformation increases with the ‘‘order of approximation’’ quantified by the even integer M , see (Scheiner and Hellmich 2009) for details. Herein, $M = 10$ is chosen, which requires all computations in the LC

space to be done with a precision higher than 21 digits (Abate and Valkó 2004; Valkó and Abate 2004). In this way, the implicit equation (55) is solved iteratively, and the calculation is stopped once subsequent homogenized relaxation functions differ by a value smaller than 10^{-25} GPa.

3.3 Identification of power-law creep properties of well-saturated cement hydrates

3.3.1 Downscaling minute-long creep test data from cement paste to hydrate level

We here identify the viscous behavior of the only creeping phase, the hydrate phase, by minimizing the error between the experimental creep functions (3.1) resulting from three minute-long creep tests, and corresponding model predictions according to Eq. (3.26). The aforementioned creep tests were conducted in parallel to the hydration process of ordinary Portland cement paste exhibiting compositions of $w/c \in \{0.42, 0.45, 0.50\}$ and material ages ranging from approximately 1 to 8 days, see (Irfan-ul-Hassan et al. 2016) for details on the test protocol. As the combination of the creep experiments with unloading tests allowed for determination of the (elastic) Young's moduli (as was confirmed by ultrasonic tests, see (Irfan-ul-Hassan et al. 2016) for details), we isolate the elastic strains from the overall creep strains and restrict the minimization process to the viscous part of the creep function, which can be almost exactly fitted with a power-law function $J_{v,cp}^{exp}$ reading as (Irfan-ul-Hassan et al. 2016)

$$J_{v,cp}^{exp}(t - \tau) = \frac{1}{E_{c,cp}^{exp}} \left(\frac{t - \tau}{t_{ref}} \right)^{\beta_{cp}^{exp}}, \quad (3.27)$$

with $E_{c,cp}^{exp}$ denoting the creep modulus and β_{cp}^{exp} representing a dimensionless power-law exponent. Both parameters are functions of the initial water-to-cement mass ratio w/c and of the (calorimetry-based) hydration degree ξ , the latter being defined as the hydrated clinker volume divided by the initial clinker volume (Irfan-ul-Hassan et al. 2016).

As concerns the aforementioned model predictions, the elastic phase properties are given in Table 3.1, and the volume fractions occurring in (55) and (3.26) are determined from the famous Powers' model (Powers and Brownyard 1947; Powers 1958). Accordingly, the cement paste-related phase volume fractions of clinker f_{clin}^{cp} , of capillary pores f_{por}^{cp} , and of hydrates f_{hyd}^{cp} , and read as (Pichler

Table 3.1: Isotropic elastic phase properties from [Pichler and Hellmich \(2011\)](#); corresponding phase stiffness tensors read as $\mathbb{C}_j = 3k_j\mathbb{I}^{vol} + 2\mu_j\mathbb{I}^{dev}$

Phase j	Bulk modulus k_j [GPa]	Shear modulus μ_j [GPa]
Air	$k_{air} = 0$	$\mu_{air} = 0$
Water	$k_{H_2O} = 0$	$\mu_{H_2O} = 0$
Hydrates	$k_{hyd} = 18.69$	$\mu_{hyd} = 11.76$
Clinker	$k_{cem} = 116.7$	$\mu_{cem} = 53.80$

and [Hellmich 2011](#)):

$$\begin{aligned}
 f_{clin}^{cp} &= \frac{20(1-\xi)}{20+63w/c} \geq 0, \\
 f_{por}^{cp} &= \frac{63(w/c - 0.367\xi)}{20+63w/c} \geq 0, \\
 f_{hyd}^{cp} &= \frac{43.15\xi}{20+63w/c}.
 \end{aligned} \tag{3.28}$$

Given the two-scale representation of cement paste (see [Fig. 3.2](#)), we also need access to hydrate foam-related volume fractions of capillary pores and hydrates (f_{por}^{hf} and f_{hyd}^{hf}). They follow from dividing the cement paste-related volume fractions by the total hydrate foam volume, $(1 - f_{clin}^{cp})$, according to

$$f_j^{hf} = \frac{f_j^{cp}}{1 - f_{clin}^{cp}} \quad \forall j \in \{por, hyd\}. \tag{3.29}$$

Given the substantial computational effort associated with the inversion of the LC transformation, it is more efficient to compare the model-predicted and experimentally measured creep function in the LC space. This requires the LC transformation ([47](#)) of $J_{v,cp}^{exp}$, in order to obtain an experimentally determined LC-transformed viscous creep function $J_{v,cp}^{exp,*}$ in the form

$$J_{v,cp}^{exp,*}(p) = \frac{1}{E_{c,cp}^{exp}} \left(\frac{1}{t_{ref}} \right)^{\beta_{cp}^{exp}} \Gamma(\beta_{cp}^{exp} + 1) p^{-\beta_{cp}^{exp}}, \tag{3.30}$$

with Γ denoting the gamma function. The model-predicted (homogenized) counterpart $J_{v,cp}^{mod,*}$ is the 1111-component of the fourth-order tensor $\mathbb{J}_{v,cp}^{mod,*}(p) = [\mathbb{R}_{cp}^*(p)]^{-1} - [\mathbb{C}_{cp}]^{-1}$, see ([3.26](#)); whereby $\mathbb{C}_{cp} = \mathbb{R}_{cp}(t=0)$ is the homogenized elastic stiffness of cement paste. Conclusively, we are minimizing the error between the model-predicted viscous part of the uniaxial creep function in the LC space, $J_{v,cp}^{mod,*}(p)$, and its experimentally measured counterpart,

$J_{v,cp}^{exp,*}(p)$; in mathematical terms,

$$\sum_{i=1}^{n_{w/c}} \sum_{j=1}^{n_{\xi}} \sum_{k=1}^{n_p} [J_{v,cp}^{mod,*}(p) - J_{v,cp}^{exp,*}(p)]^2 \rightarrow \min . \quad (3.31)$$

In Eq. (3.31), the sum over $n_{w/c} = 3$ indicates that three different cement paste mixes exhibiting $w/c \in \{0.42, 0.45, 0.50\}$ are tested, the sum over $n_{\xi} = 167$ indicates that 167 creep tests were performed on each cement composition for different maturity states, and the sum over $n_p = 20$ indicates that 20 complex LC “time” values $p \in [10^{-6}, 10^{-4}]$ are considered. The optimization problem (3.31) is solved in [MATLAB \(2013\)](#), by means of a quasi-Newtonian solver, and this provides the optimal creep parameters for well-saturated hydrates as

$$\mu_{c,hyd} = 20.93 \text{ GPa}, \quad \beta_{hyd} = 0.251 . \quad (3.32)$$

These optimal hydrate creep parameters indeed allow for satisfactory representation of the experimental results in the time domain, see Fig. 3.3. The agreement between model prediction and experiment is quantified through the mean error, defined as the sum of the absolute values of the difference between model-predicted and experimentally measured uniaxial viscous creep function, resolved for $n_t = 180$ steps within the three minute-long creep tests $t_k \in [1, 180]$, and averaged with respect to the number of creep tests ($n_{w/c} n_{\xi} \approx 500$) and the number of time steps n_t , reading as

$$\epsilon = \frac{\sum_{i=1}^{n_{w/c}} \sum_{j=1}^{n_{\xi}} \sum_{k=1}^{n_t} |J_{v,cp}^{mod}(t_k) - J_{v,cp}^{exp}(t_k)|}{n_{w/c} n_{\xi} n_t} . \quad (3.33)$$

This error amounts to $0.768 \cdot 10^{-6}/\text{MPa}$. This supports the idea that the (visco-)elastic properties of well-saturated hydrates neither change during the aging of cement paste nor upon composition change of the cement paste. Accordingly, the varying creep potential of cement pastes arises solely from varying volume dosages of the hydrates, as predicted by Powers’ hydration model.

3.3.2 Confirmation of hydrate creep properties by data from weeks-long creep test on 30 year-old cement paste

The question arises whether the intrinsic (i.e. mixture- and maturity-independent) creep properties of well-saturated hydrates as identified here from three minute creep tests on different early-age cement pastes, may be also relevant for longer creep durations, and for more mature pastes. In this context, we consider the results of [Tamtsia and Beaudoin \(2000\)](#), who performed 30 day-long uniaxial compressive creep tests on 30 year-old Portland cement paste samples with $w/c=0.5$, stored continuously under water. Given

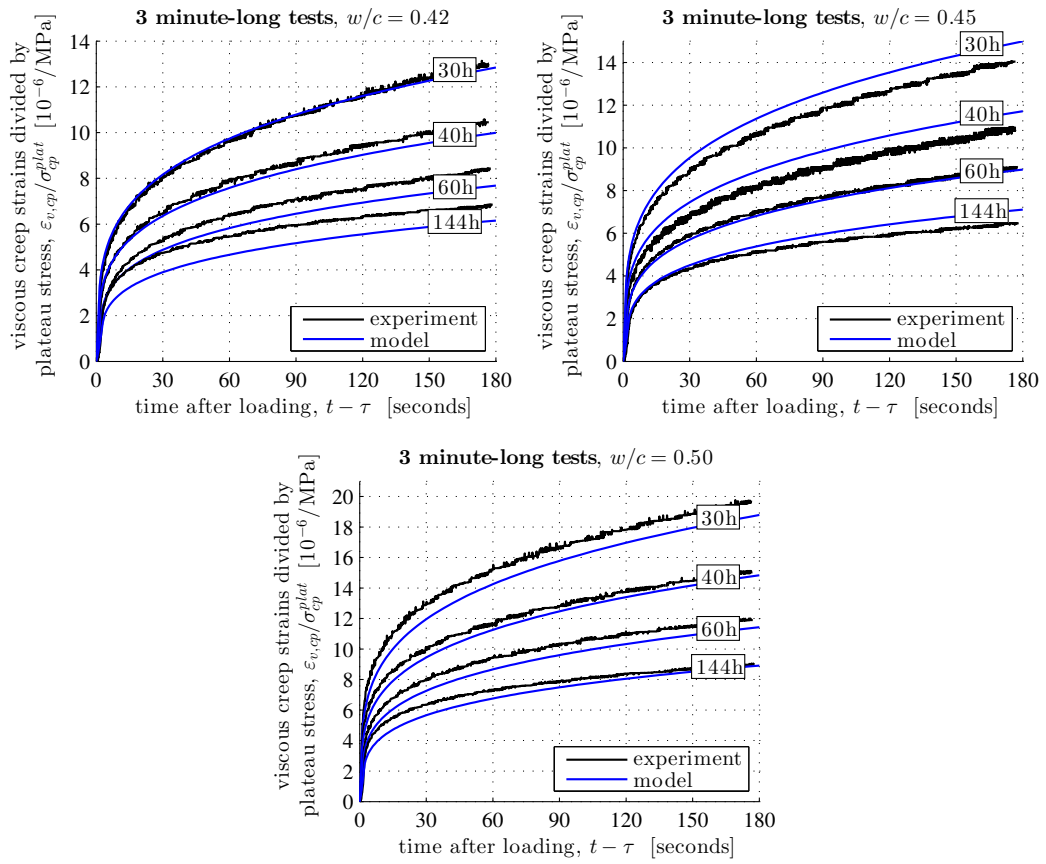


Figure 3.3: Comparison of the experimentally determined and model-predicted viscous strains of cement pastes aged 30, 40, 60, and 144 hours, respectively; the relation between material age and hydration degree is taken from [Irfan-ul-Hassan et al. \(2016\)](#)

their age, the samples can be considered to be completely hydrated; thus, also in this case, it is appropriate to consider aging effects as negligible during the test period. An estimate for the hydration degree which corresponds to full hydration of cement paste, can be obtained from the empirical relationship of [Lin and Meyer \(2009\)](#). Accordingly, a water-to-cement mass ratio of $w/c = 0.50$ and a typical Blaine fineness of $340 \text{ m}^2/\text{kg}$ ([Tamtsia et al. 2004](#)) relate to a final hydration degree of $\xi = 0.87$. The corresponding model-predicted creep function, i.e. that relating to $w/c = 0.50$, $\xi = 0.87$, and to the hydrate properties according to (3.2) and (3.32), agrees remarkably well with the aforementioned experimental results, see Fig. 3.4. This result shows

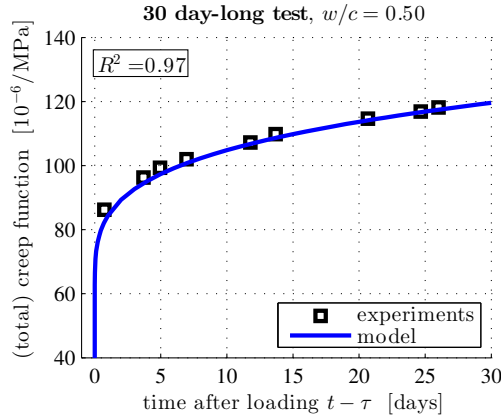


Figure 3.4: Comparison of experimental data ([Tamtsia and Beaudoin 2000](#)) for (total) creep functions of 30 year-old cement paste samples with $w/c=0.5$, with corresponding model predictions

that it is the intrinsic viscous behavior of the hydrate needles, which drives the basic creep of cement paste for time intervals ranging from a few seconds, up to several weeks. Moreover, this corroborates that the viscous behavior of well-saturated hydrates does not change.

3.4 General characteristics of the creep of well-saturated hydrates

The good agreements in Figs. 3.3 to 3.4 motivate deeper study of the features of the homogenized creep behavior of cement paste. Therefore, we represent the viscous part of the model-predicted uniaxial creep functions of cement paste very accurately, see Fig. 3.5, by means of a power function,

$$J_{v,cp}^{mod}(t - \tau) = \frac{1}{E_{c,cp}^{mod}} \left(\frac{t - \tau}{t_{ref}} \right)^{\beta_{cp}^{mod}}, \quad (3.34)$$

with $E_{c,cp}^{mod}$ denoting the model-predicted creep modulus, and β_{cp}^{mod} representing the model-predicted creep exponent. Notably, the total model-predicted creep

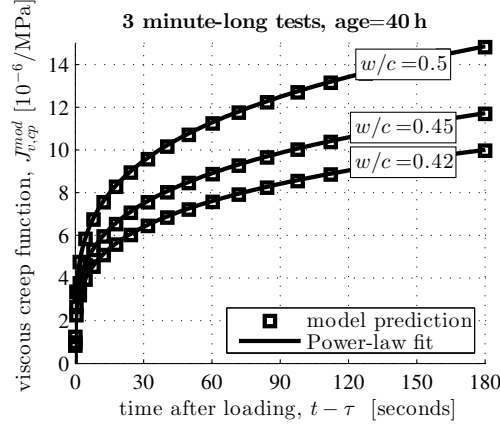


Figure 3.5: Viscous part of the uniaxial creep function of 40 h old cement paste with $w/c \in \{0.42, 0.45, 0.50\}$: point-wisely obtained model predictions and corresponding power-law fits according to Eq. (3.27), with quadratic correlations coefficients $R^2 > 99.9\%$

function then reads as $J_{cp}^{mod} = J_{v,cp}^{mod} + 1/E_{cp}^{mod}$ with E_{cp}^{mod} denoting the model-predicted Young's elastic modulus. It turns out that the elastic and creep modulus are strongly composition-dependent; they increase with increasing ξ and decreasing w/c , see Fig. 3.6. In contrast, the creep exponent appears as virtually composition- and maturity-independent quantity, being constant around $\beta \approx 0.252$ for $w/c \in [0.2, 1]$ and $\xi \in [0, 1]$. This value is even close to the hydrate creep exponent of Eq. (3.32); i.e. it is hardly effected by the upscaling scheme.

3.5 Discussion and conclusion

Concerning the invariant hydrate creep properties, expressed by Eq. (3.32) and Figs. 3.3-3.4, it is important to note that the herein investigated cement samples were all characterized by $w/c \geq 0.42$, that they were tested within the first week after production, and that they were continuously covered, in order to avoid drying. Consequently, these samples (and the hydrates within them) were well saturated, and our statement on the invariance of hydrate creep properties is valid for well saturated hydrates.

Change of this saturated state, i.e. drying, is known to significantly influence the macroscopic creep behavior of cement paste (Acker and Ulm 2001; Tamtsia and Beaudoin 2000), and of other hydrated nanolayered material systems, such as clay (Carrier et al. 2016). It is very probable that drying also changes the hydrate creep behavior itself, e.g. through reduction of so-called creep

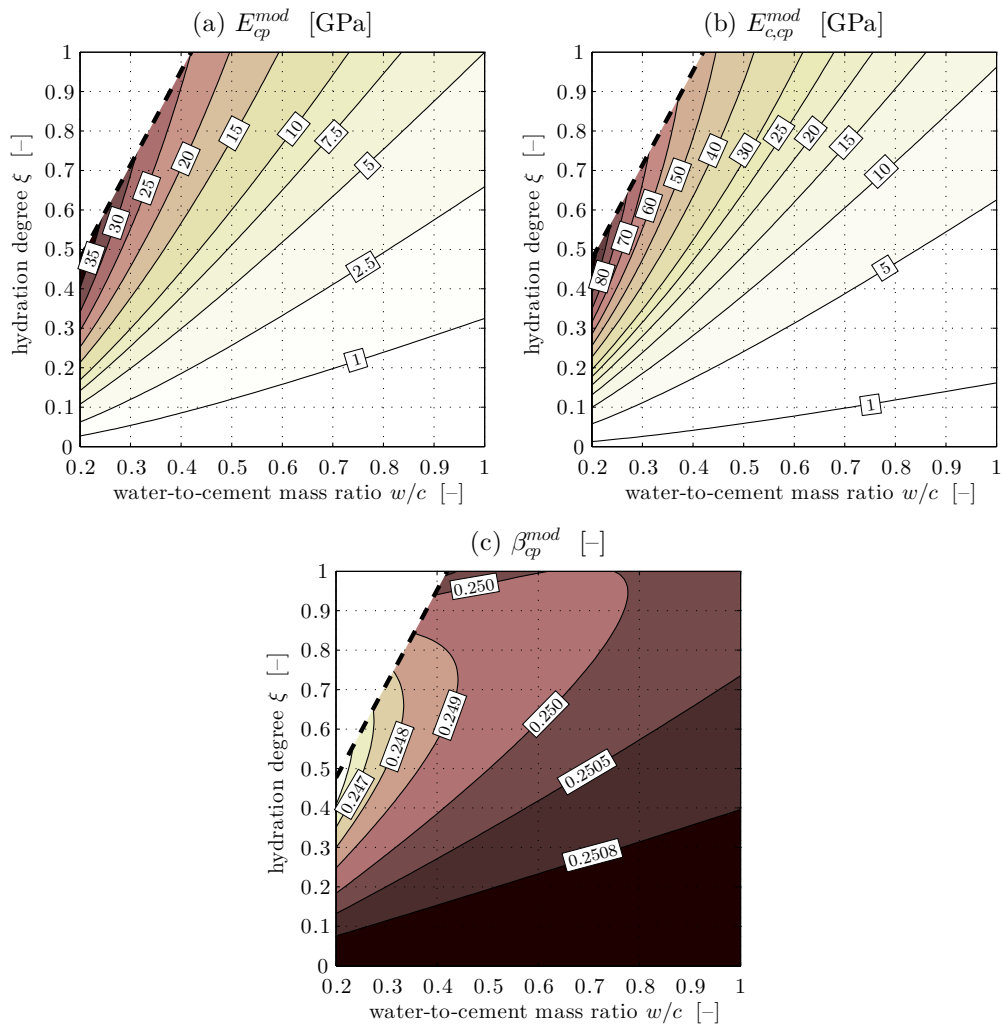


Figure 3.6: Model-predicted elastic and creep properties for hydrating cement pastes with hydration degrees $\xi \in [0, 1]$ and exhibiting water-to-cement mass ratios $w/c \in [0.2, 1]$: (a) Young's elastic modulus, (b) Young's creep modulus, (c) dimensionless creep exponent

sites within the hydrate phases (Thomas and Jennings 2006). The same authors report NMR studies which show that even under constant hydro-thermal conditions, the polymerization state within the hydrates changes, and they propose that this so-called “chemical aging of C-S-H” might also change the hydrate creep properties. More recent research results, however, seem to relativize this proposition: indeed, polymerization leads to an enlargement of the non-spherical nanoscaled solid elements within the hydrates, while the actual source of hydrate creep lies in the layered (confined) water sheets *between* these solid elements (Manzano et al. 2012, 2013; Shahidi et al. 2014, 2015b). Hence, as long as the amount of the latter “creep sites” does not change, it makes sense to expect invariant creep properties of the hydrate phases as introduced in Fig. 3.2 (b).

Fig. 3.6 and Eq. (3.34) illustrate that upscaling of a power-law creep function from needle-shaped hydrates up to the scale of cement paste results in a power-law creep function. In other words, the herein performed scale transitions do not alter the shape of the creep function, a fact that was also found for upscaling the asymptotically reached creep rates “seen” in nano- and microindentation tests (Vandamme and Ulm 2013; Zhang et al. 2014). Pursuing this argument to the scale of concrete, one will also end up with a creep function which virtually follows a power function. However, concrete creep tests or monitoring activities spanning over time periods of years, have revealed a transition to a logarithmic creep behavior (Bažant et al. 2011). Conclusively, the validity range of the hydrate creep properties identified through Eq. (3.2) and (3.32) is constrained to creep periods of weeks to months (see Fig. 3.4). During such time periods, creep of cement paste indeed follows a power-law function (Tamtsia and Beaudoin 2000; Irfan-ul-Hassan et al. 2016). Extension of the formulation (3.1) towards ultralong creep periods is beyond the scope of the present manuscript.

The quantification of the hydrate creep function according to (3.26) and (3.28)-(3.31) rests on the assumption of isochoric creep according to (3.2), implying that creeping hydrates would exhibit a time-invariant volume. This assumption is motivated by a suggestion of Bernard et al. (2003a), by results of an earlier creep micromechanics model (Scheiner and Hellmich 2009), and by theoretical considerations concerning the upscaling of sliding processes of viscous interfaces within hydrated calcium silicate (Shahidi et al. 2014, 2015a, 2016, 2015b). These viscous interfaces are located within the hydrate nanoparticles, such as solid C-S-H, see Fig. 3.7 (c). The needle-shaped hydrate phases considered in the present work are defined at a level well above the aforementioned nanoparticles: our hydrate phases are actually built up by these nanoparticles as well as by the gel porosity in between. Such nanocomposites are also referred to as “C-S-H gel” (Sanahuja and Dormieux 2010; Manzano et al. 2013). Accordingly, the isochoric creep function of the nanoparticles would actually scale up to a hydrate gel-related creep function also including volumetric creep strains (Sanahuja and Dormieux 2010). Hence, the question arises whether

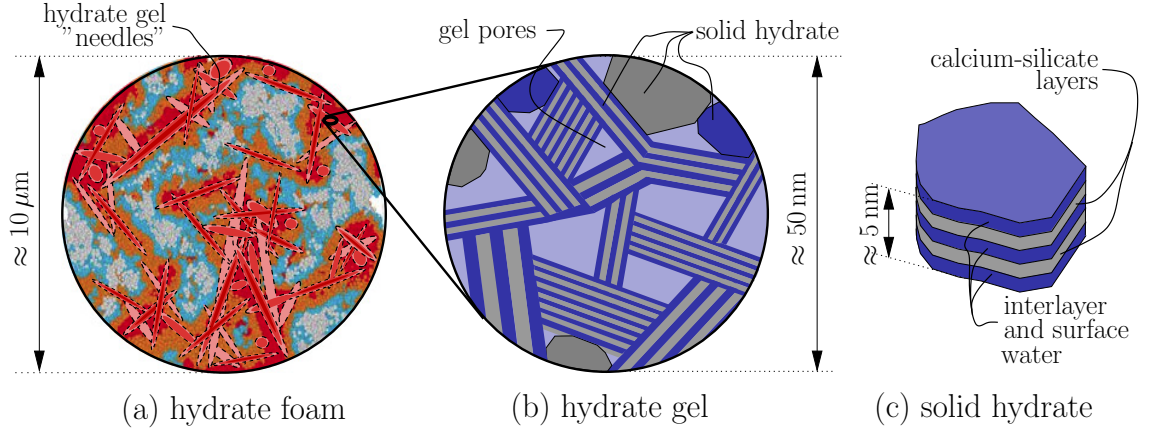


Figure 3.7: Nanoscopic downscaling from hydrate foam microstructure introduced in Fig. 3.2(b): (a) Hybrid Molecular Dynamics - Grand Canonical Monte Carlo simulations suggest emergence of elongated morphological features at the level of the hydrate foam (a); these needles, represented by the needle-shaped hydrate phases shown in Fig. 3.2(b), are made up of hydrate gel (b), consisting itself of gel pores and solid hydrates (c); the latter are built from calcium silicate layers separated or covered by films of confined water

consideration of such volumetric creep strains occurring at the level of hydrate gel [i.e. that of the needle-shaped hydrate phases in Fig. 3.2(b)] would have a remarkable effect on the results of the downscaling-based hydrate creep identification process described further above. In order to answer this question, we here repeat this process, but now based on the popular concept of a constant (elastic and creep) Poisson’s ratio as proposed by Bažant and L’Hermite (1988). Accordingly, we consider

$$\begin{aligned} \mathbb{J}_{hyd}(t - \tau) = & \left[\frac{1 - 2\nu_{hyd}}{E_{hyd}} + \frac{1 - 2\nu_{hyd}}{E_{c,hyd}} \left(\frac{t - \tau}{t_{ref}} \right)^{\beta_{hyd}} \right] \mathbb{I}_{vol} \\ & + \left[\frac{1 + \nu_{hyd}}{E_{hyd}} + \frac{1 + \nu_{hyd}}{E_{c,hyd}} \left(\frac{t - \tau}{t_{ref}} \right)^{\beta_{hyd}} \right] \mathbb{I}_{dev} \end{aligned} \quad (3.35)$$

whereby E_{hyd} denotes Young’s elastic modulus, $E_{c,hyd}$ denotes Young’s creep modulus, and ν_{hyd} denotes Poisson’s ratio. The latter follows from the elastic bulk and shear moduli of isotropic hydrates (see also Table 3.1), as $\nu_{hyd} = 0.24$. The alternative hydrate creep tensor function (3.35) is then upscaled to the level of cement paste, as described in Section “Micromechanics of creeping cement pastes”. Thereafter, the hydrate creep properties $E_{c,hyd}$ and β_{hyd} are identified by means of minimizing Eq. (3.31). The resulting prediction error ϵ according to Eq. (3.33) is, in good approximation, equal to the one obtained under the assumption of isochoric creep, see Table 3.2. Very remarkably, virtually the *same* Young’s creep modulus of hydrates, and the *same* power-law creep

Table 3.2: Comparison of hydrate creep properties of Eq. (3.2) and (3.35), identified by means of downscaling 500 macroscopic creep tests on cement pastes: isochoric creep vs. creep at constant Poisson’s ratio; prediction error ϵ according to Eq. (3.33)

assumption	$E_{c,hyd}$ [GPa]	β_{hyd}	ϵ [$10^{-6}/\text{MPa}$]
isochoric	62.8 ^a	0.251	0.768
constant Poisson’s ratio	62.4	0.250	0.765

^aThe Young’s creep modulus $E_{c,hyd}$ follows from the shear creep modulus identified in Eq. (3.32) as $E_{c,hyd} = 3\mu_{c,hyd}$

exponent of hydrates are obtained, irrespective of whether isochoric creep or creep at constant Poisson’s ratio is considered. The underlying reason seems to lie in the elongated (non-spherical) shape of the hydrate phases building up kind of a “framework”, with the capillary porosity playing the role of the “free spaces” in between. In such a “framework”, the individual needles (or “beams”) are predominantly loaded in terms of uniaxial stress states, irrespective of potential lateral deformations which remain insignificant for the overall load carrying behavior. A very similar result has been obtained in the context of homogenizing the elastic properties of various types of ceramic porous polycrystals with non-spherical (needle- or disc-shaped) solid phases (Fritsch et al. 2013), as was confirmed by very many experiments as well as by full 3D Finite Element simulations of corresponding microstructures (Sanahuja et al. 2010). In this context, we note that the morphology with non-spherical hydrate phase shapes, as depicted in Fig. 3.2 (b), was validated by various experimental sources (Pichler and Lackner 2009; Pichler and Hellmich 2011; Pichler et al. 2013). Moreover, this morphology has been, only very recently, further confirmed by a hybrid Molecular Dynamics – Grand Canonical Monte Carlo simulation (MD-GCMC) scheme (Ioannidou et al. 2016), see Fig. 3.7 (a).

Nomenclature

The following symbols are used in this paper:

$A_{\infty,j}^{*,vol}$, $A_{\infty,j}^{*,dev}$ = LC-transformed volumetric and deviatoric components of Es-helby problem-related strain concentration tensor of phase j ;

\mathbb{A}_j^* = LC transform of strain concentration tensor of phase j ;

\mathbb{C}_j = elastic stiffness tensor of phase j ;

clin = cement clinker;

cp = cement paste;

cyl = cylindrical (needle-shaped);

div = divergence operator;

E_{cp}^{exp} = experimentally determined Young's elastic modulus of cement paste;
 $E_{c,cp}^{exp}, E_{c,cp}^{mod}$ = experimentally determined and model-predicted Young's creep modulus of cement paste;
 E_{hyd} = Young's elastic modulus of the hydrates;
 $E_{c,hyd}$ = Young's creep modulus of the hydrates;
 exp = experimentally determined;
 \mathbb{F} = auxiliary anisotropic fourth-order tensor;
 f_j^{hf} = hydrate foam-related volume fraction of phase j , $j \in \{air, H_2O, hyd\}$;
 f_j^{cp} = cement paste-related volume fraction of phase j , $j \in \{clin, hf\}$;
 \mathbb{G} = auxiliary isotropic fourth-order tensor;
 G^{vol}, G^{dev} = volumetric and deviatoric components of \mathbb{G} ;
 H_2O = water;
 hf = hydrate foam;
 hyd = hydrates;
 \mathbb{I} = fourth-order identity tensor;
 $\mathbb{I}^{vol}, \mathbb{I}^{dev}$ = volumetric and deviatoric parts of fourth-order identity tensor;
 J_j = uniaxial creep function of phase j ;
 $J_{cp}^{exp}, J_{cp}^{mod}$ = experimentally determined and model-predicted uniaxial creep function of cement paste;
 $J_{e,cp}^{exp}$ = elastic part of J_{cp}^{exp} ;
 $J_{v,cp}^{exp}, J_{v,cp}^{mod}$ = viscous parts of J_{cp}^{exp} and J_{cp}^{mod} ;
 J_{hyd} = uniaxial elastic creep function of cement paste;
 $J_{e,hyd}$ = elastic part of J_{hyd} ;
 $J_{v,hyd}$ = viscous part of J_{hyd} ;
 \mathbb{J}_j = fourth-order creep tensor function of phase j ;
 $\mathbb{J}_{v,cp}^{mod,*}$ = model-predicted viscous part of the creep tensor function of cement paste in the LC space;
 k_j = bulk modulus of phase j ;
 ℓ = length of needle-shaped hydrates;
 M = number of precision digits for computations in the LC space;
 mod = model-predicted;
 \underline{n} = unit normal vector perpendicular to ∂V_{hf} ;
 $n_p, n_{w/c}, n_\xi$ = numbers over which sums in the optimization problem (3.31) extend;
 $\mathbb{F}_j^{hf,*}$ = LC-transformed Hill tensor of an inclusion with shape j , embedded in an infinite hydrate foam matrix, $j \in \{sph, cyl\}$;
 p = complex variable in the LC domain;
 $pore$ = pores;
 \mathbb{R}_j = fourth-order relaxation tensor function of phase j ;
 $\mathbb{S}_j^{hf,*}$ = LC-transformed Eshelby tensor of an inclusion with shape j embedded in an infinite hydrate foam matrix, $j \in \{sph, cyl\}$;
 $S_j^{hf,*,vol}, S_j^{hf,*,dev}$ = volumetric and deviatoric components of $\mathbb{S}_j^{hf,*}$;
 sph = spherical;
 \underline{T} = traction vector acting at ∂V_{hf} ;
 t = chronological time;

- t_{ref} = reference time, $t_{ref} = 1 \text{ d} = 86\,400 \text{ s}$;
 V_{hf} = volume of RVE of hydrate foam;
 ∂V_{hf} = boundary of RVE of hydrate foam;
 W_{hf}^{ext} = external work density, done on the boundary of the RVE of hydrate foam;
 w/c = initial water-to-cement mass ratio;
 \underline{x} = position vector labeling positions inside V_{hf} as well as at the boundary ∂V_{hf} ;
 $\beta_{cp}^{exp}, \beta_{cp}^{mod}$ = experimentally determined and model-predicted power-law exponent in the creep function of cement paste;
 β_{hyd} = power-law exponent of hydrates;
 δ_{ij} = Kronecker delta;
 $\Gamma(\cdot)$ = gamma function of real quantity (\cdot);
 ϵ = Mean error between model-predicted and experimentally measured uniaxial viscous creep functions;
 $\boldsymbol{\varepsilon}$ = second-order strain tensor;
 $\boldsymbol{\varepsilon}_j$ = second-order strain tensor of phase j ;
 $\varepsilon_{c,cp}$ = viscous cement paste strain component in loading direction;
 ϑ = zenith angle;
 μ_j = shear modulus of phase j ;
 $\mu_{c,hyd}$ = shear creep modulus of the hydrates;
 ν_{hyd} = Poisson's ratio of the hydrates;
 ξ = hydration degree;
 $\underline{\xi}$ = displacement vector;
 $\boldsymbol{\sigma}$ = second-order stress tensor;
 $\boldsymbol{\sigma}_j$ = second-order stress tensor of phase j ;
 σ_{cp} = cement paste stress component in loading direction;
 σ_{cp}^{plat} = applied uniaxial stress in creep experiment;
 τ = time instant of loading;
 φ = azimuth angle;
 $\mathbf{1}$ = second-order identity tensor;
 $(\cdot)^*$ = Laplace-Carson transform of quantity (\cdot);
 $(\hat{\cdot})$ = Laplace transform of quantity (\cdot);
 \cdot = inner product;
 $:$ = second-order tensor contraction;
 \otimes = dyadic product;
 ∇ = nabla operator.

Chapter 4

How water-aggregate interactions affect concrete creep: a multiscale analysis

4.1 Introduction

Concrete hydration is generally regarded as a process from which the aggregates, being chemically inert, are fully excluded, and which is therefore taking place exclusively in the cement paste, where water reacts with cement grains, so as to form hydrates. Correspondingly, concrete hydration models such as the famous Powers-Acker model ([Powers and Brownyard 1946](#); [Acker and Ulm 2001](#)) are typically built on evolving volume fractions of cement clinker, water, and hydrates in the cement paste; and considering the cement paste compartment as a thermodynamically closed system, all these volume fractions can be traced back to the hydration degree and to the (initial) water-to-cement mass ratio. By contrast, the volume fractions of cement paste and aggregates remain constant at the hierarchical level of concrete. Besides other applications, such hydration models have been a particularly appropriate basis for the development of multiscale mechanics models for concrete, be they related to elasticity ([Bernard et al. 2003b](#); [Hellmich and Mang 2005](#); [Sanahuja et al. 2007](#)) to poroelasticity ([Ulm and Heukamp 2004](#); [Ghabezloo 2010](#)) to viscoelasticity ([Scheiner and Hellmich 2009](#)) or to strength ([Pichler and Hellmich 2011](#); [Pichler et al. 2013](#)).

All these models have been experimentally validated up to different levels of precision, so that on the one hand, multiscale continuum mechanics has be-

come a well accepted theoretical tool in cement and concrete research; while on the other hand, the field is still open for improvements. The latter is true in particular for the very challenging topic of concrete creep, which spans several orders of time magnitude, starting from the scale of minutes (Vandamme and Ulm 2009; Delsaute et al. 2012; Boulay et al. 2012; Vandamme and Ulm 2013; Zhang et al. 2014; Irfan-ul-Hassan et al. 2016) to that of several days (Bažant et al. 1976; Tamtsia et al. 2004; Rossi et al. 2011), weeks (Tamtsia and Beaudoin 2000; Laplante 2003; Atrushi 2003; Briffaut et al. 2012), months (Rossi et al. 1994; Zhang et al. 2014), or even years (Bažant et al. 2011, 2012; Zhang et al. 2014).

In the present paper, we show that the challenge in the multiscale modeling of concrete creep probably does not lie so much in finding the appropriate micromechanical representation of the material, but rather in the reliable estimation of the evolving volume fractions of the material constituents, entering the corresponding micromechanics models as input. In this context, we abandon the aforementioned assumption of the cement paste being a thermodynamically closed system, and we explicitly introduce water migration from the inter-aggregates spaces into the aggregates, as well as back-suction of water from the aggregates into the hydrating (and therefore water-consuming) cement paste.

Accordingly, the paper is organized as follows: A simple mathematical model for water migration into and from the aggregates is formulated in Section 2. Based on the initial water-to-cement mass ratio, on the hydration degree, and on two newly introduced quantities, namely the water uptake capacity of the aggregates and the water filling extent of the cement paste voids, this model provides the volume fractions of water, cement clinker, hydrates, and aggregates within concretes and mortars with water-absorbing aggregates. These volume fractions then enter a micromechanical model for mortar and concrete creep, upscaling cement paste behavior, as quantified in the recent ultrashort-term tests of Irfan-ul-Hassan et al. (2016), to the mortar and concrete level, as detailed in Section 3. Corresponding micromechanical model predictions are then compared to a total of 32 newly performed ultrashort-term creep tests at two different mortars (made from aggregates type I - „Normensand Quartz”) and two different concretes (made from aggregates type II - „Pannonia Kies”), which are all made from the same cement, but differ in water-to-cement and aggregate-to-cement mass ratios, see Section 4. It is checked whether this comparison would allow for identification of one value each for (i) the water uptake capacity of aggregates; and (ii) the cement-specific void filling extent by water soaked out from the aggregates. Also, air entrapment between aggregates and cement paste is considered. Thereafter, the paper is terminated by a conclusion section.

4.2 Modeling hydration-dependent water migration to and from the aggregates

We consider that during the mixing of concrete or mortar, i.e. before the hydration reaction, a significant amount of water may be taken up by the aggregates. This is the case with oven-dried quartz aggregates, on which we focus throughout the present paper. Accordingly, we decompose the total mass of water, w , into that of the water residing inside the cement paste, w_{cp} , and that which is absorbed within the open porosity of quartz, w_a ,

$$w = w_{cp}(\xi) + w_a(\xi). \quad (4.1)$$

During the hydration reaction, however, part of the water which has been initially absorbed into the aggregates, is soaked back into the inter-aggregates space, which is then occupied by the cement paste. This is because the hydration products fill less volume than their unreacted counterparts. In more detail, the volume reduction during cement paste hydration [also called autogenous shrinkage (Powers and Brownyard 1946; Acker and Ulm 2001)] leads to the formation of air voids, which are partially refilled by the additional water extracted from the aggregates. Such a process driven by water supply from the aggregates is sometimes called internal curing (Bentz et al. 2005; Jensen and Lura 2006; Wyrzykowski et al. 2011; Zhutovsky and Kovler 2012; Justs et al. 2015). Maintaining the philosophy of the Powers model to identify linear relations between chemical reactants and products on the one hand, and the degree of hydration on the other hand, we envision that the amount of aggregate-extracted water increases (linearly) with the volume of voids. The latter increases (linearly) with the mass of hydrates formed, which then increases, again linearly, with the degree of hydration. Hence, the water content in the cement paste is linearly linked to the hydration degree as well, which is mathematically expressed as follows

$$\frac{w_{cp}(\xi)}{c} = d + k \xi \quad (4.2)$$

In this context, it needs to be emphasized that $w_{cp}(\xi)$ comprises the mass of *all* the water in the cement paste in the most general understanding, i.e. both the unreacted water *and* that which is chemically combined to the cement clinker; in the same sense, c denotes the *total* mass of cement, including both the unreacted cement and that which is chemically combined to water. The material constants in (4.2), d and k , are the initial value of the water-to-cement mass ratio which is effective at the cement paste level, and the hydration-dependent (linear) increase of this effective mass ratio. The former constant can be linked to the water mass which is initially uptaken by the aggregates, $w_a(0)$. This quantity is normalized by the mass of the aggregates, a , yielding the initial water-to-aggregate mass ratio in the form $w_a(0)/a$. Namely, when

splitting the (nominal) water-to-cement mass ratio into a cement paste-specific and an aggregate-specific portion, the respective mathematical expression can be readily solved for d , according to

$$\frac{w}{c} = \frac{w_{cp}(0)}{c} + \frac{w_a(0)}{a} \frac{a}{c} \quad \Rightarrow \quad d = \frac{w_{cp}(0)}{c} = (w/c) - \frac{w_a(0)}{a} (a/c) \quad (4.3)$$

Concerning the soaking of water, from the aggregates back to the inter-aggregate spaces, then occupied by cement paste, we introduce a cement-specific void-filling extent α between 0 and 1, with zero referring to no water filling of air voids formed during autogeneous shrinkage of the cement paste, while 1 relates to complete filling of the air voids by water. Thereby, the voids themselves evolve linearly with the hydration degree, as seen in Fig. 4.1. This

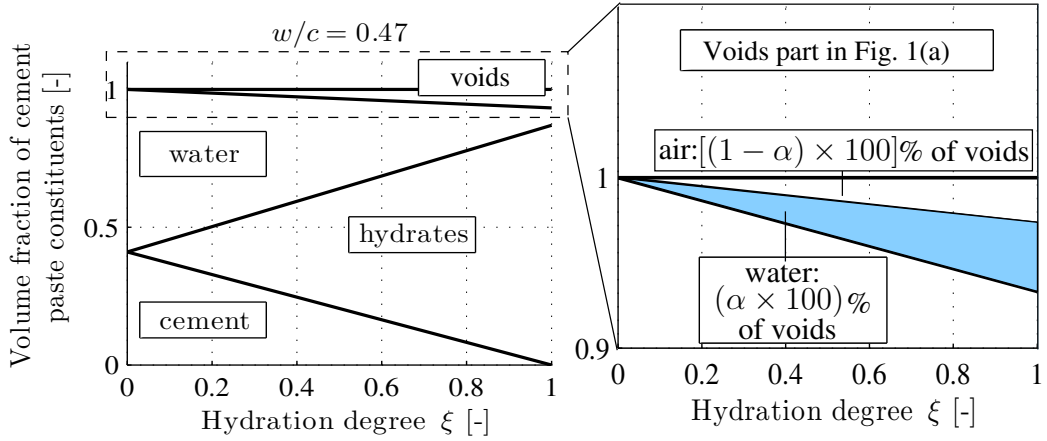


Figure 4.1: Hydration-driven evolution of volume fractions of cement paste constituents (cement, water, hydrates, and voids) according to Powers-Acker's hydration model: (a) complete phase volume evolution diagram according to (Powers and Brownyard 1946; Acker and Ulm 2001); (b) detail illustrating void filling extent α , concerning partial void filling by water that is soaked from the open porosity of quartz into the cement paste matrix

void filling extent α can be related to the back-soaking-related parameter k , by deriving an expression for the hydration-dependent water mass which was soaked into the cement paste, through combination of Eqs. (4.2) and (4.3), yielding

$$w_{cp}(\xi) - w_{cp}(0) = c k \xi \quad (4.4)$$

and by expressing this mass as the volume of voids, times the void filling extent α , times the mass density of water, yielding

$$c k \xi = V_{void} \alpha \rho_{H_2O} \quad (4.5)$$

We are left with relating the void volume V_{void} to the initial composition of the cement paste and to the hydration degree. To this end, the void volume is

considered to be equal to the volume of cement paste, V_{cp} , times the cement paste-related volume fraction of voids, f_{void}^{cp}

$$V_{void} = V_{cp} f_{void}^{cp} \quad (4.6)$$

The volume of cement paste is equal to the initial volumes of cement and water, i.e. V_c and V_w , which can be expressed by the masses of cement and water as well as by the related mass densities as

$$V_{cp} = V_c + V_w = \frac{c}{\rho_{clin}} + \frac{w_{cp}(0)}{\rho_{H_2O}} \quad (4.7)$$

Finally, the volume fraction of shrinkage-induced voids in cement paste is considered to increase proportionally to the hydration degree, as quantified through the Powers-Acker hydration model (Powers and Brownyard 1946; Acker and Ulm 2001), evaluated for the effective initial composition of the cement paste matrix, quantified in terms of the effective initial water-to-cement mass fraction $w_{cp}(0)/c$, compare Eq. (15.4) of (Pichler and Lackner 2009):

$$f_{void}^{cp} = \frac{\left(1 + 0.42 \frac{\rho_{clin}}{\rho_{H_2O}} - 1.42 \frac{\rho_{clin}}{\rho_{hyd}}\right) \xi}{1 + \frac{\rho_{clin}}{\rho_{H_2O}} (w_{cp}(0)/c)} = \frac{3.31 \xi}{20 + 63 \frac{w_{cp}(0)}{c}} \quad (4.8)$$

with $\rho_{clin} = 3.150 \text{ kg/dm}^3$ (Acker 2001), $\rho_{H_2O} = 1.000 \text{ kg/dm}^3$, and $\rho_{hyd} = 2.073 \text{ kg/dm}^3$ (Barthélémy and Dormieux 2003), denoting the mass densities of cement clinker grains, water, and hydrates, respectively. The sought relation between the constant k and the void filling extent by water, α , follows from specialization of Eq. (4.5) for Eqs. (4.6), (4.7), and (4.8), as well as from solving the resulting expression for k , yielding

$$k = \left[\frac{\rho_{H_2O}}{\rho_{clin}} + \frac{w_{cp}(0)}{c} \right] \frac{3.31 \alpha}{20 + 63 \frac{w_{cp}(0)}{c}} \quad (4.9)$$

Eq. (4.9) underlines that k , the hydration degree-related rate of the effective water-to-cement mass fraction of the cement paste matrix, see Eq. (4.2), is directly proportional to α , the extent up to which the shrinkage-induced voids in the cement paste are filled by water.

With respect to the classical Powers-Acker model, the herein developed hydration model which considers also internal curing, contains two additional quantities: (i) the water uptake capacity of the aggregates, $w_a(0)/a$, and (ii) the void filling extent by water, α . The former quantity is involved in the expression for the initial value of the effective water-to-cement mass fraction, see Eq. (4.3), while α is involved in the mathematical expression for the evolution of the water-to-cement mass ratio which is effective in the cement paste; and this expression is obtained by specializing Eq. (4.2) for d and k according

to (4.3) and (4.9), respectively, and from consideration of the mass densities $\rho_{clin} = 3.150 \text{ kg/dm}^3$ and $\rho_{H_2O} = 1.000 \text{ kg/dm}^3$, as

$$\begin{aligned} \frac{w_{cp}(\xi)}{c} &= (w/c) - \frac{w_a(0)}{a} (a/c) + \left(\left[\frac{\rho_{H_2O}}{\rho_{clin}} + \frac{w_{cp}(0)}{c} \right] \frac{3.31 \alpha}{20 + 63 \frac{w_{cp}(0)}{c}} \right) \xi \\ &= (w/c) - \frac{w_a(0)}{a} (a/c) + \left[\frac{1.051 + 3.31 [(w/c) - \frac{w_a(0)}{a} (a/c)]}{20 + 63 [(w/c) - \frac{w_a(0)}{a} (a/c)]} \right] \alpha \xi \end{aligned} \quad (4.10)$$

This is the water-to-cement mass ratio which is effective at the cement paste level, and which governs the hydration reaction taking place there.

Its initial value needs to be considered when quantifying the volume fractions of cement paste and aggregates in a material volume of concrete or mortar with water absorbing aggregates; except for the use of this effective water-to-cement mass ratio, the latter quantification follows the standard relation given in (Bernard et al. 2003b; Pichler and Lackner 2009), which finally yields

$$\begin{aligned} f_{cp}^{no-air} &= \frac{\frac{\rho_{agg}}{\rho_{clin}} + \frac{\rho_{agg}}{\rho_{H_2O}} (w_{cp}(0)/c)}{\frac{\rho_{agg}}{\rho_{clin}} + \frac{\rho_{agg}}{\rho_{H_2O}} (w_{cp}(0)/c) + (a/c)} = \frac{0.8406 + 2.648 [(w/c) - \frac{w_a(0)}{a} (a/c)]}{0.8406 + 2.648 [(w/c) - \frac{w_a(0)}{a} (a/c)] + (a/c)} \\ f_{agg}^{no-air} &= \frac{(a/c)}{\frac{\rho_{agg}}{\rho_{clin}} + \frac{\rho_{agg}}{\rho_{H_2O}} (w_{cp}(0)/c) + (a/c)} = \frac{(a/c)}{0.8406 + 2.648 [(w/c) - \frac{w_a(0)}{a} (a/c)] + (a/c)} \end{aligned} \quad (4.11)$$

with $\rho_{agg} = 2.648 \text{ kg/dm}^3$ as the mass density of quartz aggregates, considered throughout the present paper. However, it often occurs during mixing that small amounts of air get entrapped into the cement paste matrix as well. Denoting the corresponding air volume fraction by f_{air} , the volume fractions at the concrete or mortar level can be derived from the relations

$$f_{cp} + f_{agg} + f_{air} = 1 \quad \frac{f_{cp}}{f_{agg}} = \frac{f_{cp}^{no-air}}{f_{agg}^{no-air}} \quad (4.12)$$

which imply that

$$f_{cp} = \frac{1 - f_{air}}{1 + f_{agg}^{no-air}/f_{cp}^{no-air}}, \quad f_{agg} = \frac{1 - f_{air}}{1 + f_{cp}^{no-air}/f_{agg}^{no-air}}, \quad (4.13)$$

The relevance of this new water migration model and its effect on concrete composition will now be tested through a creep upscaling analysis from the cement paste level to the concrete or mortar level.

4.3 Creep homogenization of mortars and concretes

The relevance of the effective water-to-cement mass ratio according to Eq. (4.10) and of the cement paste and aggregates volume fractions according

to Eq. (4.11) and (4.13), both depending on the void filling extent α and the water uptake capacity of the aggregates, $w_a(0)/a$, will now be checked by using Eq. (4.10), (4.11), and (4.13) and the quantities appearing therein, within a creep upscaling analysis from the cement paste to the mortar and concrete level.

Thereby, the question is tackled whether the experimental results of numerous creep tests performed at the level of cement paste made from *only one* type of cement, and at the level of mortars and concretes made from *the same* type of cement, but with two different types of aggregates, can be predicted by a micromechanical model, which is based on *only one* value for the cement-specific void filling capacity α , and of *only two* aggregate-specific values for the water absorption capacity $w_a(0)/a$.

The creep tests considered in this context all follow the protocol recently reported by Irfan-ul-Hassan et al. (2016): Accordingly, three-minute creep tests on the same cement paste, mortar, or concrete samples are hourly repeated. The key idea behind this protocol is that three minutes are short enough for the microstructure to remain practically *invariant* throughout each individual test. Within one hour, on the other hand, the hydration process in early-age cementitious systems goes on in a significant manner, such that two subsequent three-minute long creep tests refer to already remarkably *different* microstructures. Hence, an upscaling analysis concerning cement paste, mortar, and concrete samples tested according to the aforementioned protocol can be performed in the theoretical framework of classical, *non-aging* microviscoelasticity (Read 1950, 1951; Laws and McLaughlin 1978; Beurthey and Zaoui 2000).

Choosing, in this context, a standard micromechanical representation for mortar and concrete (Scheiner and Hellmich 2009; Baweja et al. 1998; Bernard et al. 2003b; Hellmich and Mang 2005), namely that of a composite material consisting of a (viscoelastic) cement paste matrix with (elastic) aggregate inclusions and with (potentially occurring) air inclusions, as seen in Fig. 4.2, the (homogenized) relaxation tensor at the concrete/mortar scale, \mathbb{R}_{hom} , follow from those at the cement paste scale, \mathbb{R}_{cp} , as well as from the volume fractions of cement paste, of aggregates, and of (potentially occurring) air, as (Scheiner

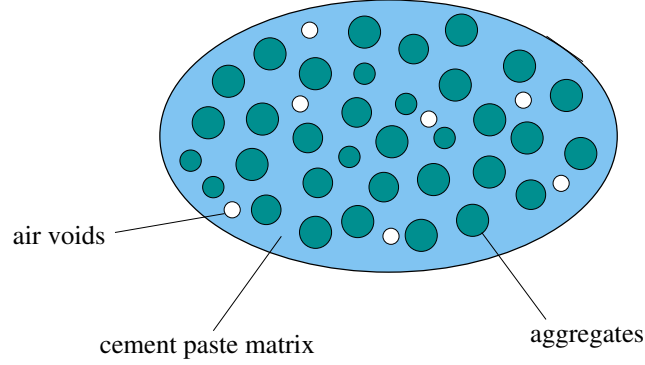


Figure 4.2: Micromechanical representation of mortar and concrete: 2D sketch of 3D matrix-inclusion composites comprising a continuous cement paste matrix with embedded spherical inclusions representing quartz aggregates and air pores

and Hellmich 2009)

$$\begin{aligned}
 \mathbb{R}_{hom}^*(p) &= 3 k_{hom}^*(p) \mathbb{I}_{vol} + 2 \mu_{hom}^*(p) \mathbb{I}_{dev} = \\
 &\left(f_{cp} \mathbb{R}_{cp}^* + f_{agg} \mathbb{R}_{agg}^* : \left\{ \mathbb{I} + \mathbb{P}_{sph}^*(p) : [\mathbb{R}_{agg}^* - \mathbb{R}_{cp}^*(p)] \right\}^{-1} \right. \\
 &\quad \left. + f_{air} \mathbb{R}_{air}^* : \left\{ \mathbb{I} + \mathbb{P}_{sph}^*(p) : [\mathbb{R}_{air}^* - \mathbb{R}_{cp}^*(p)] \right\}^{-1} \right) \\
 &: \left(f_{cp} \mathbb{I} + f_{agg} \left\{ \mathbb{I} + \mathbb{P}_{sph}^*(p) : [\mathbb{R}_{agg}^* - \mathbb{R}_{cp}^*(p)] \right\}^{-1} \right. \\
 &\quad \left. + f_{air} \left\{ \mathbb{I} + \mathbb{P}_{sph}^*(p) : [\mathbb{R}_{air}^* - \mathbb{R}_{cp}^*(p)] \right\}^{-1} \right)^{-1}
 \end{aligned} \tag{4.14}$$

where the star-indicated properties refer to the Laplace Carson (LC) transforms of the originally time-dependent quantities occurring in the standard convolution integrals of linear viscoelasticity [“correspondence principle” (Read 1950, 1951; Laws and McLaughlin 1978; Beurthey and Zaoui 2000)]

$$f^*(p) = p \hat{f}(p) = p \int_0^{\infty} f(t) \exp(-pt) dt, \tag{4.15}$$

and back-transformation of (55) from the Laplace Carson domain back to the time domain may be performed by the Gaver-Wynn-Rho algorithm (Scheiner and Hellmich 2009; Gaver 1966). Mathematical details on the LC-transformed homogenized bulk and shear moduli, k_{hom}^* and μ_{hom}^* , on the fourth-order unity tensor \mathbb{I} with its volumetric and deviatoric parts, \mathbb{I}_{vol} and \mathbb{I}_{dev} , and on the morphology tensor \mathbb{P}_{sph}^* can be found in the Appendix. The relaxation tensors

\mathbb{R}_{cp}^* correspond to a power-law-type creep behavior characterized by an elastic modulus E_{cp} , a Poisson's ratio ν_{cp} , a creep modulus $E_{c,cp}$, and a creep exponent β_{cp} ; hence they read as

$$\begin{aligned} \mathbb{R}_{cp}^*(p) &= 3 k_{cp}^*(p) \mathbb{I}_{vol} + 2 \mu_{cp}^*(p) \mathbb{I}_{dev} \\ &= \left[\frac{1 - 2 \nu_{cp}}{E_{cp}} + \frac{1 - 2 \nu_{cp}}{E_{c,cp}} \left(\frac{1}{t_{ref}} \right)^{\beta_{cp}} \Gamma(\beta_{cp} + 1) p^{-\beta_{cp}} \right]^{-1} \mathbb{I}_{vol} \\ &\quad + \left[\frac{1 + \nu_{cp}}{E_{cp}} + \frac{1 + \nu_{cp}}{E_{c,cp}} \left(\frac{1}{t_{ref}} \right)^{\beta_{cp}} \Gamma(\beta_{cp} + 1) p^{-\beta_{cp}} \right]^{-1} \mathbb{I}_{dev}. \end{aligned} \quad (4.16)$$

The aforementioned material characteristics at the cement paste level all depend on the (here effective) water-to-cement mass ratio and the hydration degree, as identified in the more than 500 creep tests on cement paste reported by [Irfan-ul-Hassan et al. \(2016\)](#), see Fig. 4.3. For considering (effective) water-

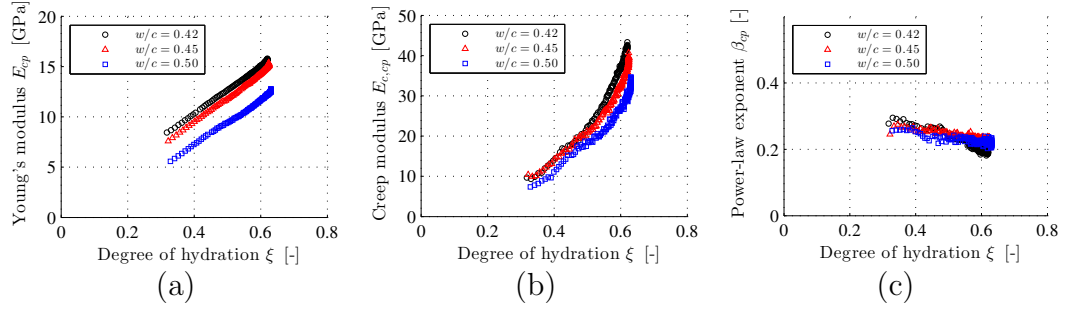


Figure 4.3: Results from hourly-repeated three-minute creep testing on cement pastes with initial water-to-cement mass ratios amounting to 0.42, 0.45, and 0.50, respectively: (a) elastic modulus E_{cp} , (b) creep modulus $E_{c,cp}$, and (c) creep exponent β_{cp} ; as functions of hydration degree, see ([Irfan-ul-Hassan et al. 2016](#))

to-cement mass ratios between those which were explicitly tested, we resort to quadratic interpolation, as exemplified in Fig. 4.4. For the quantification of Poisson's ratio, we use a validated multiscale model ([Pichler and Lackner 2008](#); [Pichler and Hellmich 2011](#)) for establishment of a relation between the latter and the elastic modulus, see Fig. 4.5.

Our present study is devoted to aggregates consisting of quartz, with elastic bulk and shear moduli amounting to ([Bass 2013](#)),

$$k_{agg} = 37.8 \text{ GPa}, \quad \mu_{agg} = 44.3 \text{ GPa} \quad \Rightarrow \quad \mathbb{R}_{agg}^* = 3 k_{agg} \mathbb{I}_{vol} + 2 \mu_{agg} \mathbb{I}_{dev} \quad (4.17)$$

while the air inclusions (if existing) dispose over only negligible elastic stiffness,

$$k_{air} = \mu_{air} = 0 \text{ GPa}, \quad \Rightarrow \quad \mathbb{R}_{air}^* = 0. \quad (4.18)$$

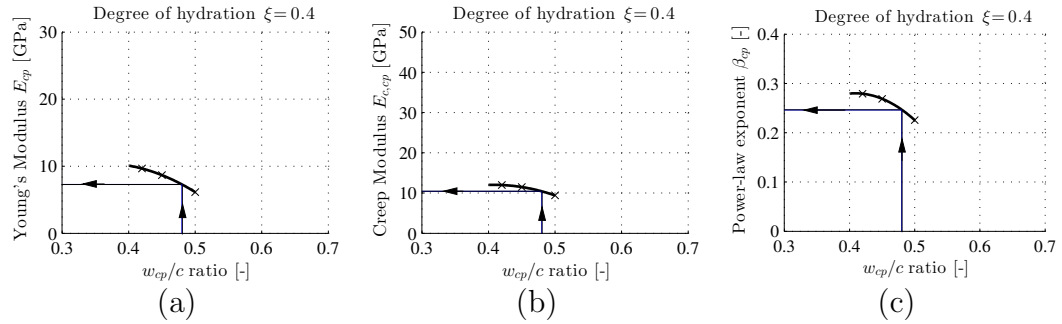


Figure 4.4: Quantification of effective viscoelastic properties of the cement paste matrix as a function of the effective water-to-cement mass fraction w_{cp}/c , by means of quadratic interpolation between creep test results on plain cement pastes with $w/c \in [0.42, 0.45, 0.50]$: (a) elastic modulus E_{cp} , (b) creep modulus $E_{c,cp}$, and (c) creep exponent β_{cp} ; at degree of hydration $\xi = 0.40$

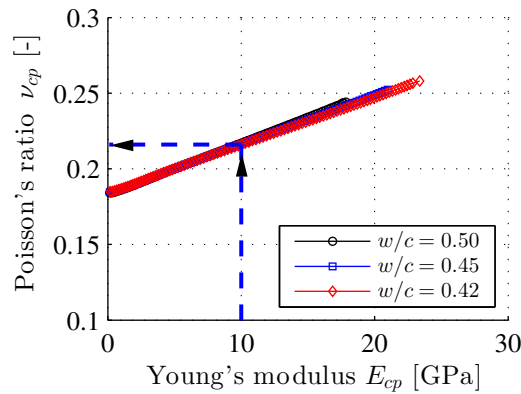


Figure 4.5: Relation between elastic modulus and Poisson's ratio of cement pastes with initial water-to-cement mass ratios amounting to 0.42, 0.45, and 0.50, respectively; predictions of the validated multiscale model of Pichler and Lackner (2009) and Pichler and Hellmich (2011)

4.4 Comparison of ultrashort creep experiments and corresponding micromechanics predictions - identification of water absorption capacities of quartz aggregates and of paste void filling extent

Experimental campaign on the mortar/concrete level

In order to assess the relevance of the newly introduced quantities, the paste void filling extent α and the water absorption capacity of aggregates, $w_a(0)/a$, expressed in corresponding creep homogenization results as described in the previous section, the latter results need to be compared to experimental data at the level of mortar and concrete. To this end, a series of three minute-long creep tests on two mortars and two concretes was performed:

Thereby, all four materials exhibited the same nominal volume fractions of quartz aggregates and of cement paste, respectively, namely amounting to 0.58 and to 0.42, respectively, see Table 4.1. Mortar #1 and Concrete #1 exhibited the same nominal composition in terms of $w/c = 0.50$ and $a/c = 3.0$. Mortar #2 and Concrete #2, in turn, exhibited $w/c = 0.42$ and $a/c = 2.7$. All four materials were produced from a commercial cement of type CEM I 42.5 N and distilled water, i.e. with the same raw materials that were also used for the production of the cement pastes discussed in [Irfan-ul-Hassan et al. \(2016\)](#). In addition, we used oven-dried aggregates made of quartz. The two mortars contain standard sand of the company “Normensand” as per standard DIN EN-196-1, consisting of rounded sand grains with diameters being smaller or equal to $d_{max} = 2$ mm. The two concretes contain aggregates of the Austrian company “Pannonia Kies”, consisting of quartz gravels with diameters being smaller or equal to $d_{max} = 8$ mm.

Table 4.1: Nominal composition of tested mortars and concretes

Material	w/c	a/c	f_{cp}^{nom}	f_{agg}^{nom}	d_{max}
Mortar #1	0.50	3.0	0.42	0.58	2 mm
Mortar #2	0.42	2.7	0.42	0.58	2 mm
Concrete #1	0.50	3.0	0.42	0.58	8 mm
Concrete #2	0.42	2.7	0.42	0.58	8 mm

The early-age testing protocol is identical to the one used to characterize cement paste [see [Irfan-ul-Hassan et al. \(2016\)](#)], i.e. the mortar and concrete specimens with dimensions (70 mm diameter and 300 mm height) were hourly

subjected to three-minute long creep tests under uniaxial stress conditions, see Fig. 4.6 (a) for the stress history in a specific three-minute long creep test. For each test, the load plateau was selected such that induced compressive stresses were smaller than 15 % of the expected compressive strength, see Fig. 4.6 (b). Using the calorimetry results described by Irfan-ul-Hassan et al. (2016), sample ages were “translated” into equivalent hydration degrees.

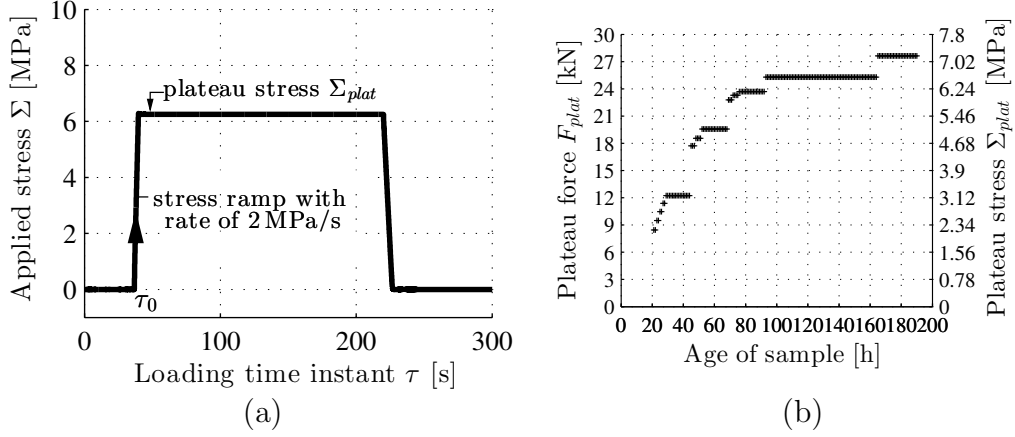


Figure 4.6: Three-minute creep tests on mortars and concretes: (a) force history during creep testing carried out at an age of 100 h on Mortar #1; and (b) prescribed load levels chosen to be smaller than or equal to 15 % of the expected compressive strength

Each tested specimen was subjected to 168 three-minute creep tests. Out of this database, we focus on the tests carried out at hydration degrees amounting to

$$\xi \in [0.32, 0.35, 0.40, 0.45, 0.50, 0.55, 0.60, 0.63] \quad (4.19)$$

The plateau stresses of Fig. 4.6, which correspond to the hydration degrees of Eq. (4.19), were

$$\Sigma_{plat} = [2.08, 2.32, 3.0, 3.0, 4.37, 4.83, 6.25, 6.25] \text{ MPa} \quad (4.20)$$

The correspondingly measured normal strains in loading direction, $E(t)$, were divided by the applied plateau stress Σ_{plat} , see Fig. 4.6, so as to arrive at a convenient illustration of the test results, as shown in Fig. 4.7

Micromechanical predictions of experimental data

For micromechanically predicting the creep test results of Fig. 4.7, the relaxation functions of Eq. (55) are transformed to creep functions according to

$$\begin{aligned} \mathbf{J}_{hom}^*(p) &= \mathbf{R}_{hom}^*(p)^{-1} \\ \mathbf{E}^*(p) &= \mathbf{J}_{hom}^*(p) : \Sigma^*(p) \end{aligned} \quad (4.21)$$

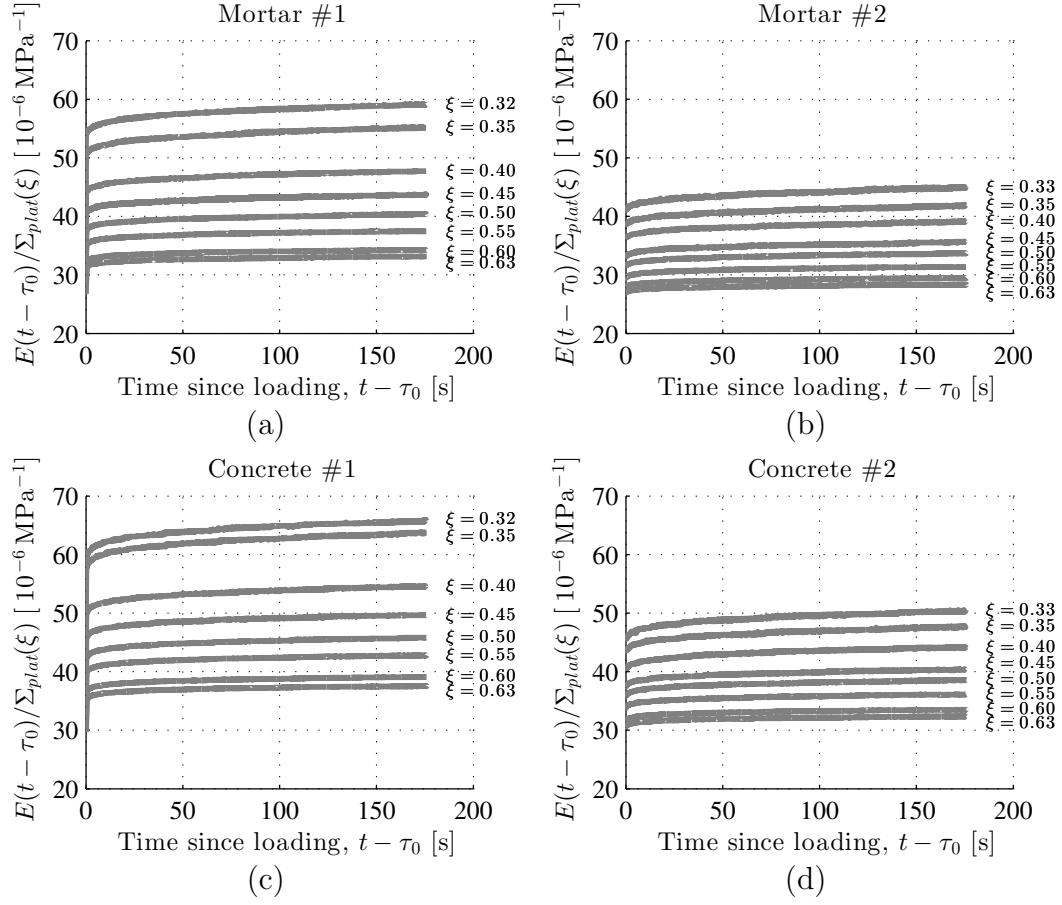


Figure 4.7: Plateau stress-normalized strains obtained from three minute-long creep tests on mortars and concretes, at the hydration degrees given in Eq. (4.19), and the corresponding load plateaus according to Eq. (4.20): (a) Mortar #1: $w/c = 0.50$, $a/c = 3.00$, (b) Mortar #2: $w/c = 0.42$, $a/c = 2.70$, (c) Concrete #1: $w/c = 0.50$, $a/c = 3.00$, (d) Concrete #2: $w/c = 0.42$, $a/c = 2.70$

and this result is then back-transformed into the time-domain, yielding

$$\mathbf{E}(\xi, t) = \int_0^t \mathbf{J}_{hom}(\xi, t - \tau) : \dot{\Sigma}(\tau) d\tau \quad (4.22)$$

This Boltzmann convolution integral is then evaluated for the volume fractions of Eqs. (4.11) and (4.13), for the cement paste properties of Fig. 4.4, and for the loading history of Fig. 4.6. These evaluations comprise two quantities which are not known *a priori*, but which are identified from a series of creep results at the concrete and mortar levels. This is described next.

Also, it needs to be emphasized that consideration of the load history of Fig. 4.6 as a continuous function, rather than as a step function, and corresponding

use of the continuous form of the Boltzmann integral (4.22), is mandatory for arriving at reliable results. This is because a ramp loading as indicated in Fig. 4.6, does not only provoke elastic, but also viscoelastic strains, as was explicitly evidenced by Irfan-ul-Hassan et al. (2016).

Identification of water uptake capacity of “Normensand” quartz aggregates and of the paste void filling extent, from experimental data concerning Mortar #1

The water uptake capacity of quartz, $w_a(0)/a$, and the paste void filling extent α , are identified from a very large set of numerical values making up the following ”search intervals”

$$\begin{aligned} w_a(0)/a &\in [0.000, 0.0001, 0.0002, \dots, 0.0199, 0.0200] \\ \alpha &\in [0.000, 0.001, 0.002, \dots, 0.999, 1.000]. \end{aligned} \quad (4.23)$$

For all data pairs $[w_a(0)/a, \alpha]$ composed from the values given in Eq. (4.23), the micromechanics model of Eqs. (55)–(4.18), together with Eqs. (4.3), (4.10), and (4.11) evaluated for $w/c = 0.50$ and $a/c = 3.0$, see Table 4.1, with the interpolation scheme of Fig. 4.4, and with the loading history of Fig. 4.6 entering Eq. (4.22), is used to predict the creep functions arising from the eight creep tests conducted on Mortar #1, as seen in Fig. 4.7(a). Eight hydration degree-specific model predictions of the normal strain histories E^{pred} , represented by 180 discrete values each, are compared to the corresponding experimentally determined strains normalized by plateau stress E^{exp} ; and the corresponding prediction error is quantified through

$$\mathcal{E} = \frac{1}{8 \times 180} \sum_{i=1}^8 \frac{1}{\Sigma_{plat}(\xi_i)} \sum_{j=1}^{180} |E^{pred}(\xi_i, t_j) - E^{exp}(\xi_i, t_j)| \quad (4.24)$$

whereby all strain values were normalized with respect to the plateau stresses Σ_{plat} . The smallest prediction error $\mathcal{E} = 1.55 \times 10^{-7} \text{ MPa}^{-1}$ (see Table 4.2) is

Table 4.2: Prediction Errors \mathcal{E} (MPa^{-1}) according to Eq. (4.24)

Material	\mathcal{E} with nominal composition	\mathcal{E} obtained with water migration model
Mortar #1	4.50×10^{-6}	1.55×10^{-7}
Mortar #2	1.50×10^{-6}	2.90×10^{-7}
Concrete #1	5.50×10^{-6}	1.50×10^{-7}
Concrete #2	1.23×10^{-6}	1.30×10^{-7}

obtained for the following values of the water uptake capacity of quartz and of the water filling extent of shrinkage-induced voids:

$$\frac{w_a(0)}{a} = 0.0099 \quad \alpha = 0.603 \quad (4.25)$$

see Fig. 4.8 (a) for the comparison of measured and modeled creep functions. The identified material constants (4.25) imply (i) that 1 kilogram of quartz takes up 9.9 gram of water during mixing of the raw materials, and (ii) that shrinkage-induced voids of the cement paste matrix soak water from the open porosity of quartz such that these voids are water-filled to an extent of 60.3 percent.

The identified material constants (4.25) provide access to the effective composition of the cement paste of Mortar #1. The initial value of the effective water-to-cement mass fraction of the cement paste matrix, for instance, follows from specialization of Eq. (4.3) for $w_a(0)/a$ from (4.25) and for the mix-related water-to-cement and quartz-to-cement mass ratios $w/c = 0.50$ and $a/c = 3.0$ as:

$$\frac{w_{cp}(0)}{c} = 0.4703 \quad (4.26)$$

This is remarkably smaller than the (nominal) mix-related water-to-cement mass ratio $w/c = 0.50$. The evolution of the effective water-to-cement mass fraction of the cement paste matrix follows from specialization of Eq. (4.10) for (4.25), $w/c = 0.50$, and $a/c = 3.0$ as

$$\frac{w_{cp}(\xi)}{c} = 0.4703 + 0.0317 \xi \quad (4.27)$$

see also Fig. 4.8 (b). The actual volume fractions of the cement paste matrix and of quartz follow from specialization of Eqs. (4.11) for Eq. (4.26), $w/c = 0.50$, and $a/c = 3.0$ as

$$f_{cp} = 0.4101, \quad f_{agg} = 0.5899. \quad (4.28)$$

Confirmation of the water uptake capacity of "Normen-sand" quartz aggregates and of the paste void filling extent, through experimental data concerning Mortar #2

Since Mortar #1 and Mortar #2 are produced with the same raw materials, the identified material constants given in Eqs. (4.25) are not only valid for Mortar #1, but they must also hold for Mortar #2, i.e. the strain evolutions measured during creep testing of Mortar #2 must be predictable, and this is checked next. To this end, the initial value of the effective water-to-cement

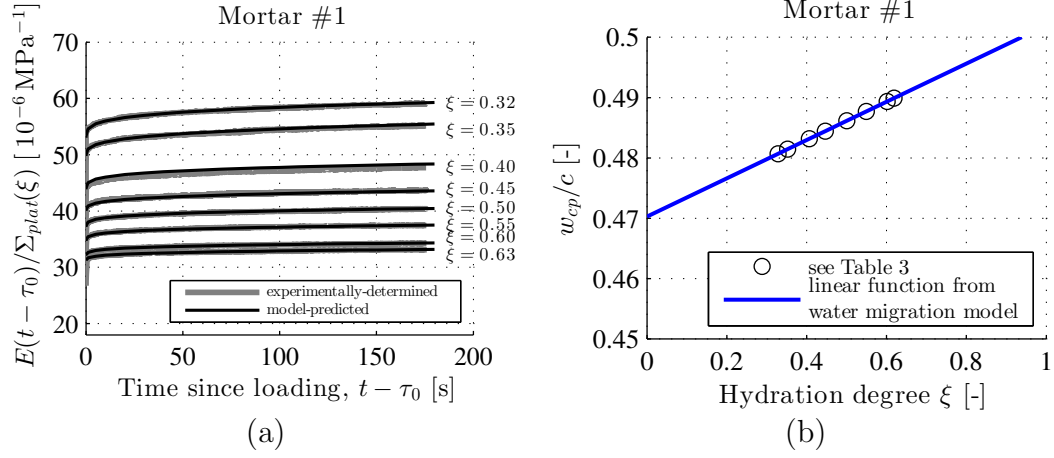


Figure 4.8: Application of the water migration model according to Eq. (4.10) to Mortar #1, with a mix-related (nominal) composition given through $w/c = 0.50$ and $a/c = 3.0$, as well as water uptake capacity of quartz and void water-filling extent according to Eq. (4.25): (a) Comparison of experimentally-determined and model-predicted plateau stress-normalized strains, at the hydration degrees given in Eq. (4.19) and the corresponding load plateaus according to Eq. (4.20); (b) evolution of the effective water-to-cement mass fraction of the cement paste matrix, as a function of degree of hydration; for the complete set of material properties of cement paste, see Table 4.3

Table 4.3: Input quantities for creep homogenization of Mortar #1 with mix-related (nominal) composition quantified through $w/c = 0.50$ and $a/c = 3.0$: effective water-to-cement mass fractions of the cement paste matrix according to Eqs. (4.10) and (4.25), as well as corresponding viscoelastic properties of the cement paste matrix found by means of interpolation (see Fig. 4.4), for hydration degrees listed in Eq. (4.19)

ξ [-]	$w_{cp}(\xi)/c$ [-]	E_{cp} [GPa]	ν_{cp} [-]	$E_{c,cp}$ [GPa]	β_{cp} [-]
0.32	0.480	6.529	0.205	9.218	0.269
0.35	0.481	7.041	0.206	8.562	0.267
0.40	0.483	8.223	0.210	13.220	0.242
0.45	0.484	9.172	0.214	15.775	0.228
0.50	0.486	10.236	0.217	19.270	0.219
0.55	0.487	11.274	0.221	23.640	0.210
0.60	0.489	12.442	0.225	29.012	0.209
0.63	0.490	12.843	0.226	30.774	0.208

mass fraction of the cement paste matrix follows from specialization of Eq. (4.3) for $w_a(0)/a$ from (4.25) and for the mix-related water-to-cement and quartz-to-cement mass ratios $w/c = 0.42$ and $a/c = 2.7$ as:

$$\frac{w_{cp}(0)}{c} = 0.3933 \quad (4.29)$$

This is significantly smaller than the mix-related water-to-cement mass ratio $w/c = 0.42$. The evolution of the effective water-to-cement mass fraction of the cement paste matrix follows from specialization of Eq. (4.10) for (4.25), $w/c = 0.42$, and $a/c = 2.7$ as

$$\frac{w_{cp}(\xi)}{c} = 0.3933 + 0.0317 \xi \quad (4.30)$$

see also Fig. 4.9 (b). The actual volume fractions of the cement paste matrix and of quartz follow from specialization of Eq. (4.11) for Eq. (4.29), $w/c = 0.42$, and $a/c = 2.7$ as

$$f_{cp} = 0.4107, \quad f_{agg} = 0.5893. \quad (4.31)$$

Viscoelastic properties of the cement paste matrix – valid for effective water-to-cement mass fractions from Eq. (4.30), evaluated for all hydration degrees of interest given in Eq. (4.19) – are quantified by means of interpolation; as described in the previous subsection, see also Fig. 4.4.

Model-predicted creep functions for Mortar #2 agree well with measured creep functions, as quantified by prediction error $\mathcal{E} = 2.90 \times 10^{-7} \text{ MPa}^{-1}$ (see Table 4.2) evaluated according to Eq. (4.24), see also Fig. 4.9 (a). This underlines not only the satisfactory predictive capabilities of the developed water migration model, see Eq. (4.10), but also the significance of the identified values of the water uptake capacity of quartz and of the water filling extent of shrinkage-induced voids, see Eqs. (4.25).

Identification of water uptake capacity of "Pannonia Kies" aggregates and of entrapped air content, from experimental data concerning Concrete #1

When it comes to model prediction of the creep strain evolutions measured in three-minutes creep tests on Concrete #1, it is important to emphasize that both concretes were produced with quartz gravel of type "Pannonia Kies", i.e. the corresponding water-uptake capacity is unknown and needs to be identified. Notably, this is not enough for obtaining a satisfactory agreement between model-predicted and measured creep functions, because the model-predicted creep functions turn out to underestimate the measured creep functions, particularly because the elastic stiffness is overestimated. In order to improve the situation, we consider that air was mixed into concrete during production.

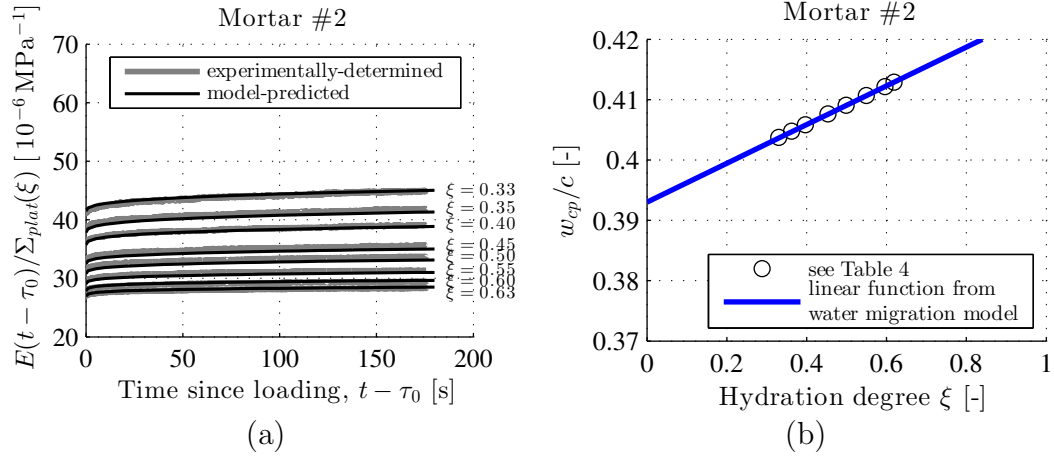


Figure 4.9: Application of the water migration model according to Eq. (4.10) to Mortar #2, with a mix-related (nominal) composition given through $w/c = 0.42$ and $a/c = 2.7$, as well as water uptake capacity of quartz and void water-filling extent according to Eq. (4.25): (a) Comparison of experimentally-determined and model-predicted plateau stress-normalized strains, at the hydration degrees given in Eq. 4.19) and the corresponding load plateaus according to Eq. (4.20); (b) evolution of effective water-to-cement mass fraction of the cement paste matrix, as a function of degree of hydration; for the complete set of material properties of cement paste, see Table 4.4

Table 4.4: Input quantities for creep homogenization of Mortar #2 with mix-related (nominal) composition quantified through $w/c = 0.42$ and $a/c = 2.7$: effective water-to-cement mass fractions of the cement paste matrix according to Eqs. (4.10) and (4.25), as well as corresponding viscoelastic properties of the cement paste matrix found by means of interpolation (see Fig. 4.4), for hydration degrees listed in Eq. (4.19)

ξ [-]	$w_{cp}(\xi)/c$ [-]	E_{cp} [GPa]	ν_{cp} [-]	$E_{c,cp}$ [GPa]	β_{cp} [-]
0.32	0.403	8.623	0.211	9.719	0.322
0.35	0.404	9.864	0.215	11.857	0.290
0.40	0.405	10.693	0.218	14.872	0.270
0.45	0.407	12.175	0.222	19.312	0.260
0.50	0.409	13.189	0.225	23.055	0.244
0.55	0.410	14.369	0.229	30.780	0.222
0.60	0.412	15.417	0.232	38.460	0.196
0.62	0.413	16.146	0.234	44.927	0.192

Since all eight considered creep tests were carried out on the *same* specimen, just one entrapped air content, as appearing in Eq. (4.13) needs to be identified.

Similar to the identification process described for Mortar #1, the water uptake capacity of “Pannonia Kies” quartz and the entrapped air content are identified from the following search intervals:

$$\begin{aligned} w_a(0)/a &\in [0.000, 0.0001, 0.0002, \dots, 0.0199, 0.0200] \\ f_{air} &\in [0.000, 0.001, 0.002, \dots, 0.049, 0.050] \end{aligned} \quad (4.32)$$

The identified void filling extent α according to Eq. (4.25), in turn, is treated as being also applicable to both concretes.

Accordingly, for all data pairs $[w_a/a(0), f_{air}]$ composed from the values given in Eq. (4.32), the micromechanics model of Eqs. (55)–(4.18), together with Eqs. (4.3), (4.10), and (4.11) evaluated for $\alpha = 0.603$, as well as for $w/c = 0.50$ and $a/c = 3.0$, see Table 4.1, with the interpolation scheme of Fig. 4.4 and with the loading history of Fig. 4.6 entering Eq. (4.22), is used to predict the creep functions arising from the eight creep tests conducted on Concrete #1, as seen in Fig. 4.7 (c). Model-predicted creep functions are compared to measured creep functions, and model prediction errors are quantified according to Eq. (4.24). The smallest prediction error amounts to $\mathcal{E} = 1.5 \times 10^{-7} \text{ MPa}^{-1}$ (see Table 4.2), and the corresponding values of the water uptake capacity and of the air volume fraction read as

$$\frac{w_a(0)}{a} = 0.0089 \quad f_{air} = 0.026 \quad (4.33)$$

see Fig. 4.10 (a) for the comparison of measured and model-predicted creep functions. The identified water uptake capacity given in (4.33) implies that 1 kilogram of “Pannonia Kies” quartz takes up 8.9 gram of water during mixing of the raw materials. The corresponding initial value of the effective water-to-cement mass fraction of the cement paste matrix follows from specialization of Eq. (4.3) for $w_a(0)/a$ from (4.33) and for the mix-related water-to-cement and quartz-to-cement mass ratios $w/c = 0.50$ and $a/c = 3.0$ as:

$$\frac{w_{cp}(0)}{c} = 0.4733 \quad (4.34)$$

This is significantly smaller than the mix-related water-to-cement mass ratio $w/c = 0.50$. The evolution of the effective water-to-cement mass fraction of the cement paste matrix follows from specialization of Eq. (4.10) for α from (4.25), for $w_a(0)/a$ from (4.33), for $w/c = 0.50$, and for $a/c = 3.0$, as

$$\frac{w_{cp}(\xi)}{c} = 0.4733 + 0.0317 \xi \quad (4.35)$$

see also Fig. 4.10 (b). Finally, the actual volume fractions of the cement paste matrix and of quartz follow from Eqs. (4.33), (4.34), $w/c = 0.50$, $a/c = 3.0$,

(4.11), and (4.13) as:

$$f_{cp} = 0.4004, \quad f_{agg} = 0.5736. \quad (4.36)$$

The satisfactory agreement between between model-predicted and measured creep functions further corroborates the developed water migration model, see Eq. (4.10), and the void water-filling extent α given in Eq. (4.25).

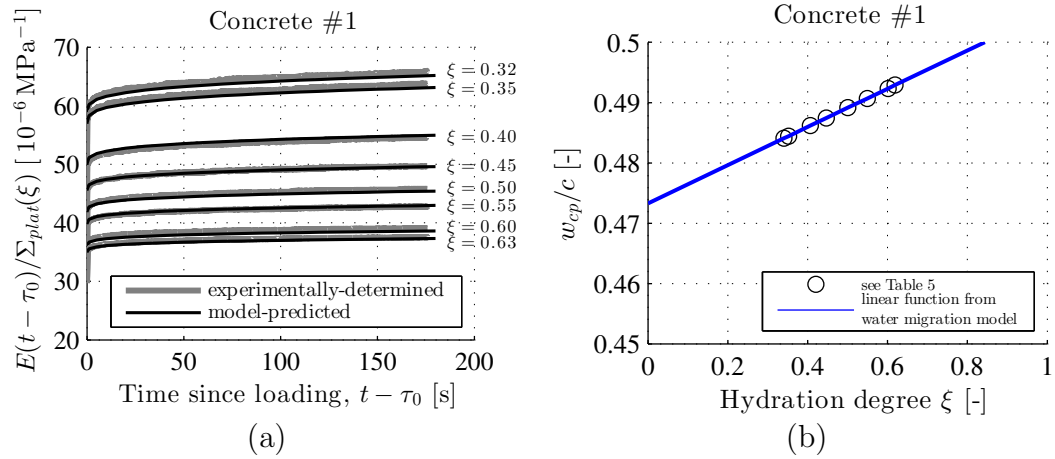


Figure 4.10: Application of the water migration model according to Eq. (4.10) to Concrete #1, with a mix-related (nominal) composition given through $w/c = 0.50$ and $a/c = 3.0$, with void water-filling extent according to Eqs. (4.25), as well as with water uptake capacity of quartz and entrapped air volume fraction according to Eq. (4.33): (a) Comparison of experimentally-determined and model-predicted plateau stress-normalized strains, at the hydration degrees given in Eq. (4.19) and the corresponding load plateaus according to Eq. (4.20); (b) evolution of effective water-to-cement mass fraction of the cement paste matrix, as a function of degree of hydration; for the complete set of material properties of cement paste, see Table 4.5

Confirmation of water uptake capacity of "Pannonia Kies" aggregates, through experimental data concerning Concrete #2

Since Concretes #1 and #2 were produced with the same quartz gravel, the water uptake capacity is already known, see Eq. (4.33). Also, the void water-filling ratio α is already identified, see Eq. (4.25). However, Concrete #2 was tested on a specific specimen, and the related air volume fraction is to be identified. By analogy to the previously described identification processes, the

Table 4.5: Input quantities for creep homogenization of Concrete #1 with mix-related (nominal) composition quantified through $w/c = 0.50$ and $a/c = 3.0$: effective water-to-cement mass fractions of the cement paste matrix according to Eqs. (4.10), with void water-filling extent according to Eq. (4.25), and with water uptake capacity of quartz and entrapped air volume fraction according to Eq. (4.33), as well as corresponding viscoelastic properties of the cement paste matrix found by means of interpolation (see Fig. 4.4), for hydration degrees listed in Eq. (4.19)

ξ [-]	$w_{cp}(\xi)/c$ [-]	E_{cp} [GPa]	ν_{cp} [-]	$E_{c,cp}$ [GPa]	β_{cp} [-]
0.33	0.484	6.720	0.205	9.096	0.262
0.35	0.4845	6.927	0.206	9.531	0.257
0.40	0.486	7.966	0.210	12.332	0.244
0.44	0.487	8.900	0.213	15.582	0.240
0.50	0.489	9.940	0.216	18.548	0.232
0.55	0.490	10.884	0.219	21.911	0.227
0.60	0.492	12.115	0.224	27.777	0.215
0.63	0.493	12.569	0.225	30.116	0.218

entrapped air volume fraction is found as

$$f_{air} = 0.027 \quad (4.37)$$

The initial value of the effective water-to-cement mass fraction of the cement paste matrix follows from specialization of Eq. (4.3) for $w_a(0)/a$ from (4.33) and for the mix-related water-to-cement and quartz-to-cement mass ratios $w/c = 0.42$ and $a/c = 2.7$ as:

$$\frac{w_{cp}(0)}{c} = 0.3960 \quad (4.38)$$

This is significantly smaller than the mix-related water-to-cement mass ratio $w/c = 0.42$. The evolution of the effective water-to-cement mass fraction of the cement paste matrix follows from specialization of Eq. (4.10) for α from (4.25), for $w_a(0)/a$ from (4.33), for $w/c = 0.42$, and for $a/c = 2.7$, as

$$\frac{w_{cp}(\xi)}{c} = 0.3960 + 0.0317 \xi \quad (4.39)$$

see also Fig. 4.11 (b). Finally, the actual volume fractions of the cement paste matrix and of quartz follow from Eqs. (4.33), (4.38), $w/c = 0.42$, $a/c = 2.7$, (4.11), and (4.13) as:

$$f_{cp} = 0.4005, \quad f_{agg} = 0.5725. \quad (4.40)$$

The satisfactory agreement between between model-predicted and measured creep functions, as quantified by prediction error $\mathcal{E} = 1.30 \times 10^{-7} \text{ MPa}^{-1}$ (see Table 4.2) further corroborates the developed water migration model, see Eq. (4.10), evaluated according to Eq. (4.24) the void water-filling extent α given in Eq. (4.25), and the water uptake capacity $w_a(0)/a$ given in Eqs. (4.33).

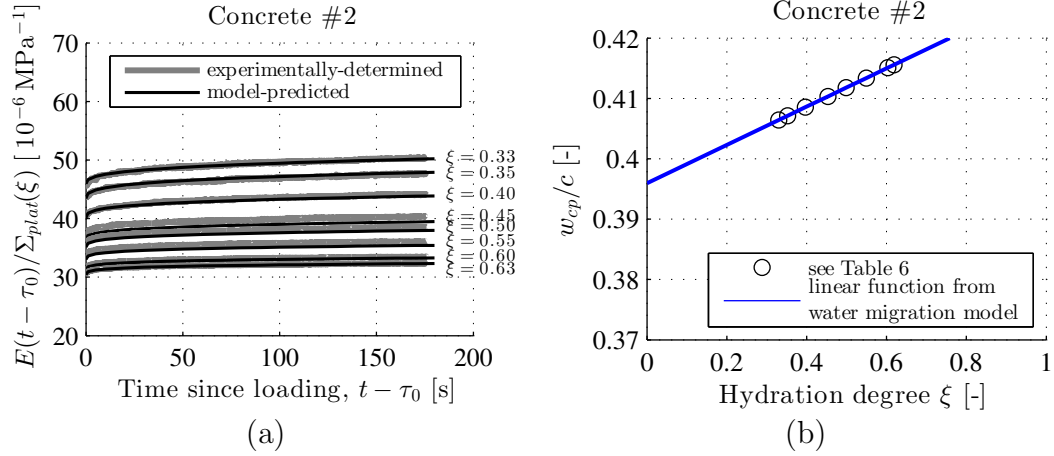


Figure 4.11: Application of the water migration model according to Eq. (4.10) to Concrete #2, with a mix-related (nominal) composition given through $w/c = 0.42$ and $a/c = 2.7$, with void water-filling extent according to Eq. (4.25), with water uptake capacity of quartz according to Eqs. (4.33) and with entrapped air volume fraction according to Eq. (4.37): (a) Comparison of experimentally-determined and model-predicted plateau stress-normalized strains, at the hydration degrees given in Eq. (4.19) and the corresponding load plateaus according to Eq. (4.20); (b) evolution of effective water-to-cement mass fraction of the cement paste matrix, as a function of degree of hydration; for the complete set of material properties of cement paste, see Table 4.6

4.5 Conclusions

We here presented an extension of the classical Powers hydration model with respect to internal curing, and checked the relevance of the latter through micromechanical upscaling of effective water-to-cement mass ratio-dependent cement paste creep functions, up to the levels of mortar/concrete. Remarkably, internal curing can be considered in terms of only two additional quantities: an aggregate-specific uptake capacity, and a cement-paste specific void filling extent. Identifying these quantities herein for two types of oven-dried quartz aggregates, and for one type of cement, allowed for satisfactory prediction

Table 4.6: Input quantities for creep homogenization of Concrete #2 with mix-related (nominal) composition quantified through $w/c = 0.42$ and $a/c = 2.7$: effective water-to-cement mass fractions of the cement paste matrix according to Eq. (4.10), with void water-filling extent according to Eq. (4.25), with water uptake capacity of quartz according to Eqs. (4.33), and with entrapped air volume fraction according to Eq. (4.37), as well as corresponding viscoelastic properties of the cement paste matrix found by means of interpolation (see Fig. 4.4), for hydration degrees listed in Eq. (4.19)

ξ [-]	$w_{cp}(\xi)/c$ [-]	E_{cp} [GPa]	ν_{cp} [-]	$E_{c,cp}$ [GPa]	β_{cp} [-]
0.33	0.406	8.519	0.211	9.597	0.312
0.35	0.407	9.268	0.213	10.701	0.286
0.40	0.408	10.477	0.217	14.669	0.265
0.45	0.410	11.921	0.221	19.020	0.255
0.50	0.411	12.791	0.224	22.434	0.238
0.55	0.413	13.940	0.228	29.692	0.218
0.60	0.415	15.153	0.231	38.407	0.195
0.62	0.415	15.672	0.233	43.084	0.191

of numerous ultrashort-term creep tests on two mortars and two concretes, see Figs. 4.8 to 4.11. Such creep tests directly deliver the hydration-dependent (non-aging) creep properties, also valid for medium-term creep tests on very old pastes, see (Irfan-ul-Hassan et al. 2016). Neglecting internal curing effects, i.e. initial water uptake through the aggregates followed by "back-soaking" of this water from the aggregates domain to that of the maturing cement paste, would clearly *not* allow for satisfactory micromechanical prediction of the creep properties at the mortar and concrete level, as is quantified in Table 4.2 and illustrated in Fig. 4.12, showing predictions based on $w_a(0)/a = \alpha = f_{air} = 0$, while keeping all other input variables as defined earlier in this paper. Obviously, the creep response predicted by the micromechanical model of Fig. 4.2 would be too soft under these conditions. It is also illustrative to quantify the degree of hydration when the "back-suction" of water from aggregates to the cement paste is finished, simply because no water is left any more in the aggregates. To this end, $w_{cp}(\xi)/c$ in Eq. (4.10) is set equal to w/c , and the resulting expression is solved for hydration degree ξ . This delivers

$$\xi^* = \frac{\frac{w_a(0)}{a} (a/c) \left\{ 20 + 63 \left[w/c - \frac{w_a(0)}{a} (a/c) \right] \right\}}{\alpha \left\{ 1.051 + 3.31 \left[w/c - \frac{w_a(0)}{a} (a/c) \right] \right\}} \quad (4.41)$$

Notably, the creep tests which were analyzed herein refer to hydration degrees smaller than ξ^* , see Figs. 4.8 (b), 4.9 (b), 4.10 (b), and 4.11 (b).

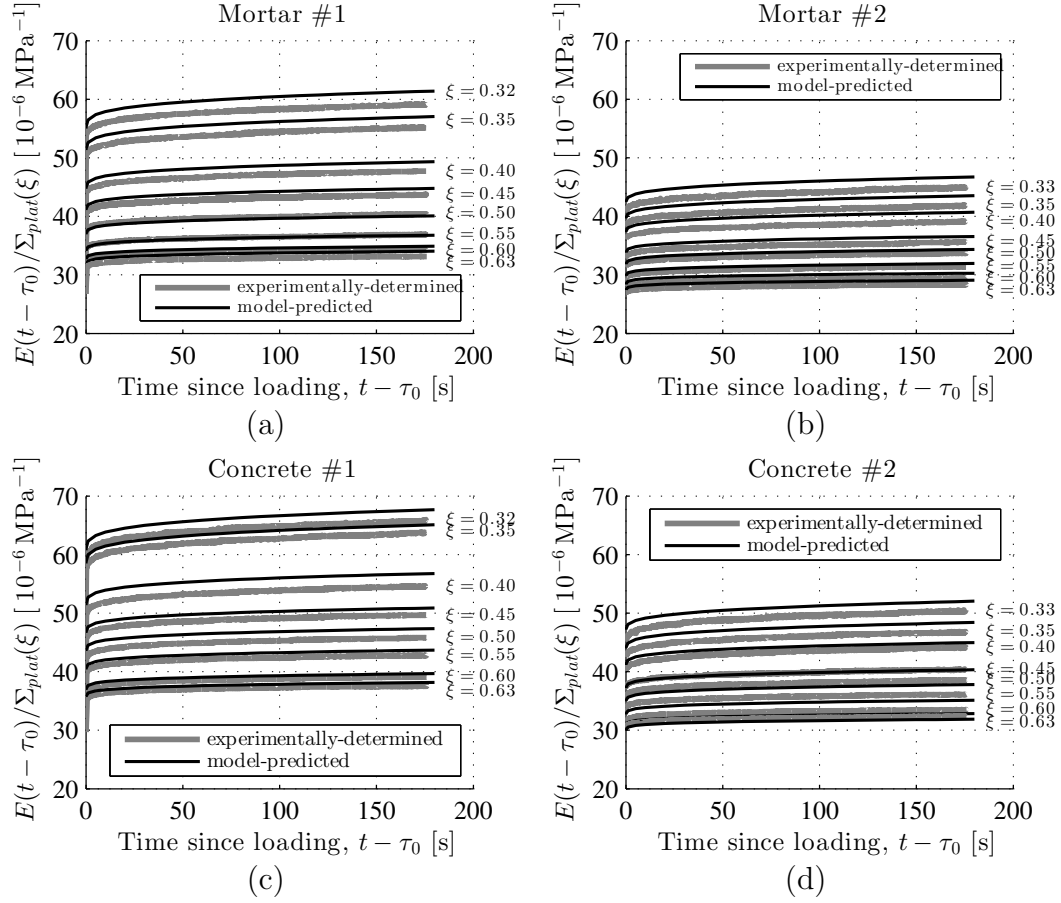


Figure 4.12: Comparison of experimentally-determined and model-predicted plateau stress-normalized strains, using nominal compositions as input, see Table 4.1, at the hydration degrees given in Eq. (4.19) and the corresponding load plateaus according to Eq. (4.20); For (a) Mortar #1, (b) Mortar #2, (c) Concrete #1, and (d) Concrete #2: Model predicted strains overestimate the experimentally measured strains; see also Table 4.2

The method described herein, showing how to integrate internal curing events into micromechanical modeling of concrete, in particular concerning creep, can be straightforwardly extended to aging creep behavior, based on earlier contributions such as those of Scheiner and Hellmich (2009) or Sanahuja (2013b).

Another obvious extension concerns the deeper reasons for the dependencies of the creep properties of cement paste, on the water-to-cement mass ratio as depicted in Fig. 4.4, which may be deciphered through micromechanical resolution down to the level of the hydrates (Königsberger et al. 2016), or even, down to the level of lubricating water layers between calcium silicate sheets, (Pellenq et al. 2009; Sanahuja and Dormieux 2010; Shahidi et al. 2014, 2015a; Vandamme et al. 2015; Shahidi et al. 2016).

4.6 Acknowledgment

We cordially thank for valuable help of the laboratory staff of the Institute of Mechanics of Materials and Structures, TU Wien – Vienna University of Technology. The first author also wishes to thank the Higher Education Commission (HEC) Pakistan and the University of Engineering and Technology, Lahore, Pakistan, for their support.

Nomenclature

Symbols:

$A_{\infty,agg}^{*,vol}$	LC-transformed volumetric component of Eshelby problem-related strain concentration tensor of aggregates
$A_{\infty,agg}^{*,dev}$	LC-transformed deviatoric component of Eshelby problem-related strain concentration tensor of aggregates
$A_{\infty,air}^{*,vol}$	LC-transformed volumetric component of Eshelby problem-related strain concentration tensor of air
$A_{\infty,air}^{*,dev}$	LC-transformed deviatoric component of Eshelby problem-related strain concentration tensor of air
a	mass of aggregates
a/c	aggregate-to-cement mass ratio
α	water filling extent of shrinkage induced voids in cement paste
β_{cp}	power-law creep exponent for cement paste
c	mass of cement paste
d	a material constant equal to $w_{cp}(0)/c$
d_{max}	maximum diameter of aggregates
δ_{ij}	Kronecker delta
E	macroscopic uniaxial strain
\mathbf{E}	macroscopic strain tensor
E^{exp}	experimentally-determined macroscopic uniaxial strain
E^{pred}	model-predicted macroscopic uniaxial strain
E_{cp}	Young's elastic modulus of cement paste
$E_{c,cp}$	Young's creep modulus of cement paste
\mathcal{E}	prediction error
F_{plat}	plateau force
f_{cp}	volume fraction of the cement paste
f_{agg}	volume fraction of the aggregates
f_{air}	volume fraction of the air
f_{agg}^{no-air}	volume fraction of aggregates without entrapped air
f_{cp}^{no-air}	volume fraction of cement paste without entrapped air
f_{void}^{cp}	cement paste-related volume fraction of voids
\mathbb{G}	auxiliary isotropic fourth-order tensor
G^{vol}, G^{dev}	volumetric and deviatoric components of \mathbb{G}
\mathbb{I}	fourth-order identity tensor
$\mathbf{1}$	second-order identity tensor
$\mathbb{I}^{vol}, \mathbb{I}^{dev}$	volumetric and deviatoric parts of \mathbb{I}
\mathbb{J}_{hom}	homogenized fourth-order tensorial creep function
k	a material constant equal to rate of w_{cp}/c
k_{agg}	bulk modulus of aggregates
k_{air}	bulk modulus of air
k_{cp}	bulk modulus of cement paste
k_{hom}	bulk modulus of mortar or concrete
LC	Laplace-Carson

μ_{agg}	shear modulus of aggregates
μ_{air}	shear modulus of air
μ_{cp}	shear modulus of cement paste
μ_{hom}	shear modulus of mortar or concrete
ν_{cp}	Poisson's ratio of cement paste
p	complex variable in the LC domain
\mathbb{P}_{sph}^*	LC-transformed Hill tensor of spherical inclusions, embedded in an infinite cement paste matrix
\mathbb{R}_{agg}^*	LC-transformed fourth-order relaxation tensor function of aggregates
\mathbb{R}_{air}^*	LC-transformed fourth-order relaxation tensor function of air
\mathbb{R}_{cp}^*	LC-transformed fourth-order relaxation tensor function of cement paste
\mathbb{R}_{hom}^*	LC-transformed fourth-order relaxation tensor function of mortar or concrete
ρ_{agg}	mass density of aggregates
ρ_{clin}	mass density of cement clinker
ρ_{H_2O}	mass density of water
ρ_{hyd}	mass density of hydrates
Σ	macroscopic stress tensor
Σ_{plat}	plateau stress
\mathbb{S}_{sph}^*	LC-transformed Eshelby tensor of spherical inclusion, embedded in an infinite cement paste matrix
$S_{sph}^{*,vol}, S_{sph}^{*,dev}$	volumetric and deviatoric components of \mathbb{S}_{sph}^*
t	chronological time
τ	time instant during creep test
τ_0	time instant at start of the loading ramp
t_{ref}	reference time, $t_{ref} = 1 \text{ d} = 86\,400 \text{ s}$
V_c	volume of cement
V_{cp}	volume of cement paste
V_{void}	volume of voids
V_w	volume of water
w	total water mass
w_a	water absorbed into the aggregates
$w_a(0)/a$	initial water-to-aggregate mass ratio
w_{cp}	water residing inside the cement paste
w_{cp}/c	effective water-to-cement mass ratio
$w_{cp}(0)/c$	initial value of the effective water-to-cement mass ratio
w/c	(nominal) water-to-cement mass ratio
ξ	hydration degree
ξ^*	hydration degree at which all aggregates-absorbed water is soaked to cement paste
<i>Operators:</i>	
$(\cdot)^*$	Laplace-Carson transform of quantity (\cdot)
\cdot	inner product

$\hat{(\cdot)}$	Laplace transform of quantity (\cdot)
\times	multiplication
$:$	second-order tensor contraction
$\Gamma(\cdot)$	gamma function of real quantity (\cdot)
$\dot{(\cdot)}$	time derivative of quantity (\cdot)

Chapter 5

Creep testing database: results from hourly-repeated three-minute creep tests on cement pastes, mortars, and concretes

This chapter contains the collection of results from all creep tests on cement pastes, mortars, and concretes, which were carried out according to the test protocol described in Chapter 2. All tested materials were produced from the same sources, i.e. from one commercial cement of type CEM I 42.5 N, from distilled water, and – as far as mortars and concretes are concerned – from quartz, i.e. either from “Normensand” or from “Pannonia Kies”, with maximum grain sizes amounting to 2 mm and to 8 mm, respectively. Material compositions were defined in terms of the mixing-related water-to-cement and aggregate-to-cement mass ratios, see Table 5.1. Cylindrical specimens exhibited a diameter of 70 mm and a central displacement measurement length of 164 mm. Specimens were tested inside a temperature chamber with air temperature controlled to 20 °C. In order to study the influence of ambient air temperature on the evolution of non-aging stiffness and creep properties of cement pastes, specific specimens were also tested at 30 °C and at 10 °C, respectively (Table 5.1). In order to underline the very satisfactory repeatability of the testing approach, every test was repeated, i.e. results from two nominally identical specimens are available for each type of test, labeled as “S-1” and “S-

2". As for illustration of measurement results, the evaluated strain evolution is normalized with respect to the plateau stress, and this quantity is plotted over the time since start of loading.

Table 5.1: Mix composition and testing temperature of characterized cement pastes, mortars, and concretes

Materials	Sample ID	w/c	a/c	f_{cp}^{nom}	f_{agg}^{nom}	d_{max}	Temp. °C
Cement pastes	CP-1	0.42	-	1.00	-	-	20
	CP-2	0.45	-	1.00	-	-	20
	CP-3	0.50	-	1.00	-	-	20
Cement pastes	CP-4	0.42	-	1	-	-	30
	CP-5	0.42	-	1	-	-	10
Mortars	M-1	0.42	2.7	0.42	0.58	2 mm	20
	M-2	0.45	2.8	0.45	0.58	2 mm	20
	M-3	0.50	3.0	0.42	0.58	2 mm	20
	M-4	0.42	1.35	0.42	0.58	2 mm	20
	M-5	0.45	1.50	0.45	0.58	2 mm	20
Concretes	C-1	0.42	2.7	0.42	0.58	8 mm	20
	C-2	0.50	3.0	0.42	0.58	8 mm	20

During three-minute creep testing of cement pastes, specimens were subjected to uniaxial compressive stress states ranging from 10 to 15 percent of the uniaxial compressive strength at the time of testing, see Fig. 5.1. Similar load intensities were used for three-minute creep testing of mortars and concretes, see Fig. 5.2.

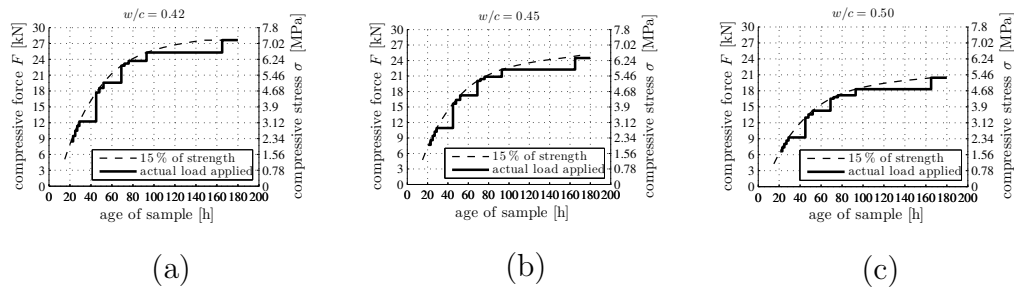


Figure 5.1: Force and stress values prescribed during loading plateau for creep testing of cement pastes; (a) CP-1, $w/c = 0.42$, (b) CP-2, $w/c = 0.45$, and (c) CP-3, $w/c = 0.50$

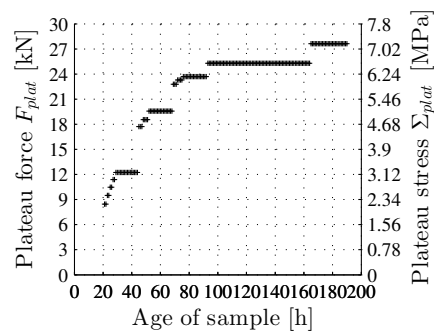


Figure 5.2: Force and stress values prescribed during loading plateau for creep testing of mortars and concretes

5.1 Results from characterization of cement pastes at different temperatures

5.1.1 Water-cement ratio = 0.42, Temperature = 20 °C

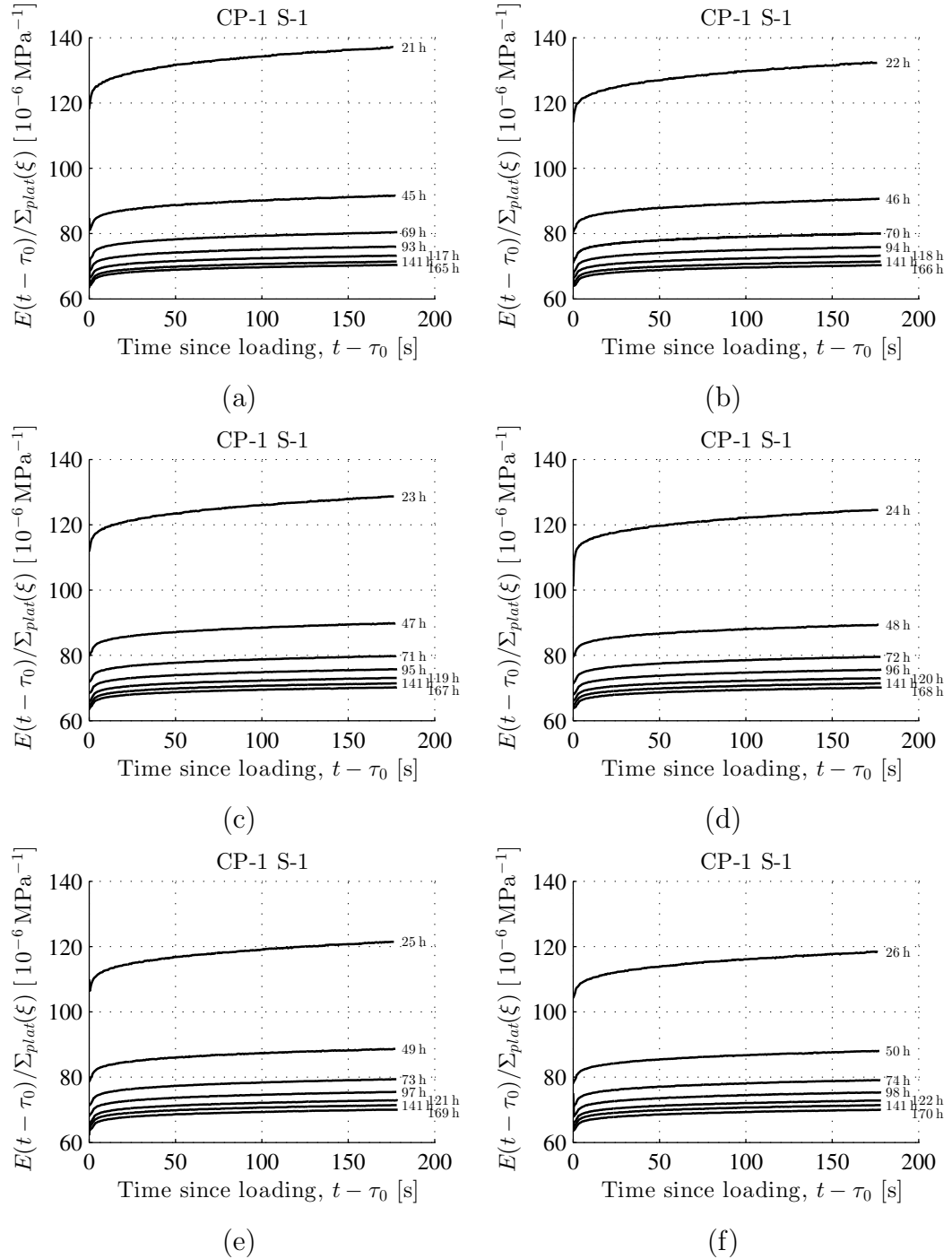


Figure 5.3: Measured strain evolution normalized with respect to the plateau stress as a function of the time since start of loading: cement paste with $w/c = 0.42$; ambient air temperature = 20 °C; ID = “CP-1 S-1”, see Table 5.1; as for load levels, see Fig. 5.1(a)

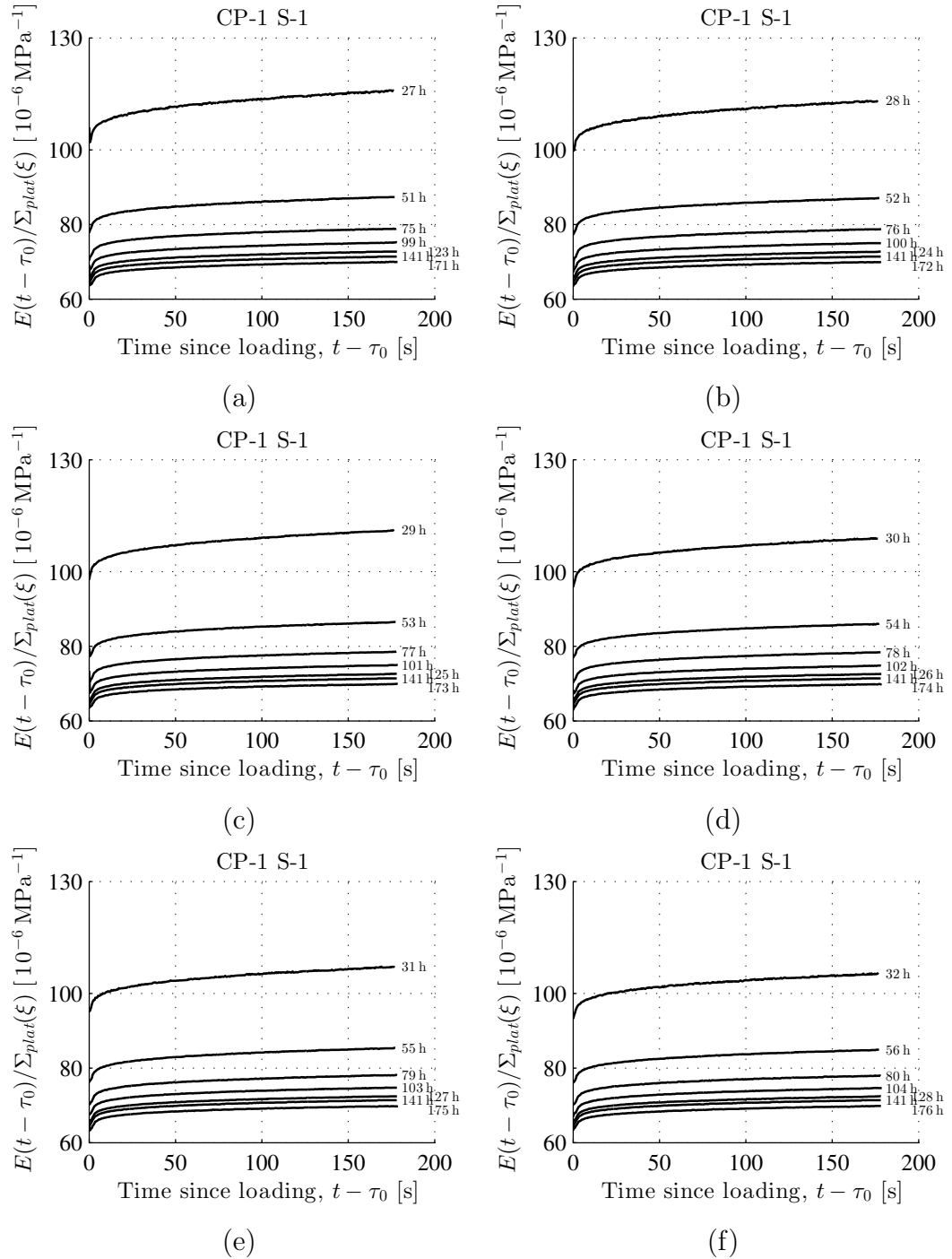


Figure 5.4: Measured strain evolution normalized with respect to the plateau stress as a function of the time since start of loading: cement paste with $w/c = 0.42$; ambient air temperature = 20°C ; ID = “CP-1 S-1”, see Table 5.1; as for load levels, see Fig. 5.1(a)

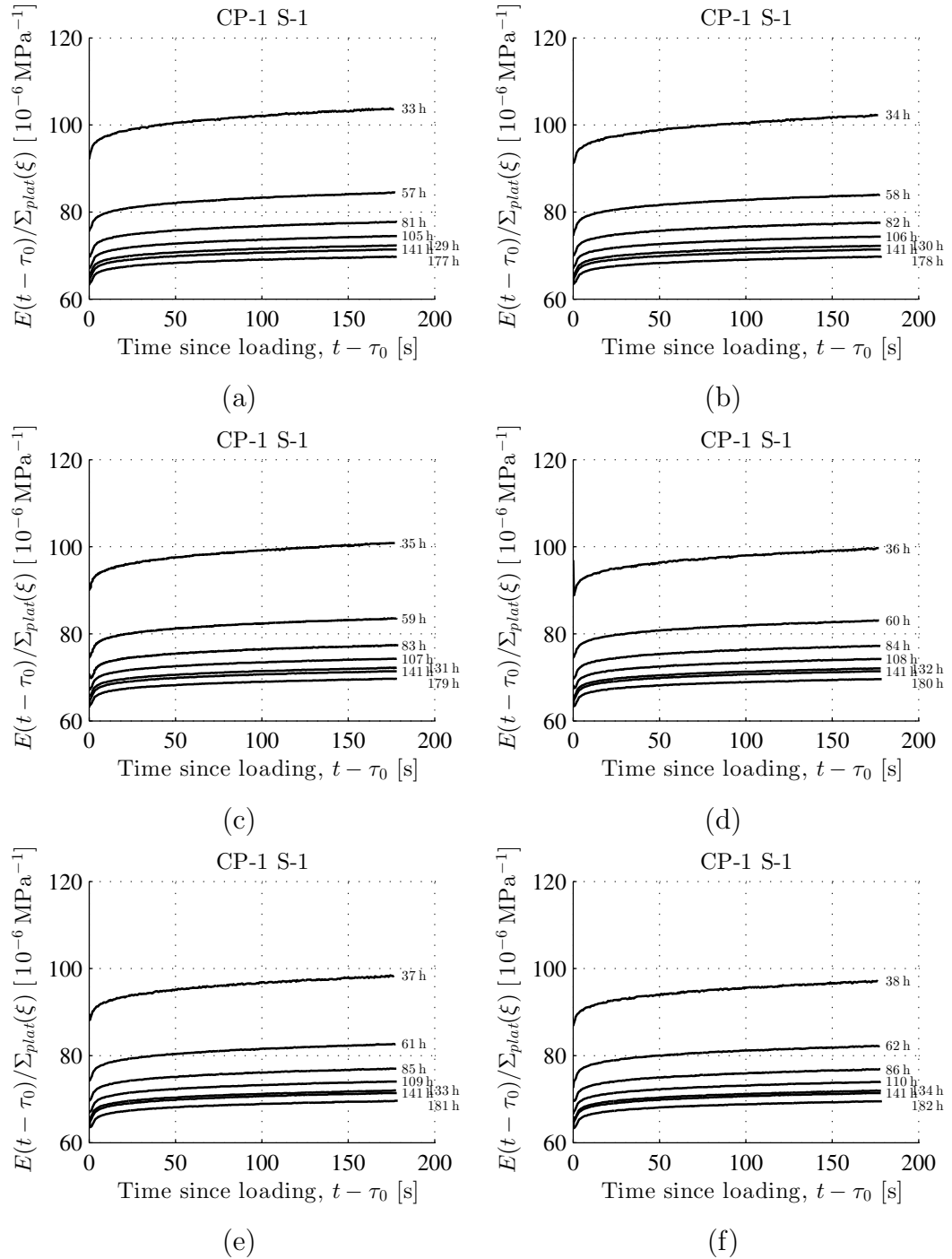


Figure 5.5: Measured strain evolution normalized with respect to the plateau stress as a function of the time since start of loading: cement paste with $w/c = 0.42$; ambient air temperature = 20°C ; ID = "CP-1 S-1", see Table 5.1; as for load levels, see Fig. 5.1(a)

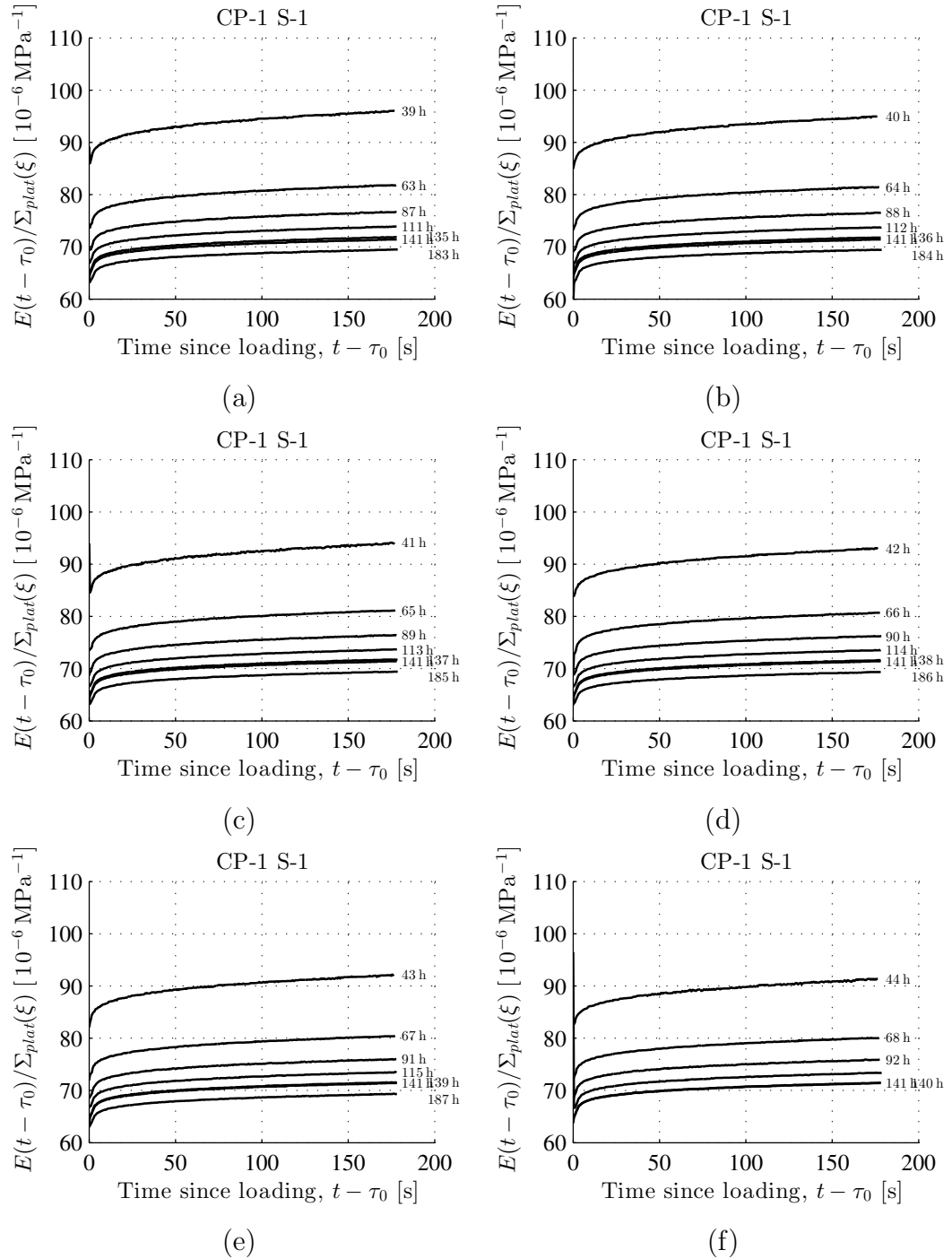


Figure 5.6: Measured strain evolution normalized with respect to the plateau stress as a function of the time since start of loading: cement paste with $w/c = 0.42$; ambient air temperature = 20°C ; ID = “CP-1 S-1”, see Table 5.1; as for load levels, see Fig. 5.1(a)

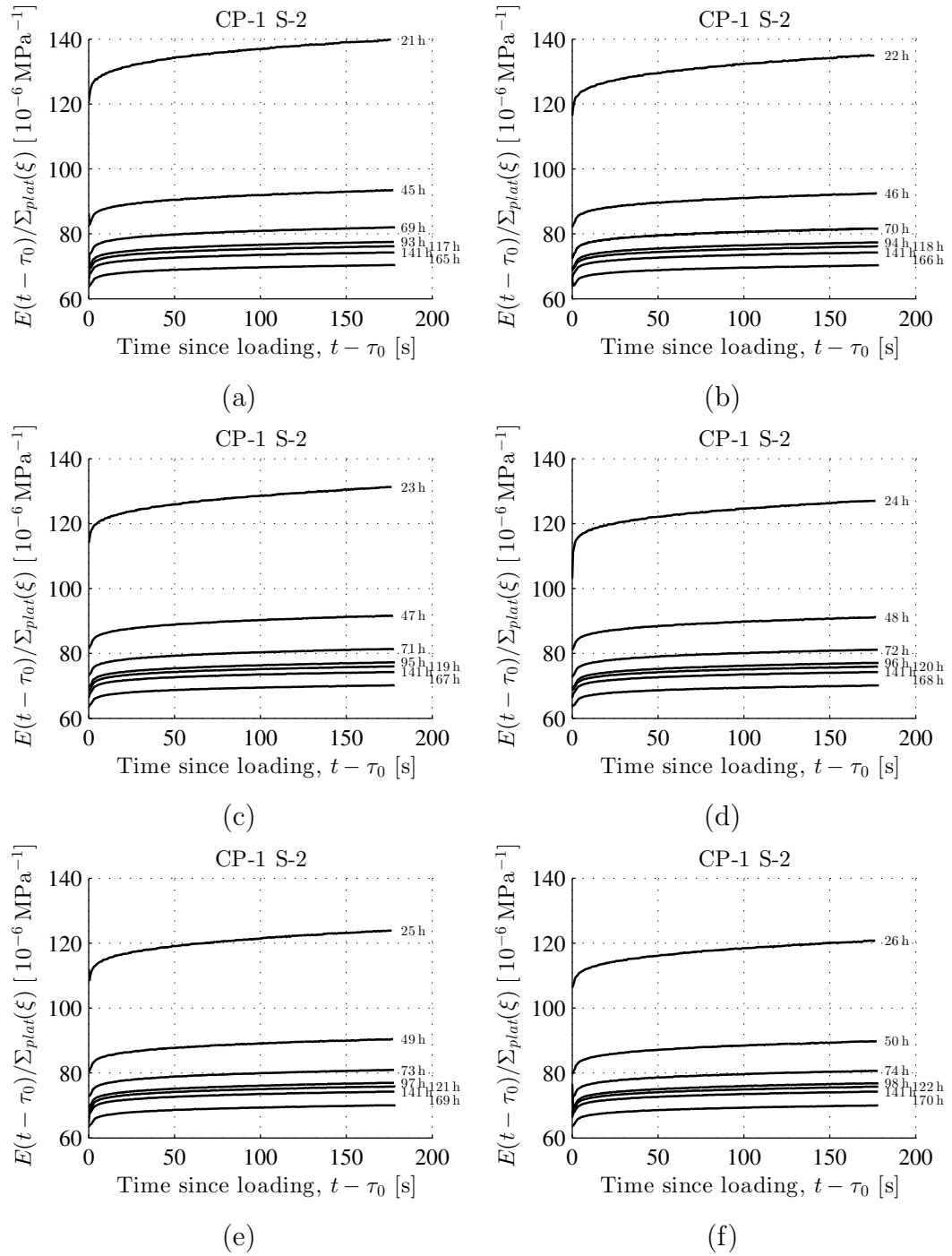


Figure 5.7: Measured strain evolution normalized with respect to the plateau stress as a function of the time since start of loading: cement paste with $w/c = 0.42$; ambient air temperature = 20°C ; ID = “CP-1 S-2”, see Table 5.1; as for load levels, see Fig. 5.1(a)

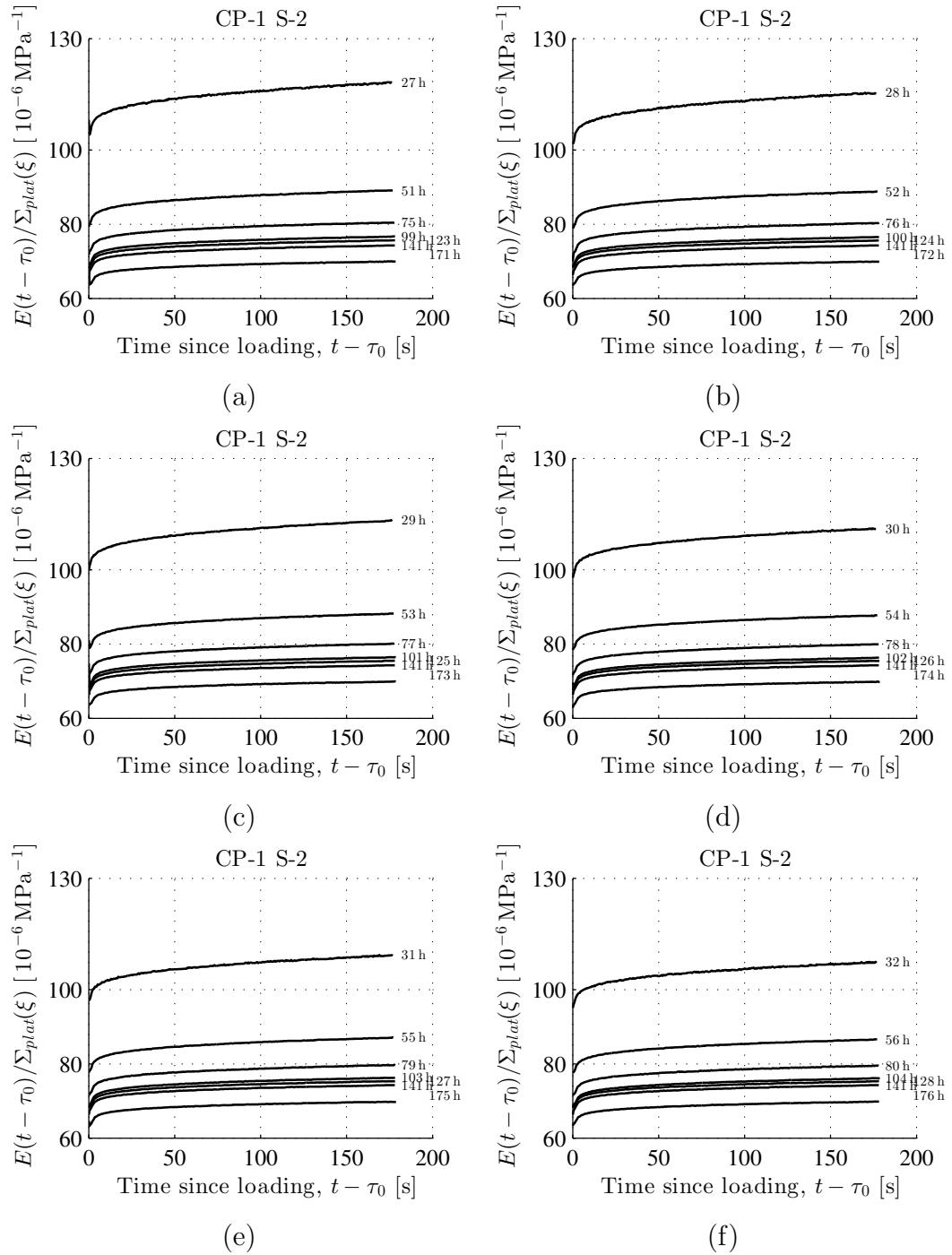


Figure 5.8: Measured strain evolution normalized with respect to the plateau stress as a function of the time since start of loading: cement paste with $w/c = 0.42$; ambient air temperature = 20°C ; ID = “CP-1 S-2”, see Table 5.1; as for load levels, see Fig. 5.1(a)

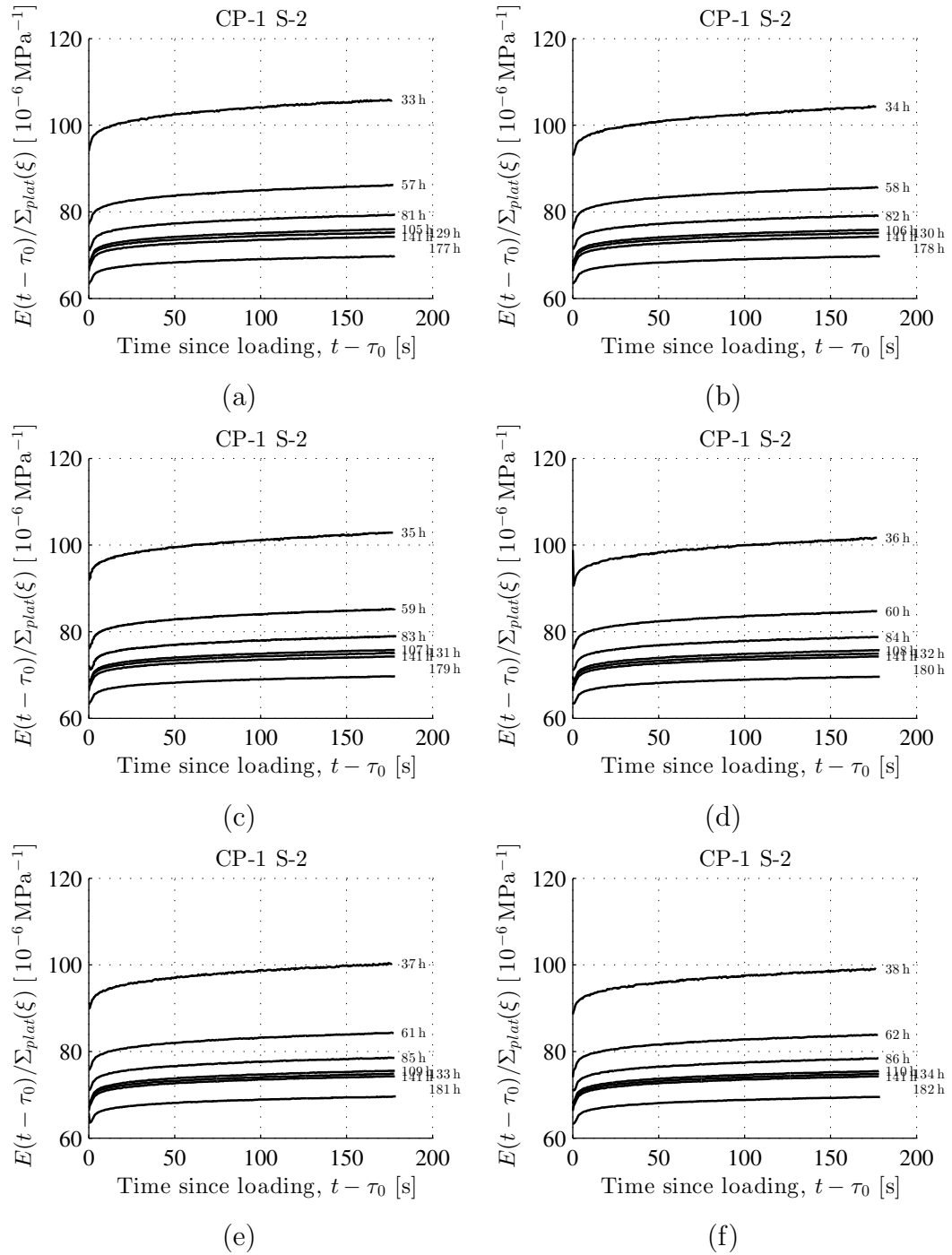


Figure 5.9: Measured strain evolution normalized with respect to the plateau stress as a function of the time since start of loading: cement paste with $w/c = 0.42$; ambient air temperature = 20°C ; ID = "CP-1 S-2", see Table 5.1; as for load levels, see Fig. 5.1(a)

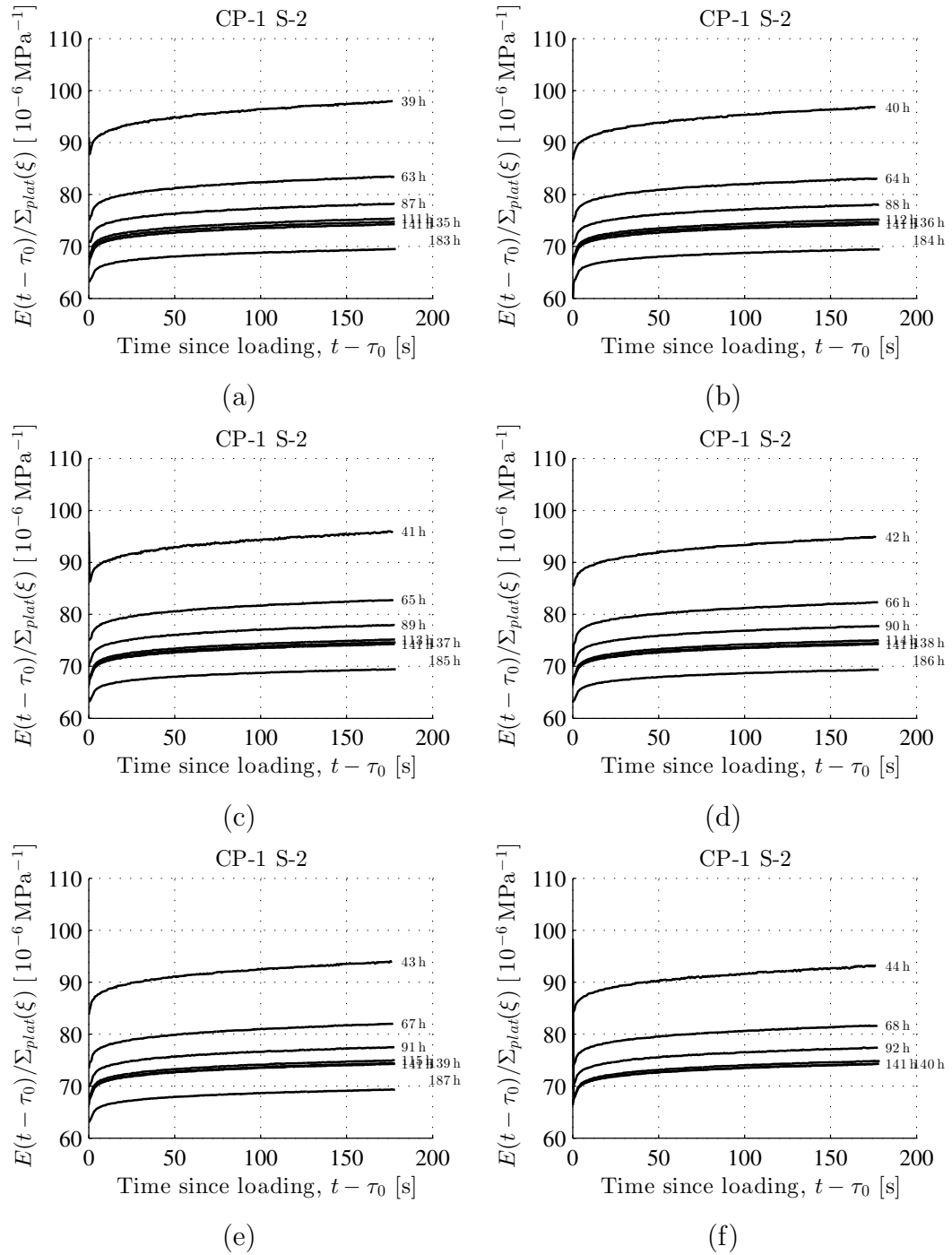


Figure 5.10: Measured strain evolution normalized with respect to the plateau stress as a function of the time since start of loading: cement paste with $w/c = 0.42$; ambient air temperature = 20°C ; ID = "CP-1 S-2", see Table 5.1; as for load levels, see Fig. 5.1(a)

5.1.2 Water-cement ratio = 0.45, Temperature = 20 °C

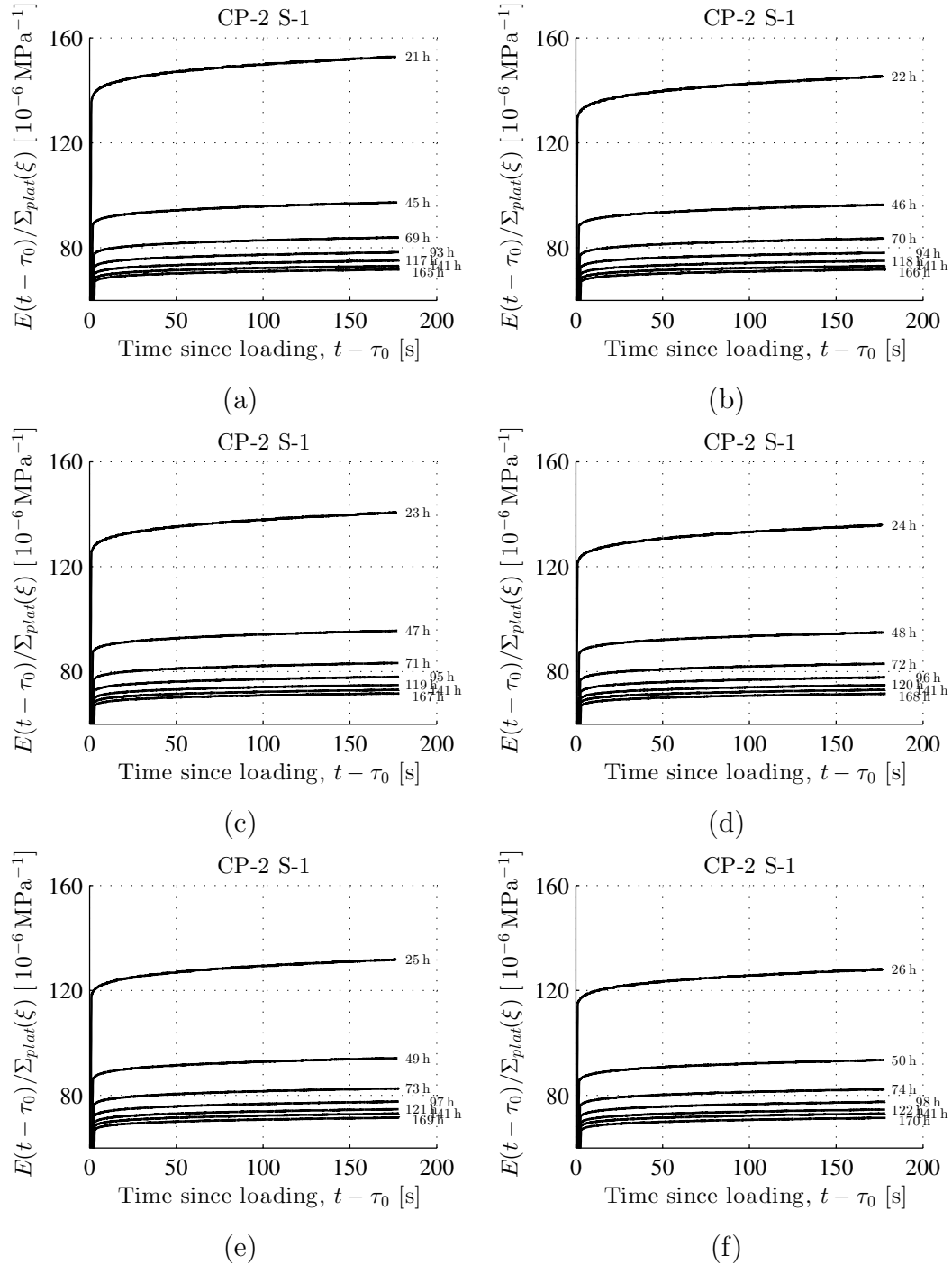


Figure 5.11: Measured strain evolution normalized with respect to the plateau stress as a function of the time since start of loading: cement paste with $w/c = 0.45$; ambient air temperature = 20 °C; ID = “CP-2 S-1”, see Table 5.1; as for load levels, see Fig. 5.1(b)

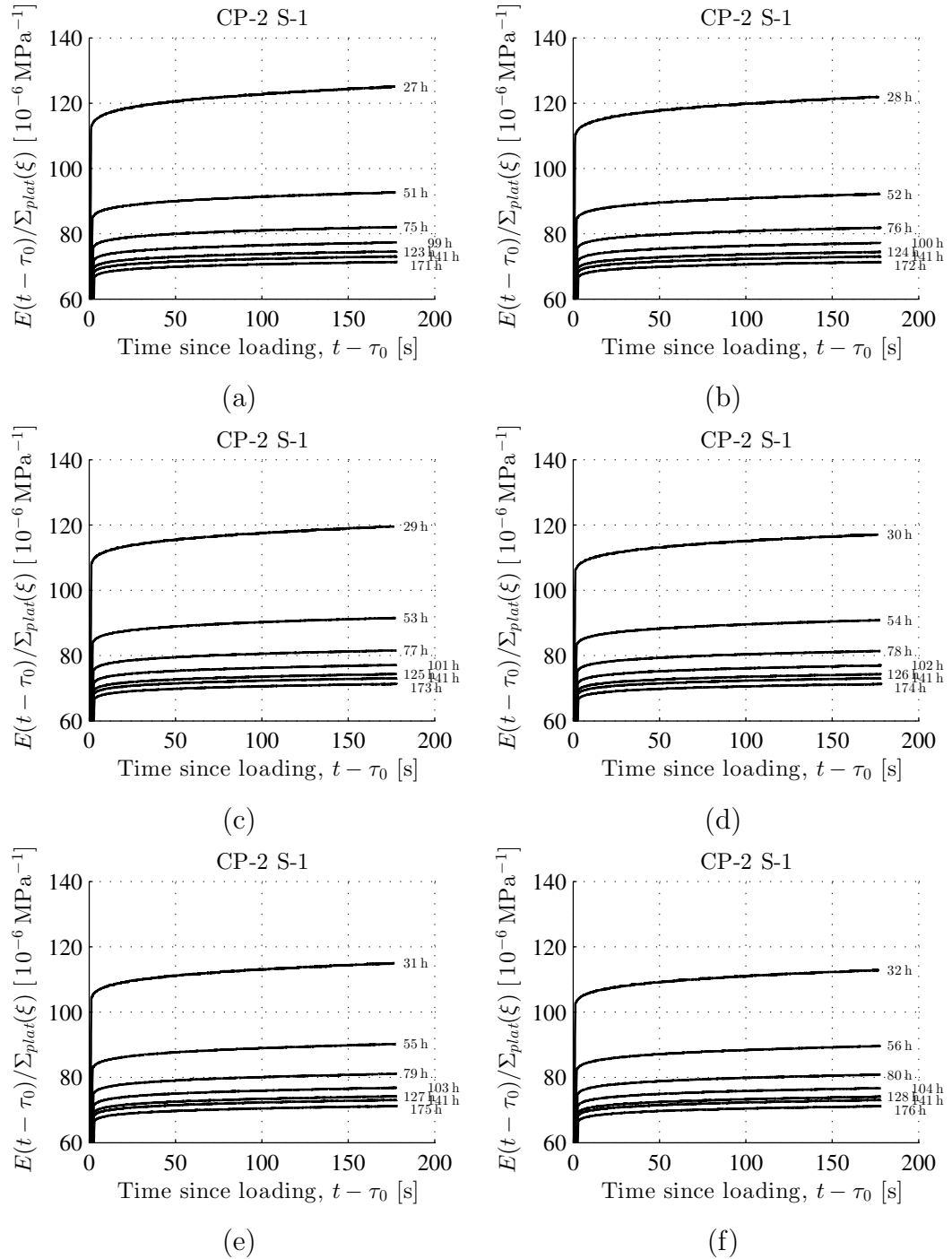


Figure 5.12: Measured strain evolution normalized with respect to the plateau stress as a function of the time since start of loading: cement paste with $w/c = 0.45$; ambient air temperature = 20°C ; ID = "CP-2 S-1", see Table 5.1; as for load levels, see Fig. 5.1(b)

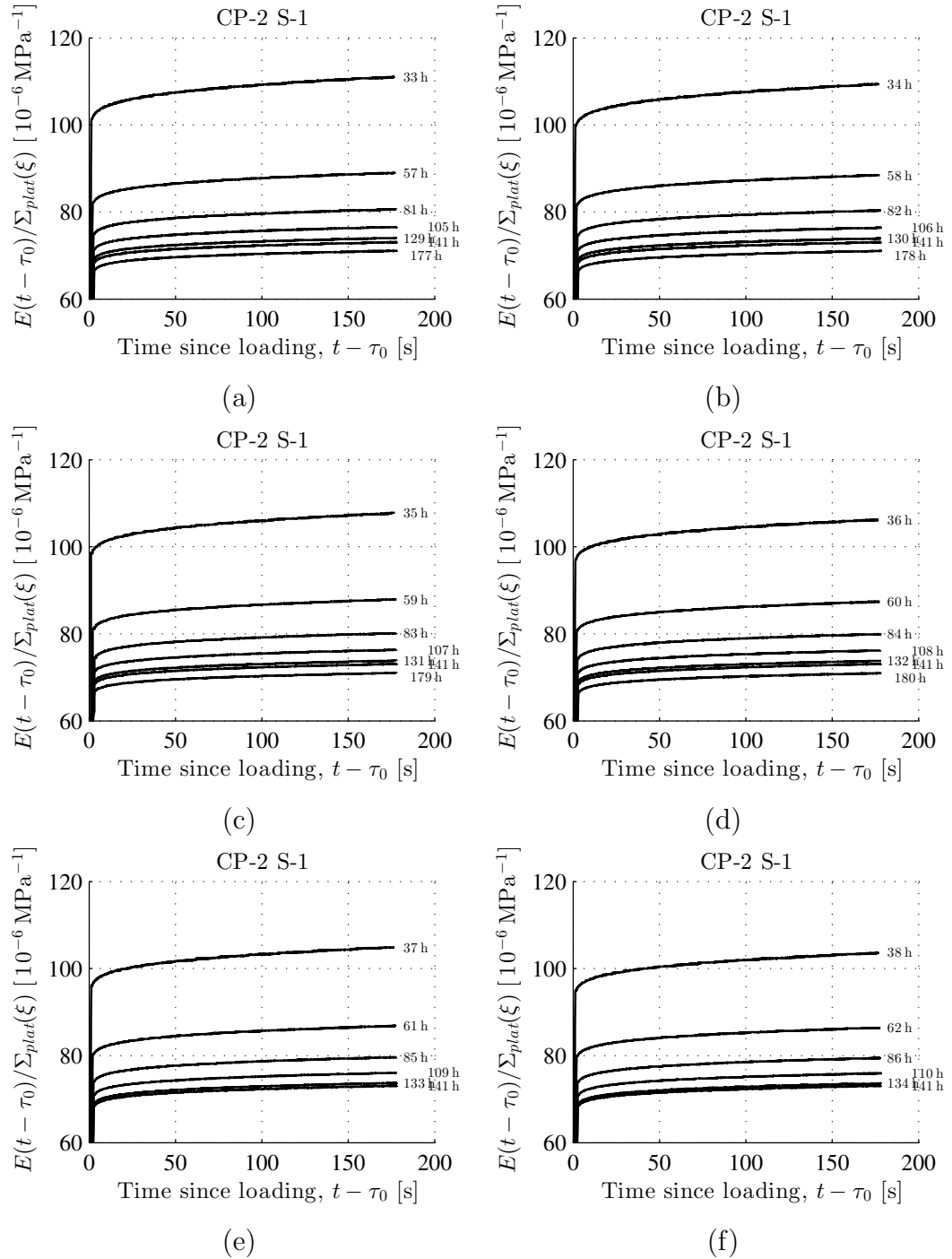


Figure 5.13: Measured strain evolution normalized with respect to the plateau stress as a function of the time since start of loading: cement paste with $w/c = 0.45$; ambient air temperature = 20°C ; ID = "CP-2 S-1", see Table 5.1; as for load levels, see Fig. 5.1(b)

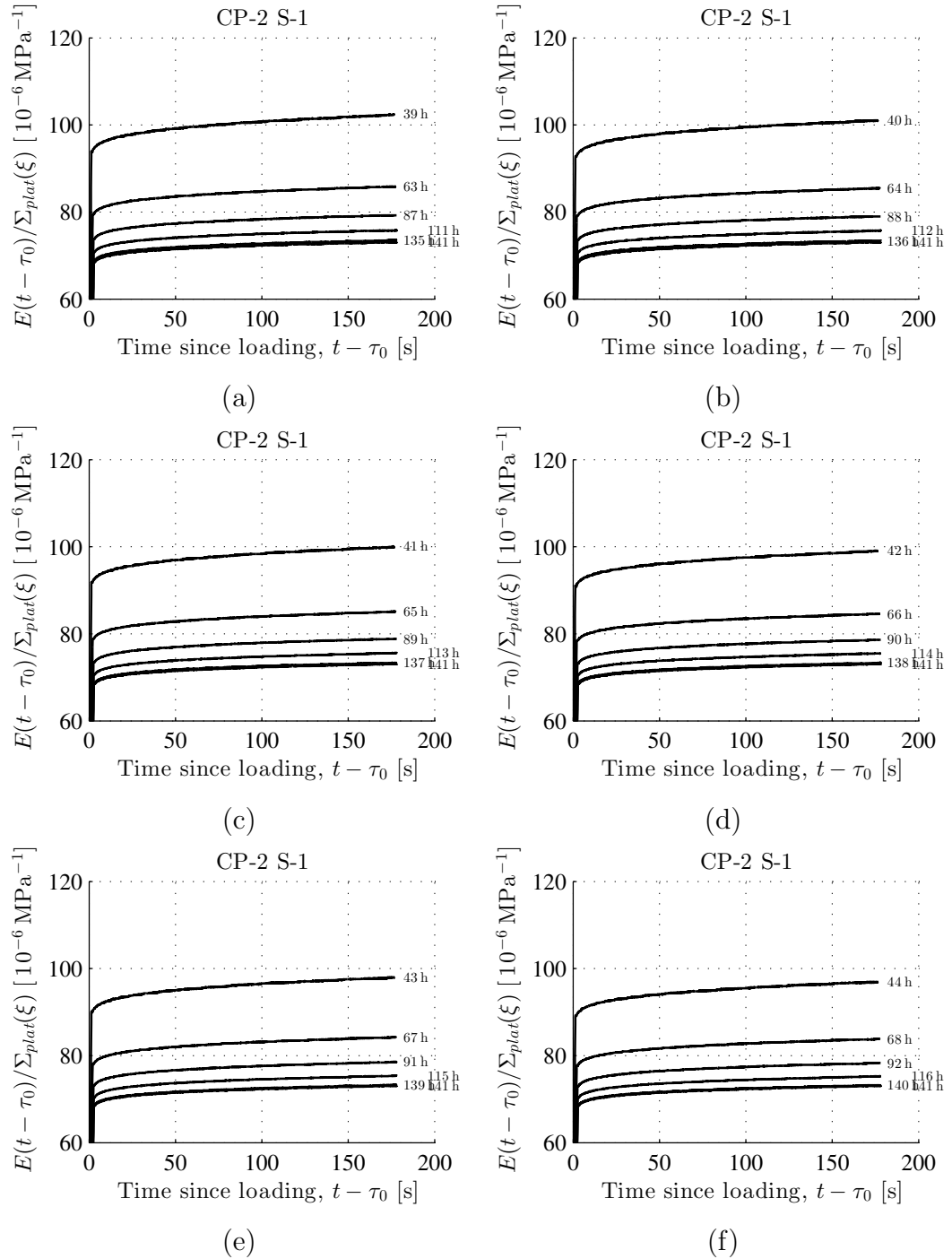


Figure 5.14: Measured strain evolution normalized with respect to the plateau stress as a function of the time since start of loading: cement paste with $w/c = 0.45$; ambient air temperature = 20°C ; ID = "CP-2 S-1", see Table 5.1; as for load levels, see Fig. 5.1(b)

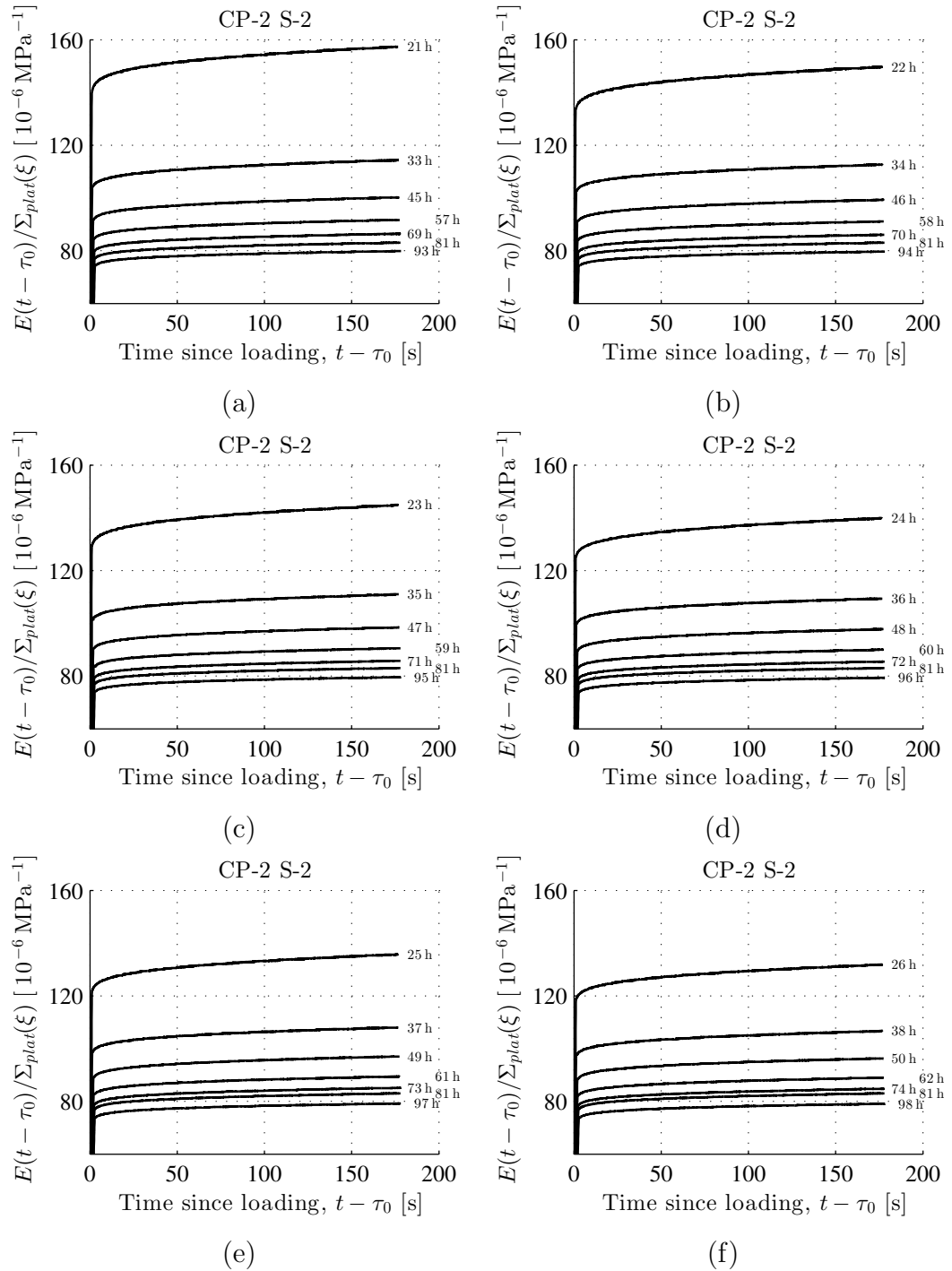


Figure 5.15: Measured strain evolution normalized with respect to the plateau stress as a function of the time since start of loading: cement paste with $w/c = 0.45$; ambient air temperature = 20°C ; ID = “CP-2 S-2”, see Table 5.1; as for load levels, see Fig. 5.1(b)

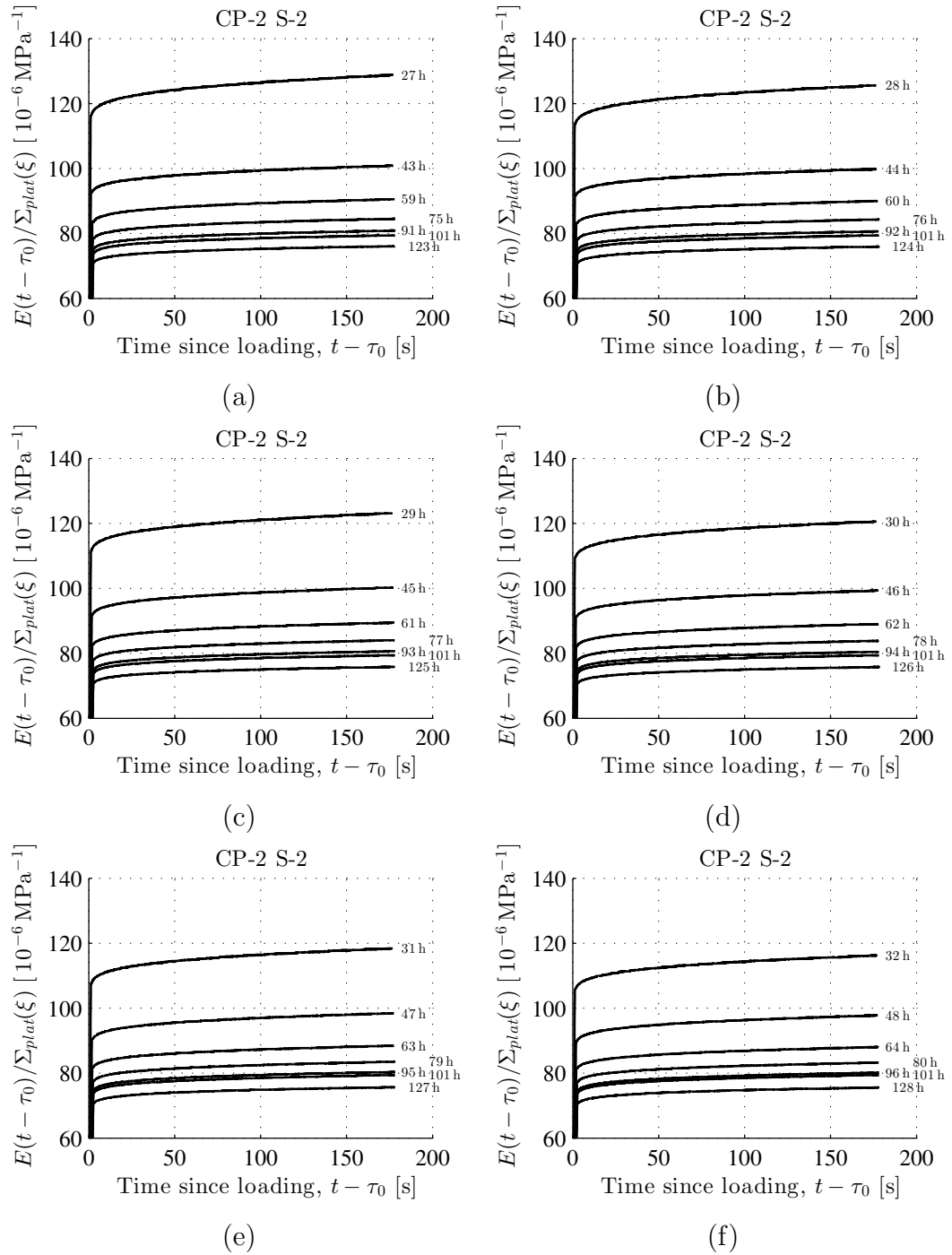


Figure 5.16: Measured strain evolution normalized with respect to the plateau stress as a function of the time since start of loading: cement paste with $w/c = 0.45$; ambient air temperature = 20°C ; ID = “CP-2 S-2”, see Table 5.1; as for load levels, see Fig. 5.1(b)

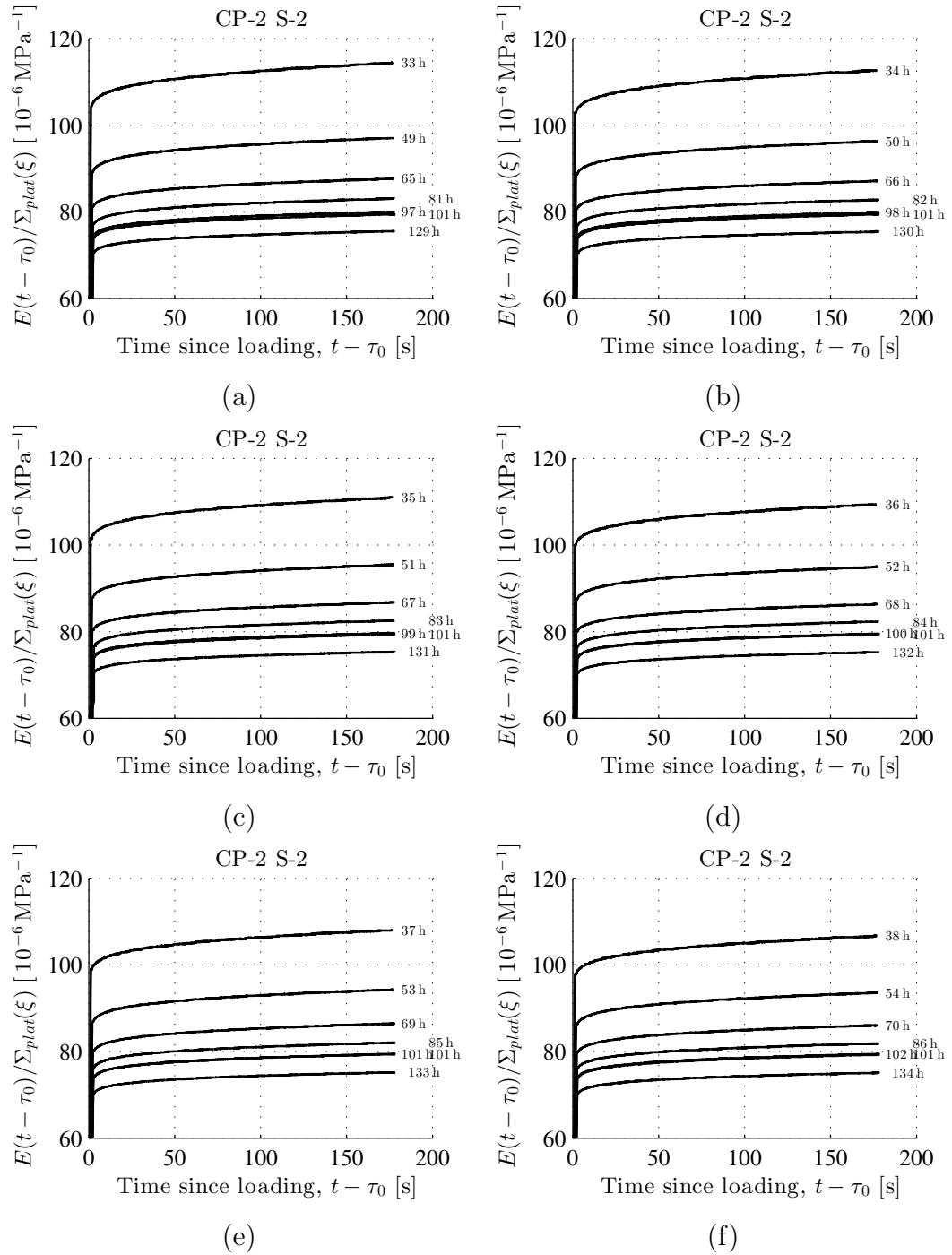


Figure 5.17: Measured strain evolution normalized with respect to the plateau stress as a function of the time since start of loading: cement paste with $w/c = 0.45$; ambient air temperature = 20°C ; ID = “CP-2 S-2”, see Table 5.1; as for load levels, see Fig. 5.1(b)

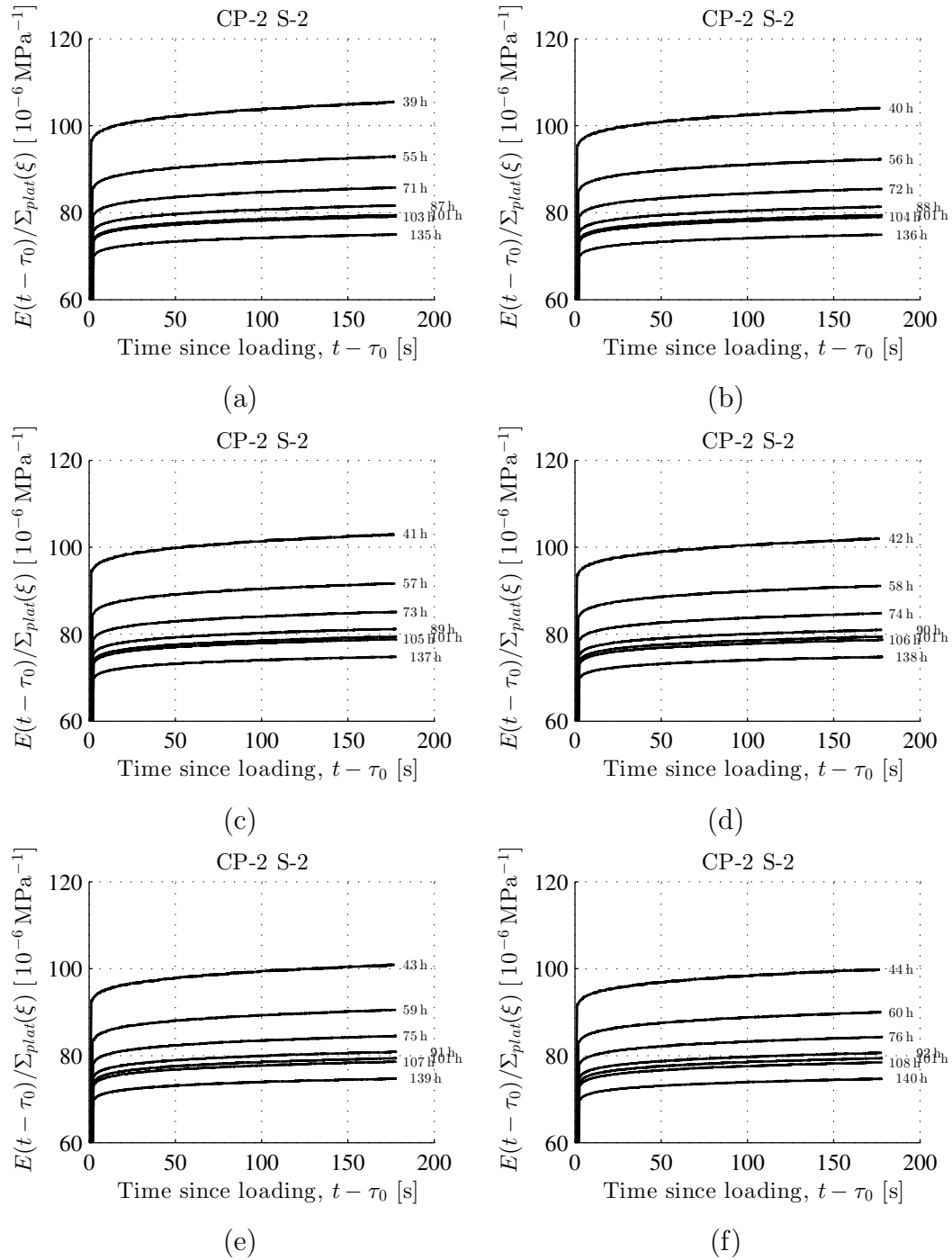


Figure 5.18: Measured strain evolution normalized with respect to the plateau stress as a function of the time since start of loading: cement paste with $w/c = 0.45$; ambient air temperature = 20°C ; ID = "CP-2 S-2", see Table 5.1; as for load levels, see Fig. 5.1(b)

5.1.3 Water-cement ratio = 0.50, Temperature = 20 °C

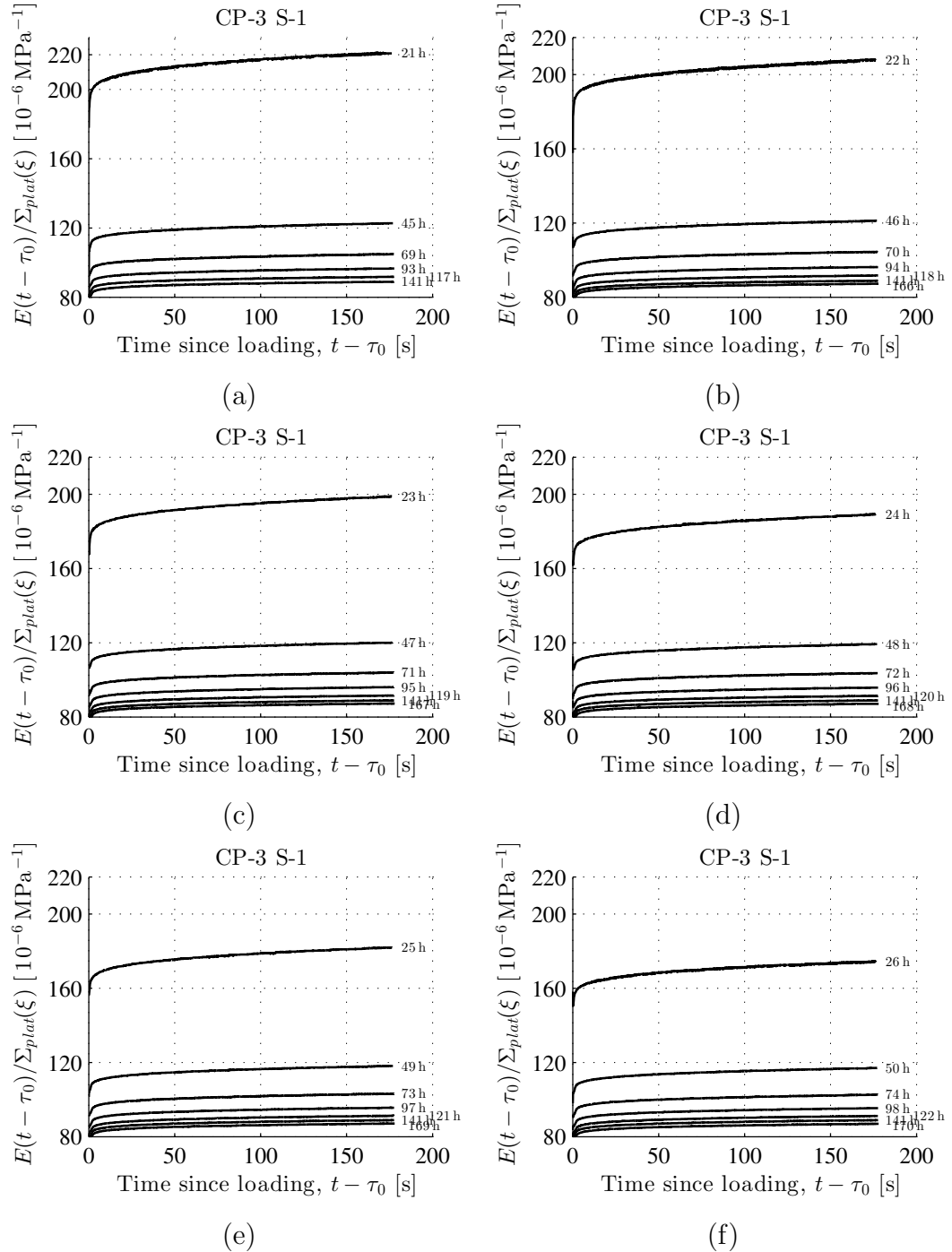


Figure 5.19: Measured strain evolution normalized with respect to the plateau stress as a function of the time since start of loading: cement paste with $w/c = 0.50$; ambient air temperature = 20 °C; ID = “CP-3 S-1”, see Table 5.1; as for load levels, see Fig. 5.1(c)

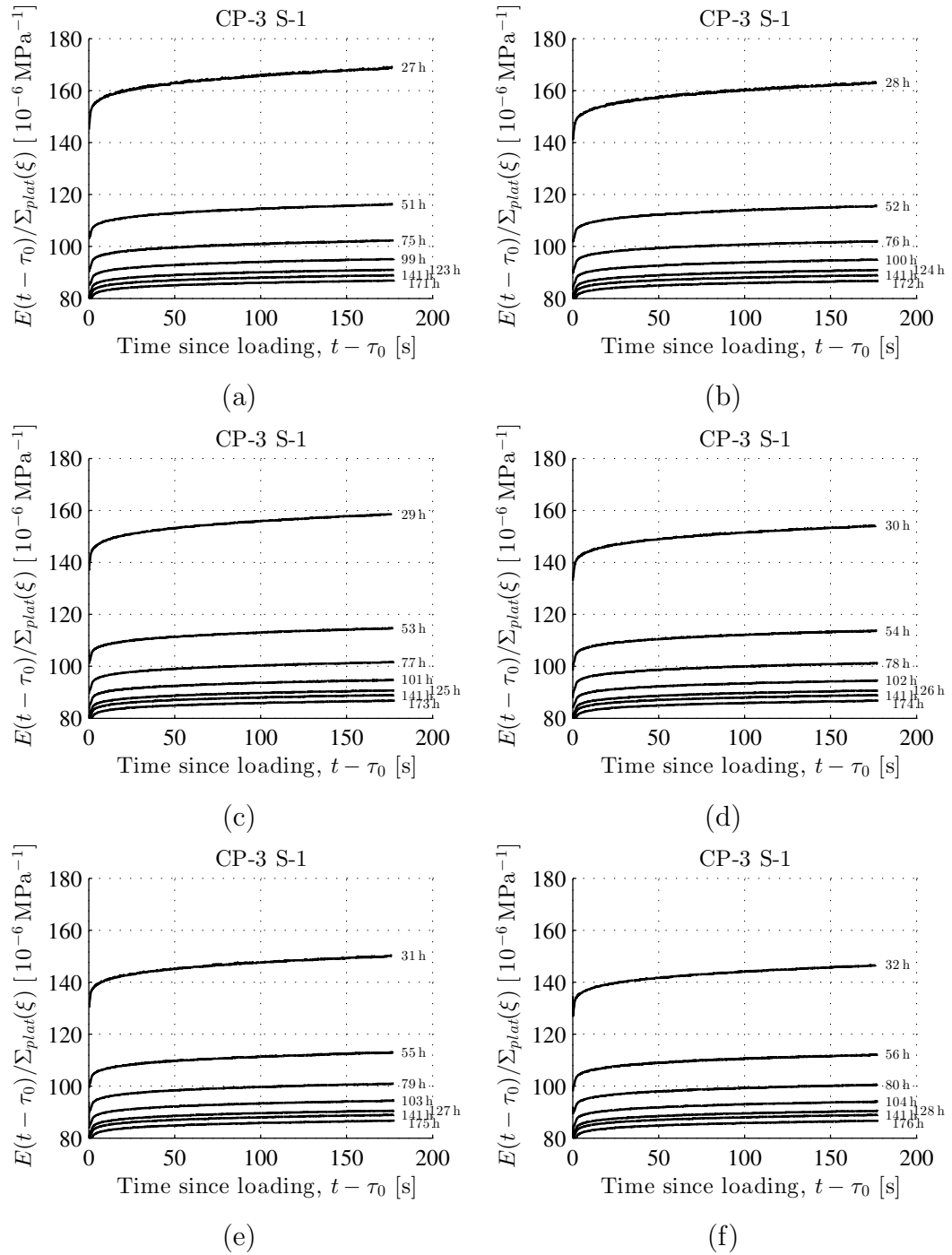


Figure 5.20: Measured strain evolution normalized with respect to the plateau stress as a function of the time since start of loading: cement paste with $w/c = 0.50$; ambient air temperature = 20°C ; ID = “CP-3 S-1”, see Table 5.1; as for load levels, see Fig. 5.1(c)

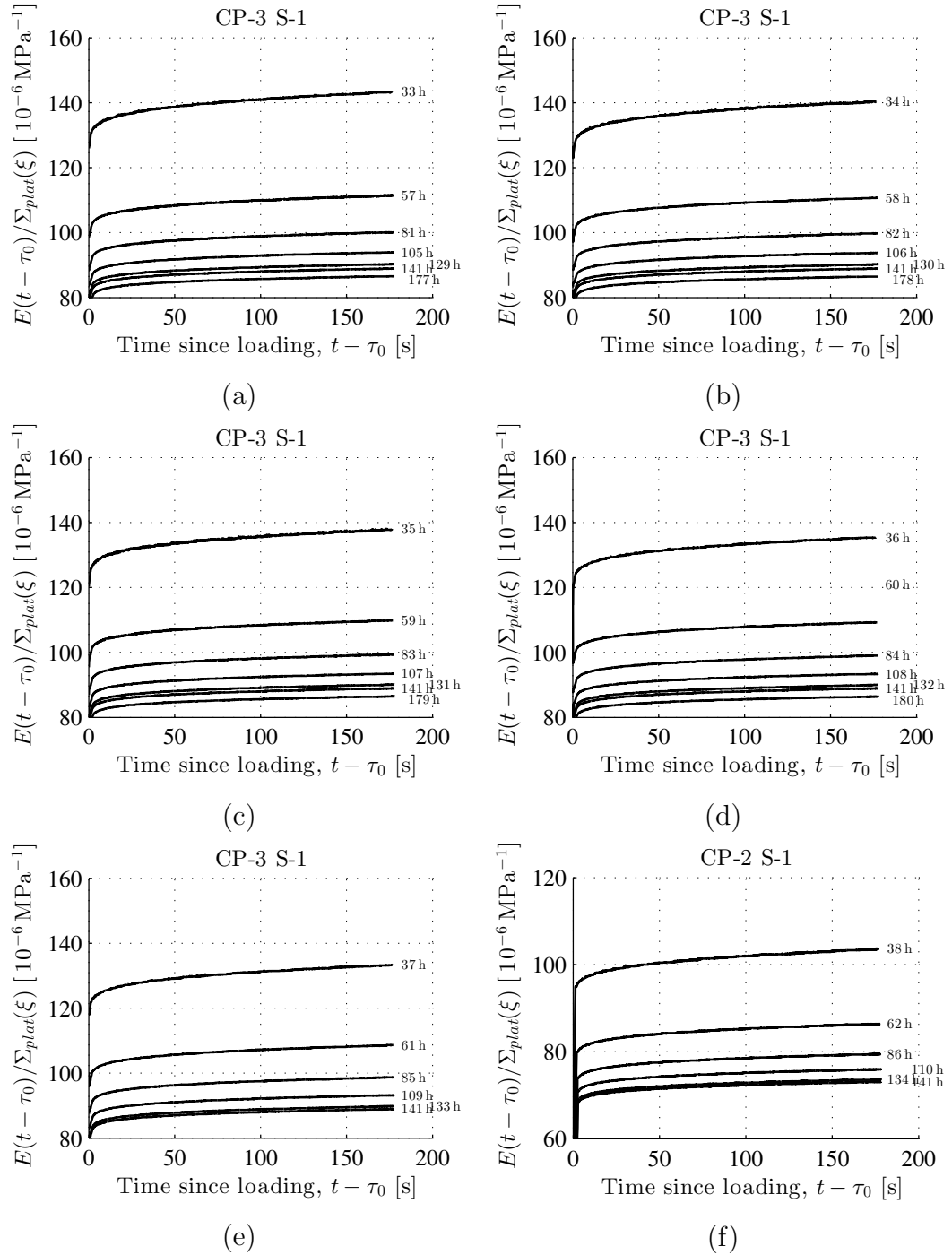


Figure 5.21: Measured strain evolution normalized with respect to the plateau stress as a function of the time since start of loading; cement paste with $w/c = 0.50$; ambient air temperature = 20°C ; ID = “CP-3 S-1”, see Table 5.1; as for load levels, see Fig. 5.1(c)

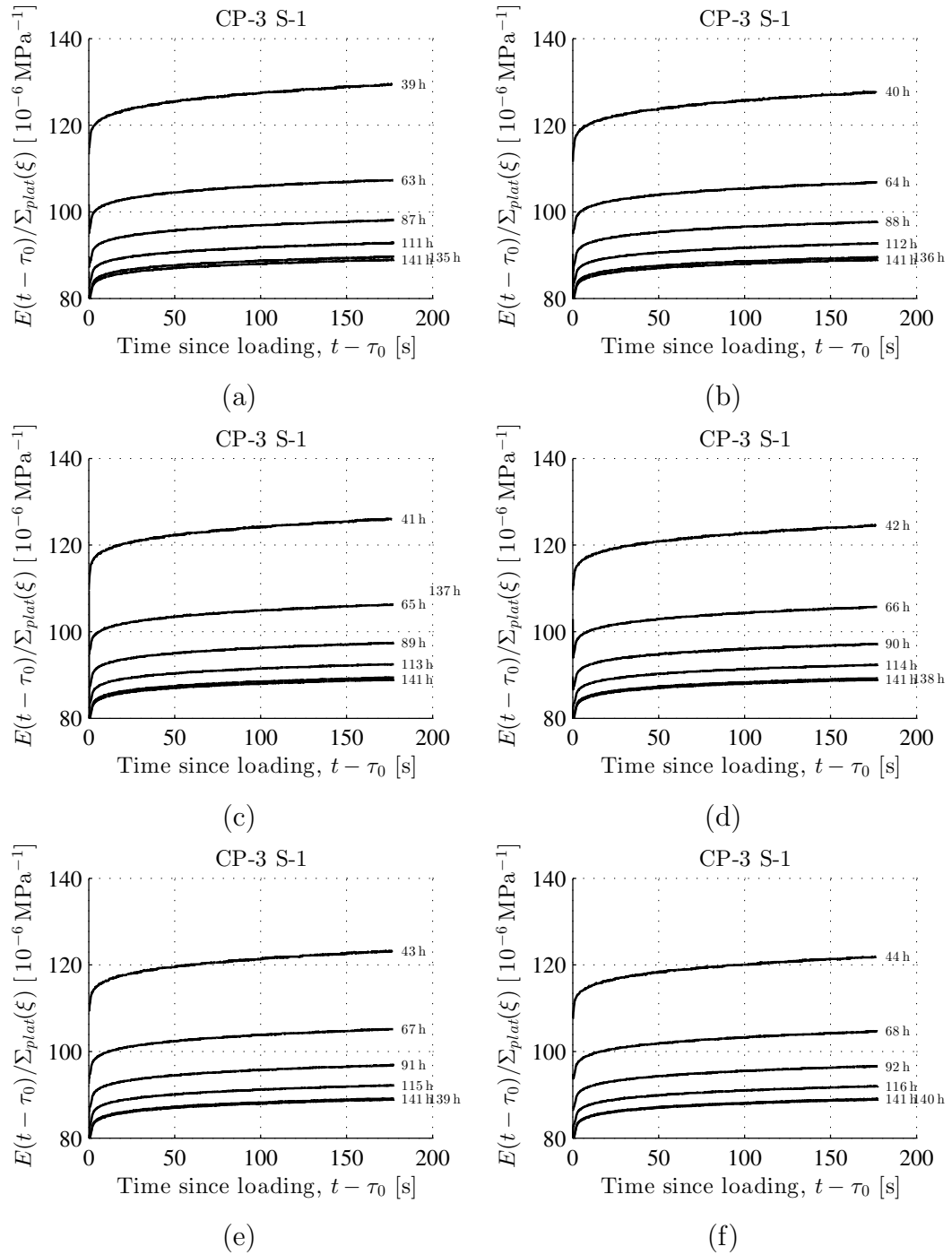


Figure 5.22: Measured strain evolution normalized with respect to the plateau stress as a function of the time since start of loading: cement paste with $w/c = 0.50$; ambient air temperature = 20°C ; ID = “CP-3 S-1”, see Table 5.1; as for load levels, see Fig. 5.1(c)

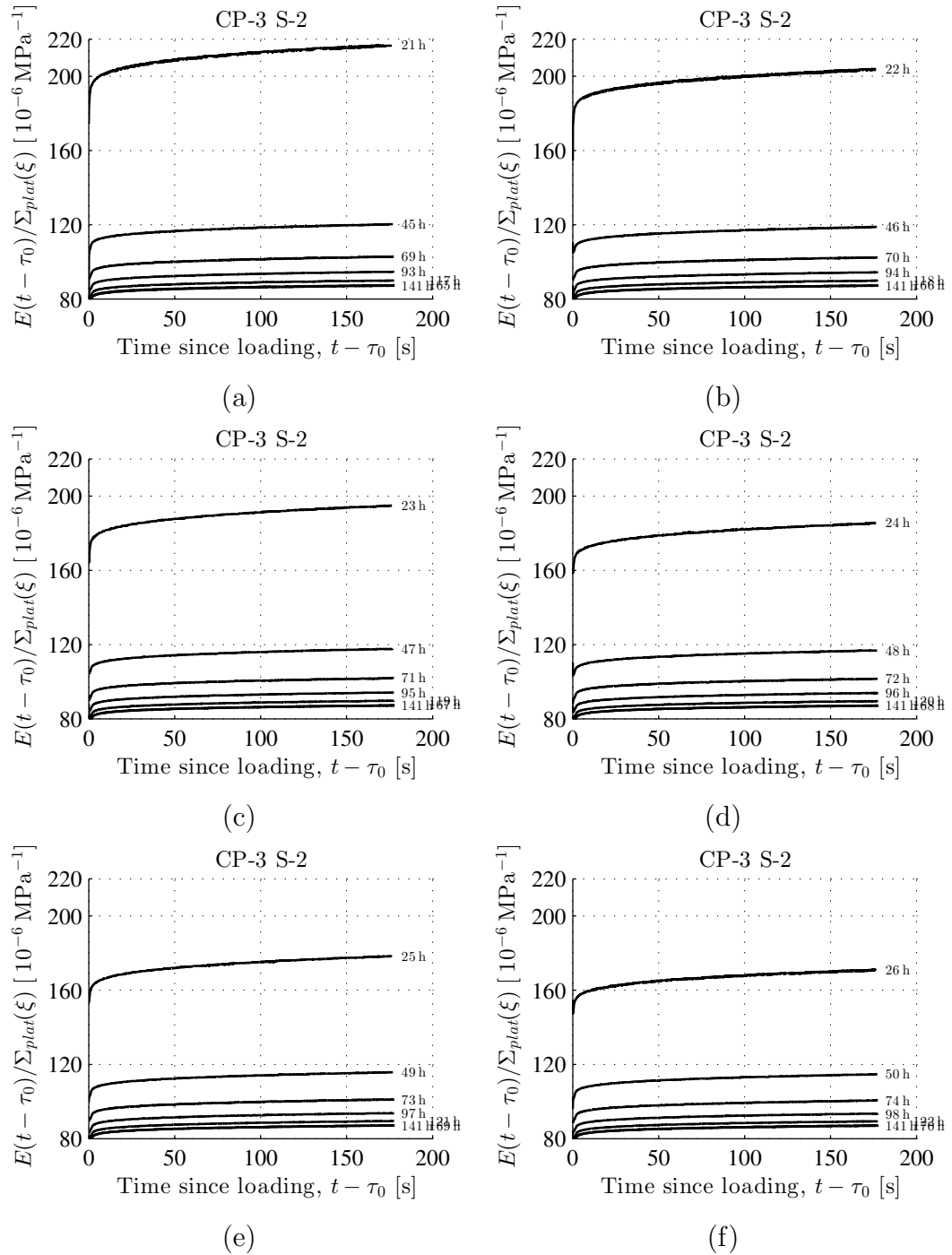


Figure 5.23: Measured strain evolution normalized with respect to the plateau stress as a function of the time since start of loading: cement paste with $w/c = 0.50$; ambient air temperature = 20 °C; ID = “CP-3 S-2”, see Table 5.1; as for load levels, see Fig. 5.1(c)

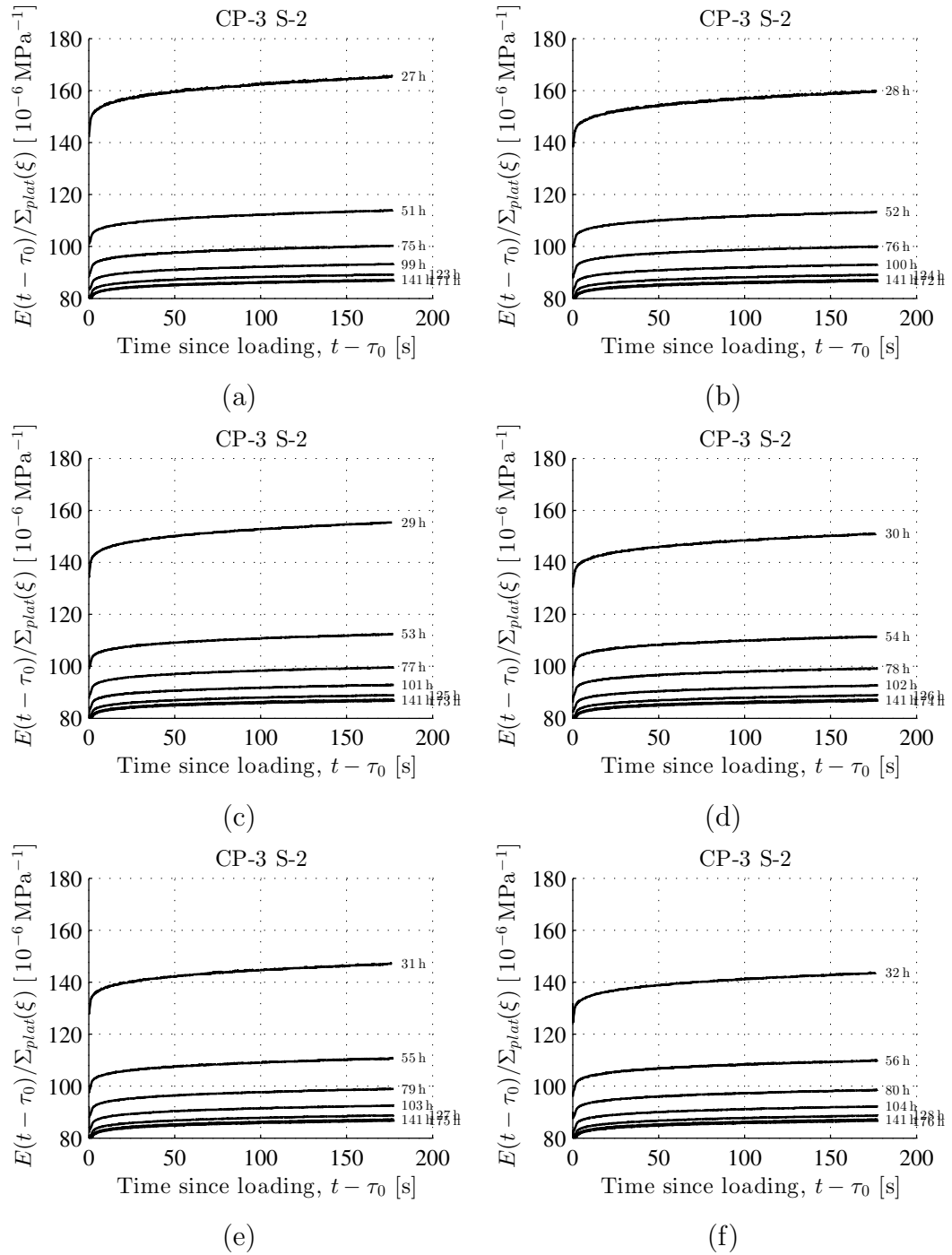


Figure 5.24: Measured strain evolution normalized with respect to the plateau stress as a function of the time since start of loading: cement paste with $w/c = 0.50$; ambient air temperature = 20°C ; ID = “CP-3 S-2”, see Table 5.1; as for load levels, see Fig. 5.1(c)

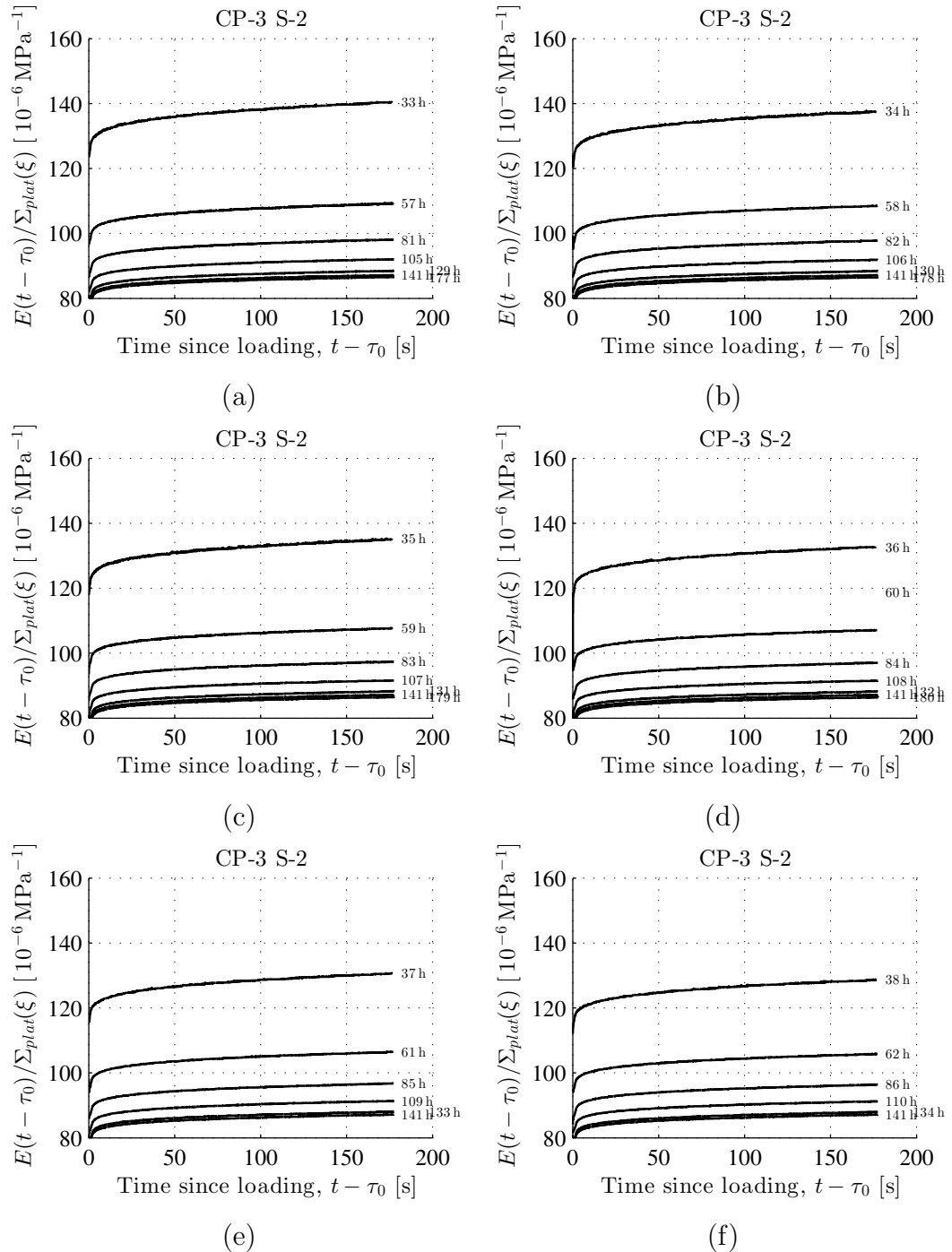


Figure 5.25: Measured strain evolution normalized with respect to the plateau stress as a function of the time since start of loading: cement paste with $w/c = 0.50$; ambient air temperature = 20°C ; ID = “CP-3 S-2”, see Table 5.1; as for load levels, see Fig. 5.1(c)

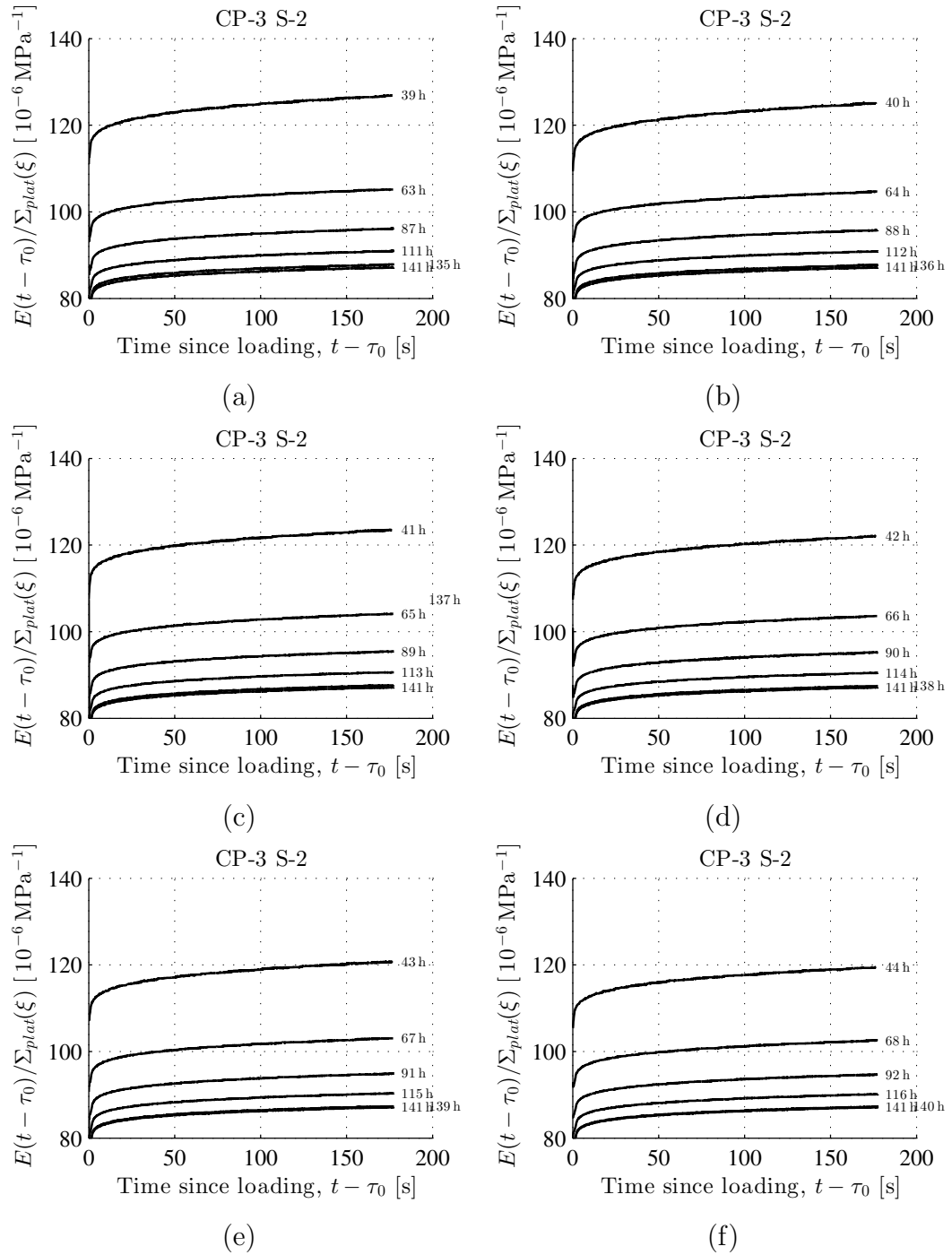


Figure 5.26: Measured strain evolution normalized with respect to the plateau stress as a function of the time since start of loading: cement paste with $w/c = 0.50$; ambient air temperature = 20°C ; ID = “CP-3 S-2”, see Table 5.1; as for load levels, see Fig. 5.1(c)

5.1.4 Water-cement ratio = 0.42, Temperature = 30 °C

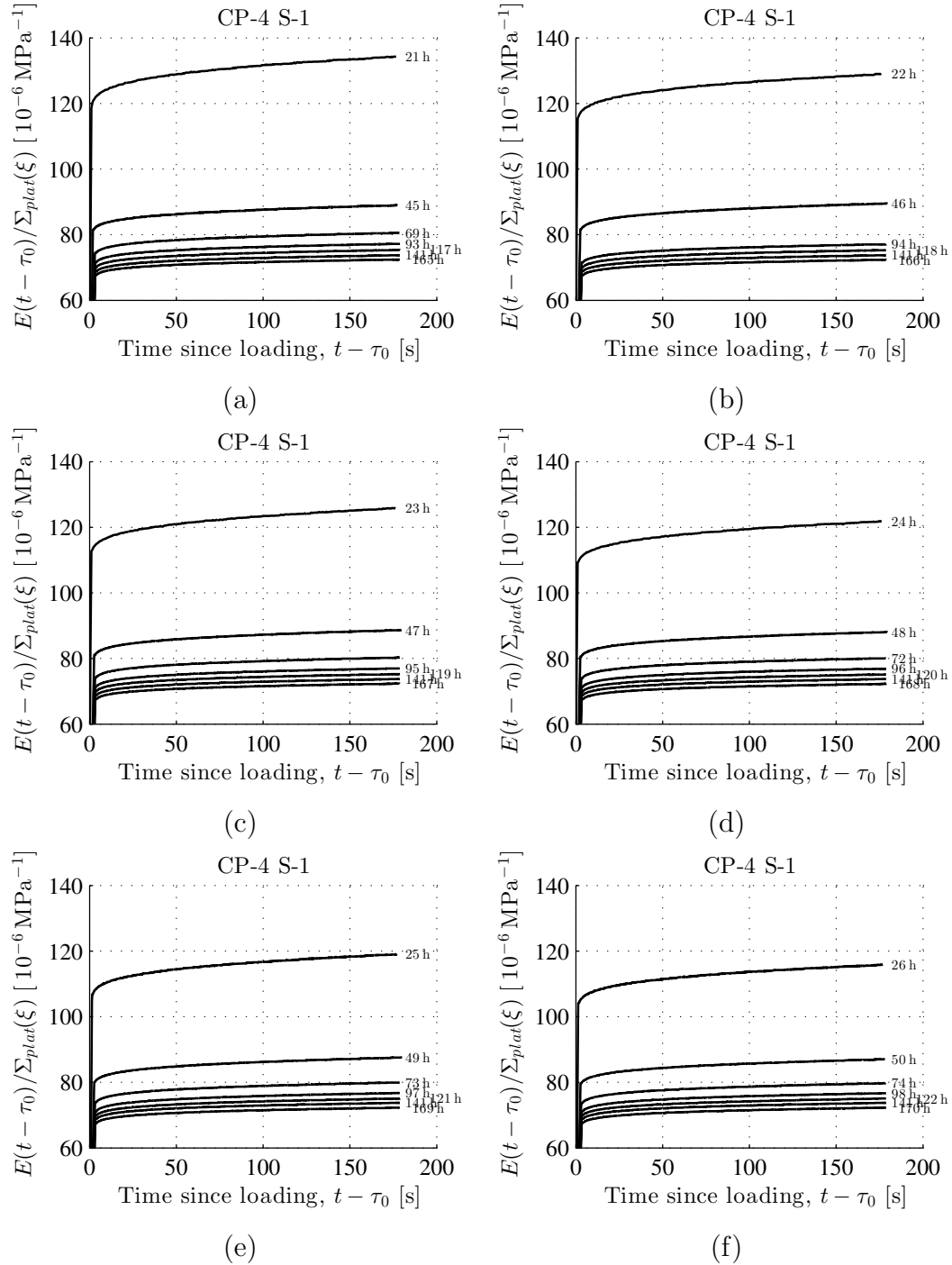


Figure 5.27: Measured strain evolution normalized with respect to the plateau stress as a function of the time since start of loading; cement paste with $w/c = 0.42$; ambient air temperature = 30 °C; ID = "CP-4 S-1", see Table 5.1; as for load levels, see Fig. 5.1(a)

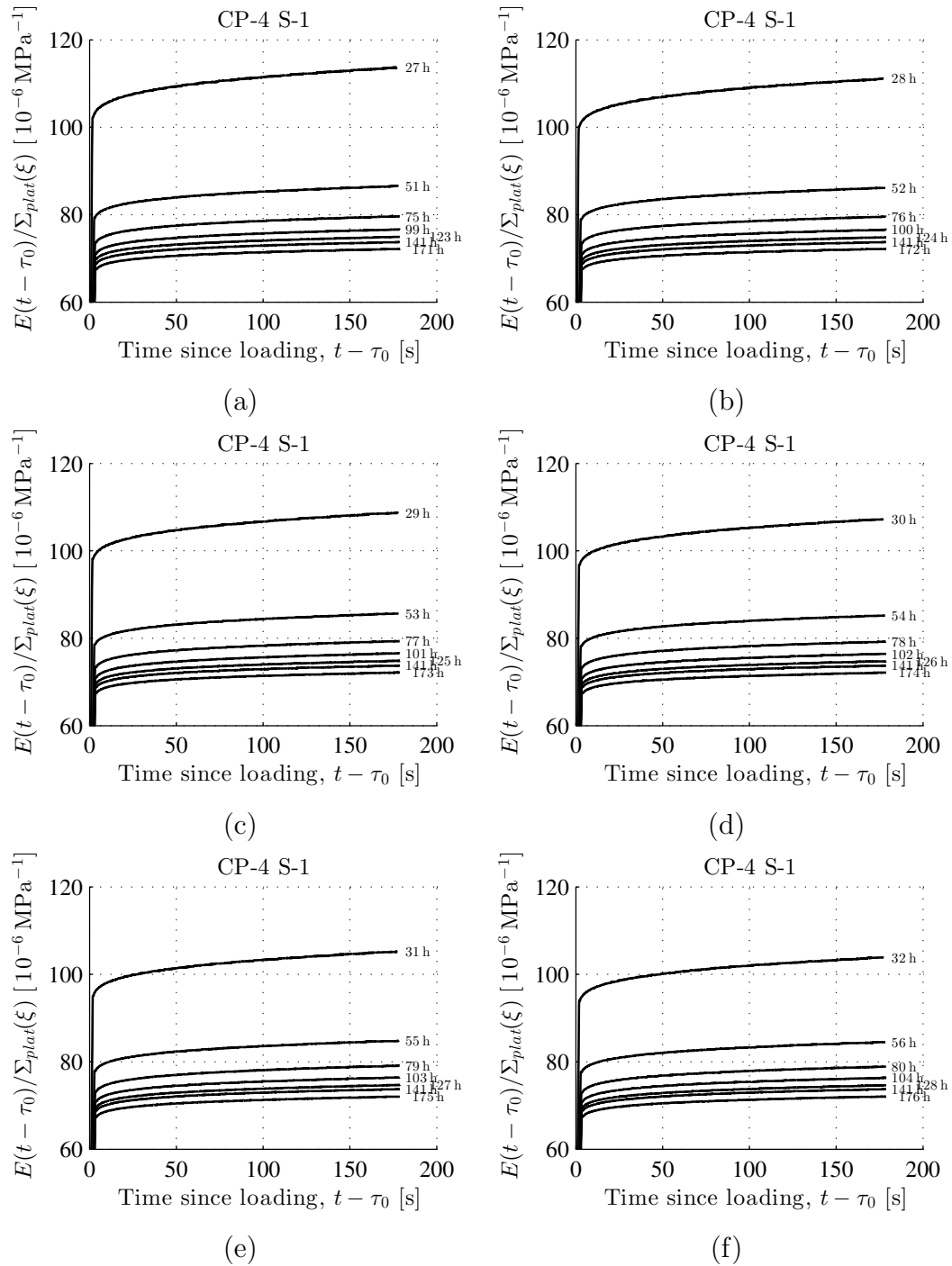


Figure 5.28: Measured strain evolution normalized with respect to the plateau stress as a function of the time since start of loading: cement paste with $w/c = 0.42$; ambient air temperature = 30°C ; ID = “CP-4 S-1”, see Table 5.1; as for load levels, see Fig. 5.1(a)

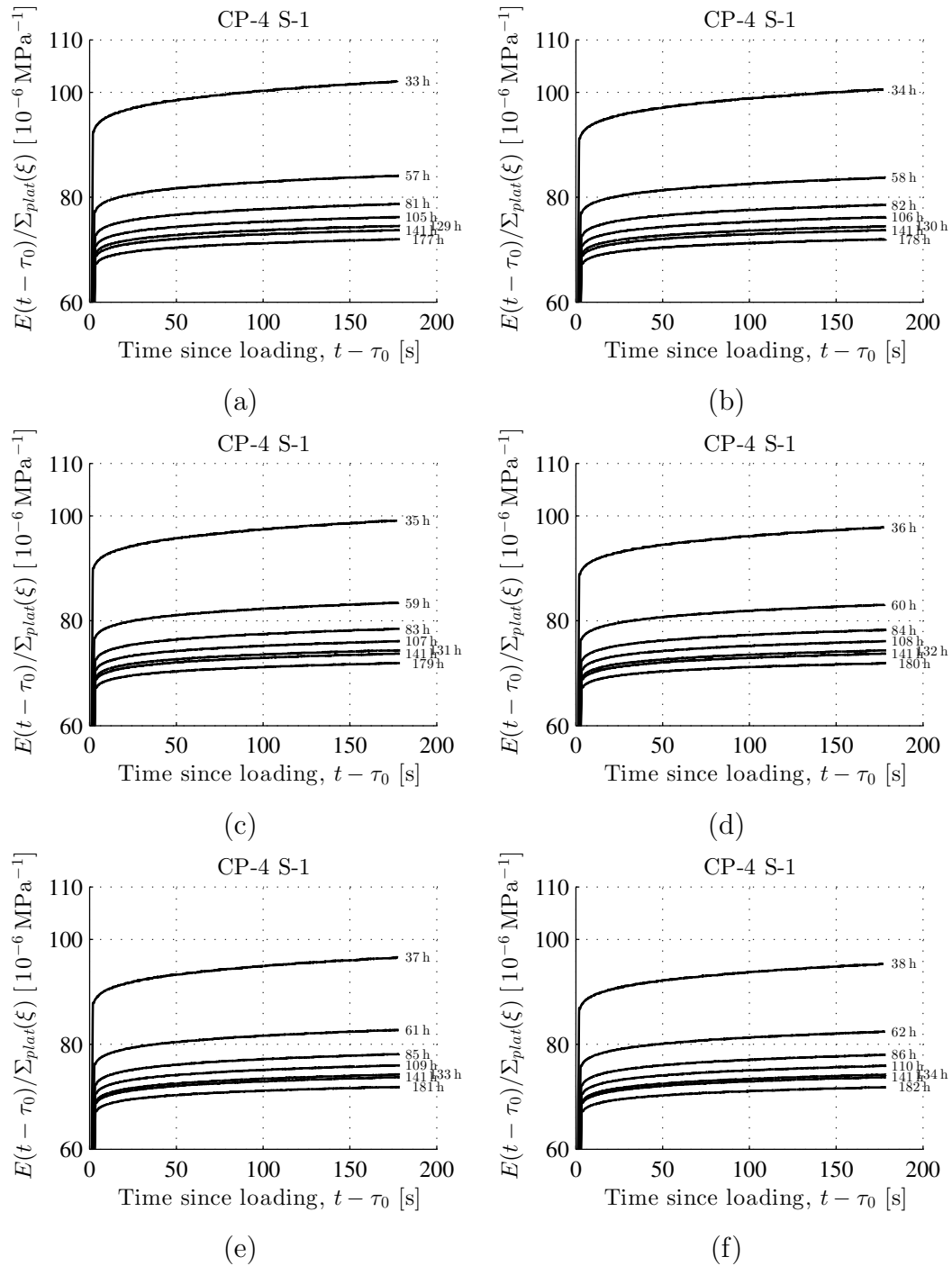


Figure 5.29: Measured strain evolution normalized with respect to the plateau stress as a function of the time since start of loading: cement paste with $w/c = 0.42$; ambient air temperature = 30°C ; ID = "CP-4 S-1", see Table 5.1; as for load levels, see Fig. 5.1(a)

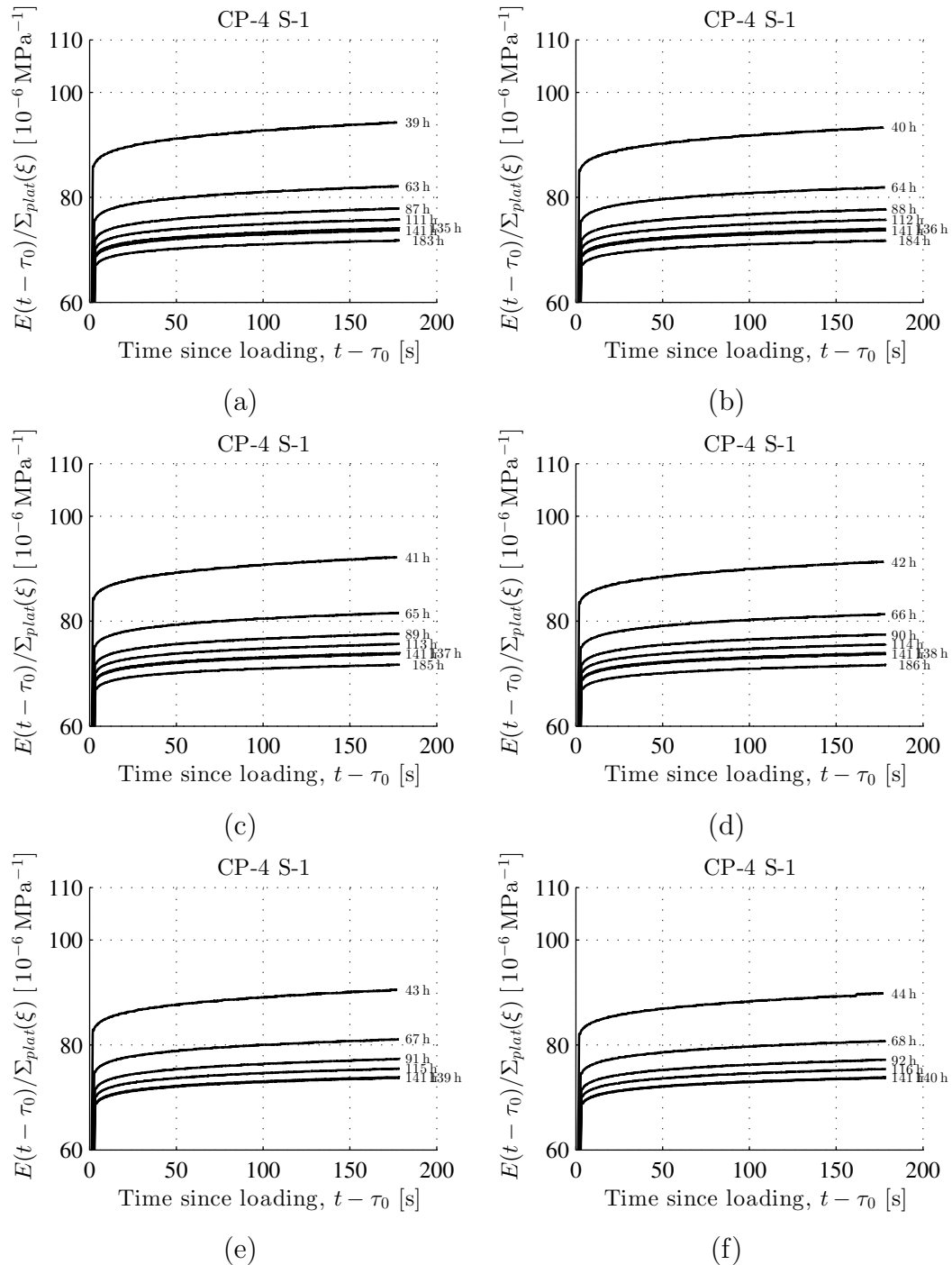


Figure 5.30: Measured strain evolution normalized with respect to the plateau stress as a function of the time since start of loading: cement paste with $w/c = 0.42$; ambient air temperature = 30°C ; ID = "CP-4 S-1", see Table 5.1; as for load levels, see Fig. 5.1(a)

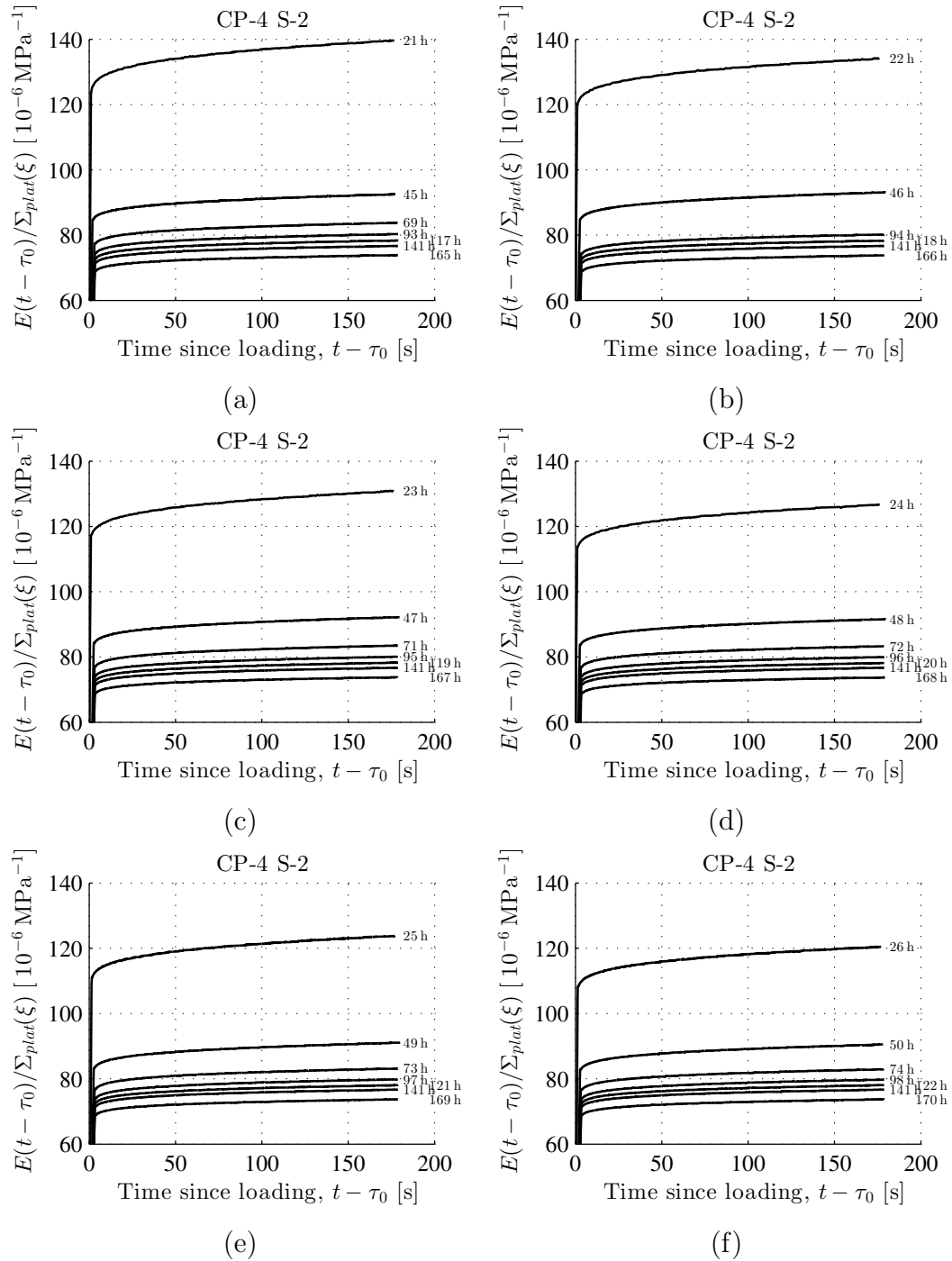


Figure 5.31: Measured strain evolution normalized with respect to the plateau stress as a function of the time since start of loading: cement paste with $w/c = 0.42$; ambient air temperature = $30\text{ }^\circ\text{C}$; ID = “CP-4 S-2”, see Table 5.1; as for load levels, see Fig. 5.1(a)

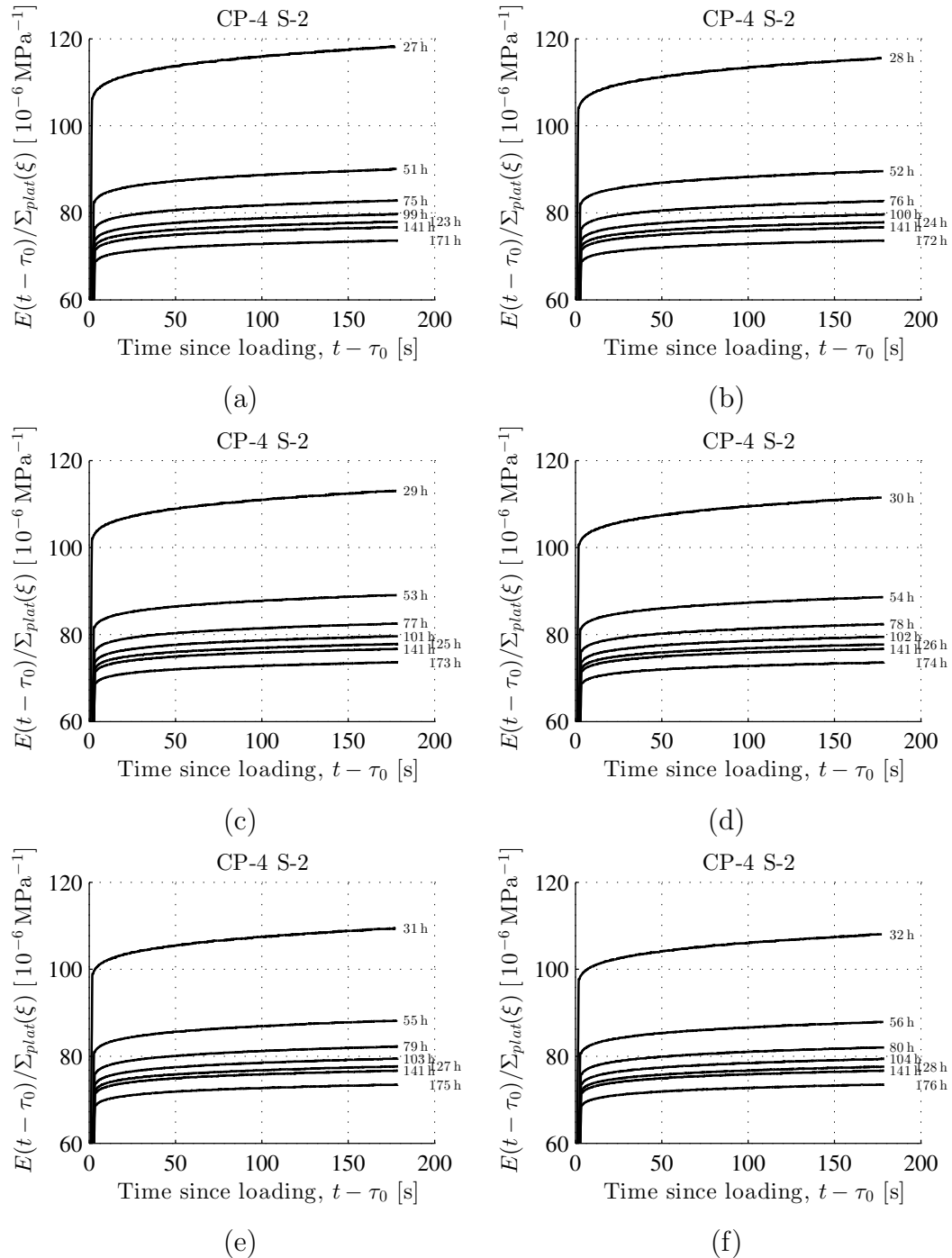


Figure 5.32: Measured strain evolution normalized with respect to the plateau stress as a function of the time since start of loading: cement paste with $w/c = 0.42$; ambient air temperature = 30°C ; ID = “CP-4 S-2”, see Table 5.1; as for load levels, see Fig. 5.1(a)

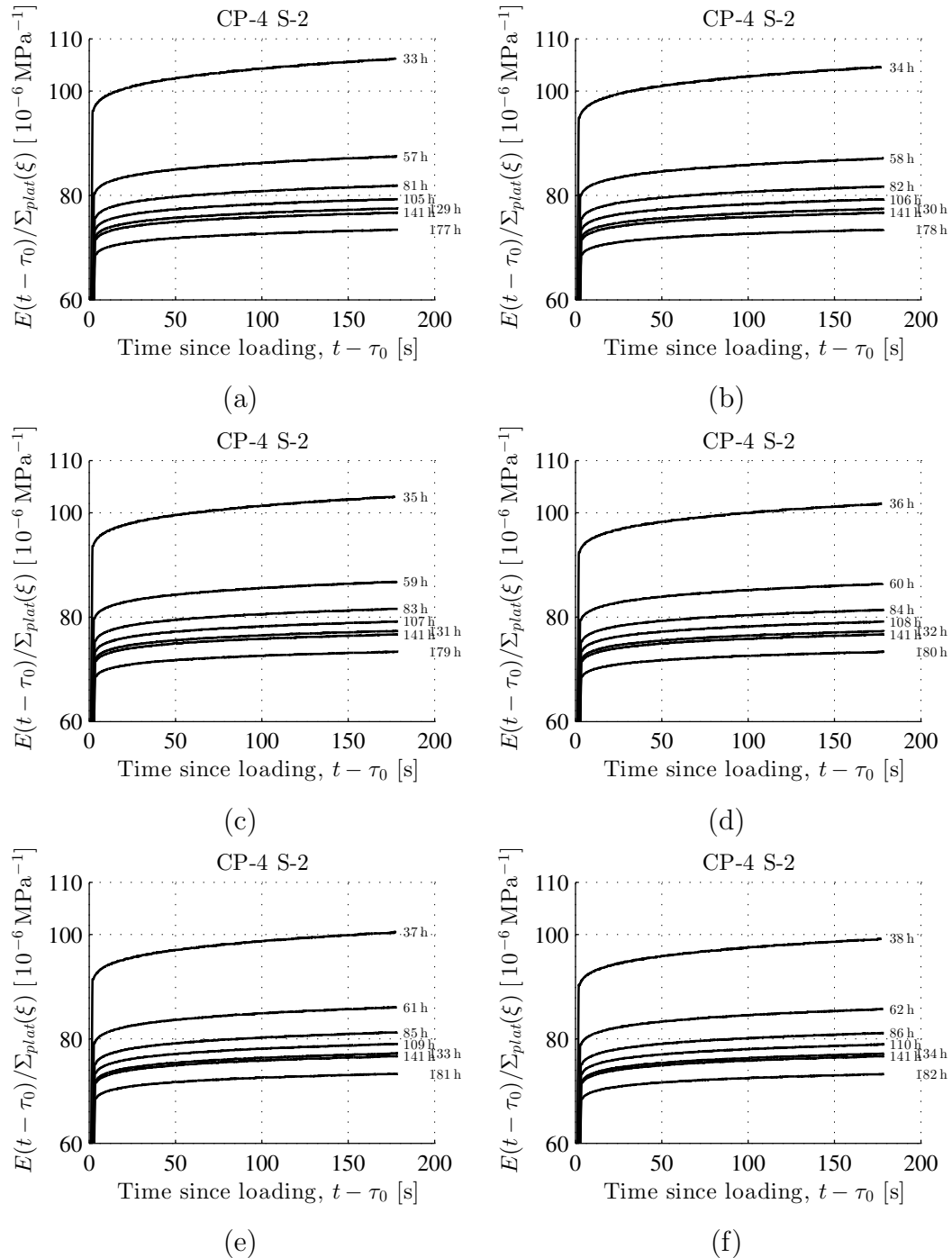


Figure 5.33: Measured strain evolution normalized with respect to the plateau stress as a function of the time since start of loading: cement paste with $w/c = 0.42$; ambient air temperature = $30\text{ }^{\circ}\text{C}$; ID = “CP-4 S-2”, see Table 5.1; as for load levels, see Fig. 5.1(a)

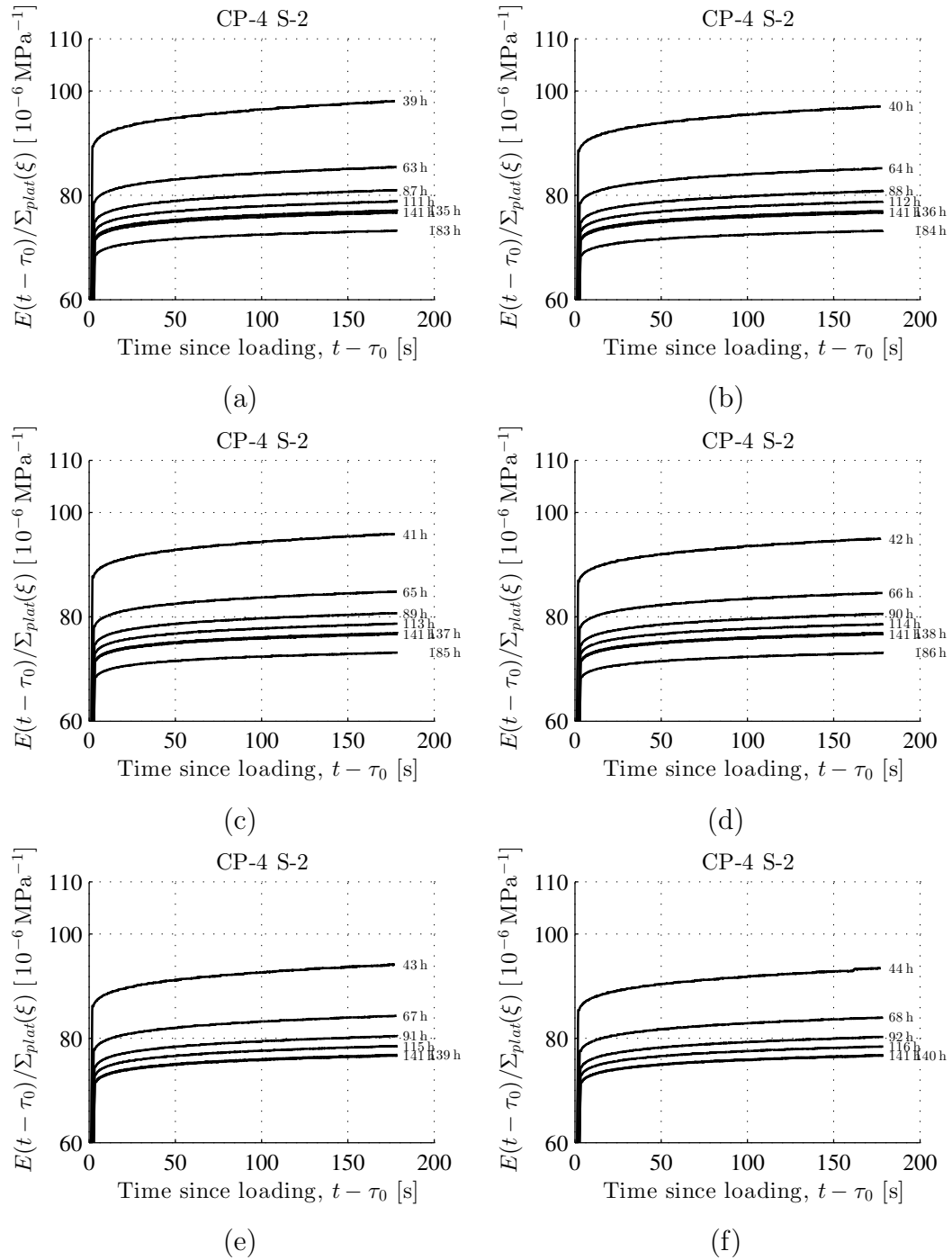


Figure 5.34: Measured strain evolution normalized with respect to the plateau stress as a function of the time since start of loading: cement paste with $w/c = 0.50$; ambient air temperature = 30°C ; ID = “CP-4 S-2”, see Table 5.1; as for load levels, see Fig. 5.1(a)

5.1.5 Water-cement ratio = 0.42, Temperature = 10 °C

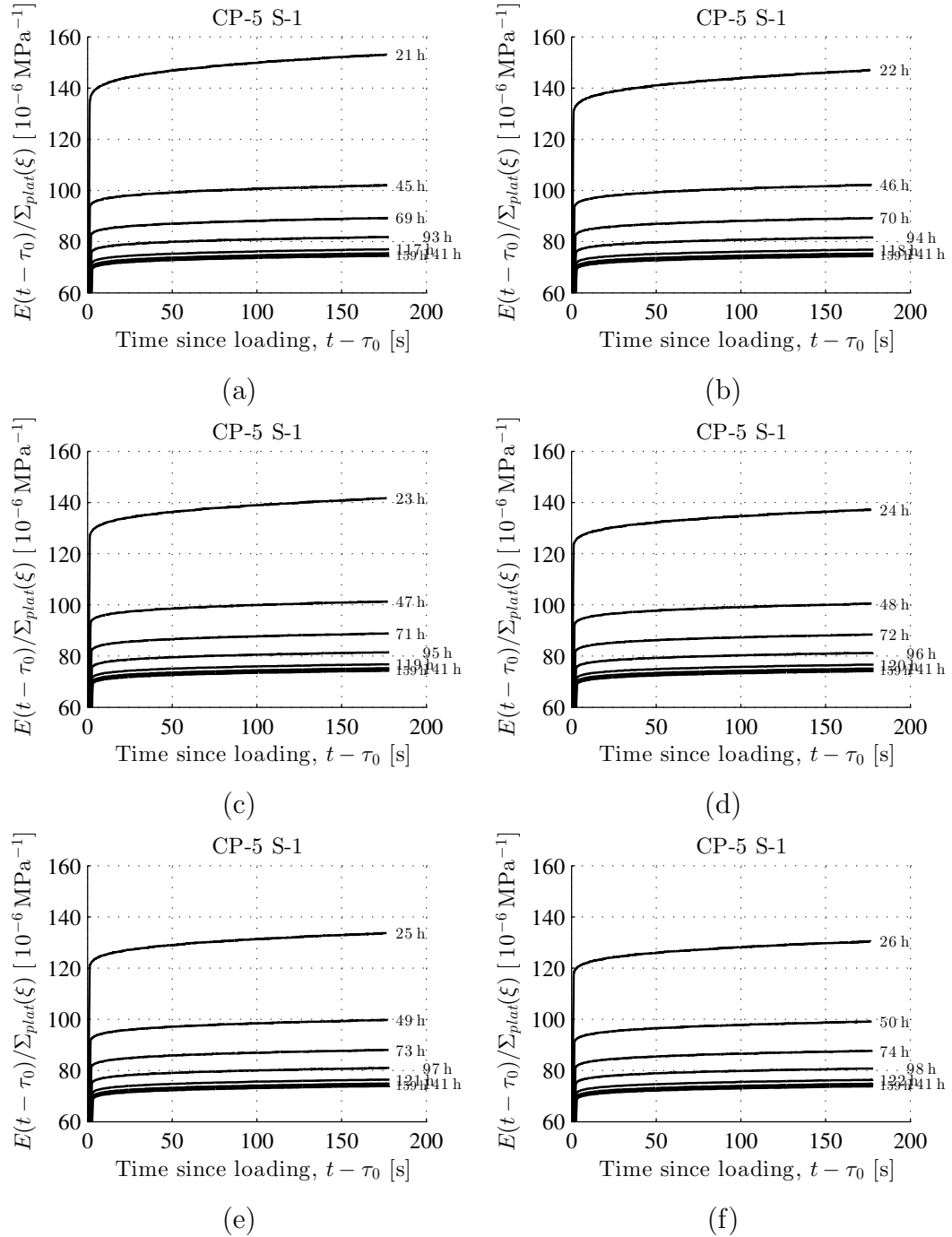


Figure 5.35: Measured strain evolution normalized with respect to the plateau stress as a function of the time since start of loading: cement paste with $w/c = 0.42$; ambient air temperature = 10 °C; ID = "CP-5 S-1", see Table 5.1; as for load levels, see Fig. 5.1(a)

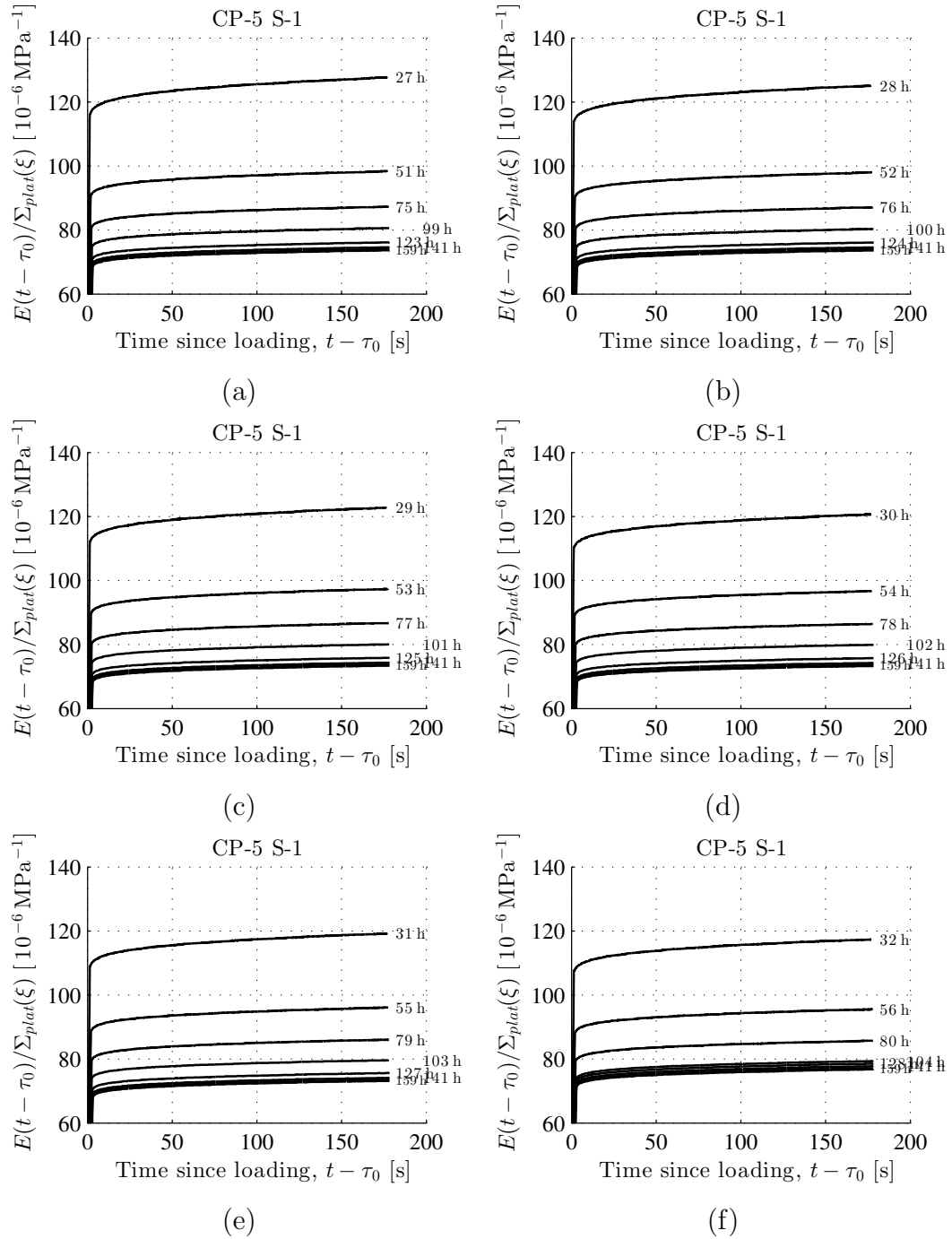


Figure 5.36: Measured strain evolution normalized with respect to the plateau stress as a function of the time since start of loading: cement paste with $w/c = 0.42$; ambient air temperature = $10\text{ }^{\circ}\text{C}$; ID = "CP-5 S-1", see Table 5.1; as for load levels, see Fig. 5.1(a)

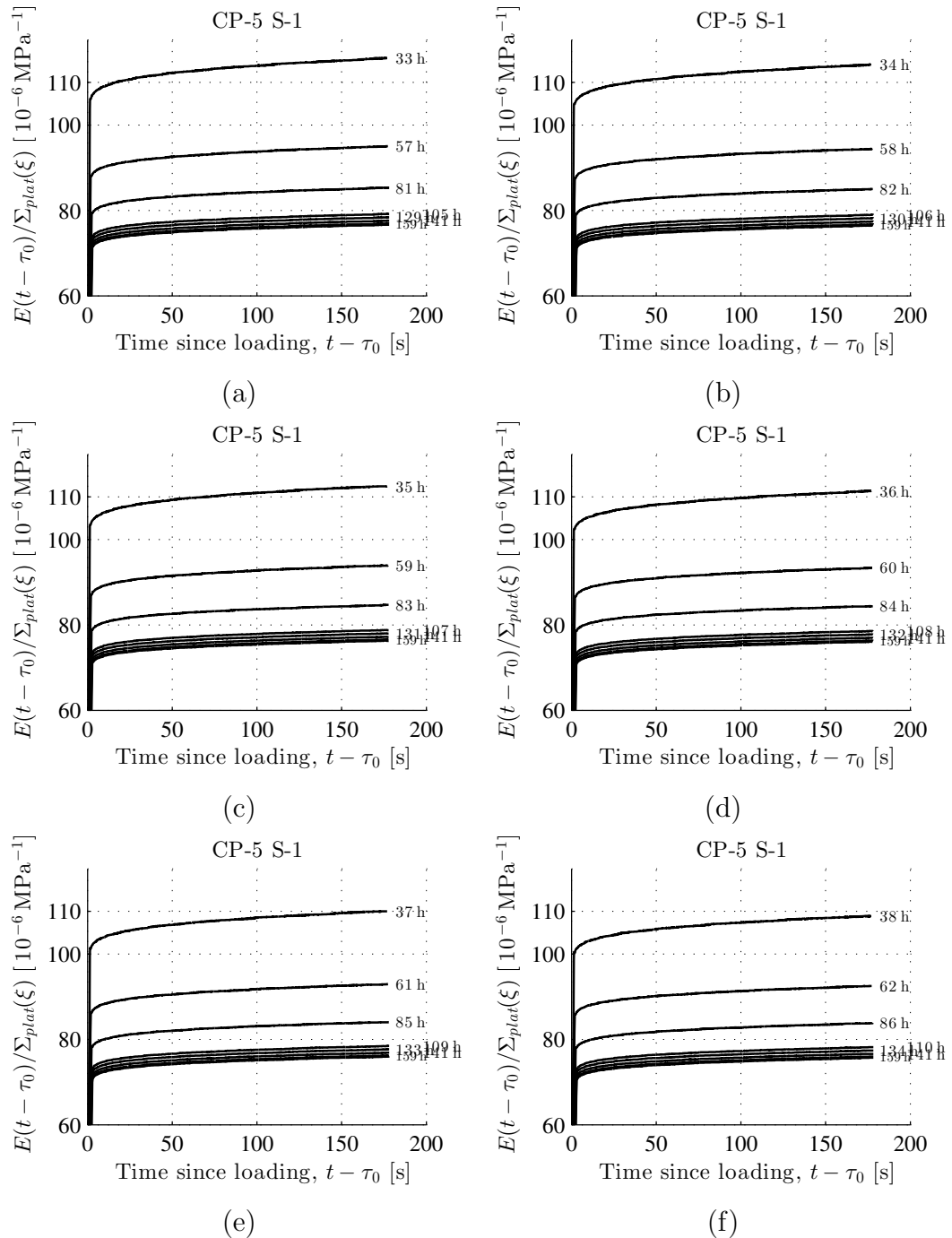


Figure 5.37: Measured strain evolution normalized with respect to the plateau stress as a function of the time since start of loading: cement paste with $w/c = 0.42$; ambient air temperature = $10\text{ }^{\circ}\text{C}$; ID = "CP-5 S-1", see Table 5.1; as for load levels, see Fig. 5.1(a)

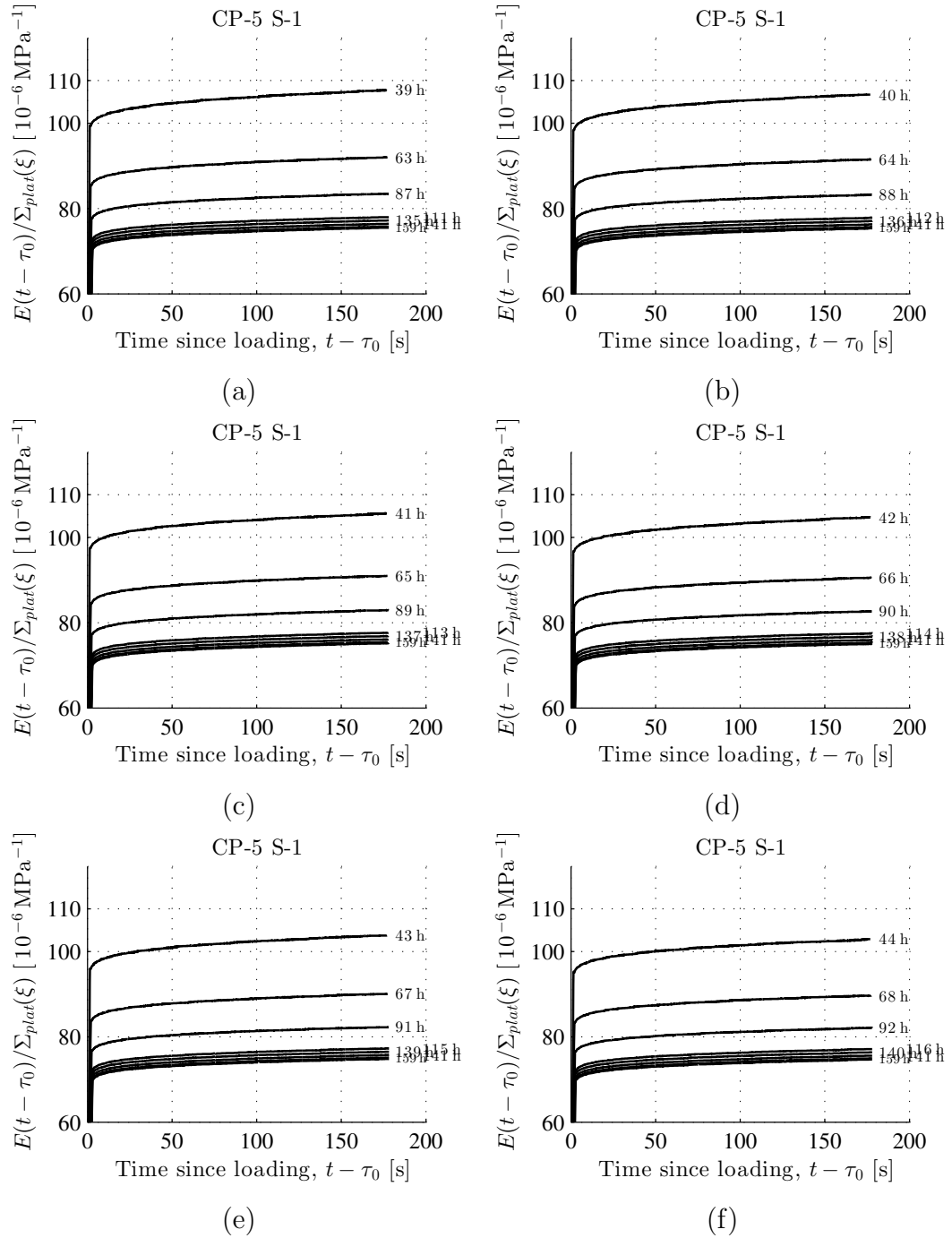


Figure 5.38: Measured strain evolution normalized with respect to the plateau stress as a function of the time since start of loading: cement paste with $w/c = 0.42$; ambient air temperature = 10°C ; ID = “CP-5 S-1”, see Table 5.1; as for load levels, see Fig. 5.1(a)

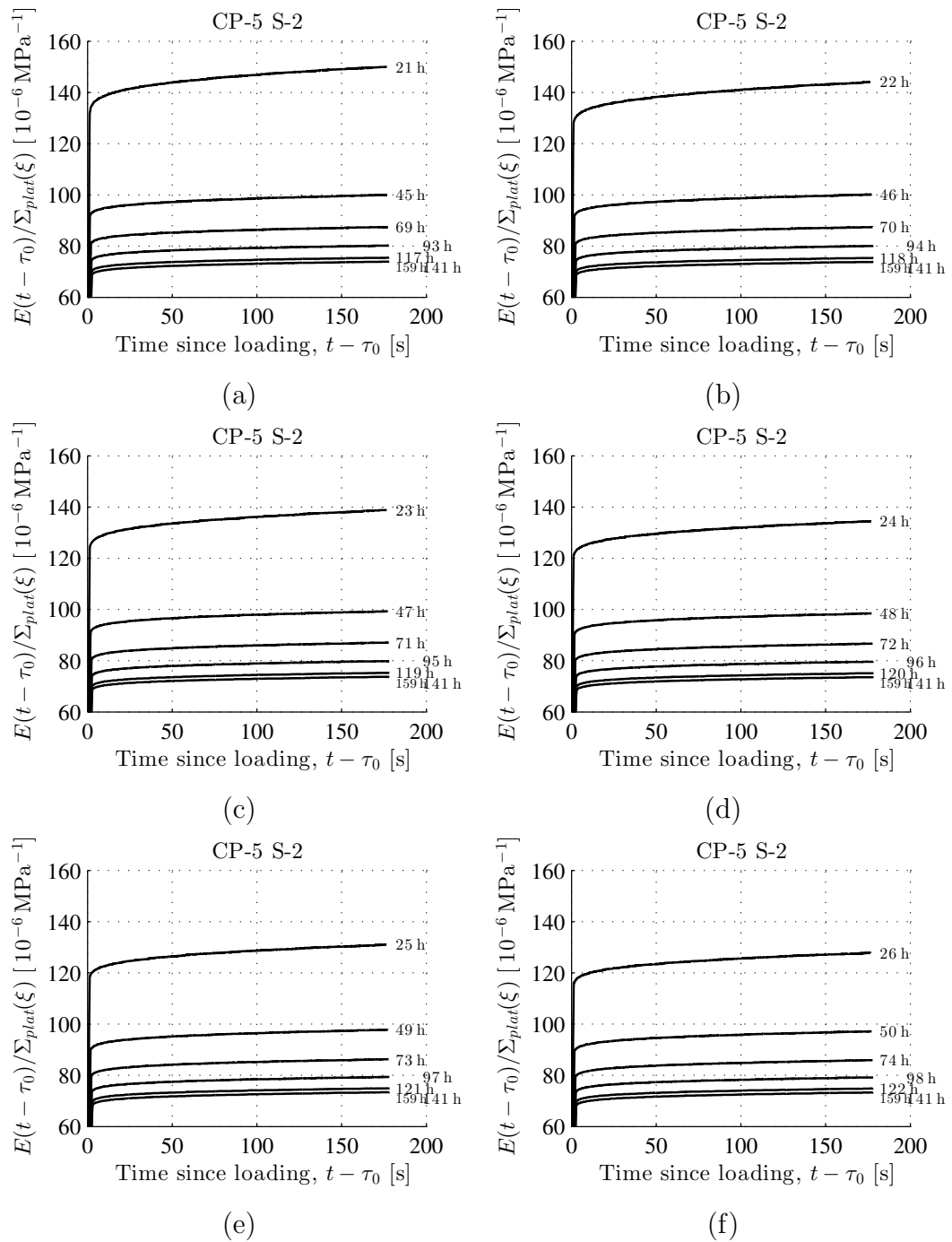


Figure 5.39: Measured strain evolution normalized with respect to the plateau stress as a function of the time since start of loading: cement paste with $w/c = 0.42$; ambient air temperature = 10°C ; ID = “CP-5 S-2”, see Table 5.1; as for load levels, see Fig. 5.1(a)

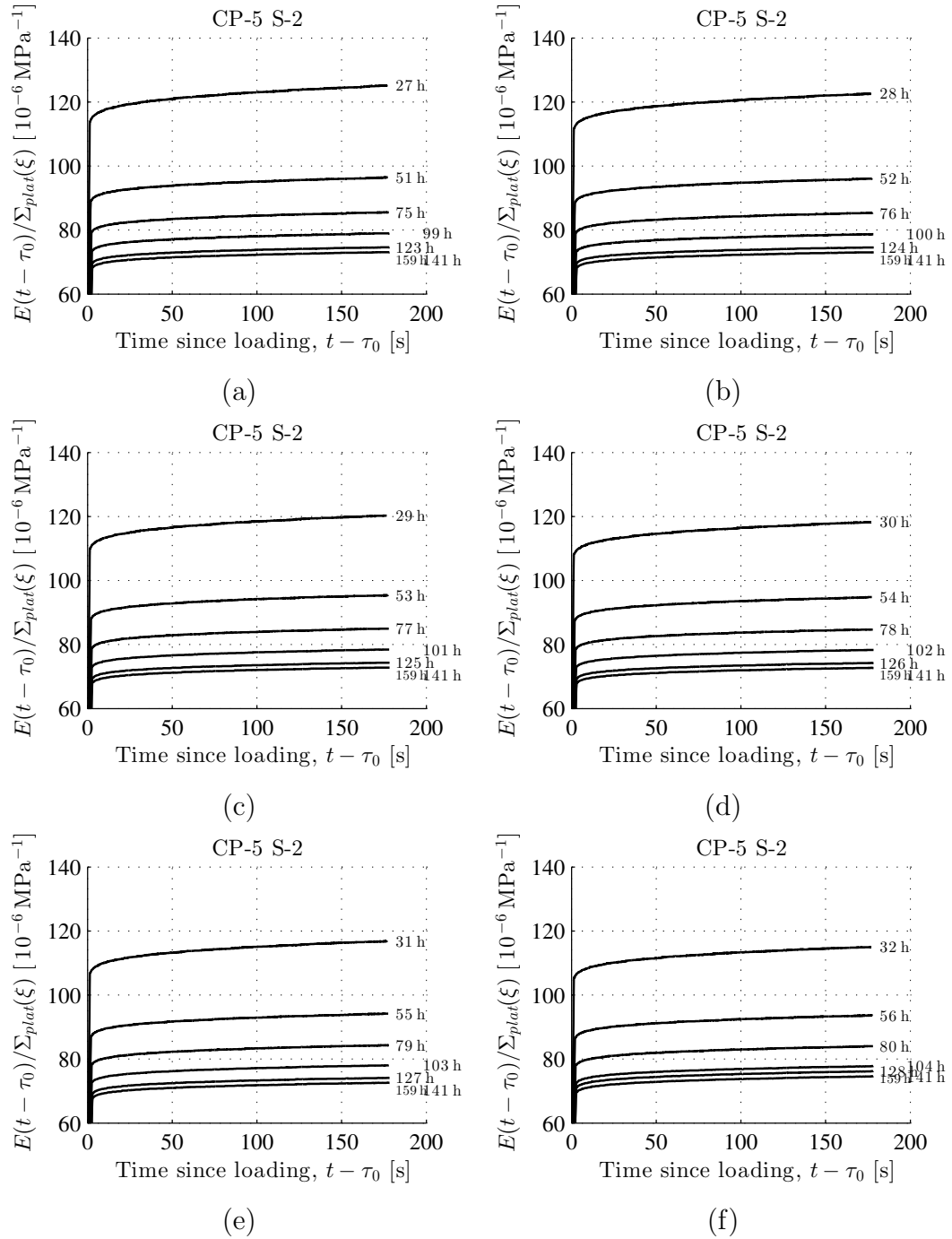


Figure 5.40: Measured strain evolution normalized with respect to the plateau stress as a function of the time since start of loading: cement paste with $w/c = 0.42$; ambient air temperature = $10\text{ }^{\circ}\text{C}$; ID = "CP-5 S-2", see Table 5.1; as for load levels, see Fig. 5.1(a)

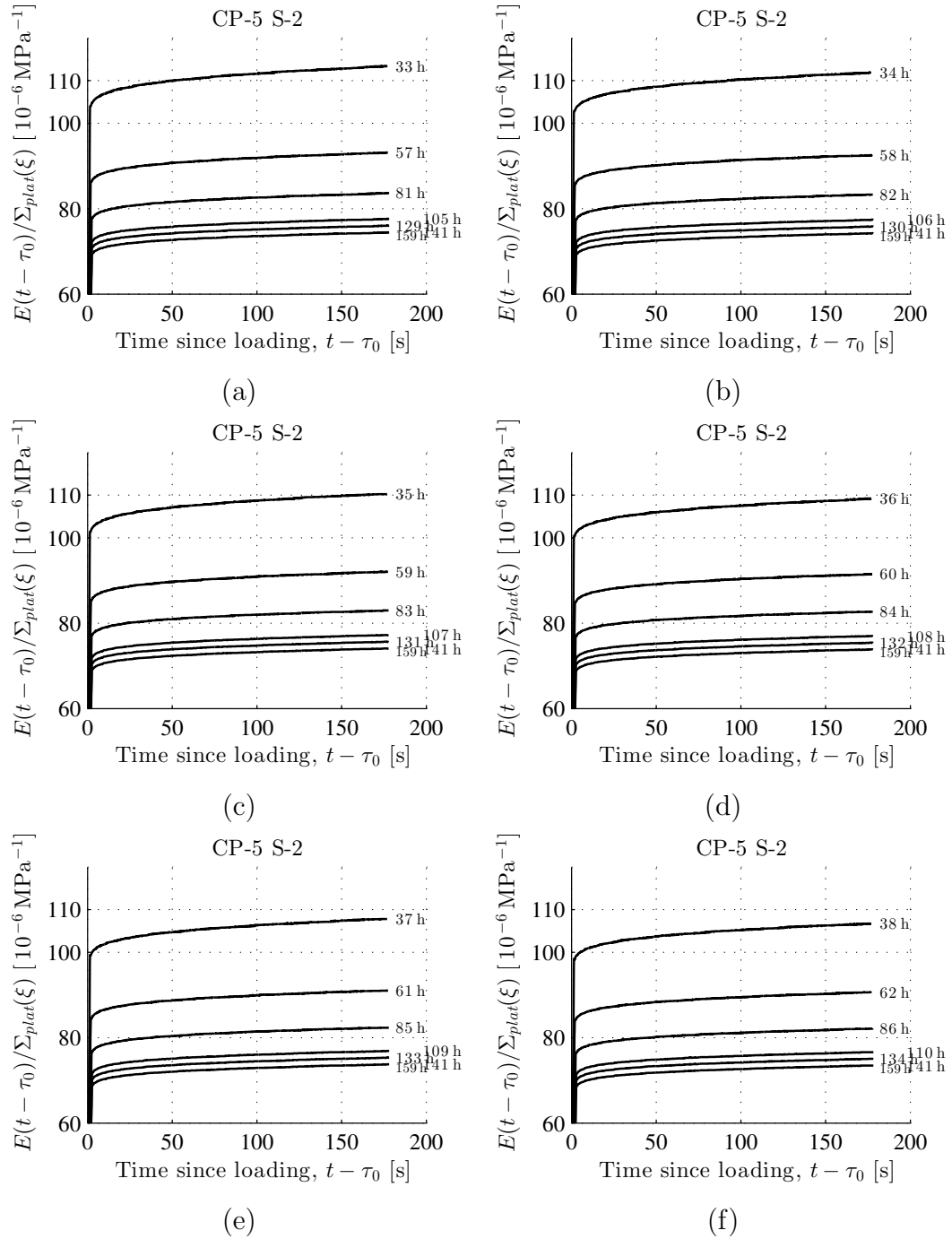


Figure 5.41: Measured strain evolution normalized with respect to the plateau stress as a function of the time since start of loading: cement paste with $w/c = 0.42$; ambient air temperature = 10°C ; ID = “CP-5 S-2”, see Table 5.1; as for load levels, see Fig. 5.1(a)

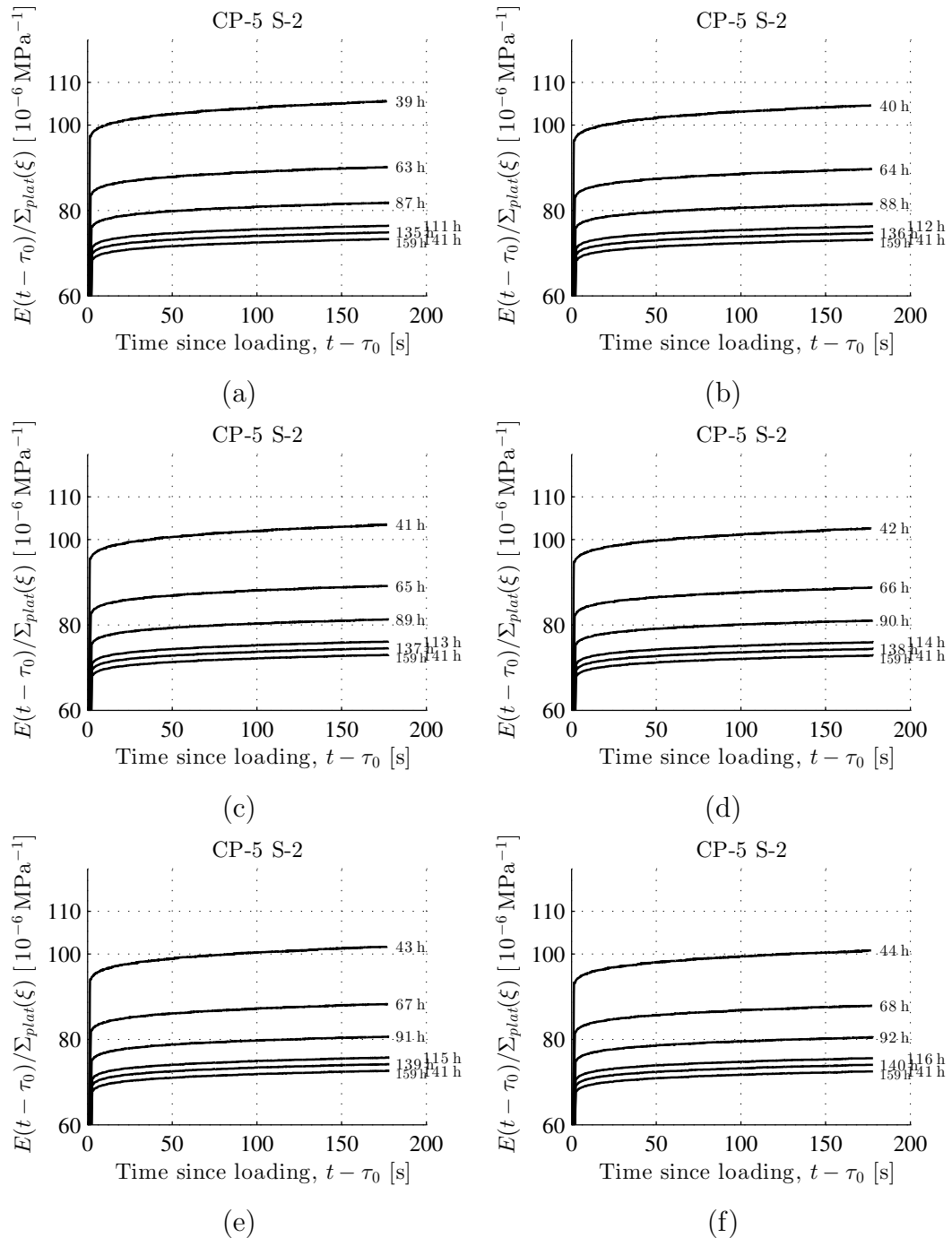


Figure 5.42: Measured strain evolution normalized with respect to the plateau stress as a function of the time since start of loading: cement paste with $w/c = 0.42$; ambient air temperature = $10\text{ }^{\circ}\text{C}$; ID = "CP-5 S-2", see Table 5.1; as for load levels, see Fig. 5.1(a)

5.2 Identified elastic and creep properties of cement pastes

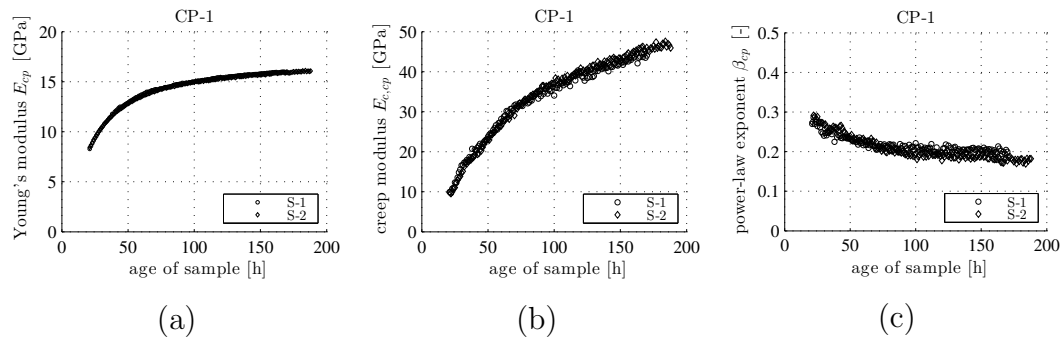


Figure 5.43: Evolution of (a) elastic Young's modulus E_{cp} (b) creep modulus $E_{c,cp}$ (c) power-law exponent β_{cp} , for cement paste CP-1

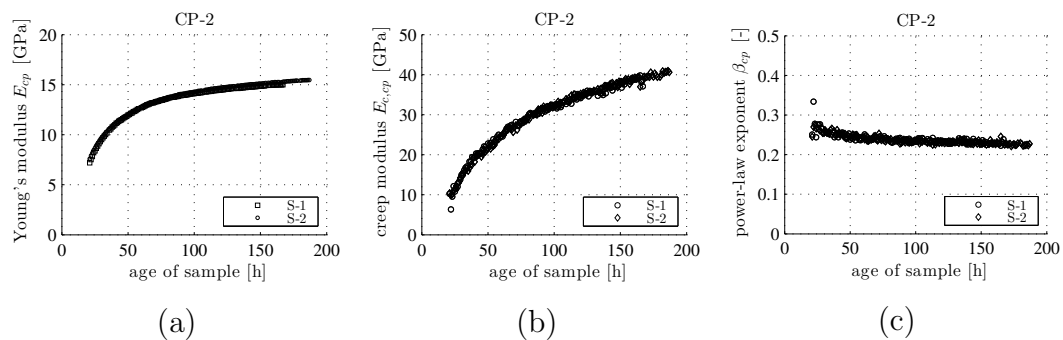


Figure 5.44: Evolution of (a) elastic Young's modulus E_{cp} (b) creep modulus $E_{c,cp}$ (c) power-law exponent β_{cp} , for cement paste CP-2

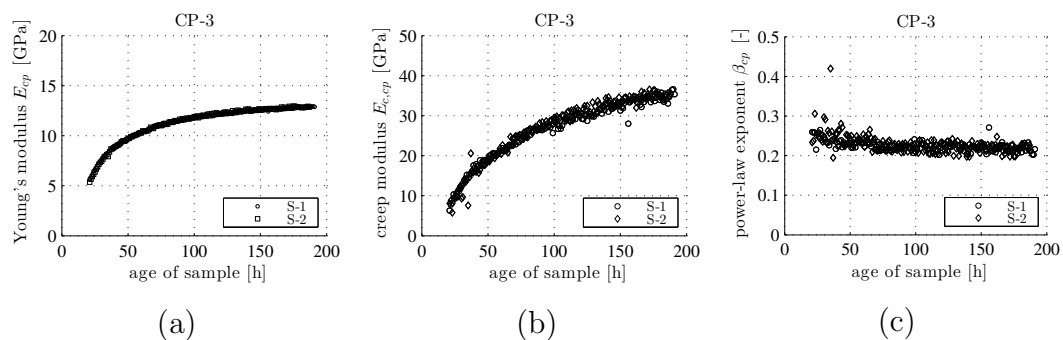


Figure 5.45: Evolution of (a) elastic Young's modulus E_{cp} (b) creep modulus $E_{c,cp}$ (c) power-law exponent β_{cp} , for cement paste CP-3

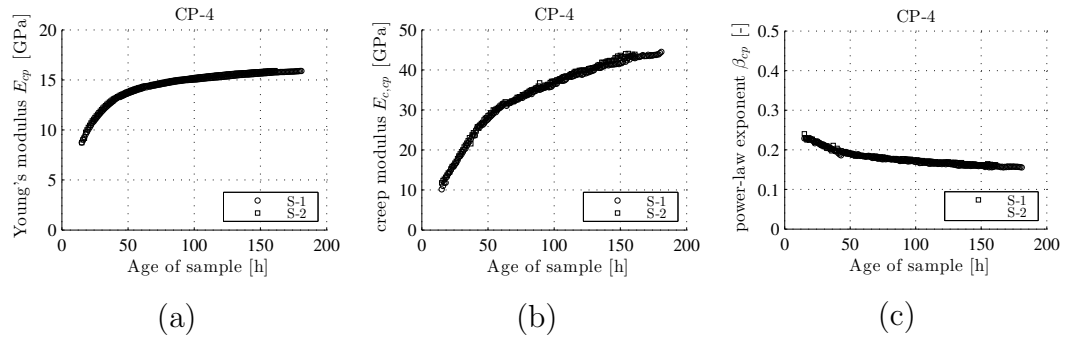


Figure 5.46: Evolution of (a) elastic Young's modulus E_{cp} (b) creep modulus $E_{c,cp}$ (c) power-law exponent β_{cp} , for cement paste CP-4

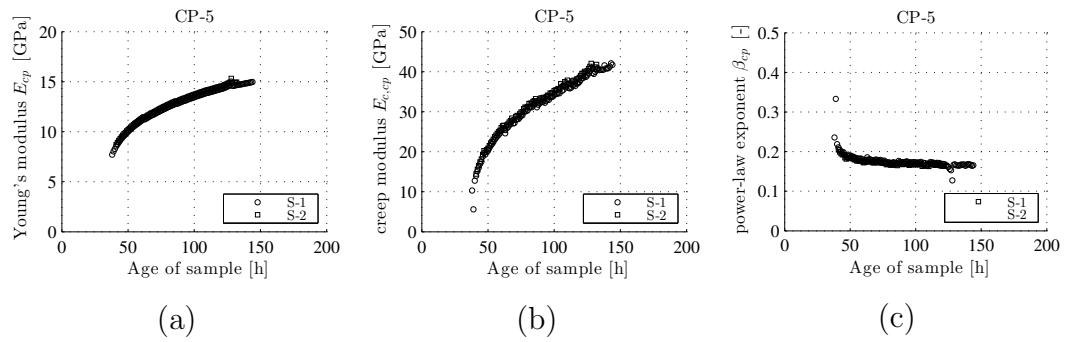


Figure 5.47: Evolution of (a) elastic Young's modulus E_{cp} (b) creep modulus $E_{c,cp}$ (c) power-law exponent β_{cp} , for cement paste CP-5

5.3 Results from characterization of mortars and concretes at 20 °C

5.3.1 Mortar: $w/c = 0.42$, $a/c = 2.70$

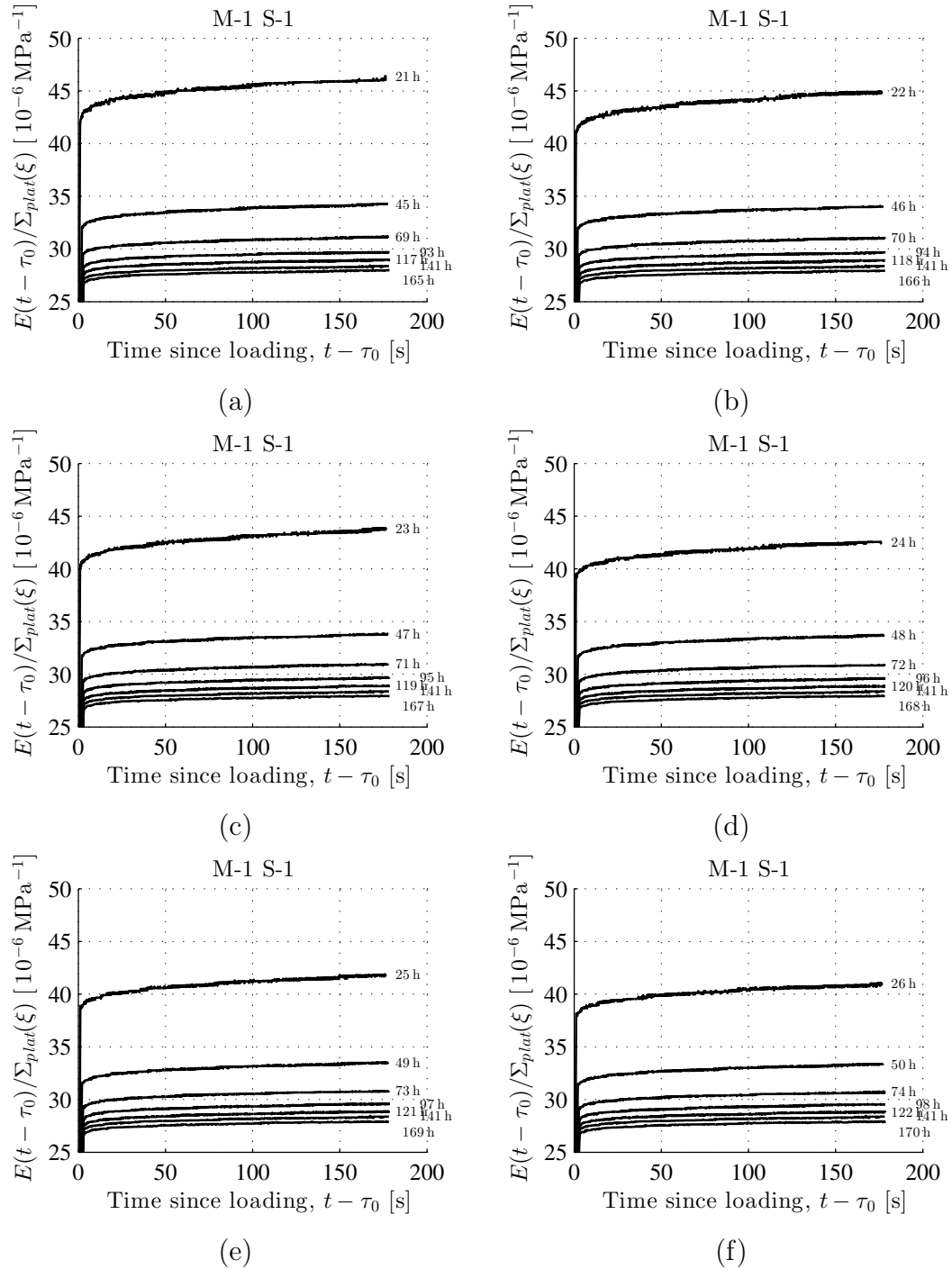


Figure 5.48: Measured strain evolution normalized with respect to the plateau stress as a function of the time since start of loading: mortar with $w/c = 0.42$, $a/c = 2.70$; ambient air temperature = $20\text{ }^{\circ}\text{C}$; ID = “M-1 S-1”, see Table 5.1; as for load levels, see Fig. 5.2

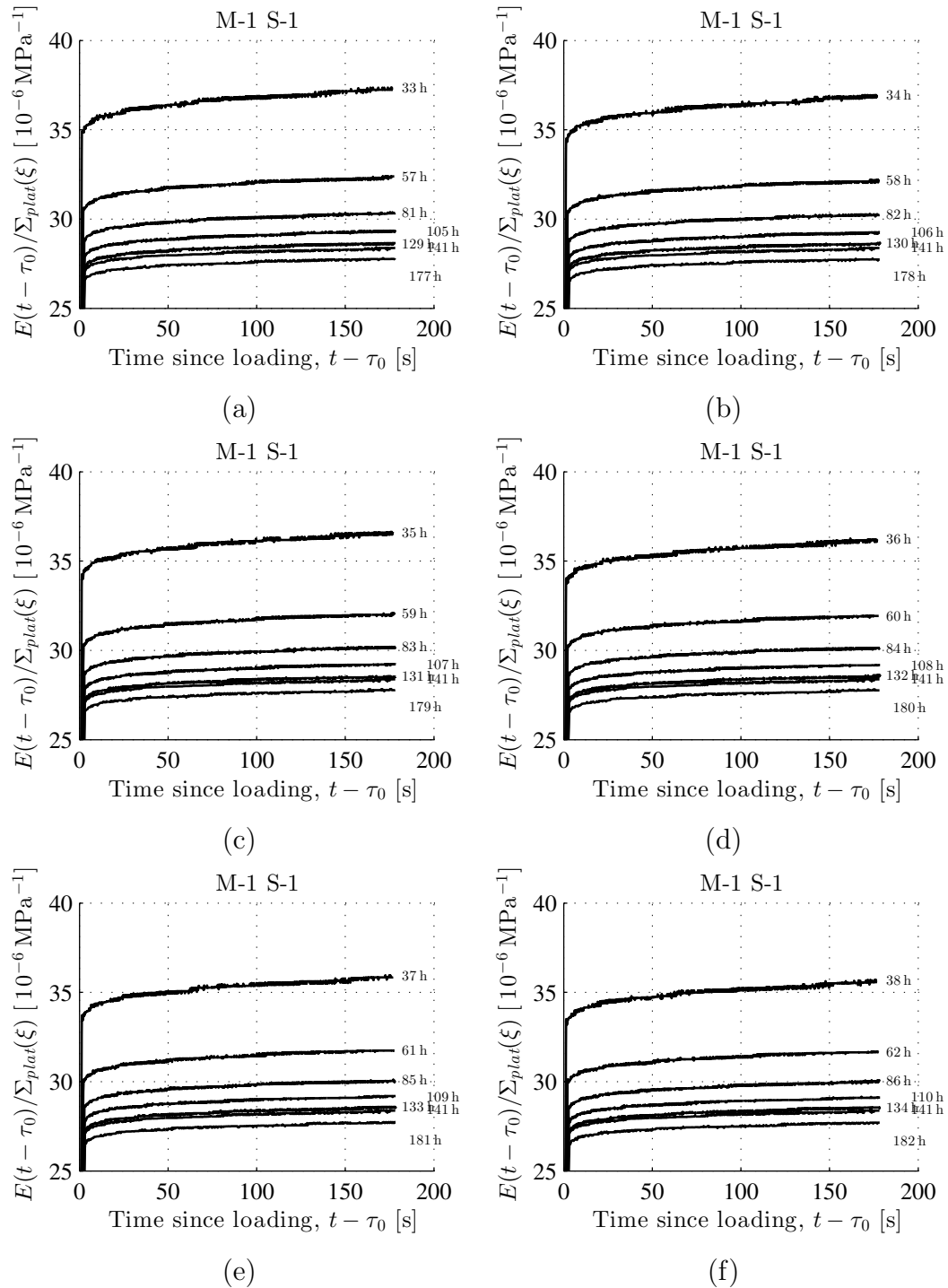


Figure 5.50: Measured strain evolution normalized with respect to the plateau stress as a function of the time since start of loading: cement paste with $w/c = 0.42$, $a/c = 2.70$; ambient air temperature = 20°C ; ID = "M-1 S-1", see Table 5.1; as for load levels, see Fig. 5.2

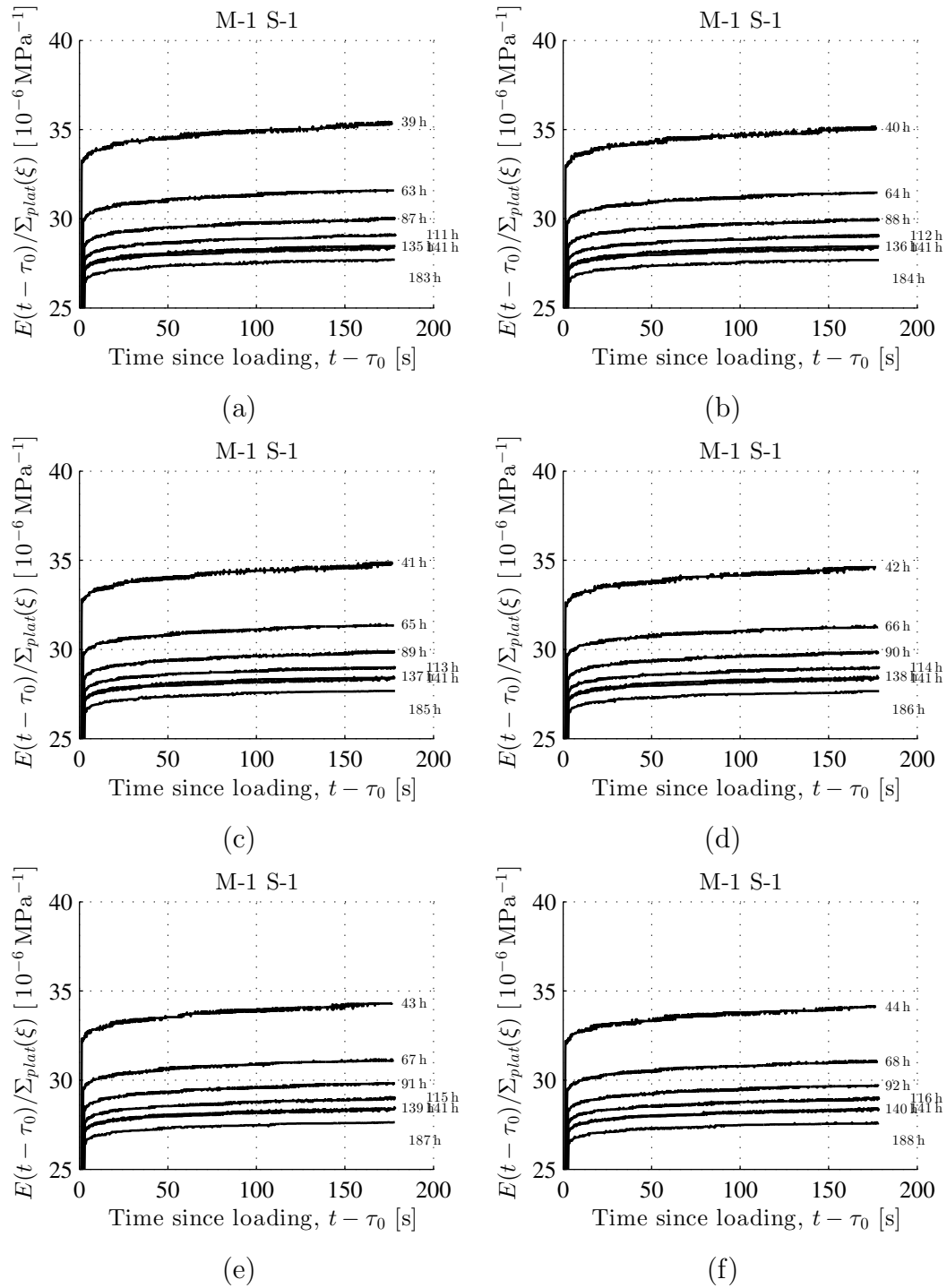


Figure 5.51: Measured strain evolution normalized with respect to the plateau stress as a function of the time since start of loading: mortar with $w/c = 0.42$, $a/c = 2.70$; ambient air temperature = 20°C ; ID = “M-1 S-1”, see Table 5.1; as for load levels, see Fig. 5.2

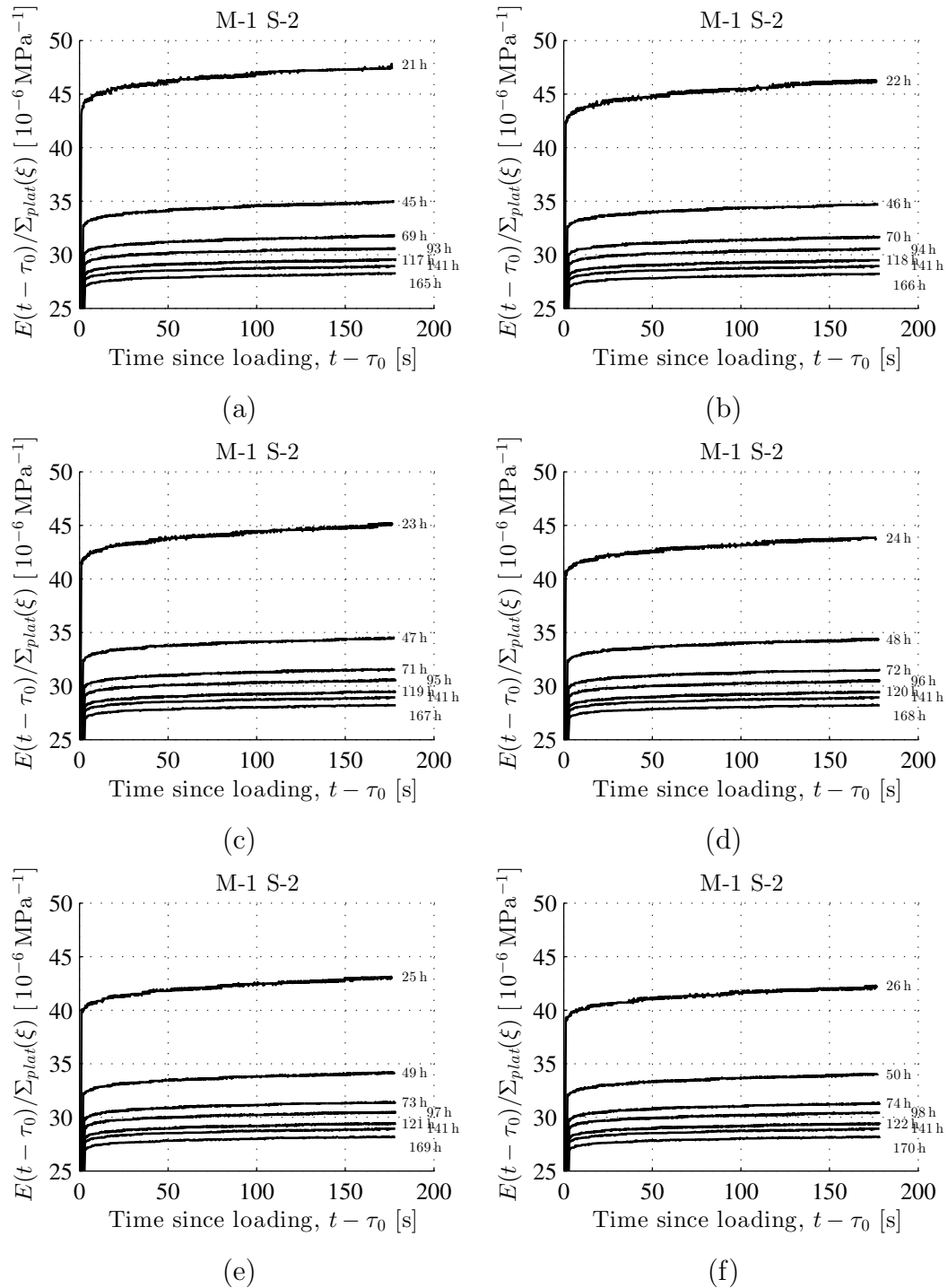


Figure 5.52: Measured strain evolution normalized with respect to the plateau stress as a function of the time since start of loading: mortar with $w/c = 0.42$, $a/c = 2.70$; ambient air temperature = 20°C ; ID = “M-1 S-2”, see Table 5.1; as for load levels, see Fig. 5.2

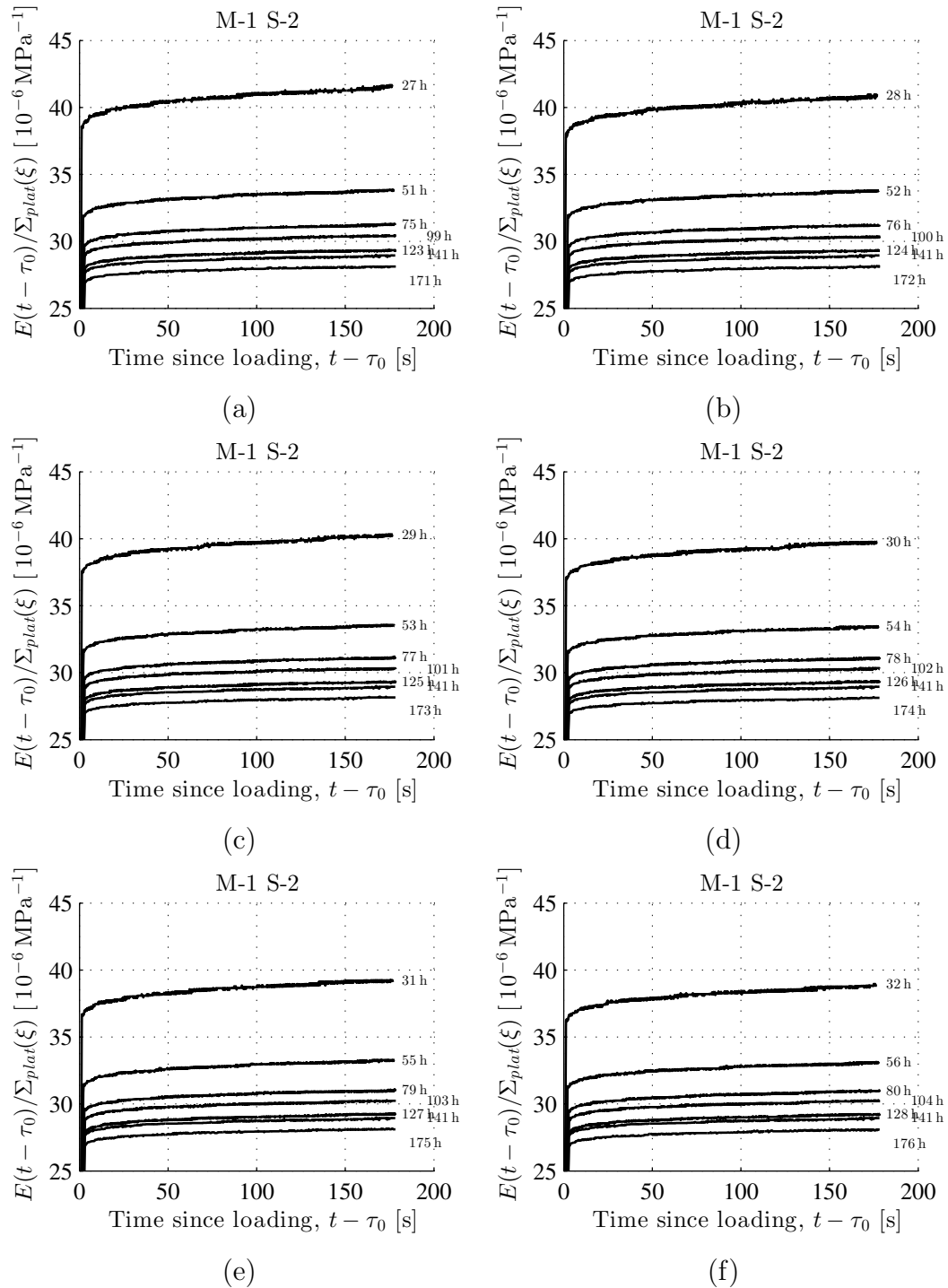


Figure 5.53: Measured strain evolution normalized with respect to the plateau stress as a function of the time since start of loading: mortar with $w/c = 0.42$, $a/c = 2.70$; ambient air temperature = 20°C ; ID = “M-1 S-2”, see Table 5.1; as for load levels, see Fig. 5.2

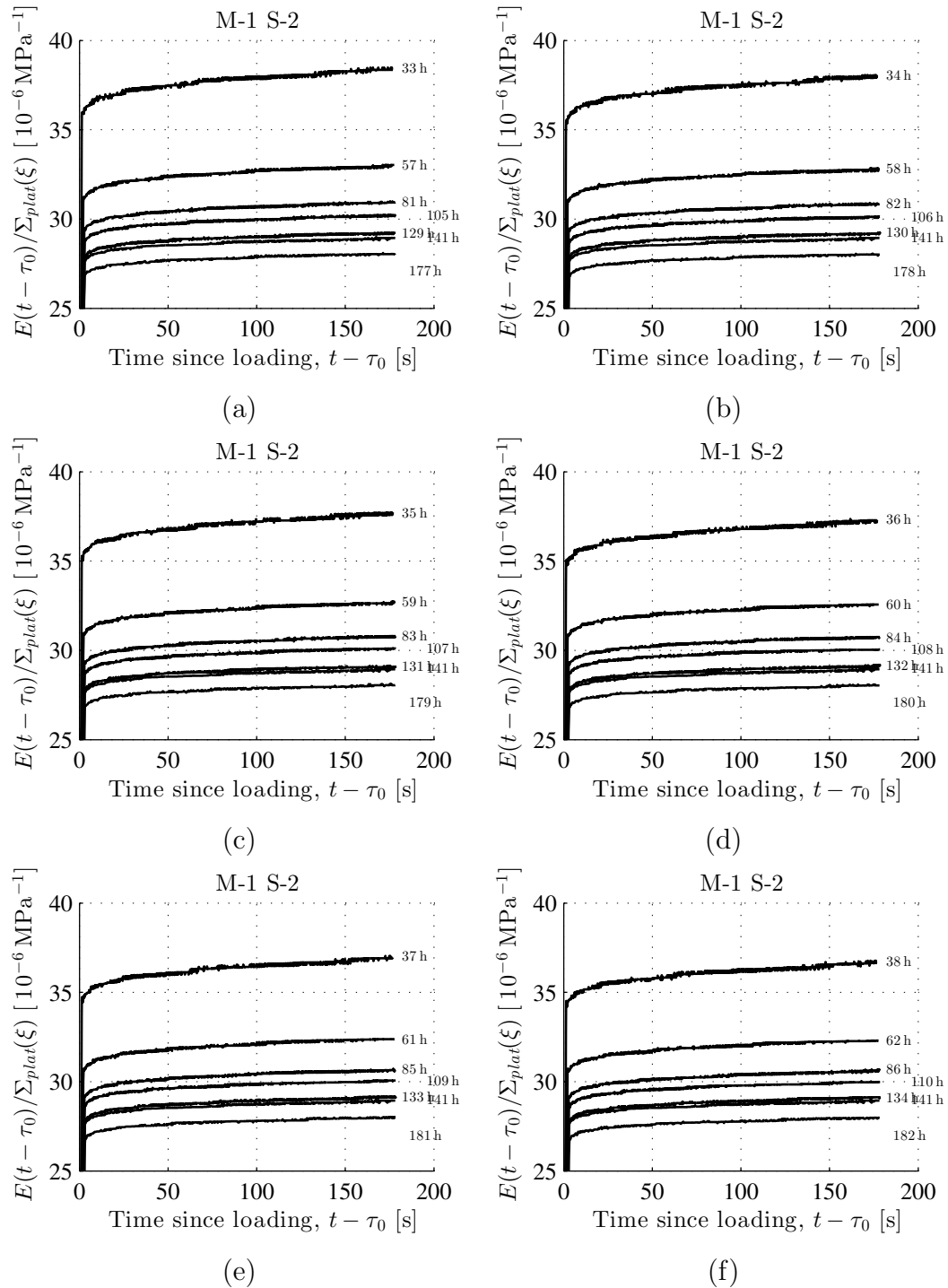


Figure 5.54: Measured strain evolution normalized with respect to the plateau stress as a function of the time since start of loading: mortar with $w/c = 0.42$, $a/c = 2.70$; ambient air temperature = 20°C ; ID = “M-1 S-2”, see Table 5.1; as for load levels, see Fig. 5.2

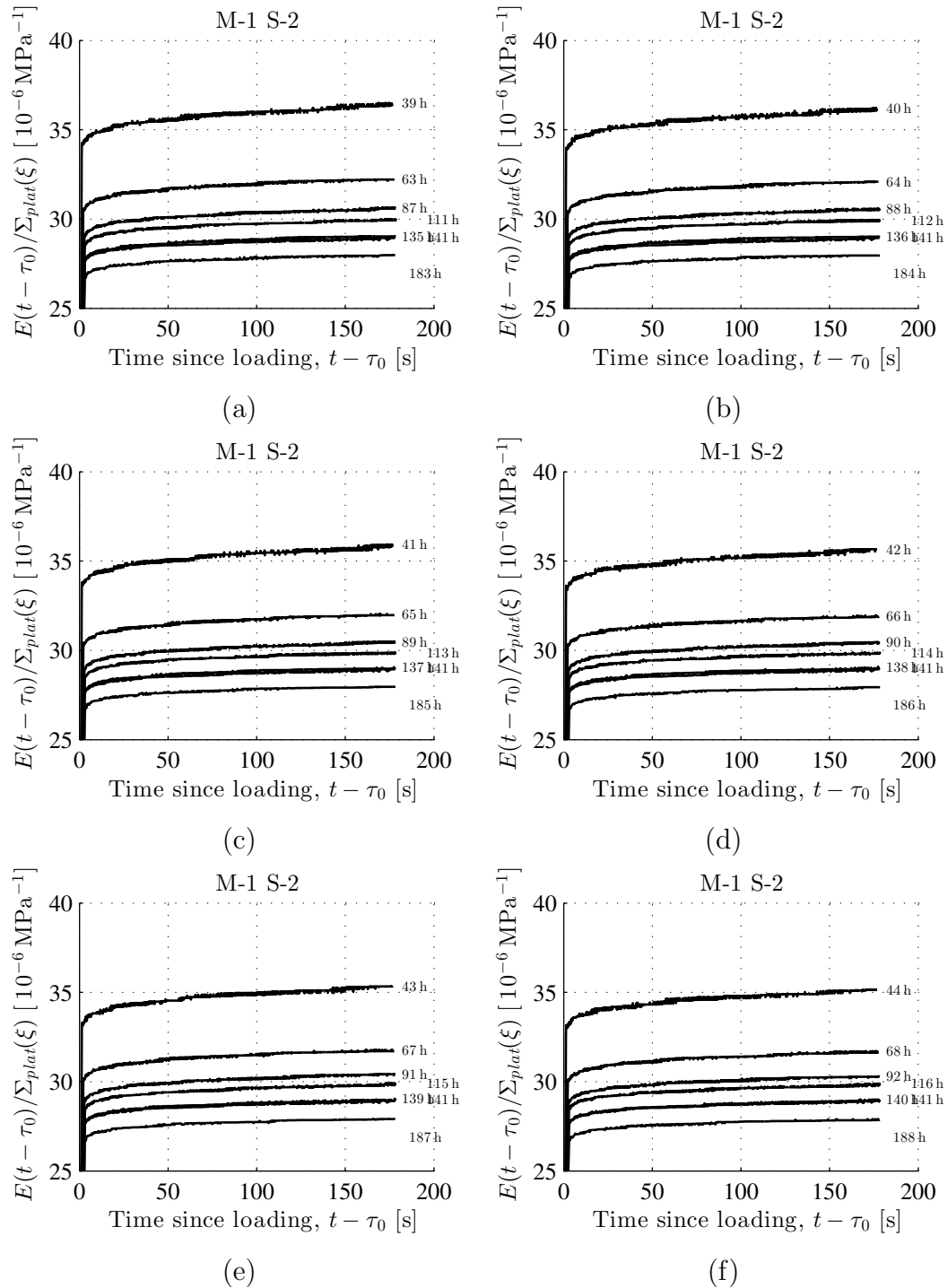


Figure 5.55: Measured strain evolution normalized with respect to the plateau stress as a function of the time since start of loading: mortar with $w/c = 0.42$, $a/c = 2.70$; ambient air temperature = 20°C ; ID = “M-1 S-2”, see Table 5.1; as for load levels, see Fig. 5.2

5.3.2 Mortar: $w/c = 0.45$, $a/c = 2.80$

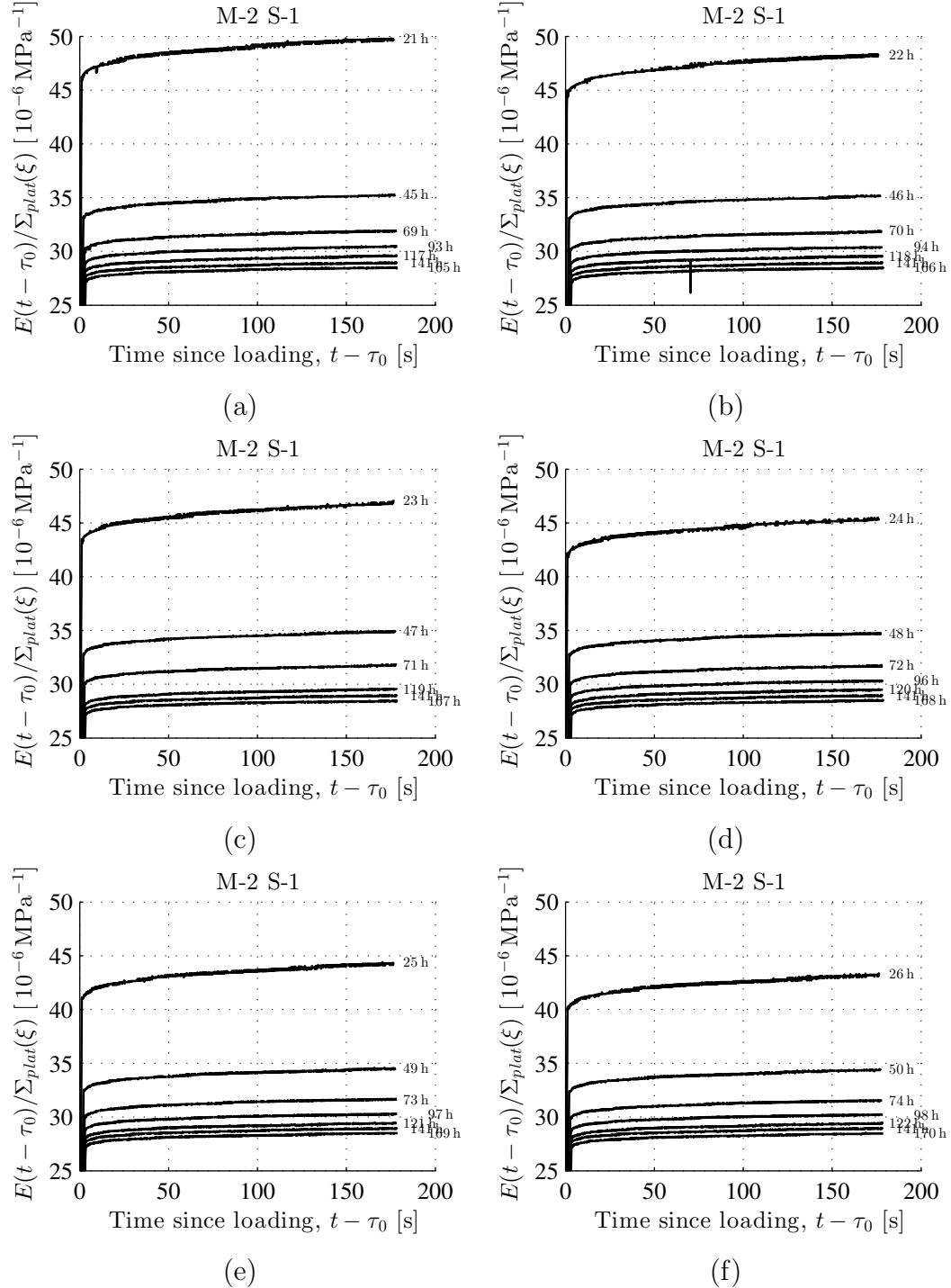


Figure 5.56: Measured strain evolution normalized with respect to the plateau stress as a function of the time since start of loading: mortar with $w/c = 0.45$, $a/c = 2.80$; ambient air temperature = $20\text{ }^{\circ}\text{C}$; ID = “M-2 S-1”, see Table 5.1; as for load levels, see Fig. 5.2

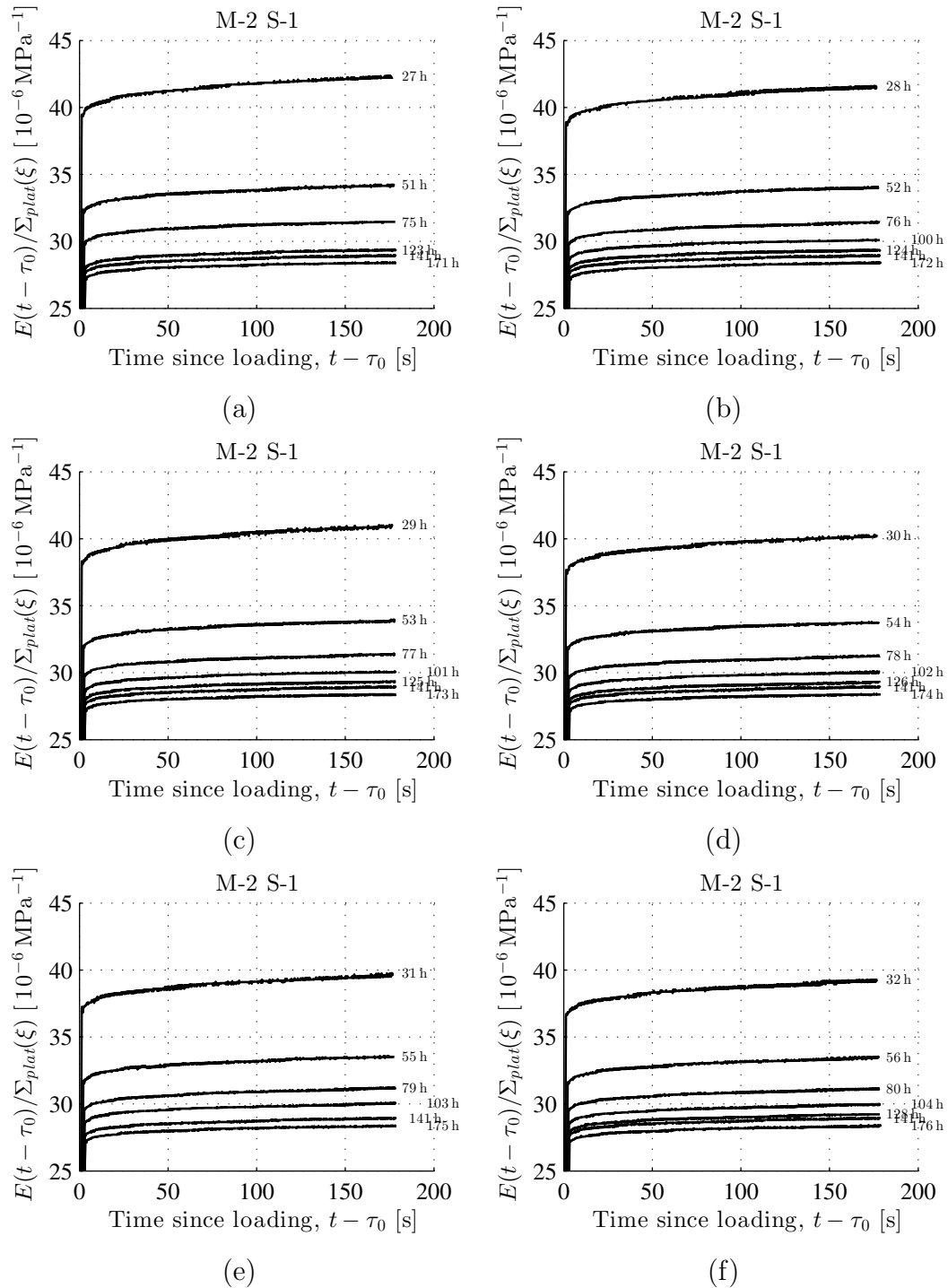


Figure 5.57: Measured strain evolution normalized with respect to the plateau stress as a function of the time since start of loading: mortar with $w/c = 0.45$, $a/c = 2.80$; ambient air temperature = 20°C ; ID = “M-2 S-1”, see Table 5.1; as for load levels, see Fig. 5.2

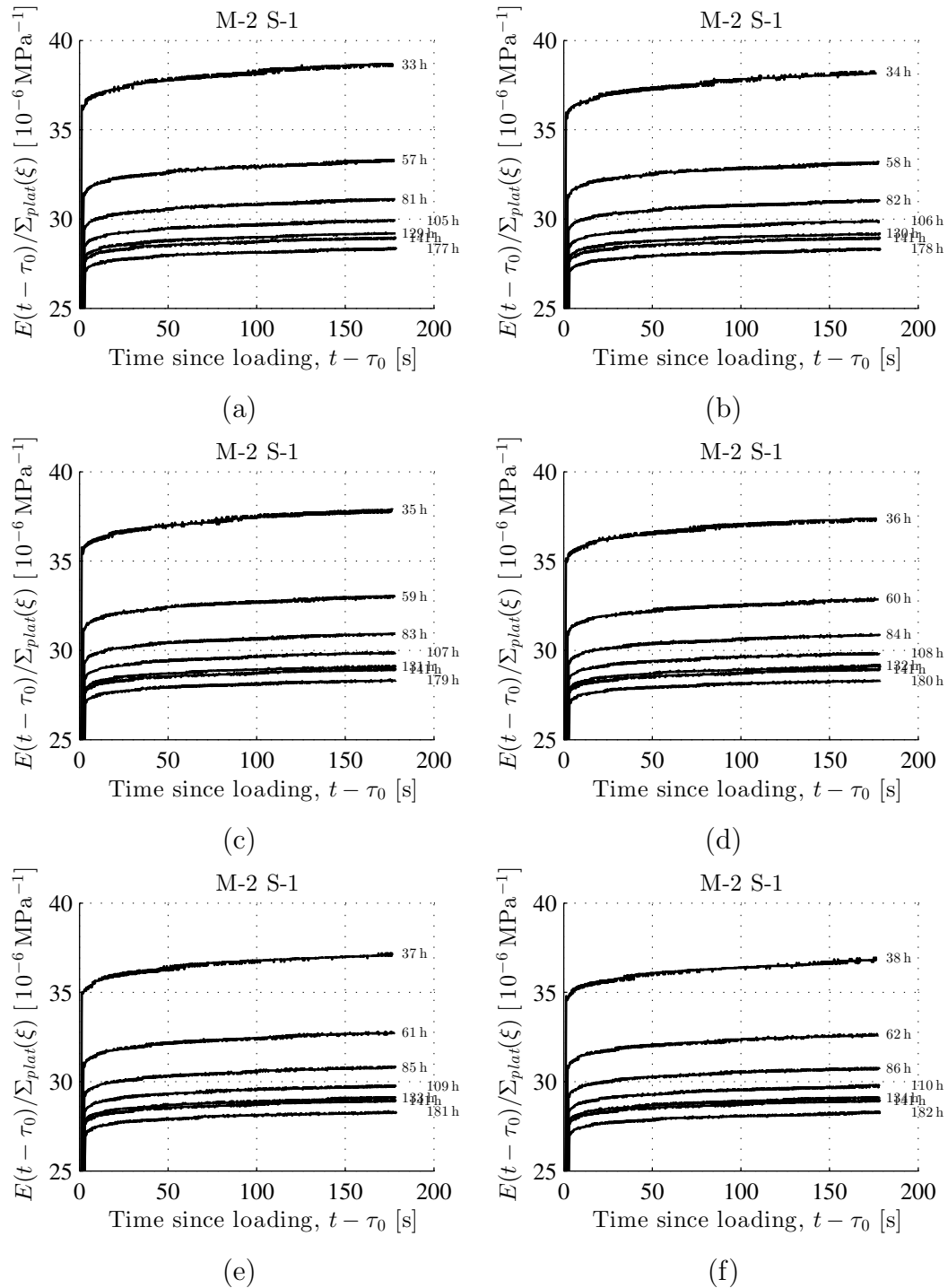


Figure 5.58: Measured strain evolution normalized with respect to the plateau stress as a function of the time since start of loading: mortar with $w/c = 0.45$, $a/c = 2.80$; ambient air temperature = $20\text{ }^{\circ}\text{C}$; ID = “M-2 S-1”, see Table 5.1; as for load levels, see Fig. 5.2

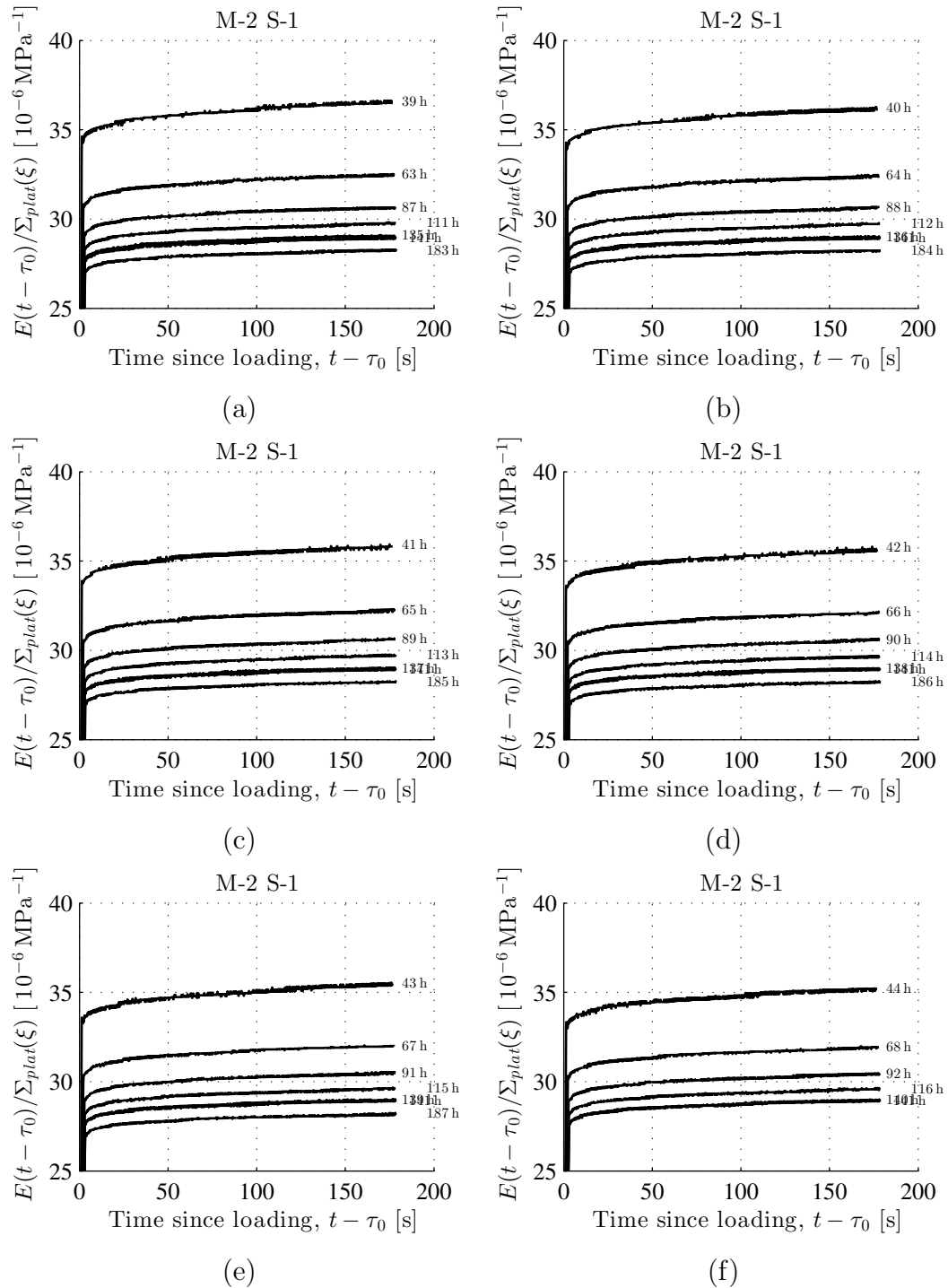


Figure 5.59: Measured strain evolution normalized with respect to the plateau stress as a function of the time since start of loading: mortar with $w/c = 0.45$, $a/c = 2.80$; ambient air temperature = 20°C ; ID = "M-2 S-1", see Table 5.1; as for load levels, see Fig. 5.2

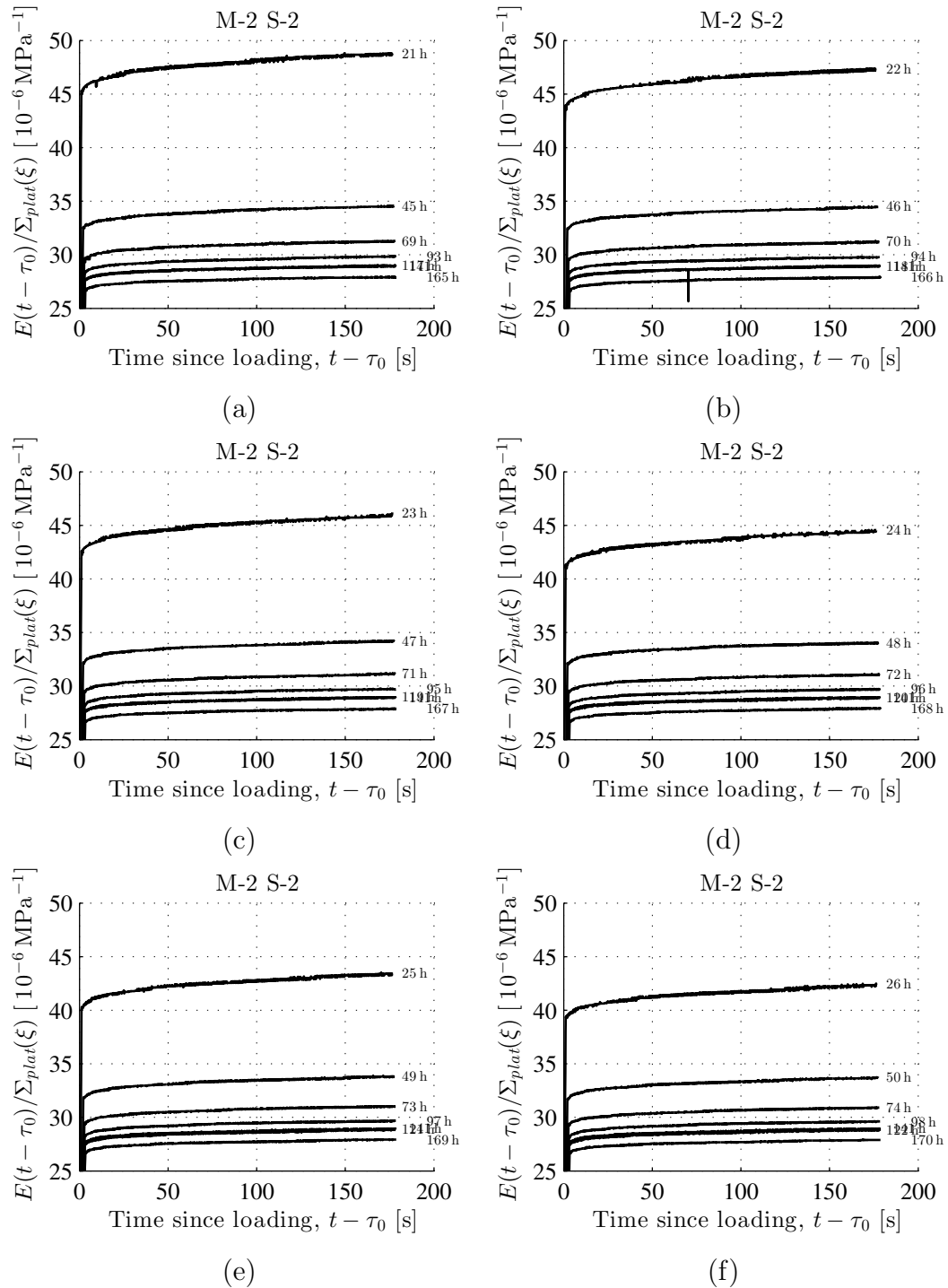


Figure 5.60: Measured strain evolution normalized with respect to the plateau stress as a function of the time since start of loading: mortar with $w/c = 0.45$, $a/c = 2.80$; ambient air temperature = 20°C ; ID = “M-2 S-2”, see Table 5.1; as for load levels, see Fig. 5.2

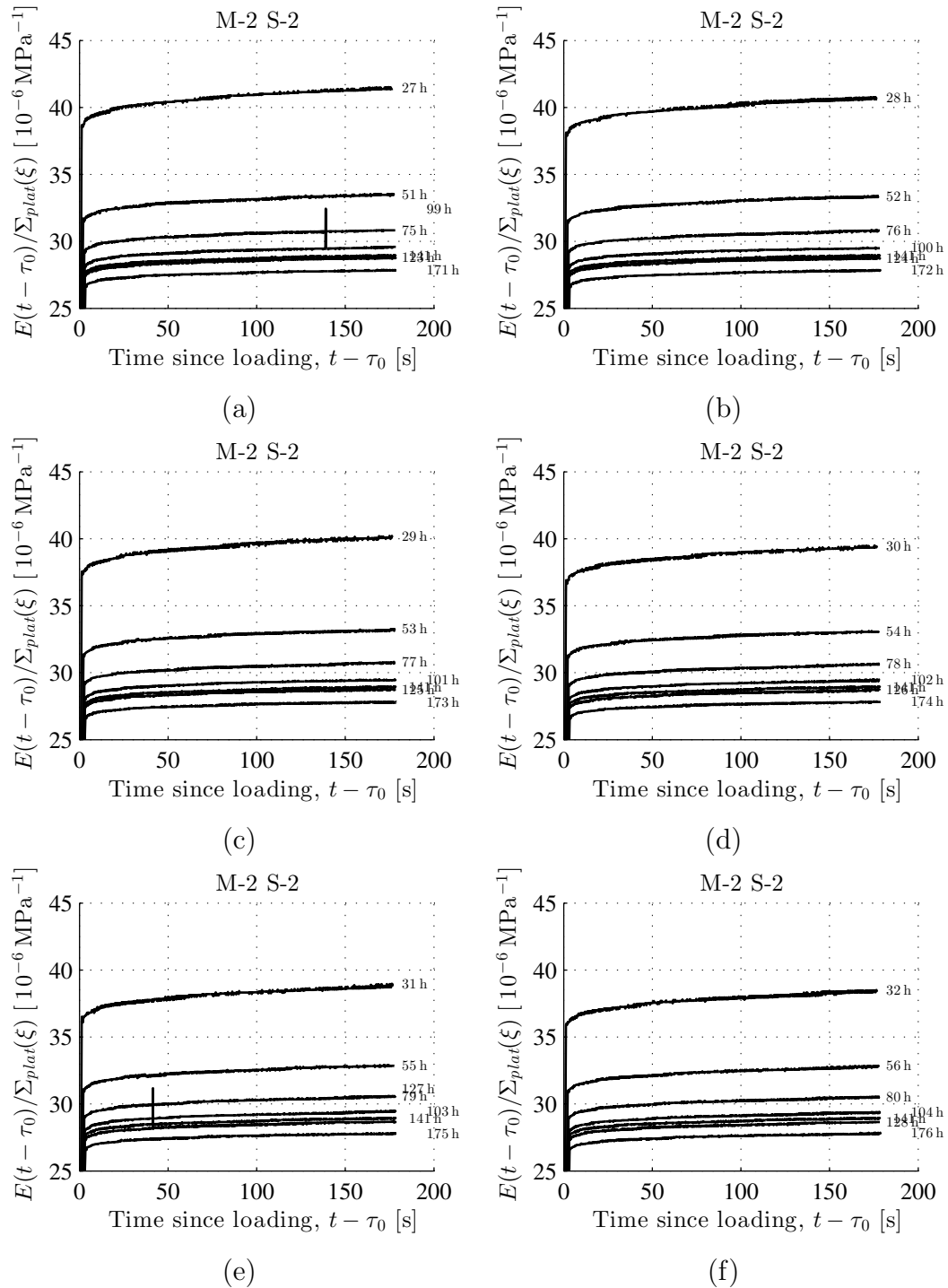


Figure 5.61: Measured strain evolution normalized with respect to the plateau stress as a function of the time since start of loading: mortar with $w/c = 0.45$, $a/c = 2.80$; ambient air temperature = 20°C ; ID = “M-2 S-2”, see Table 5.1; as for load levels, see Fig. 5.2

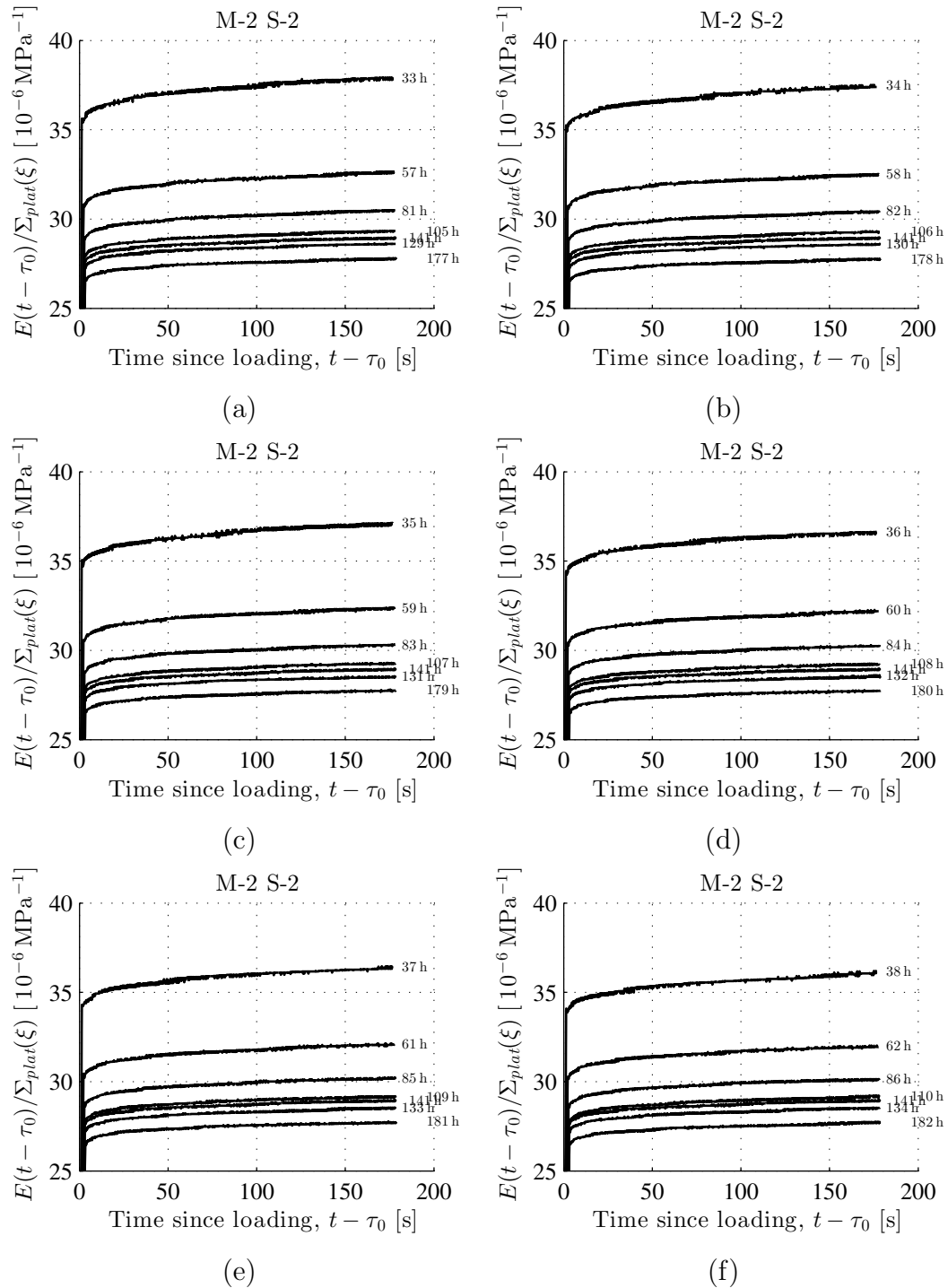


Figure 5.62: Measured strain evolution normalized with respect to the plateau stress as a function of the time since start of loading: mortar with $w/c = 0.45$, $a/c = 2.80$; ambient air temperature = 20°C ; ID = "M-2 S-2", see Table 5.1; as for load levels, see Fig. 5.2

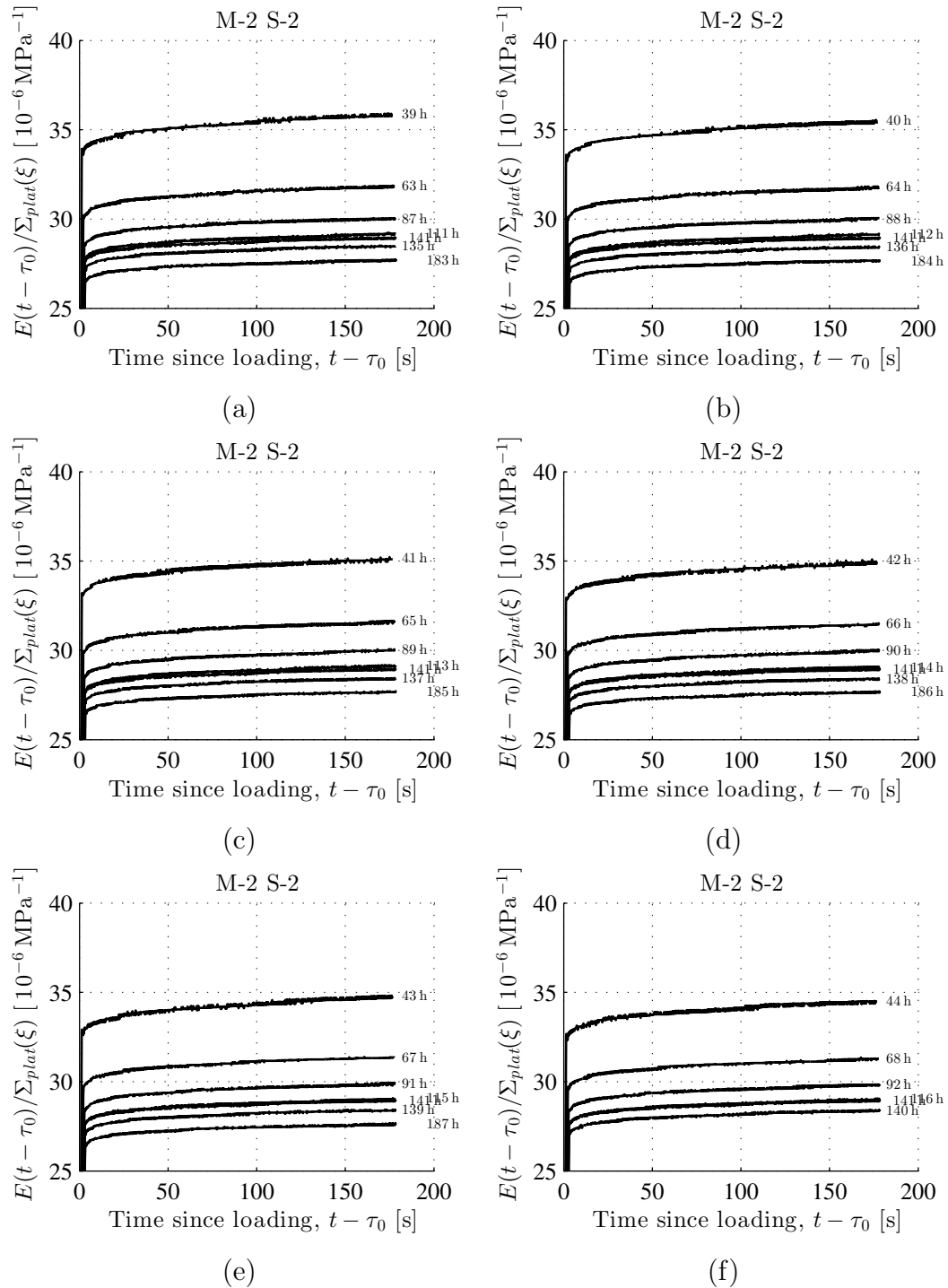


Figure 5.63: Measured strain evolution normalized with respect to the plateau stress as a function of the time since start of loading: mortar with $w/c = 0.45$, $a/c = 2.80$; ambient air temperature = 20°C ; ID = “M-2 S-2”, see Table 5.1; as for load levels, see Fig. 5.2

5.3.3 Mortar: $w/c = 0.50$, $a/c = 3.0$

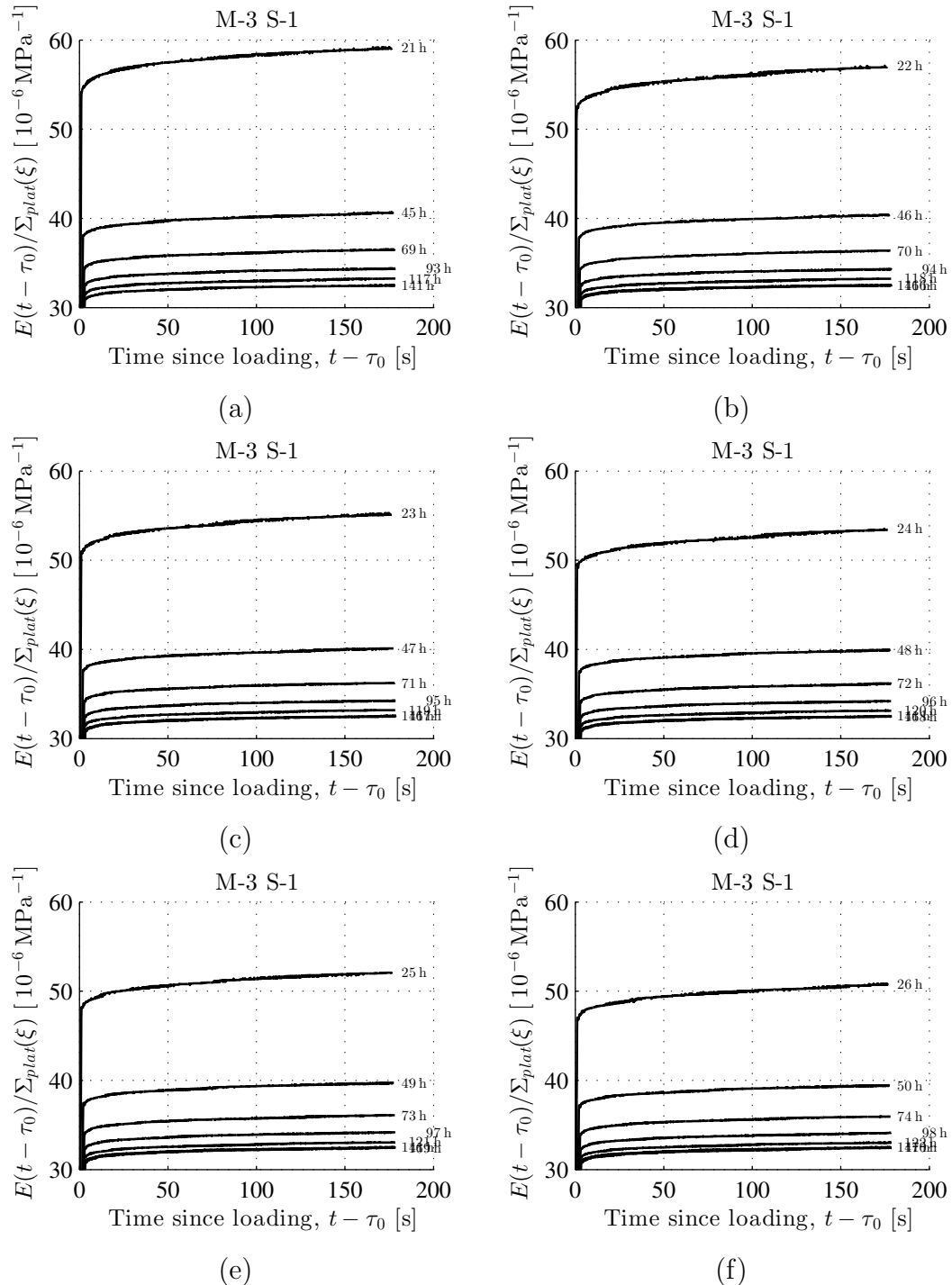


Figure 5.64: Measured strain evolution normalized with respect to the plateau stress as a function of the time since start of loading: mortar with $w/c = 0.50$, $a/c = 3.0$; ambient air temperature = 20°C ; ID = “M-3 S-1”, see Table 5.1; as for load levels, see Fig. 5.2

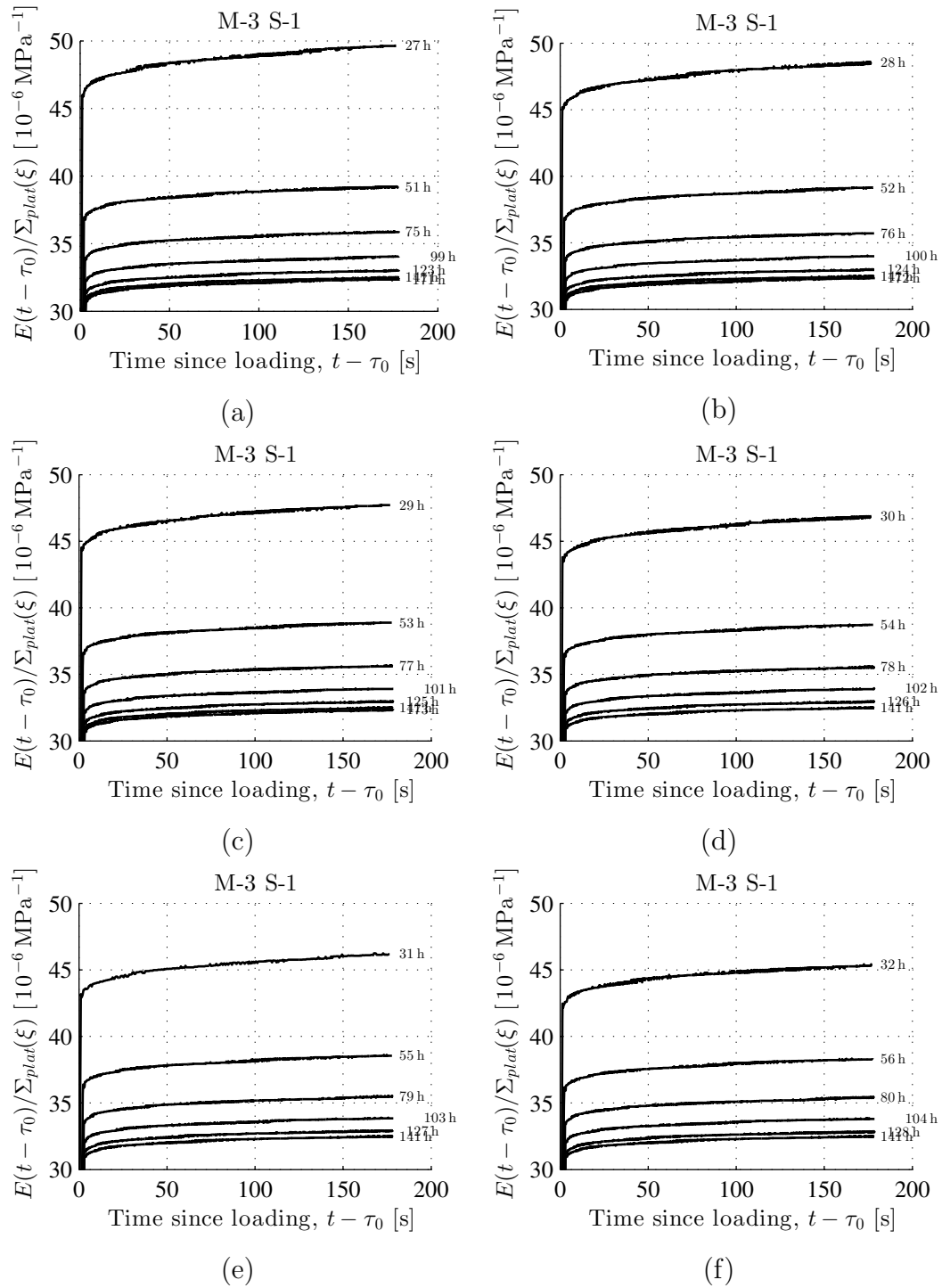


Figure 5.65: Measured strain evolution normalized with respect to the plateau stress as a function of the time since start of loading: mortar with $w/c = 0.50$, $a/c = 3.0$; ambient air temperature = $20\text{ }^{\circ}\text{C}$; ID = “M-3 S-1”, see Table 5.1; as for load levels, see Fig. 5.2

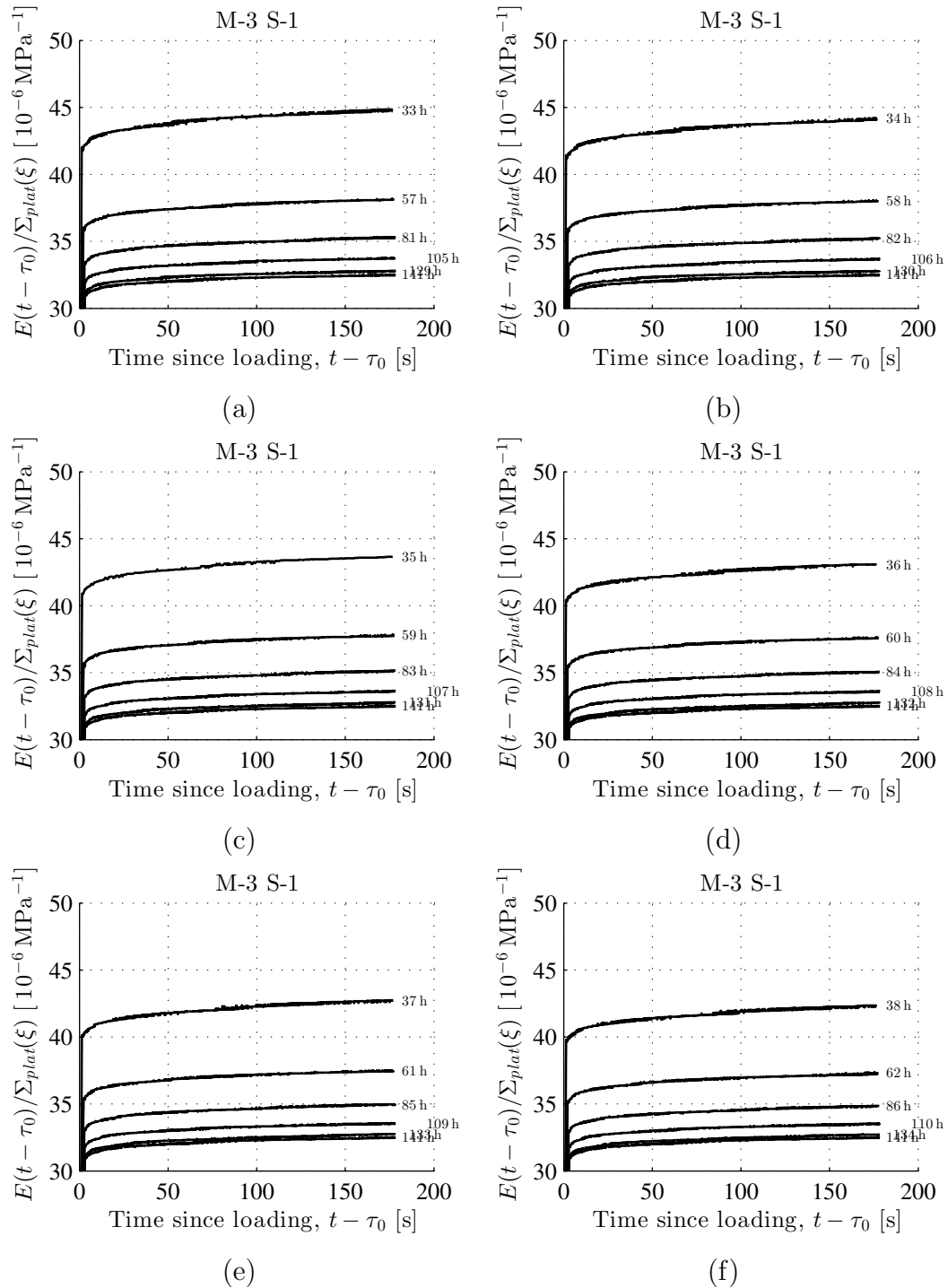


Figure 5.66: Measured strain evolution normalized with respect to the plateau stress as a function of the time since start of loading: mortar with $w/c = 0.50$, $a/c = 3.0$; ambient air temperature = 20°C ; ID = “M-3 S-1”, see Table 5.1; as for load levels, see Fig. 5.2

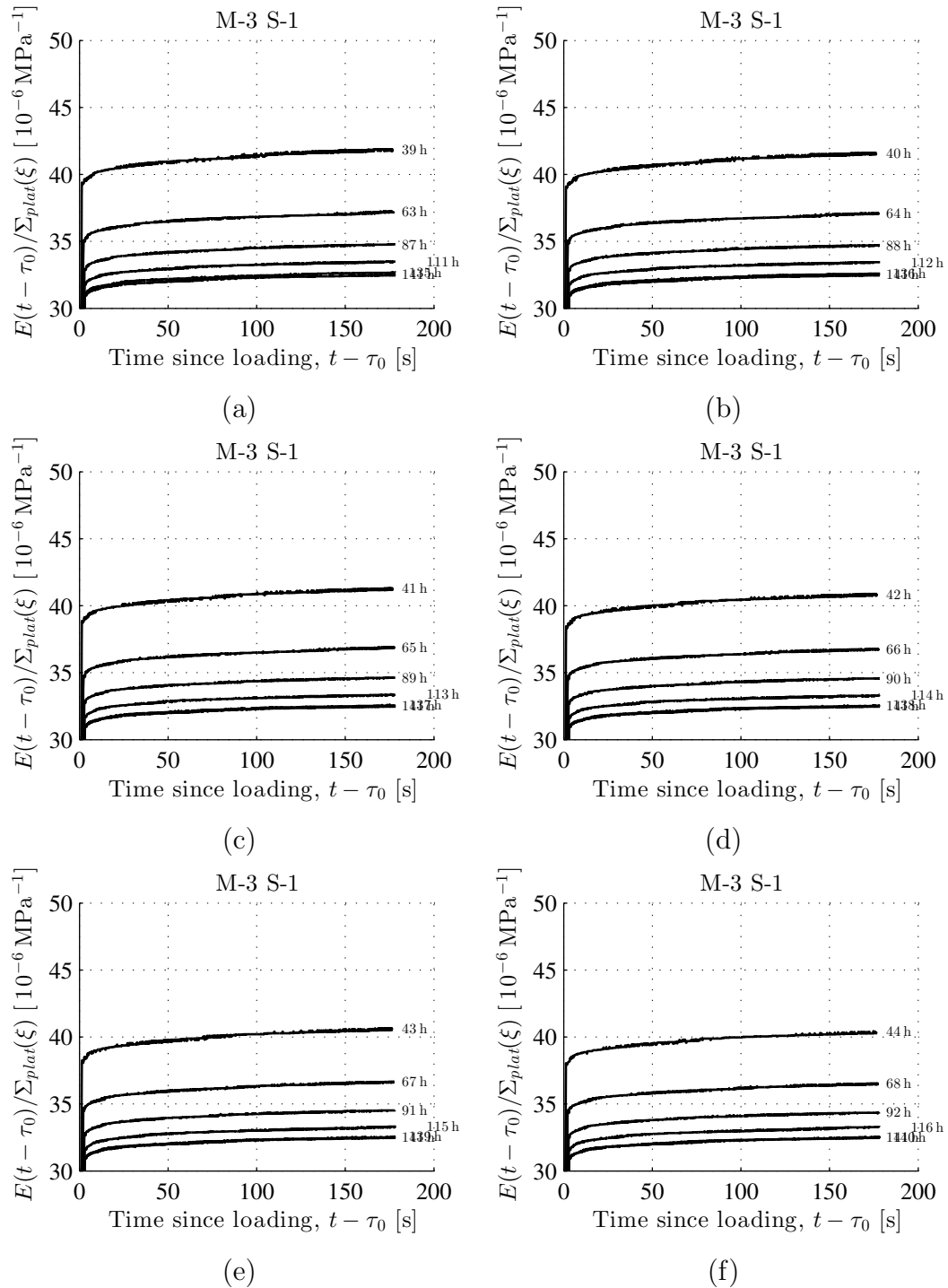


Figure 5.67: Measured strain evolution normalized with respect to the plateau stress as a function of the time since start of loading: mortar with $w/c = 0.50$, $a/c = 3.0$; ambient air temperature = 20°C ; ID = “M-3 S-1”, see Table 5.1; as for load levels, see Fig. 5.2

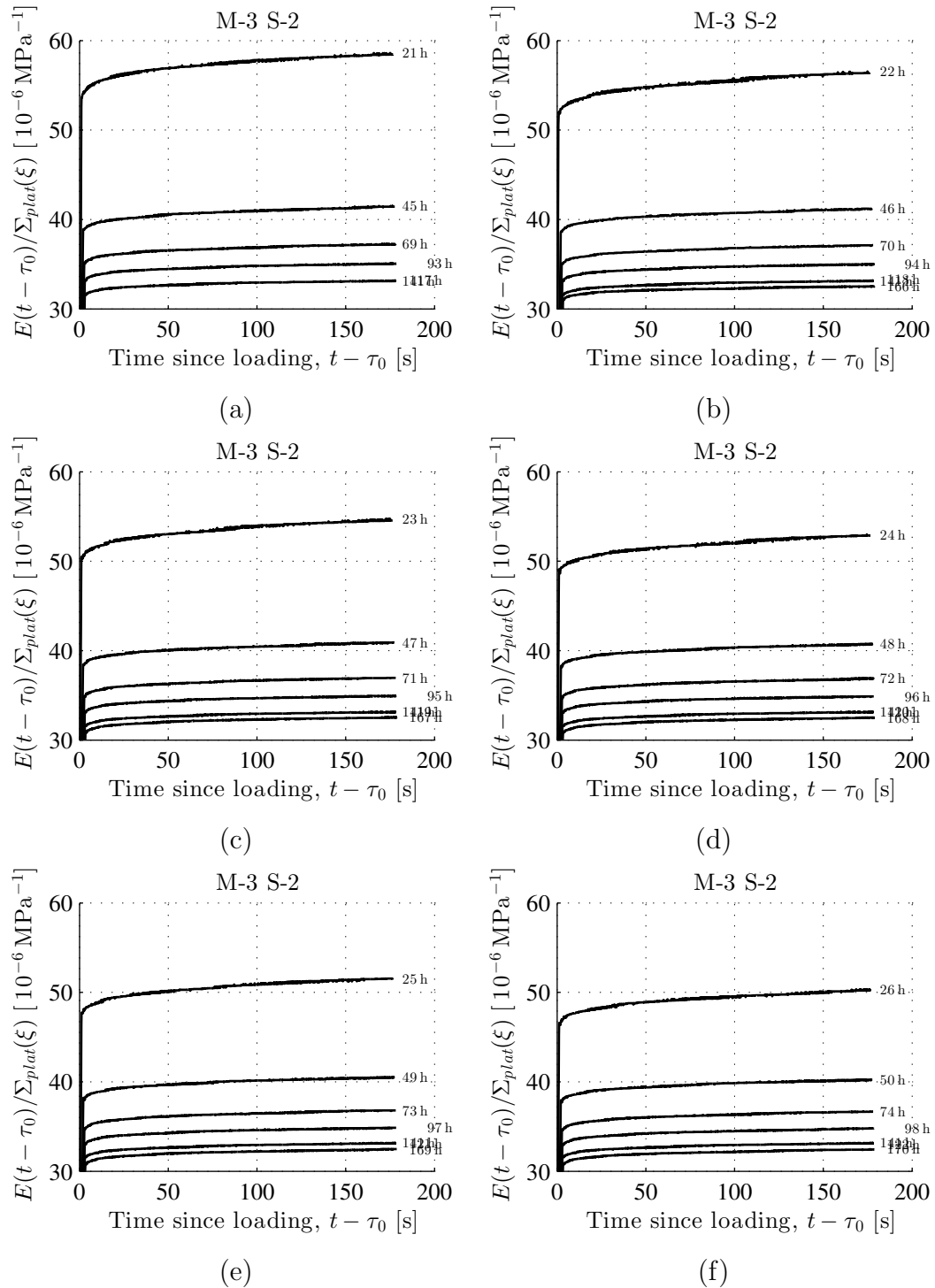


Figure 5.68: Measured strain evolution normalized with respect to the plateau stress as a function of the time since start of loading: mortar with $w/c = 0.50$, $a/c = 3.0$; ambient air temperature = 20°C ; ID = “M-3 S-2”, see Table 5.1; as for load levels, see Fig. 5.2

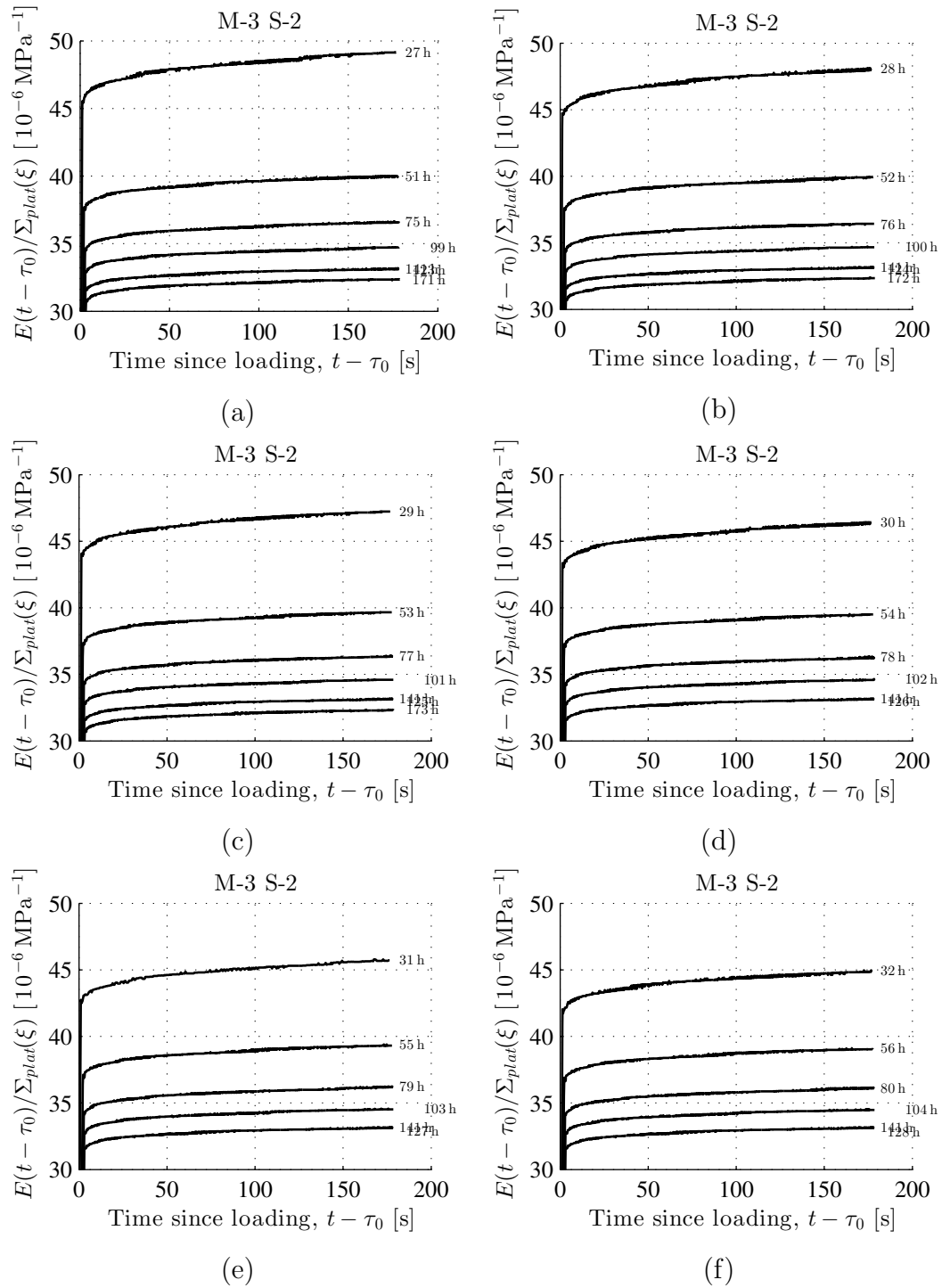


Figure 5.69: Measured strain evolution normalized with respect to the plateau stress as a function of the time since start of loading: mortar with $w/c = 0.50$, $a/c = 3.0$; ambient air temperature = 20°C ; ID = “M-3 S-2”, see Table 5.1; as for load levels, see Fig. 5.2

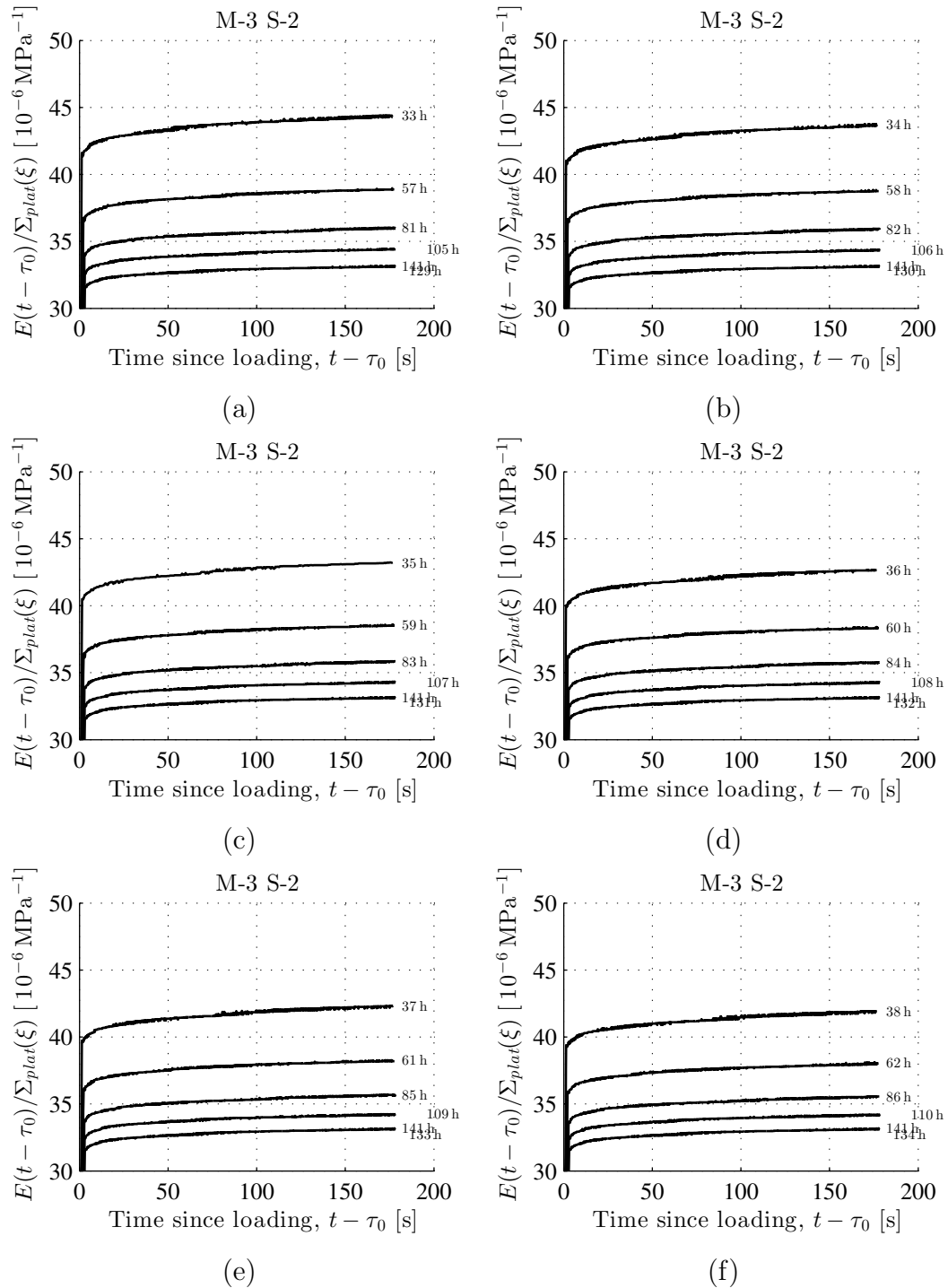


Figure 5.70: Measured strain evolution normalized with respect to the plateau stress as a function of the time since start of loading: mortar with $w/c = 0.50$, $a/c = 3.0$; ambient air temperature = 20°C ; ID = “M-3 S-2”, see Table 5.1; as for load levels, see Fig. 5.2

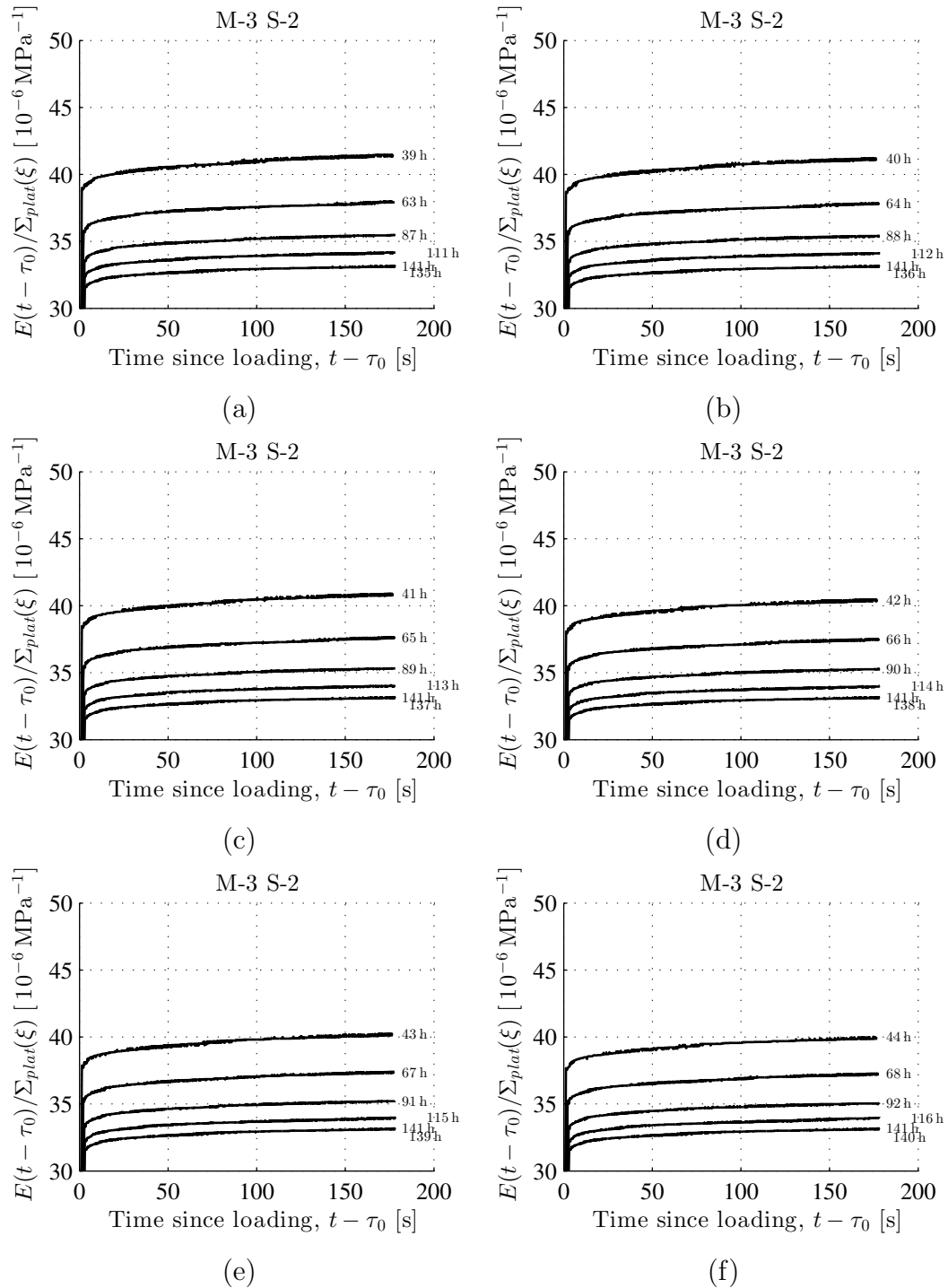


Figure 5.71: Measured strain evolution normalized with respect to the plateau stress as a function of the time since start of loading: mortar with $w/c = 0.50$, $a/c = 3.0$; ambient air temperature = 20°C ; ID = "M-3 S-2", see Table 5.1; as for load levels, see Fig. 5.2

5.3.4 Mortar: $w/c = 0.42$, $a/c = 1.35$

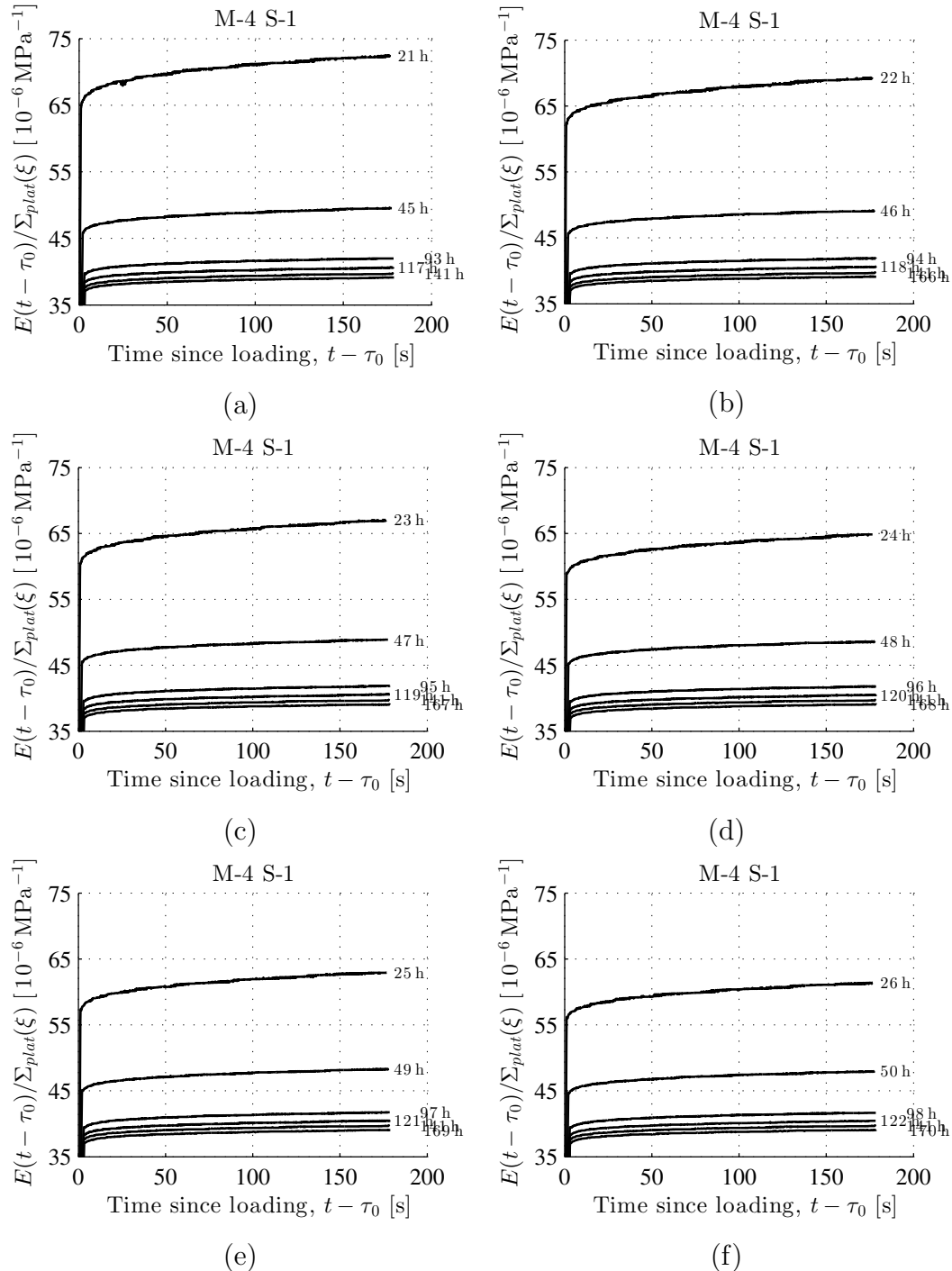


Figure 5.72: Measured strain evolution normalized with respect to the plateau stress as a function of the time since start of loading: mortar with $w/c = 0.42$, $a/c = 1.35$; ambient air temperature = 20°C ; ID = “M-4 S-1”, see Table 5.1; as for load levels, see Fig. 5.2

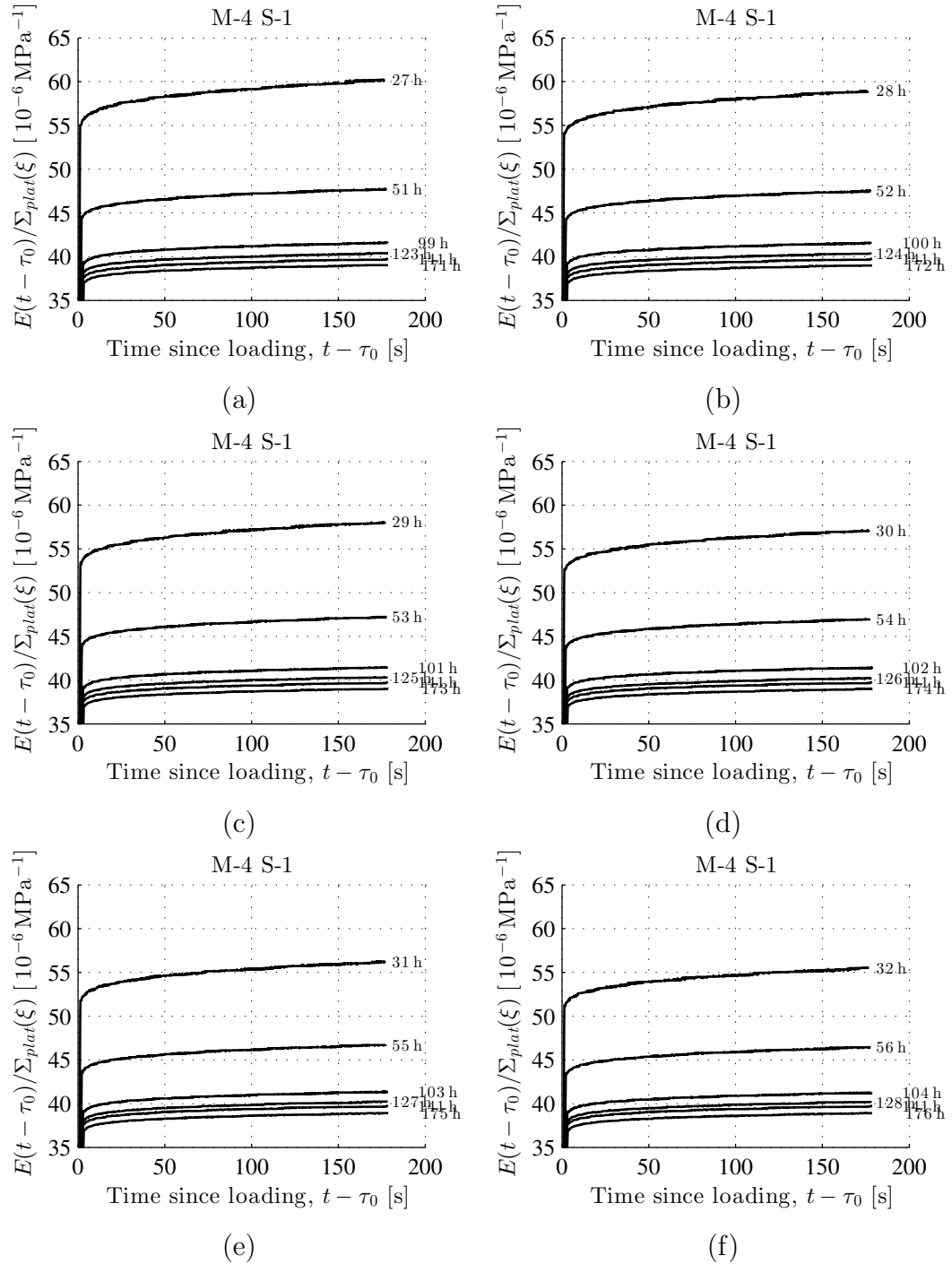


Figure 5.73: Measured strain evolution normalized with respect to the plateau stress as a function of the time since start of loading: mortar with $w/c = 0.42$, $a/c = 1.35$; ambient air temperature = $20\text{ }^{\circ}\text{C}$; ID = "M-4 S-1", see Table 5.1; as for load levels, see Fig. 5.2

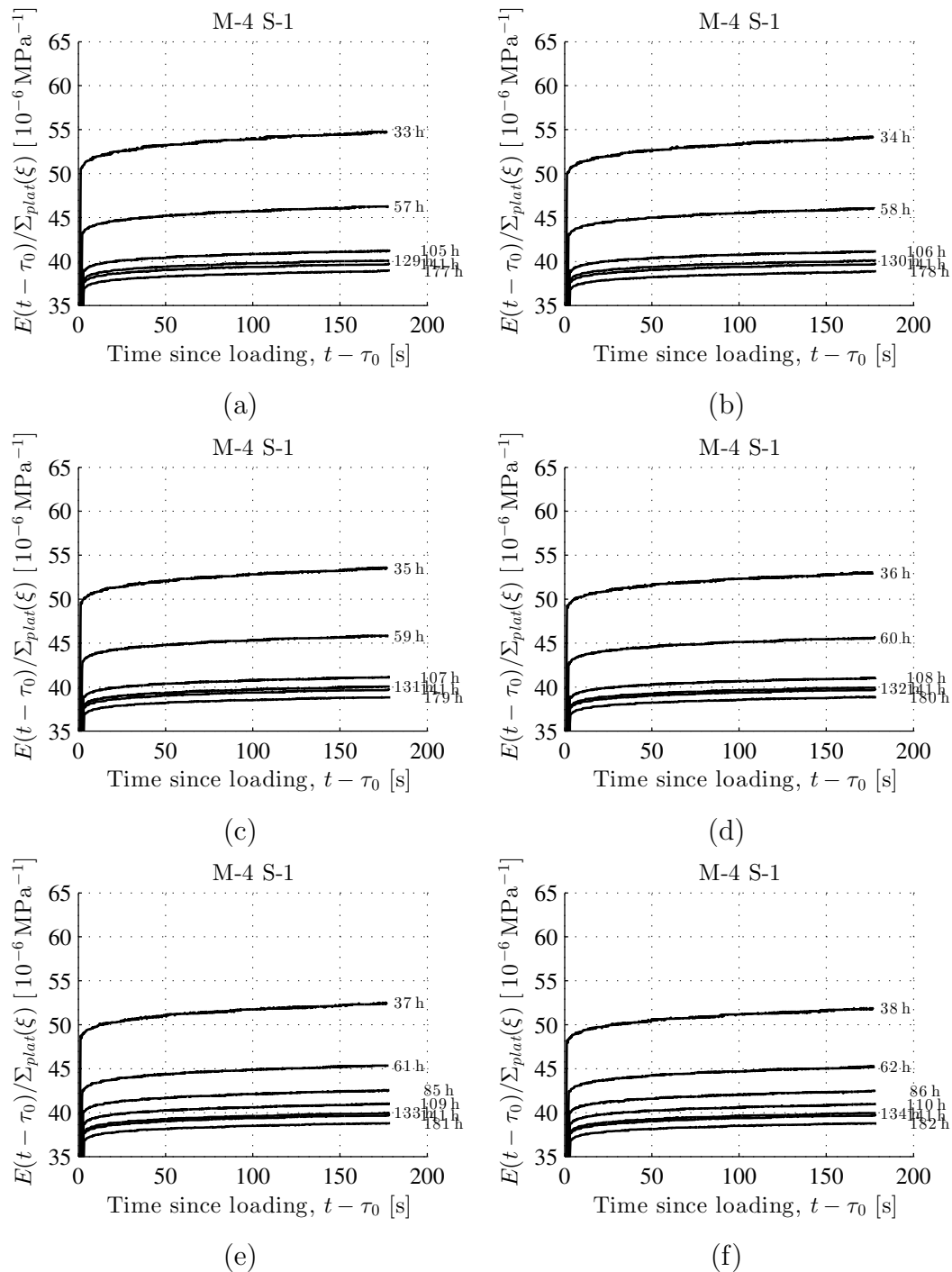


Figure 5.74: Measured strain evolution normalized with respect to the plateau stress as a function of the time since start of loading: mortar with $w/c = 0.42$, $a/c = 1.35$; ambient air temperature = $20\text{ }^{\circ}\text{C}$; ID = “M-4 S-1”, see Table 5.1; as for load levels, see Fig. 5.2

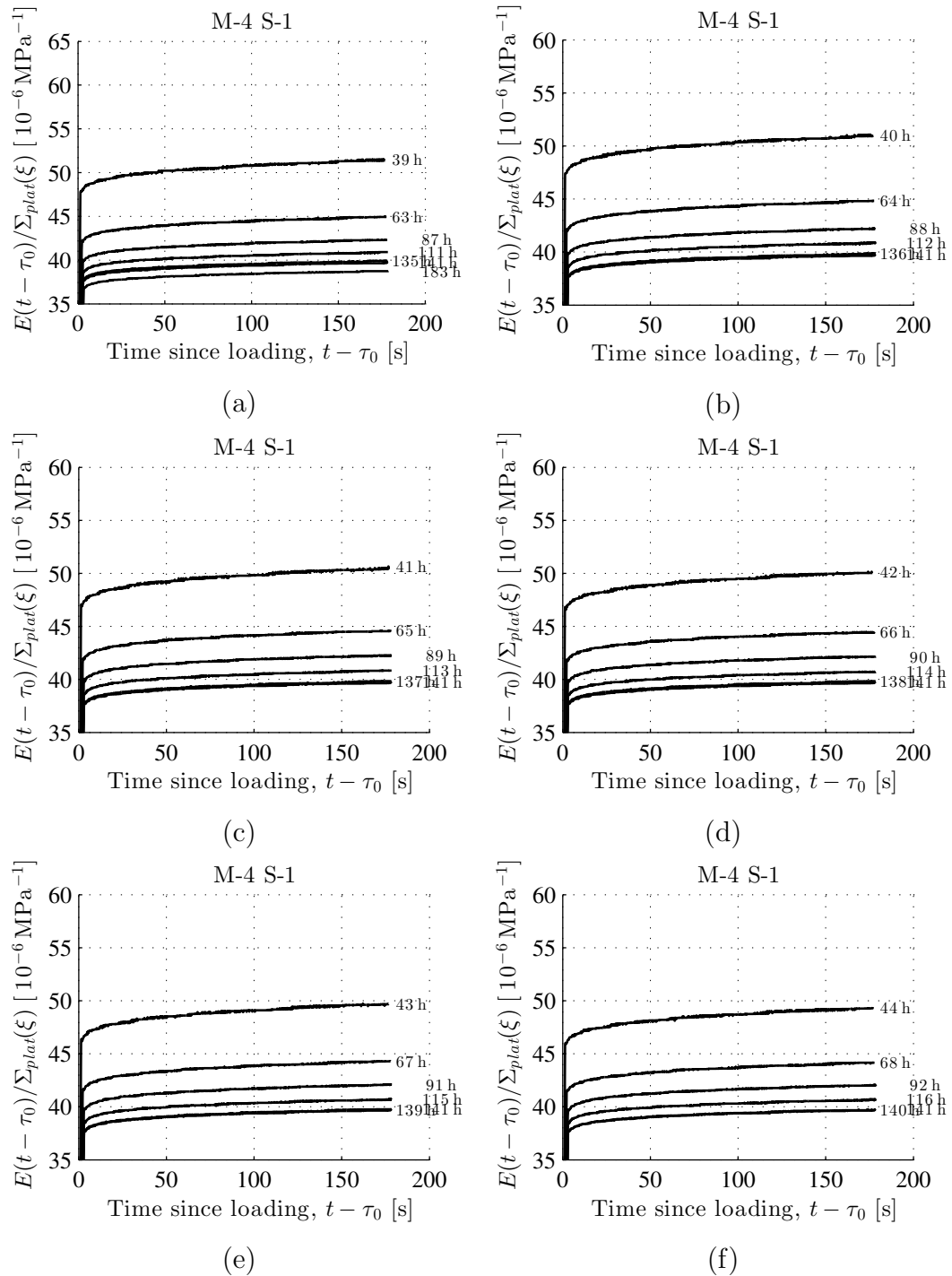


Figure 5.75: Measured strain evolution normalized with respect to the plateau stress as a function of the time since start of loading: mortar with $w/c = 0.42$, $a/c = 1.35$; ambient air temperature = $20\text{ }^{\circ}\text{C}$; ID = "M-4 S-1", see Table 5.1; as for load levels, see Fig. 5.2

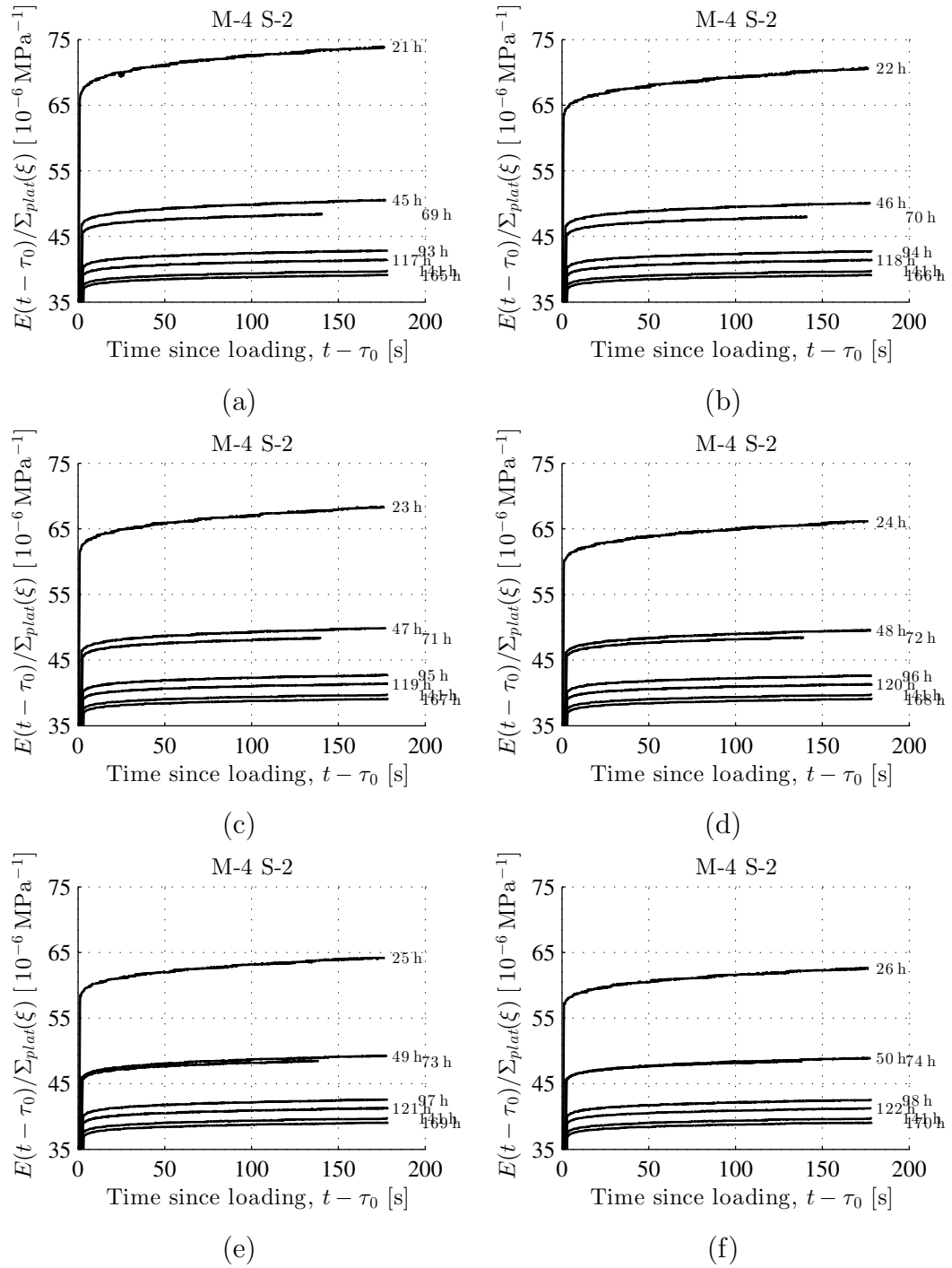


Figure 5.76: Measured strain evolution normalized with respect to the plateau stress as a function of the time since start of loading: mortar with $w/c = 0.42$, $a/c = 1.35$; ambient air temperature = 20°C ; ID = "M-4 S-2", see Table 5.1; as for load levels, see Fig. 5.2

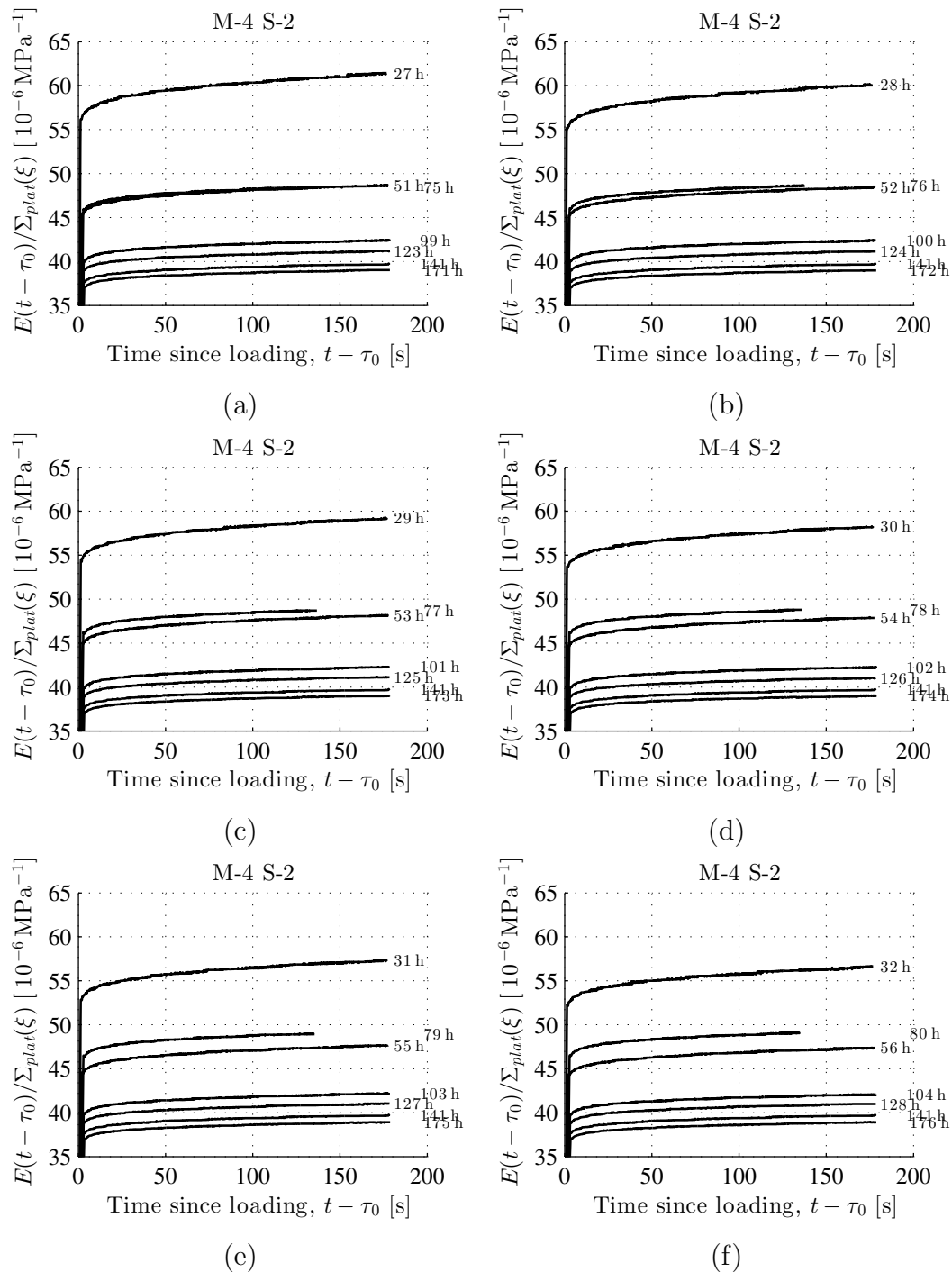


Figure 5.77: Measured strain evolution normalized with respect to the plateau stress as a function of the time since start of loading: mortar with $w/c = 0.42$, $a/c = 1.35$; ambient air temperature = 20°C ; ID = "M-4 S-2", see Table 5.1; as for load levels, see Fig. 5.2

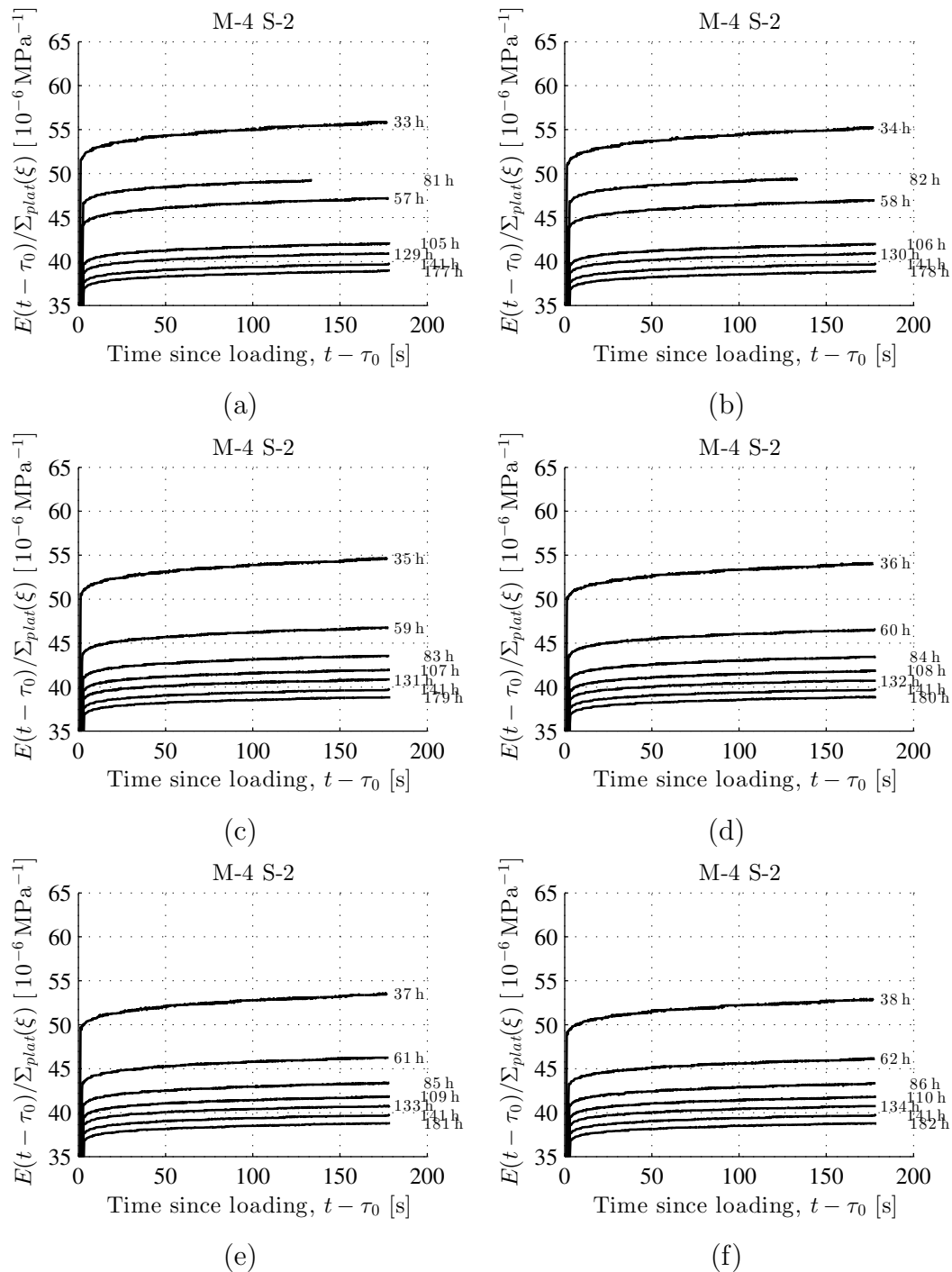


Figure 5.78: Measured strain evolution normalized with respect to the plateau stress as a function of the time since start of loading: mortar with $w/c = 0.42$, $a/c = 1.35$; ambient air temperature = 20°C ; ID = "M-4 S-2", see Table 5.1; as for load levels, see Fig. 5.2

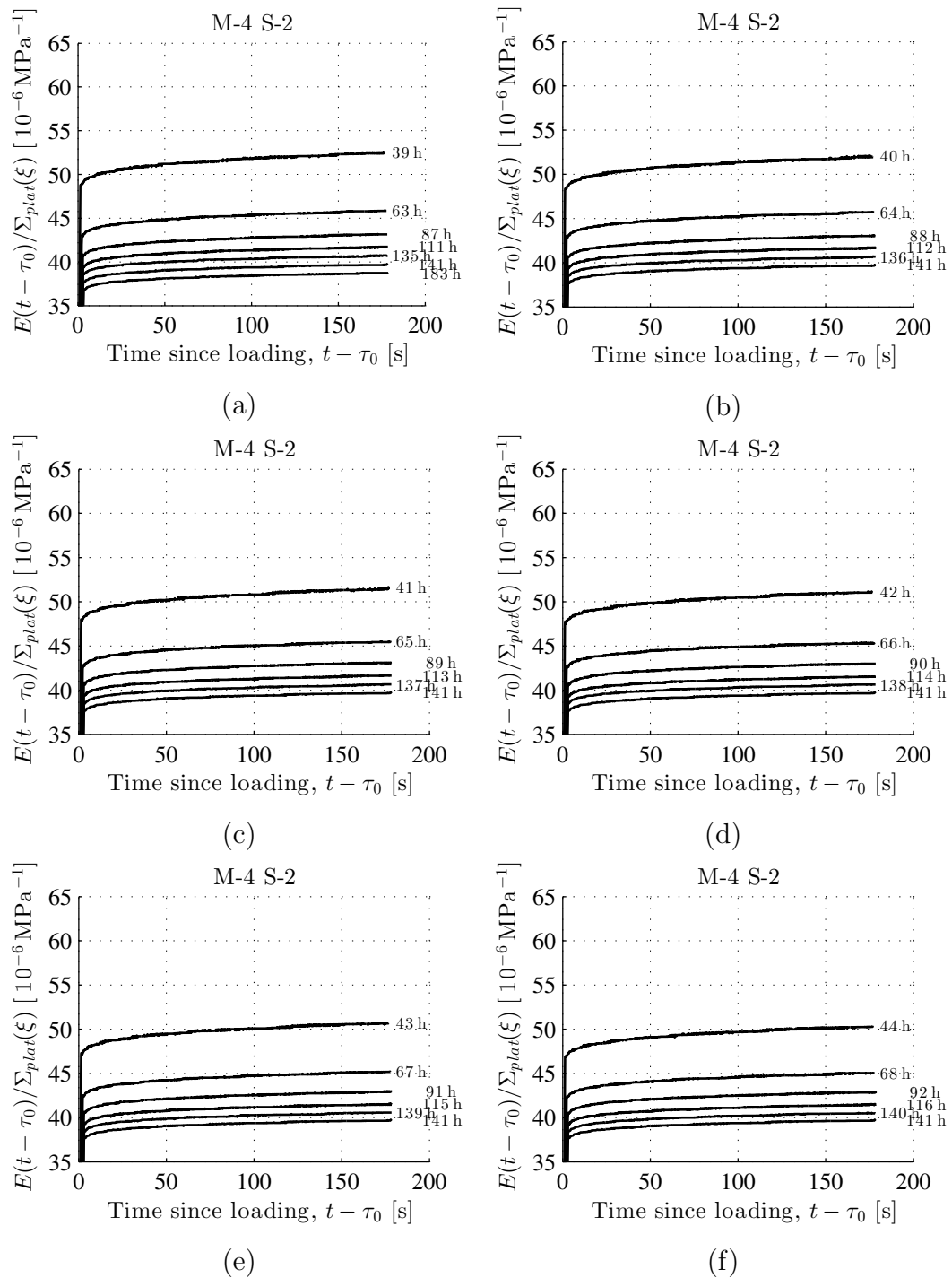


Figure 5.79: Measured strain evolution normalized with respect to the plateau stress as a function of the time since start of loading: mortar with $w/c = 0.42$, $a/c = 1.35$; ambient air temperature = $20\text{ }^{\circ}\text{C}$; ID = “M-4 S-2”, see Table 5.1; as for load levels, see Fig. 5.2

5.3.5 Mortar: $w/c = 0.50$, $a/c = 1.50$

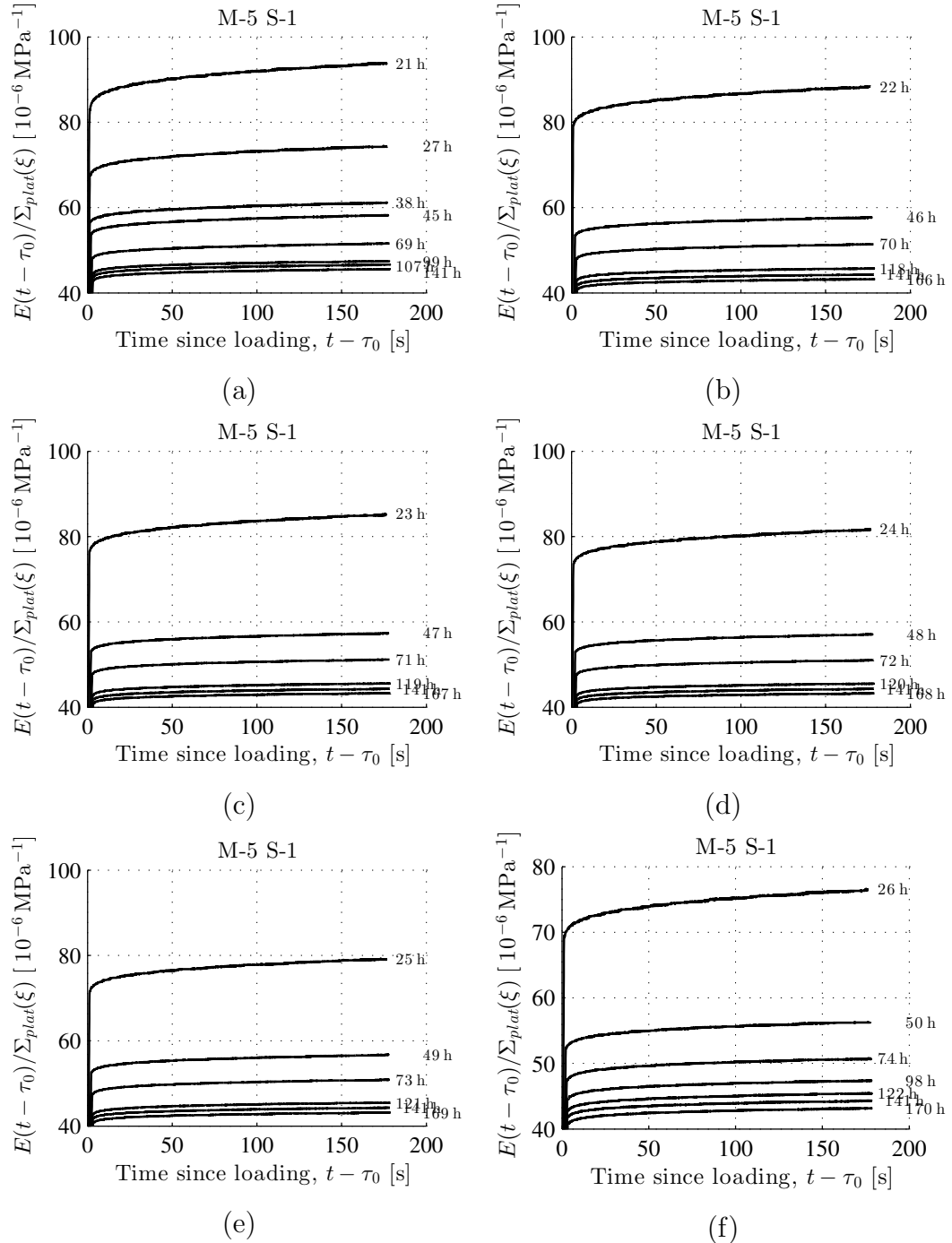


Figure 5.80: Measured strain evolution normalized with respect to the plateau stress as a function of the time since start of loading: mortar with $w/c = 0.50$, $a/c = 1.50$; ambient air temperature = 20°C ; ID = “M-5 S-1”, see Table 5.1; as for load levels, see Fig. 5.2

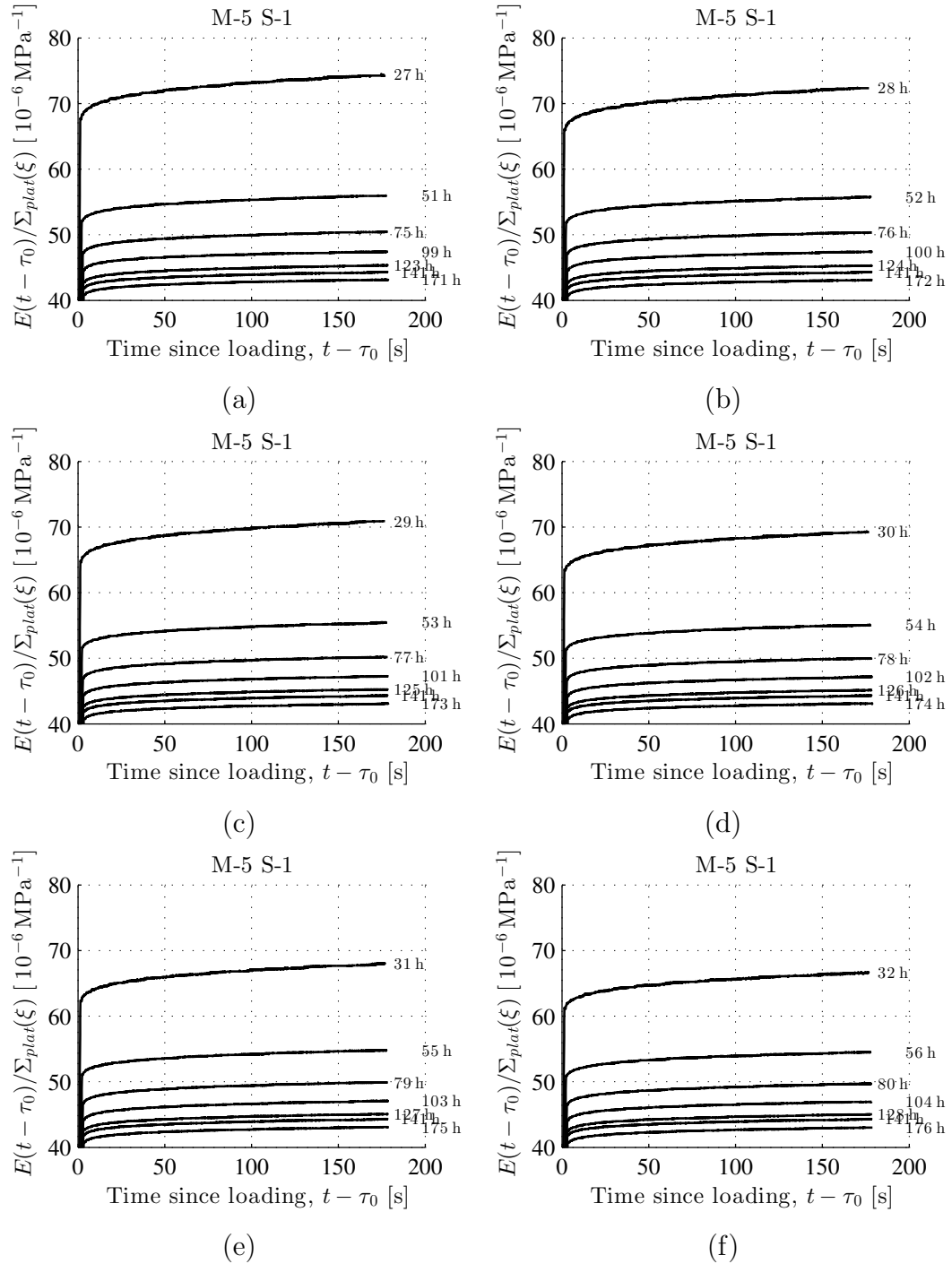


Figure 5.81: Measured strain evolution normalized with respect to the plateau stress as a function of the time since start of loading: mortar with $w/c = 0.50$, $a/c = 1.50$; ambient air temperature = 20°C ; ID = "M-5 S-1", see Table 5.1; as for load levels, see Fig. 5.2

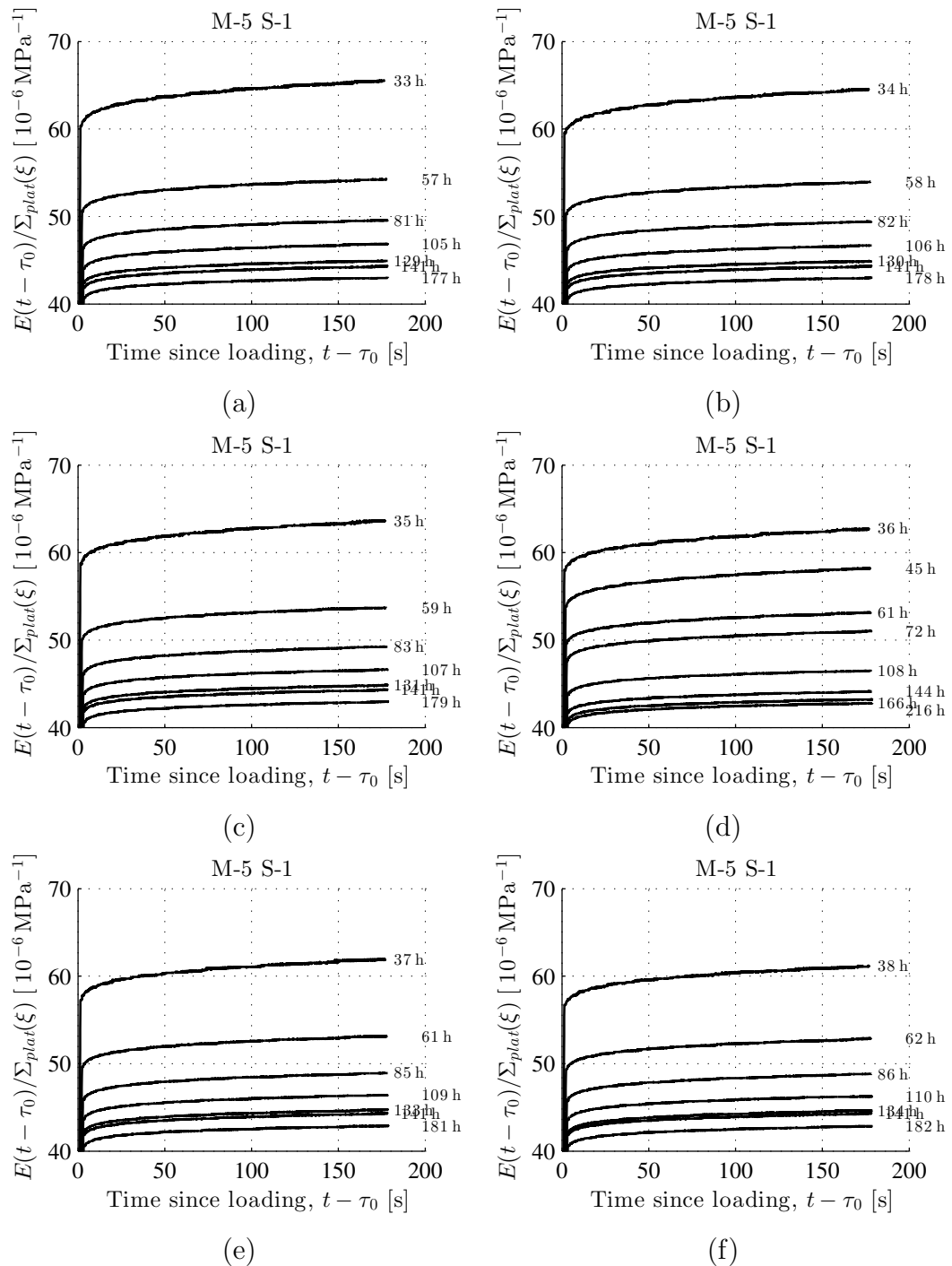


Figure 5.82: Measured strain evolution normalized with respect to the plateau stress as a function of the time since start of loading: mortar with $w/c = 0.50$, $a/c = 1.50$; ambient air temperature = 20°C ; ID = "M-5 S-1", see Table 5.1; as for load levels, see Fig. 5.2

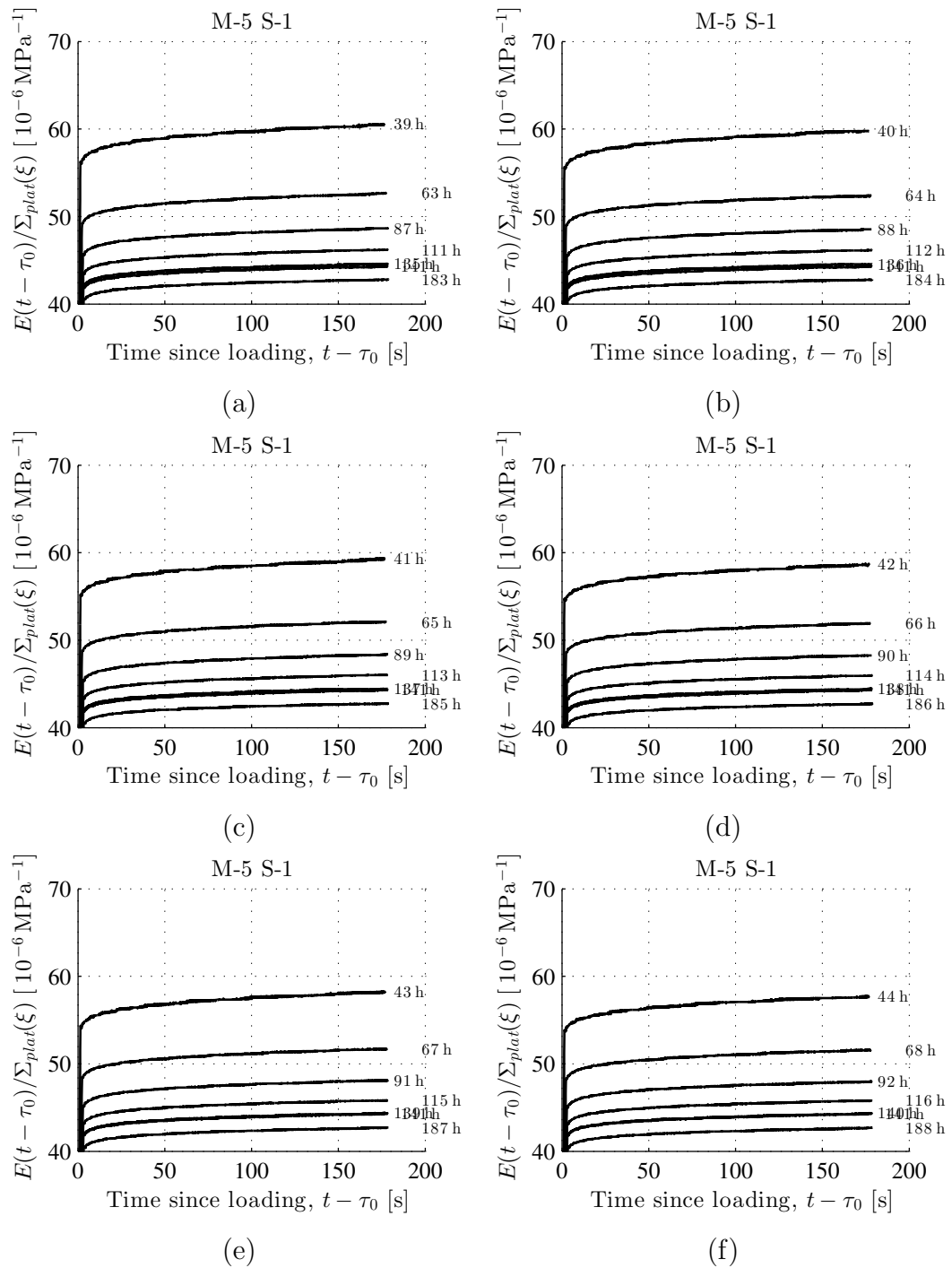


Figure 5.83: Measured strain evolution normalized with respect to the plateau stress as a function of the time since start of loading: mortar with $w/c = 0.50$, $a/c = 1.50$; ambient air temperature = 20°C ; ID = "M-5 S-1", see Table 5.1; as for load levels, see Fig. 5.2

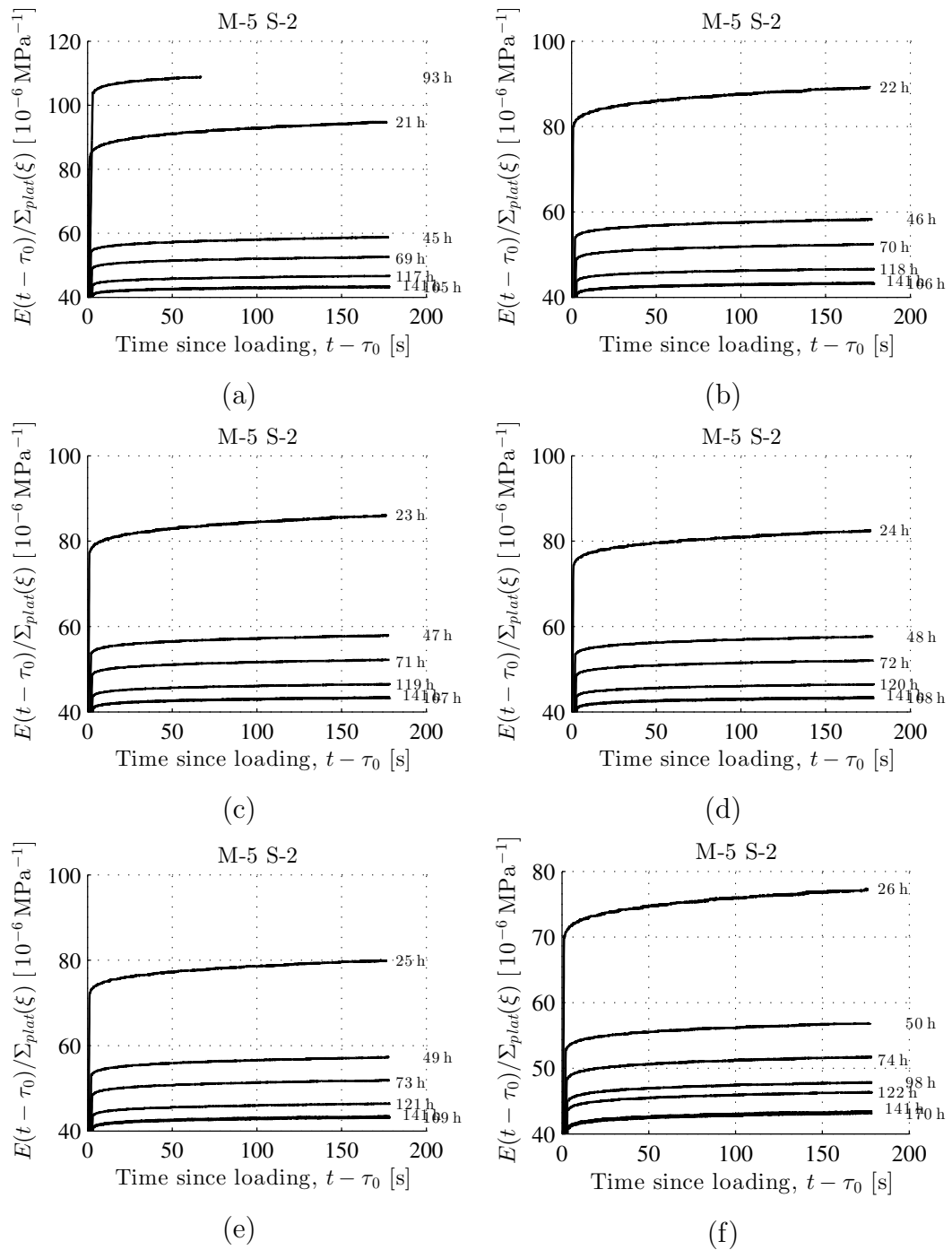


Figure 5.84: Measured strain evolution normalized with respect to the plateau stress as a function of the time since start of loading: mortar with $w/c = 0.50$, $a/c = 1.50$; ambient air temperature = $20\text{ }^{\circ}\text{C}$; ID = “M-5 S-2”, see Table 5.1; as for load levels, see Fig. 5.2

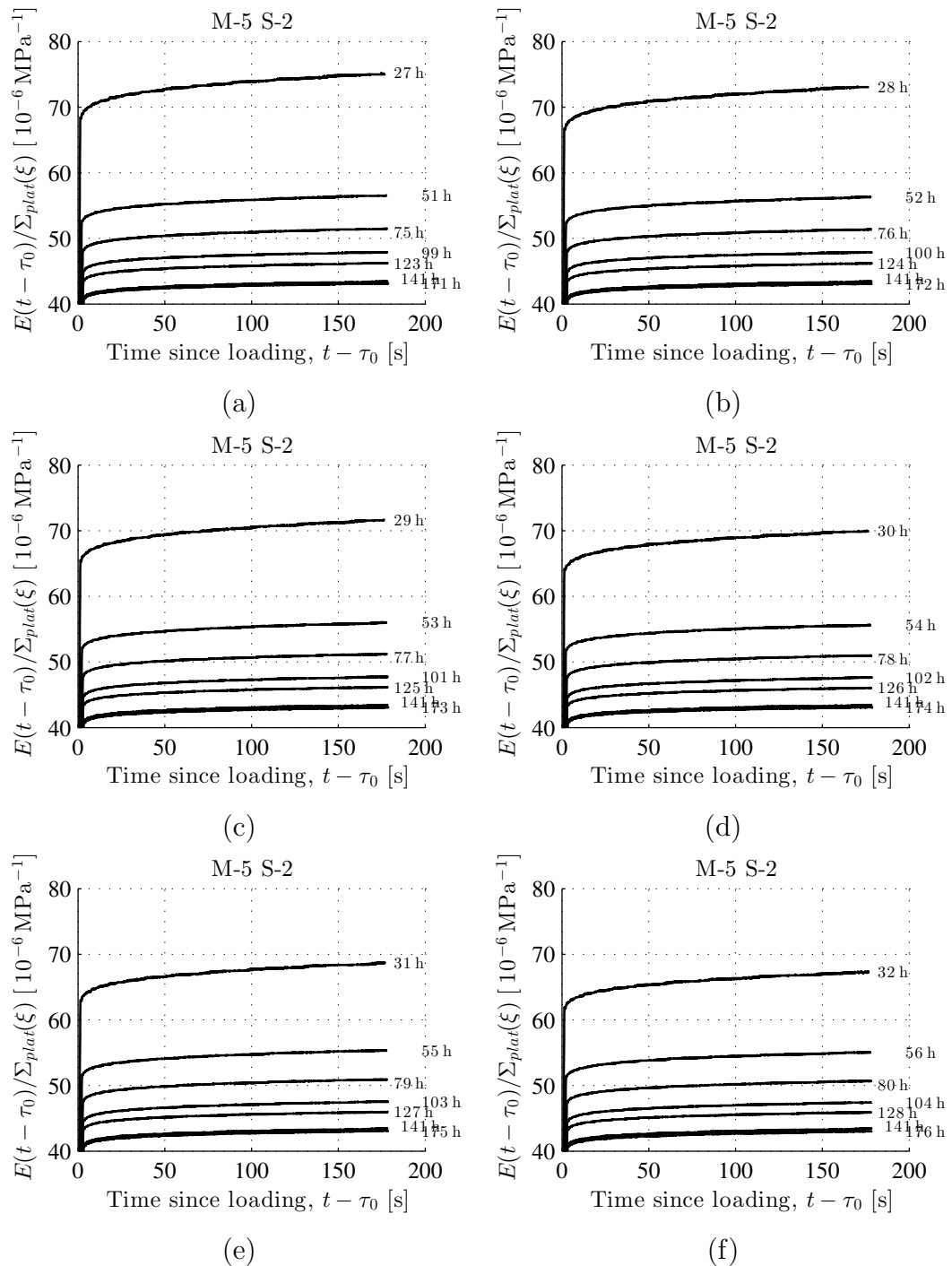


Figure 5.85: Measured strain evolution normalized with respect to the plateau stress as a function of the time since start of loading: mortar with $w/c = 0.50$, $a/c = 1.50$; ambient air temperature = $20\text{ }^{\circ}\text{C}$; ID = "M-5 S-2", see Table 5.1; as for load levels, see Fig. 5.2

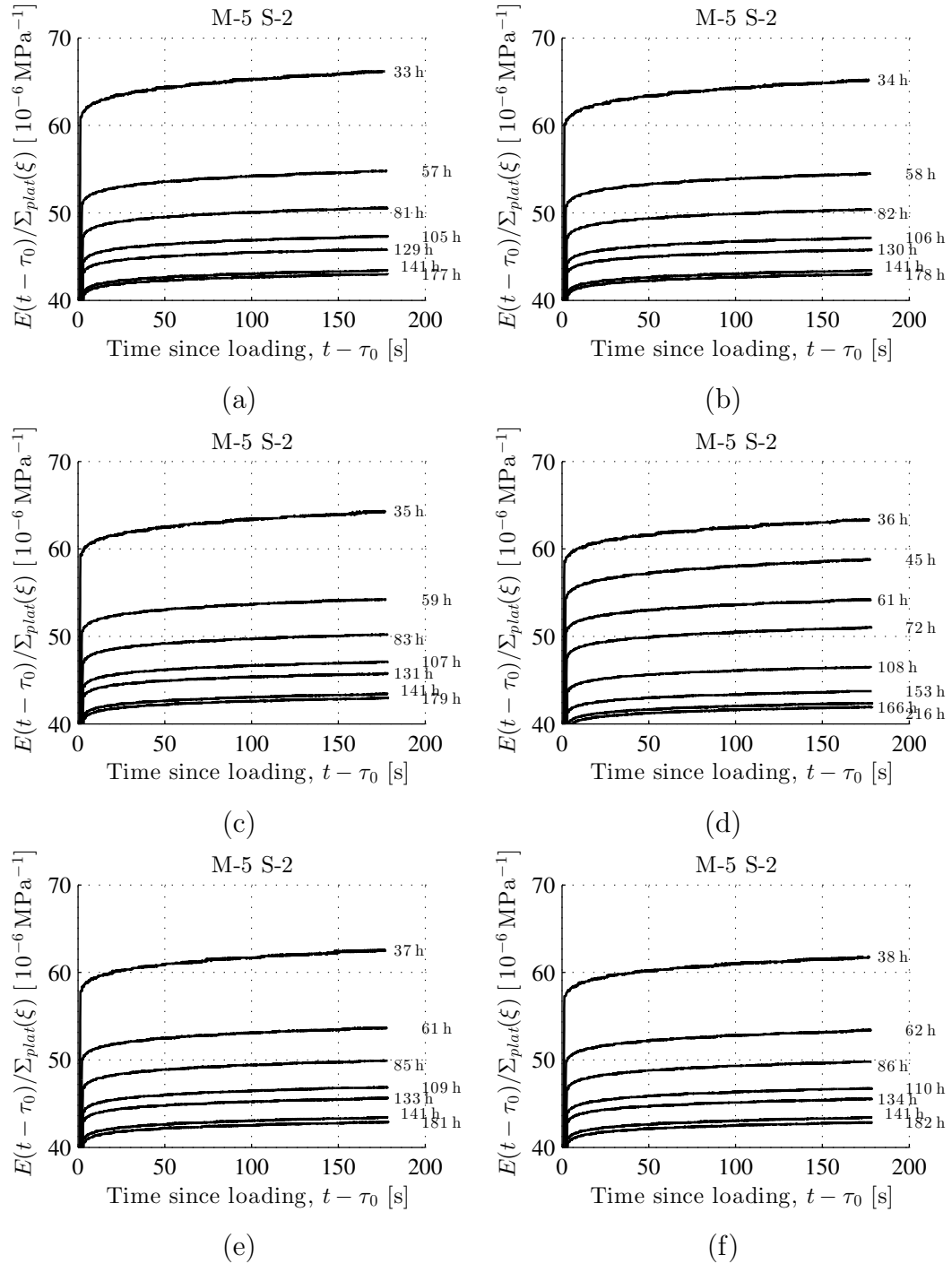


Figure 5.86: Measured strain evolution normalized with respect to the plateau stress as a function of the time since start of loading: mortar with $w/c = 0.50$, $a/c = 1.50$; ambient air temperature = $20\text{ }^{\circ}\text{C}$; ID = “M-5 S-2”, see Table 5.1; as for load levels, see Fig. 5.2

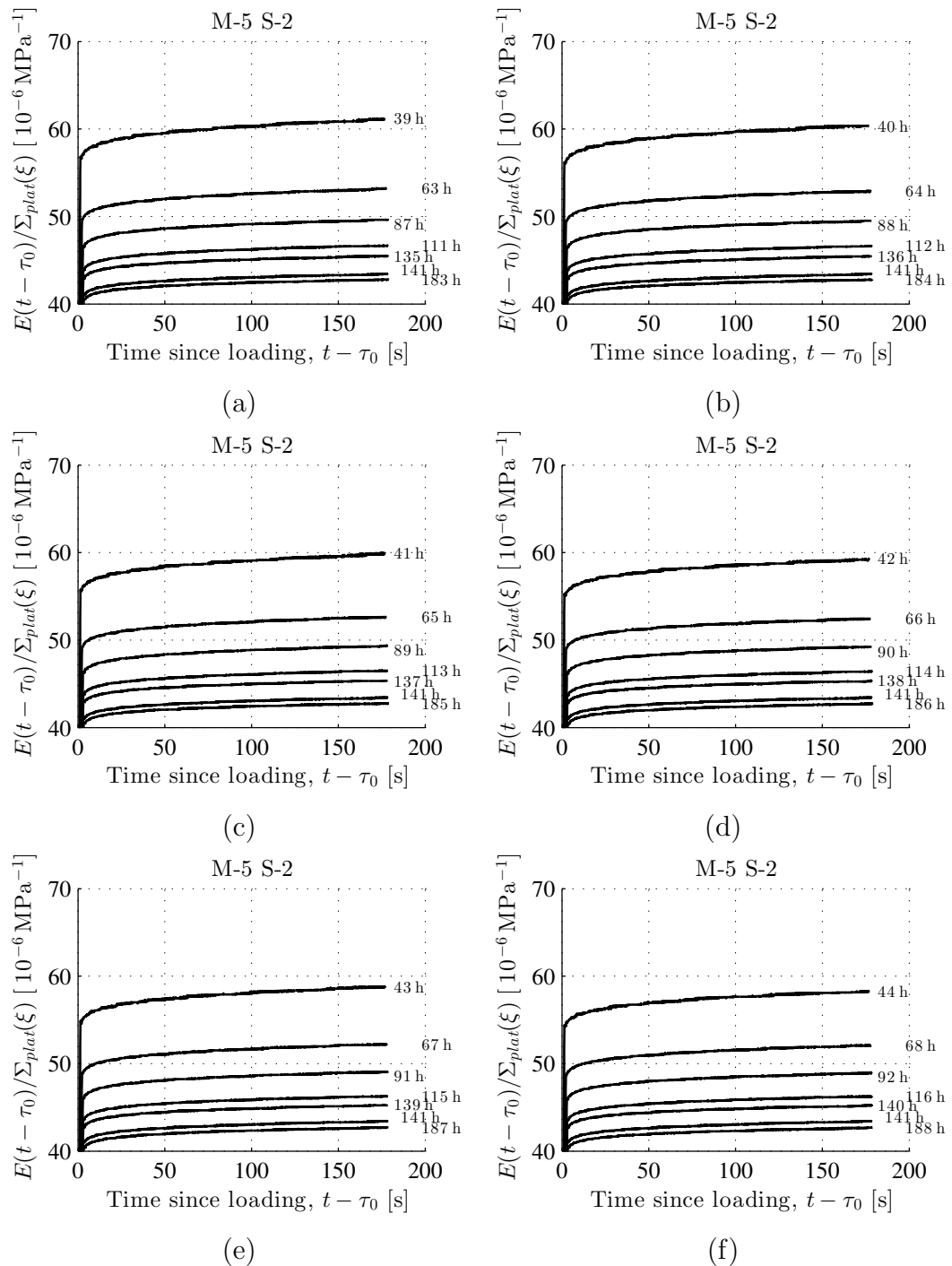


Figure 5.87: Measured strain evolution normalized with respect to the plateau stress as a function of the time since start of loading: mortar with $w/c = 0.50$, $a/c = 1.50$; ambient air temperature = $20\text{ }^{\circ}\text{C}$; ID = "M-5 S-2", see Table 5.1; as for load levels, see Fig. 5.2

5.3.6 Concrete: $w/c = 0.42$, $a/c = 2.70$

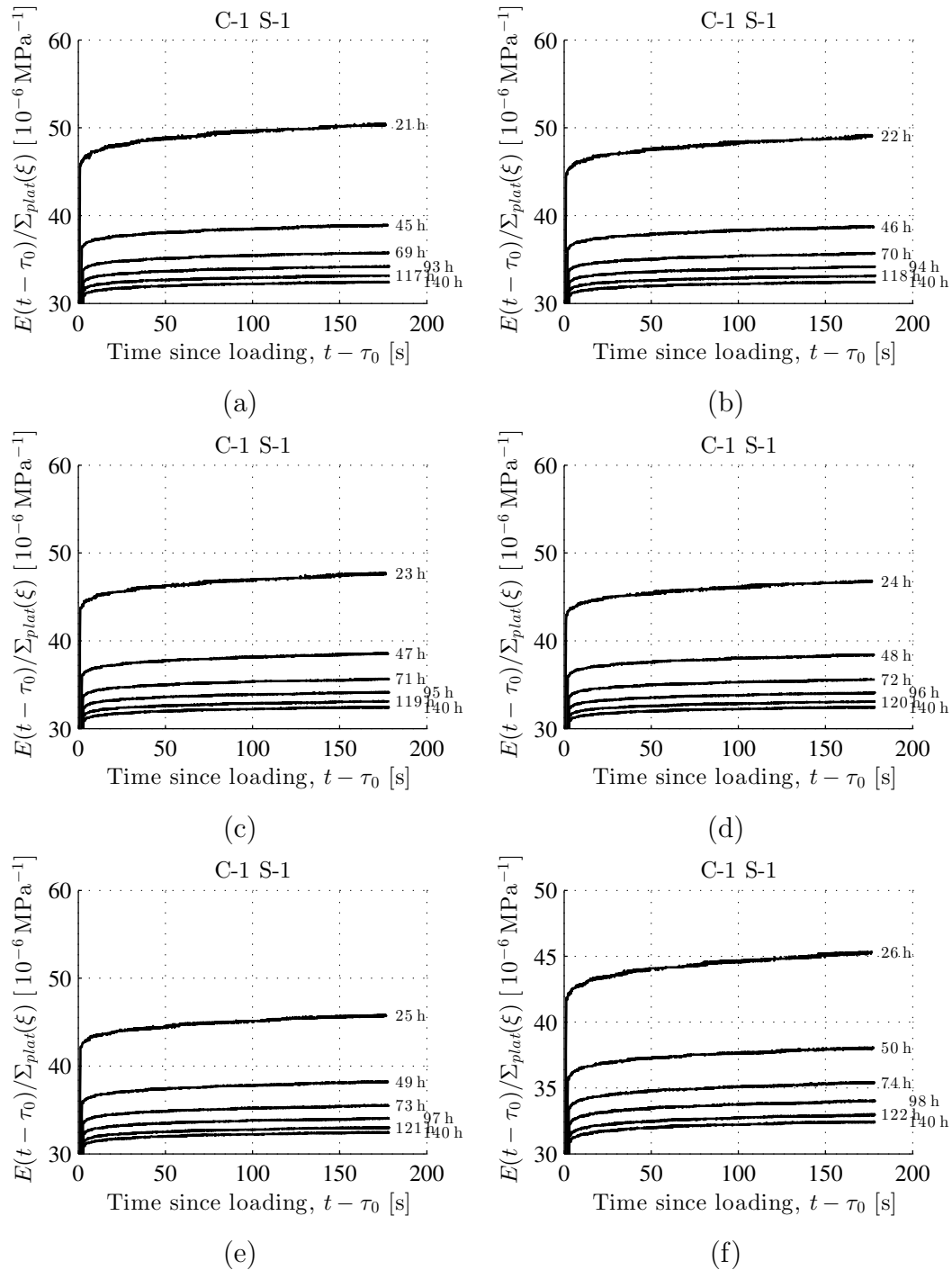


Figure 5.88: Measured strain evolution normalized with respect to the plateau stress as a function of the time since start of loading: concrete with $w/c = 0.42$, $a/c = 2.70$; ambient air temperature = 20°C ; ID = "C-1 S-1", see Table 5.1; as for load levels, see Fig. 5.2

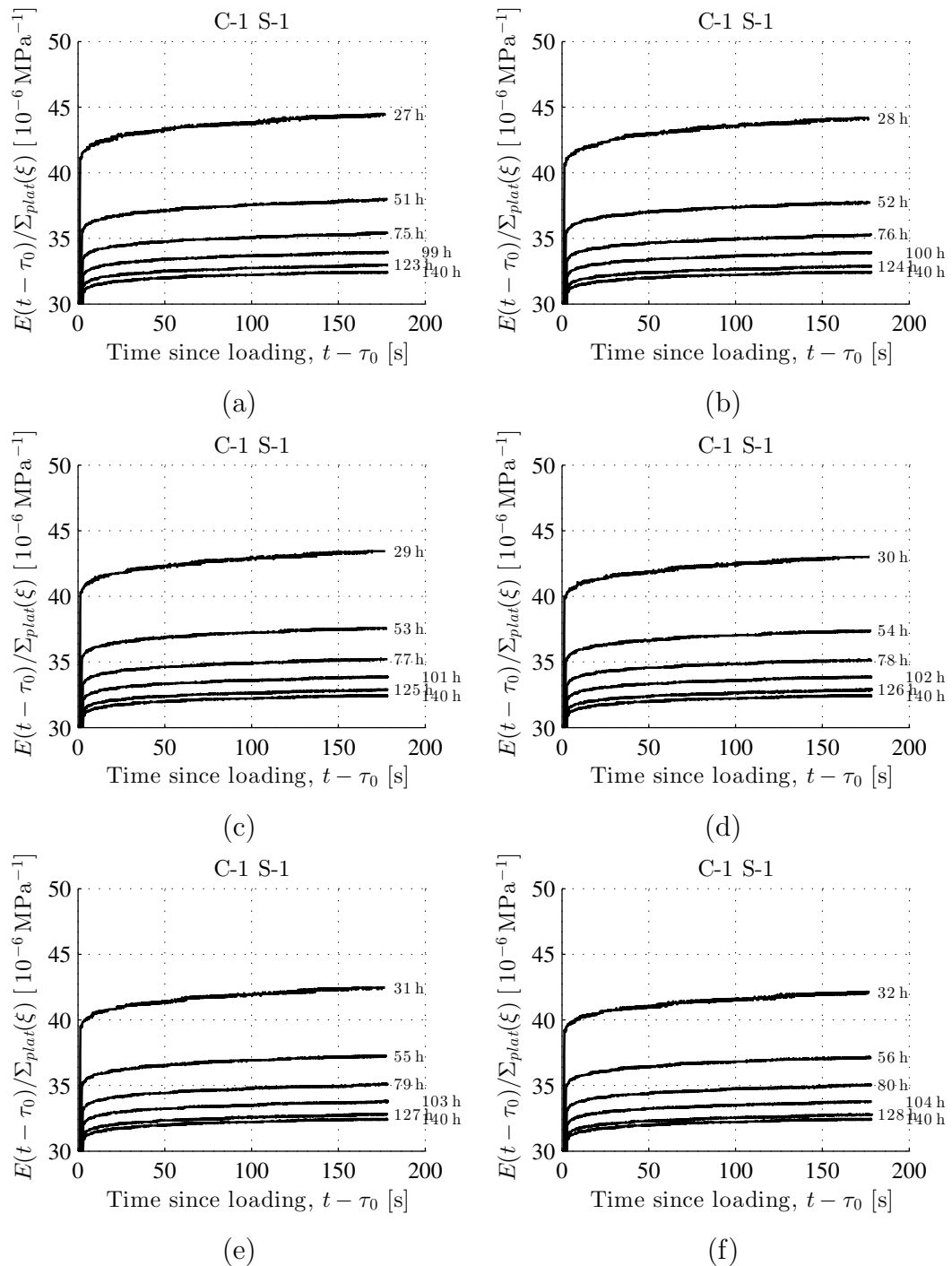


Figure 5.89: Measured strain evolution normalized with respect to the plateau stress as a function of the time since start of loading: concrete with $w/c = 0.42$, $a/c = 2.70$; ambient air temperature = 20°C ; ID = "C-1 S-1", see Table 5.1; as for load levels, see Fig. 5.2

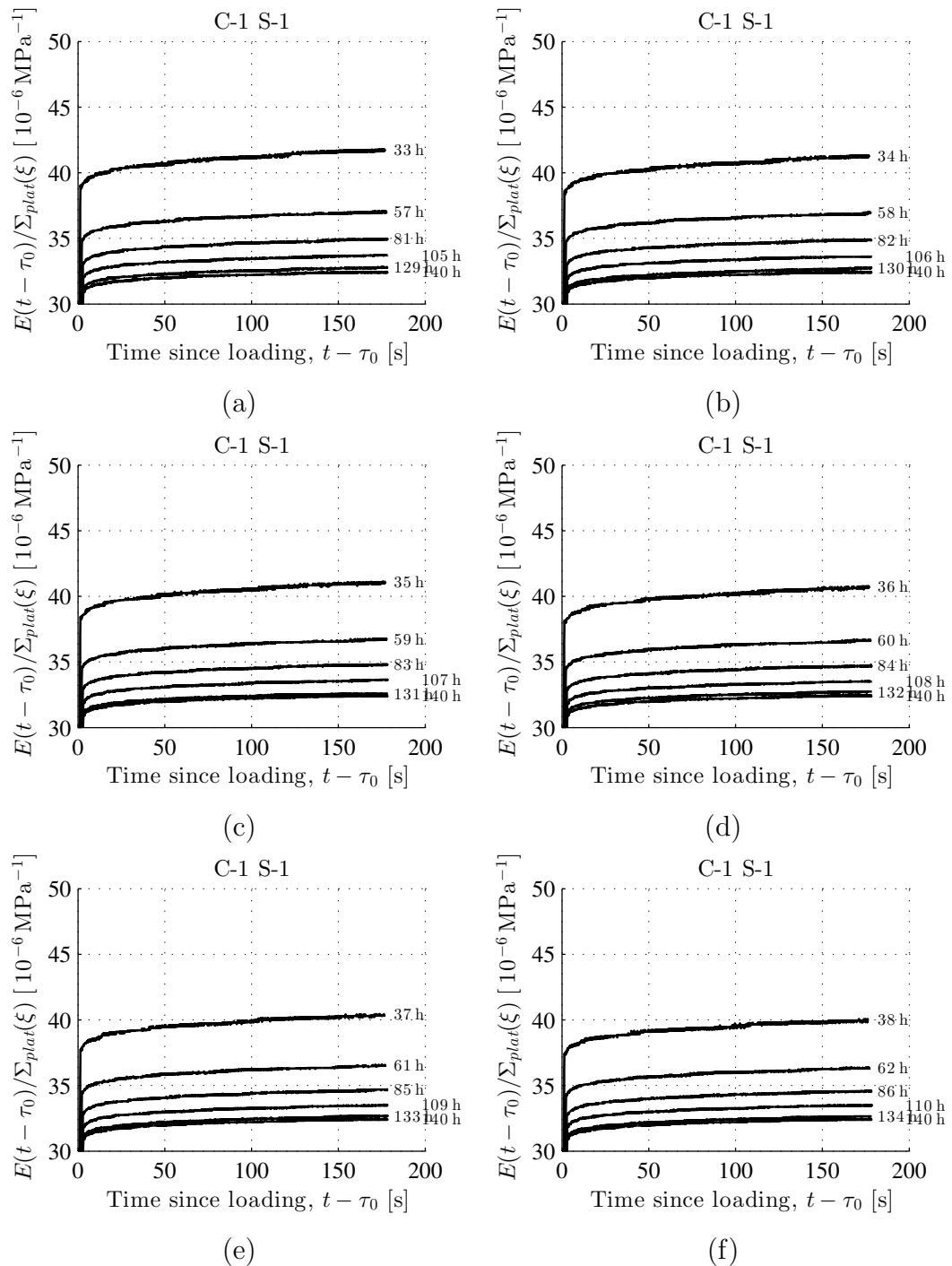


Figure 5.90: Measured strain evolution normalized with respect to the plateau stress as a function of the time since start of loading: concrete with $w/c = 0.42$, $a/c = 2.70$; ambient air temperature = 20°C ; ID = "C-1 S-1", see Table 5.1; as for load levels, see Fig. 5.2

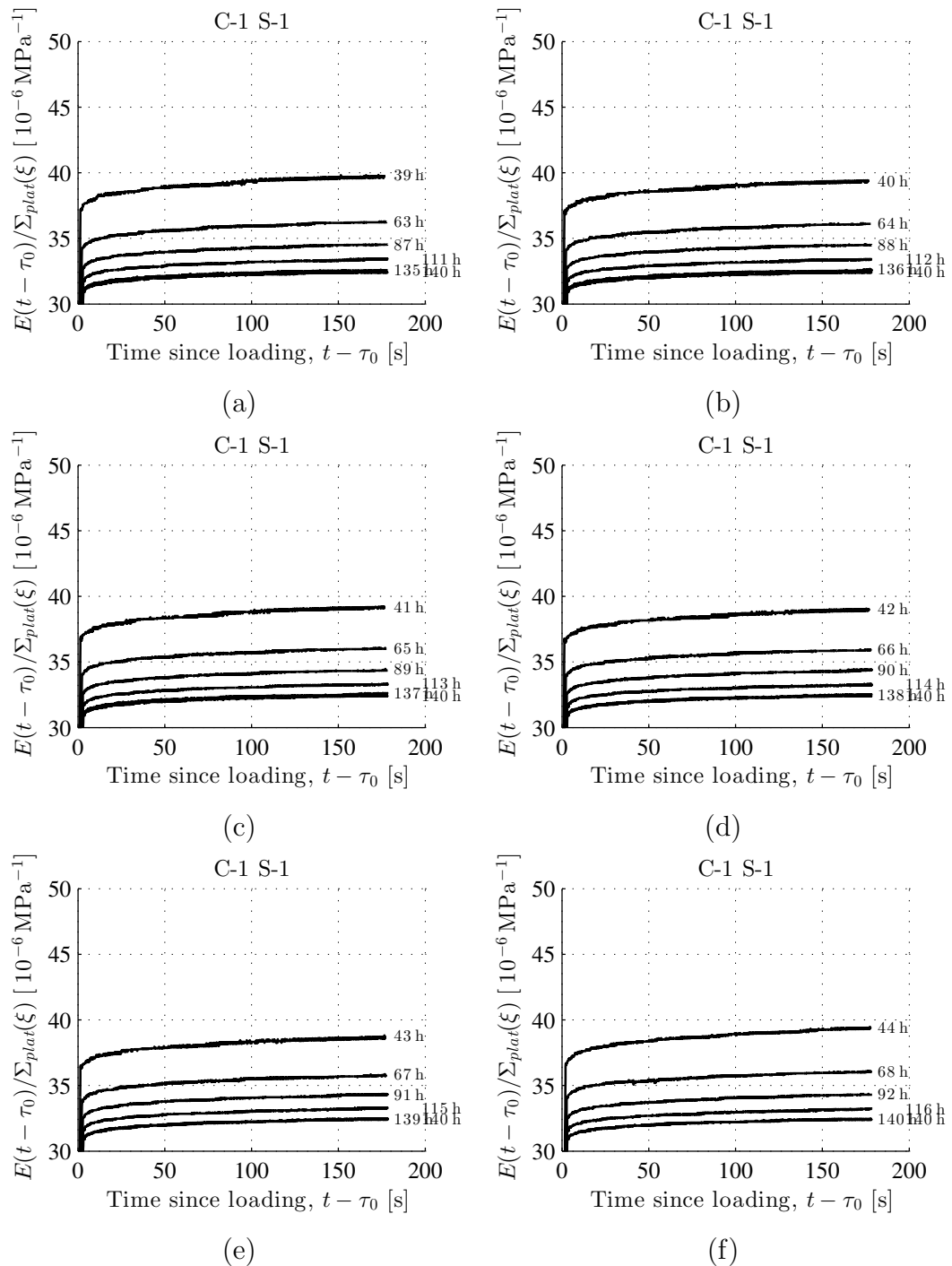


Figure 5.91: Measured strain evolution normalized with respect to the plateau stress as a function of the time since start of loading: concrete with $w/c = 0.42$, $a/c = 2.70$; ambient air temperature = 20°C ; ID = "C-1 S-1", see Table 5.1; as for load levels, see Fig. 5.2

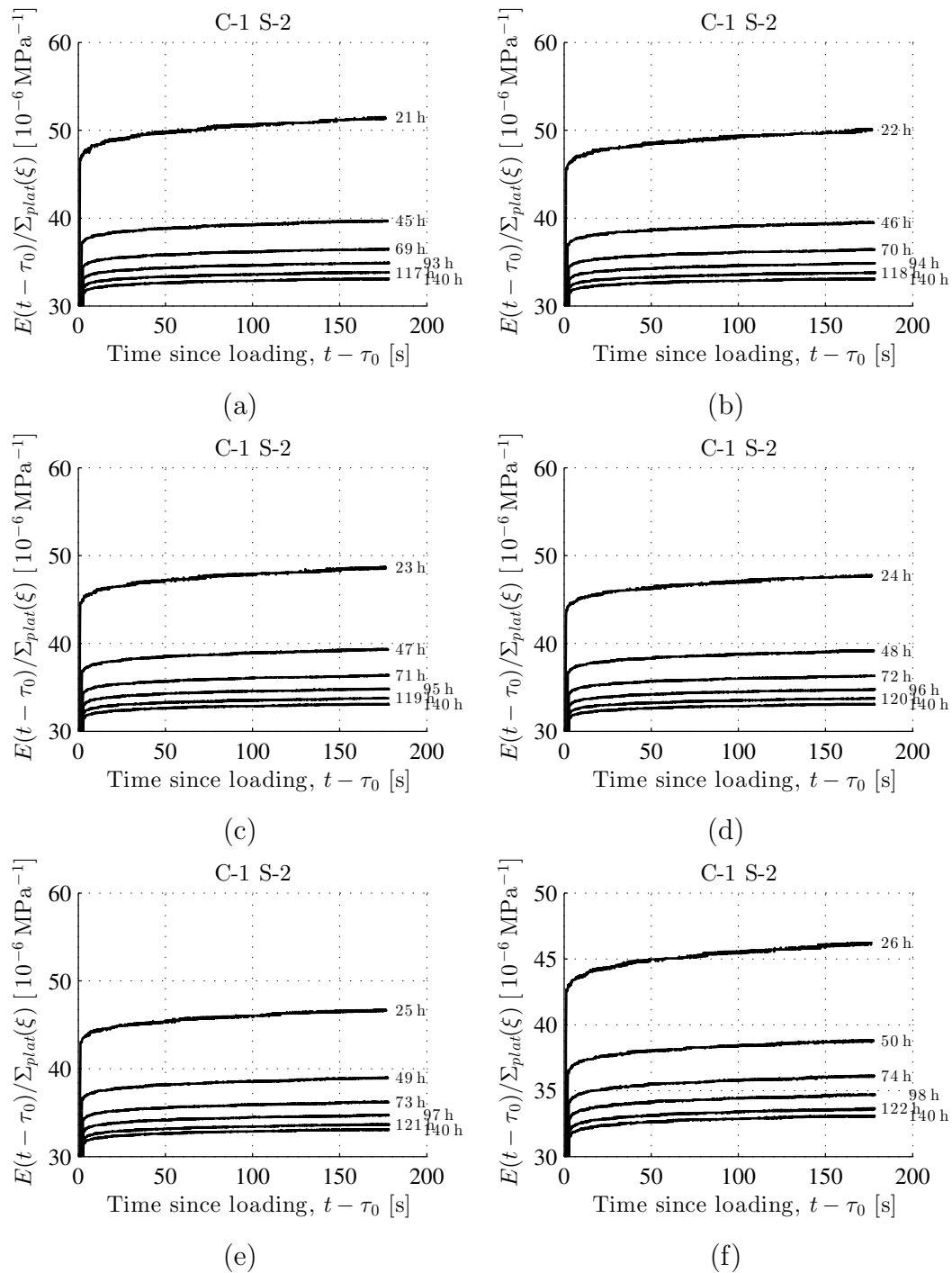


Figure 5.92: Measured strain evolution normalized with respect to the plateau stress as a function of the time since start of loading: concrete with $w/c = 0.42$, $a/c = 2.70$; ambient air temperature = 20°C ; ID = "C-1 S-2", see Table 5.1; as for load levels, see Fig. 5.2

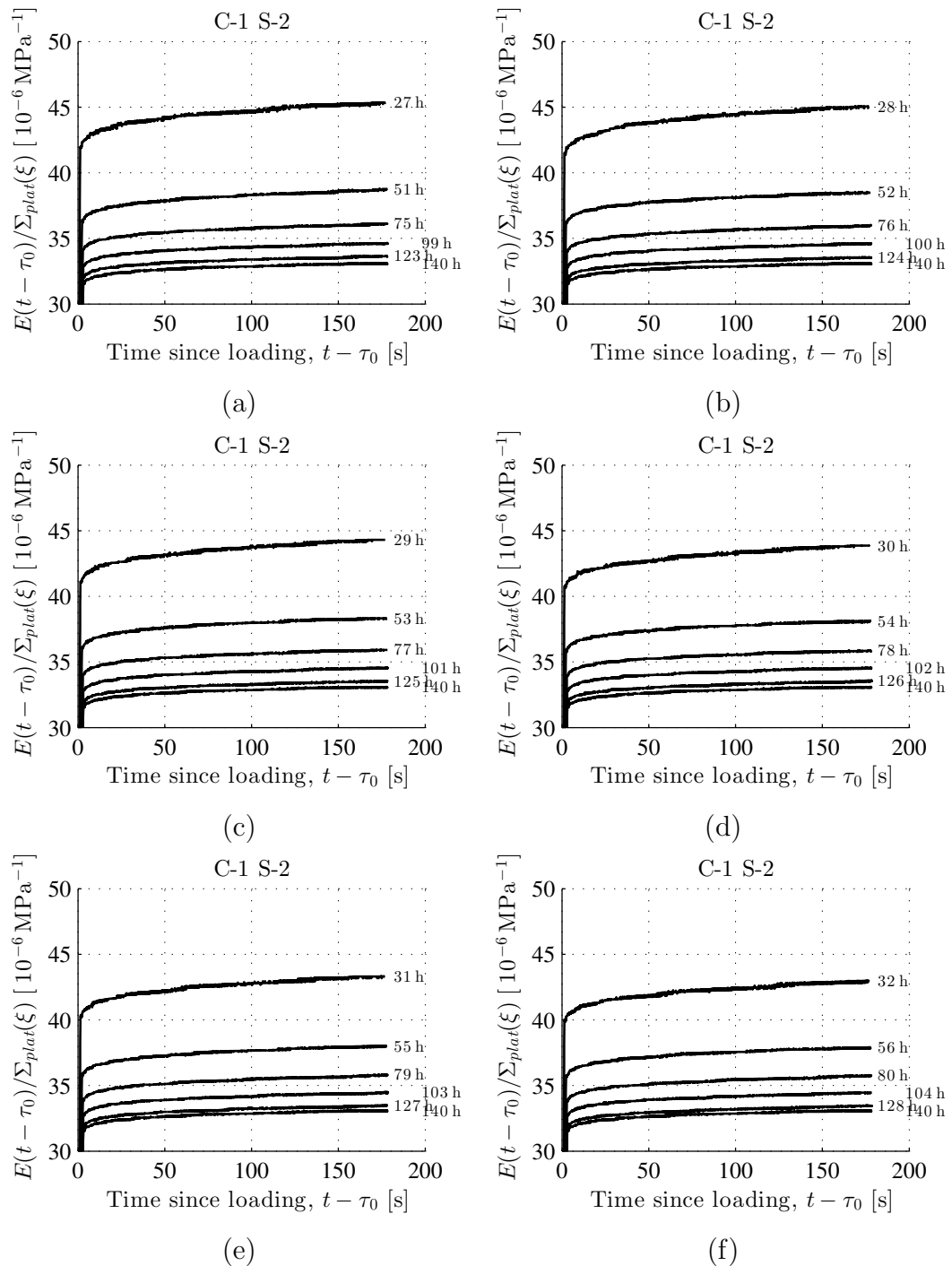


Figure 5.93: Measured strain evolution normalized with respect to the plateau stress as a function of the time since start of loading: concrete with $w/c = 0.42$, $a/c = 2.70$; ambient air temperature = 20°C ; ID = "C-1 S-2", see Table 5.1; as for load levels, see Fig. 5.2

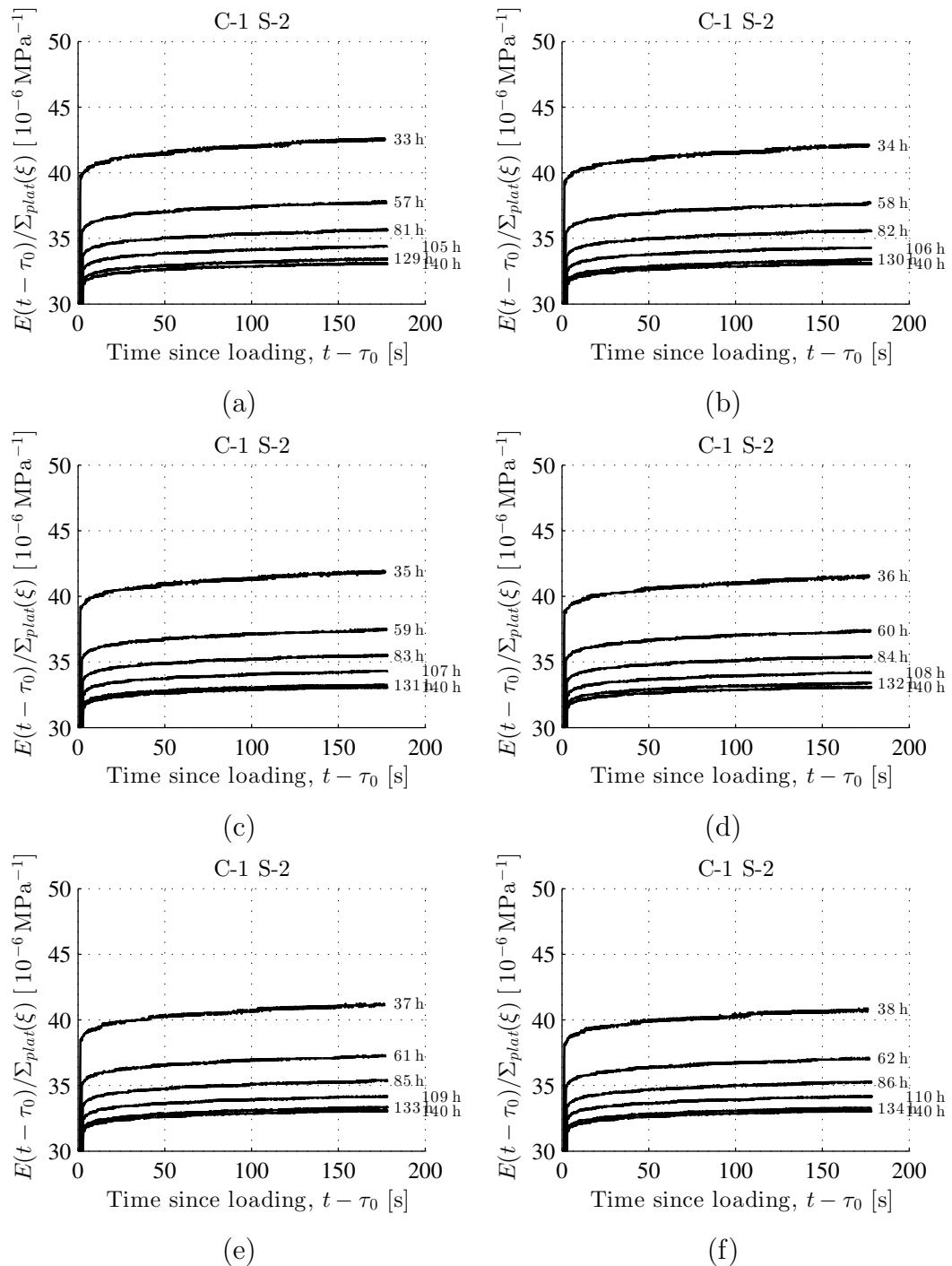


Figure 5.94: Measured strain evolution normalized with respect to the plateau stress as a function of the time since start of loading: concrete with $w/c = 0.42$, $a/c = 2.70$; ambient air temperature = 20°C ; ID = "C-1 S-2", see Table 5.1; as for load levels, see Fig. 5.2

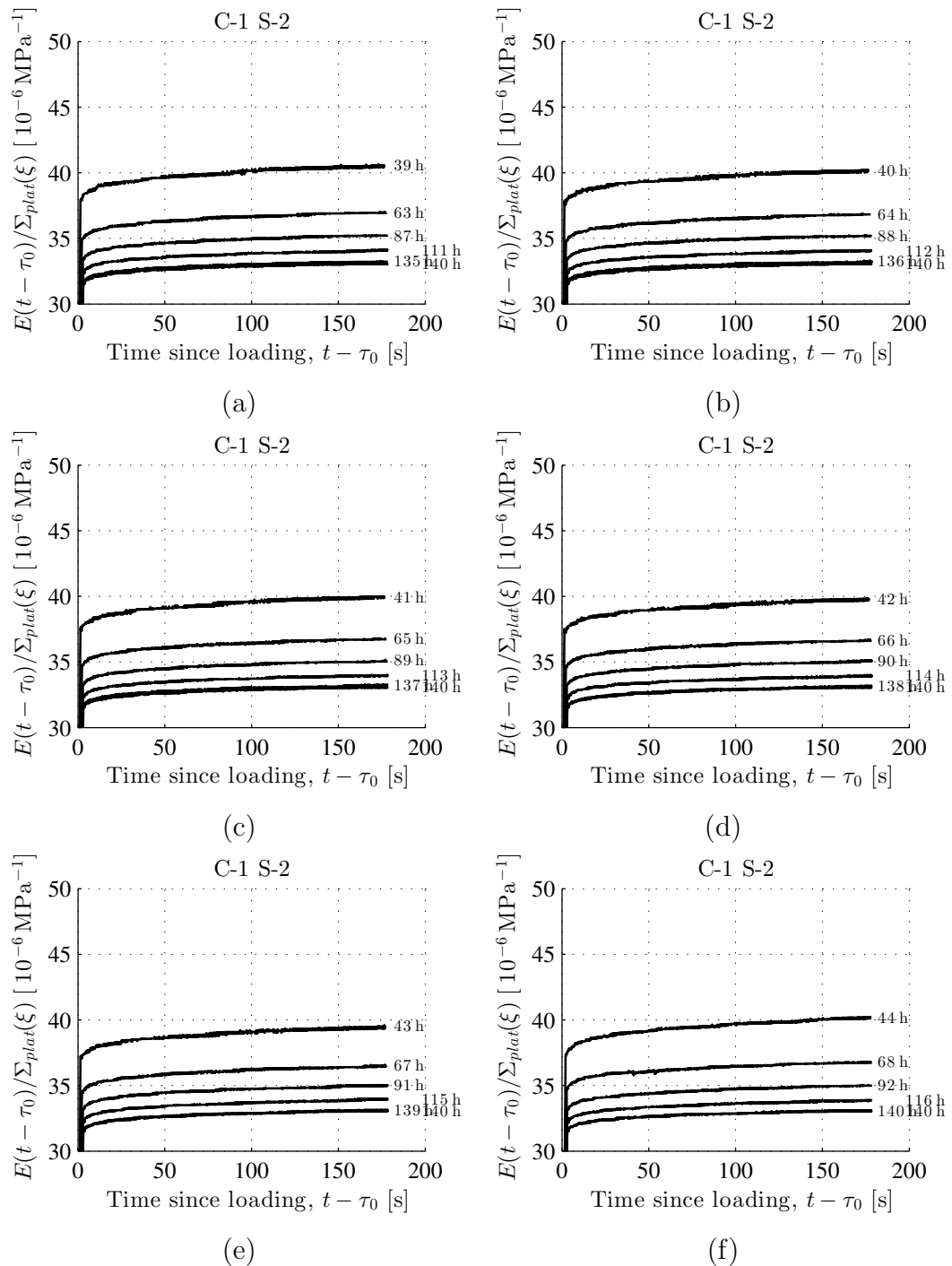


Figure 5.95: Measured strain evolution normalized with respect to the plateau stress as a function of the time since start of loading: concrete with $w/c = 0.42$, $a/c = 2.70$; ambient air temperature = 20°C ; ID = "C1 S-2", see Table 5.1; as for load levels, see Fig. 5.2

5.3.7 Concrete: $w/c = 0.50$, $a/c = 3.0$

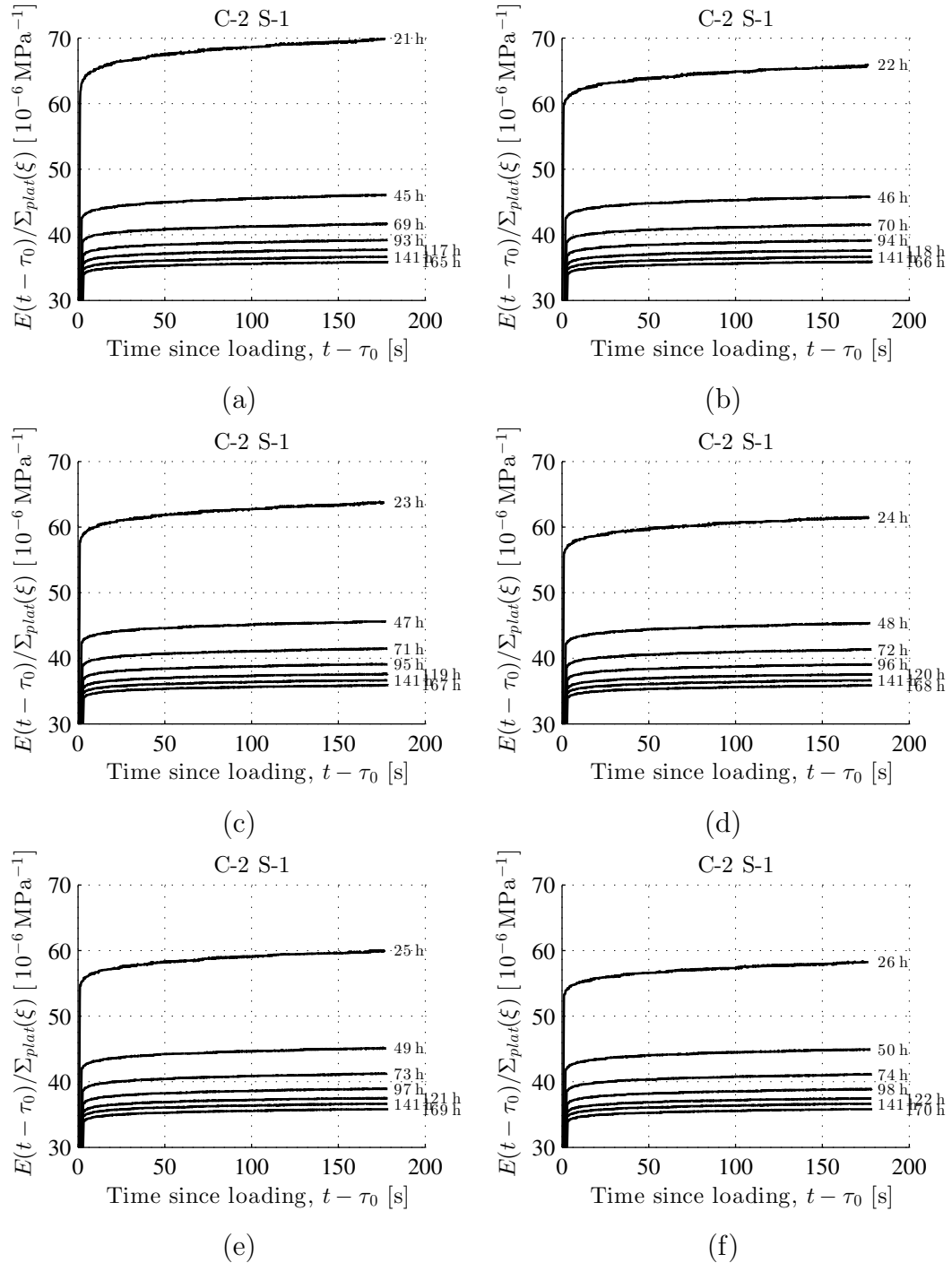


Figure 5.96: Measured strain evolution normalized with respect to the plateau stress as a function of the time since start of loading: concrete with $w/c = 0.50$, $a/c = 3.0$; ambient air temperature = 20°C ; ID = “C-2 S-1”, see Table 5.1; as for load levels, see Fig. 5.2

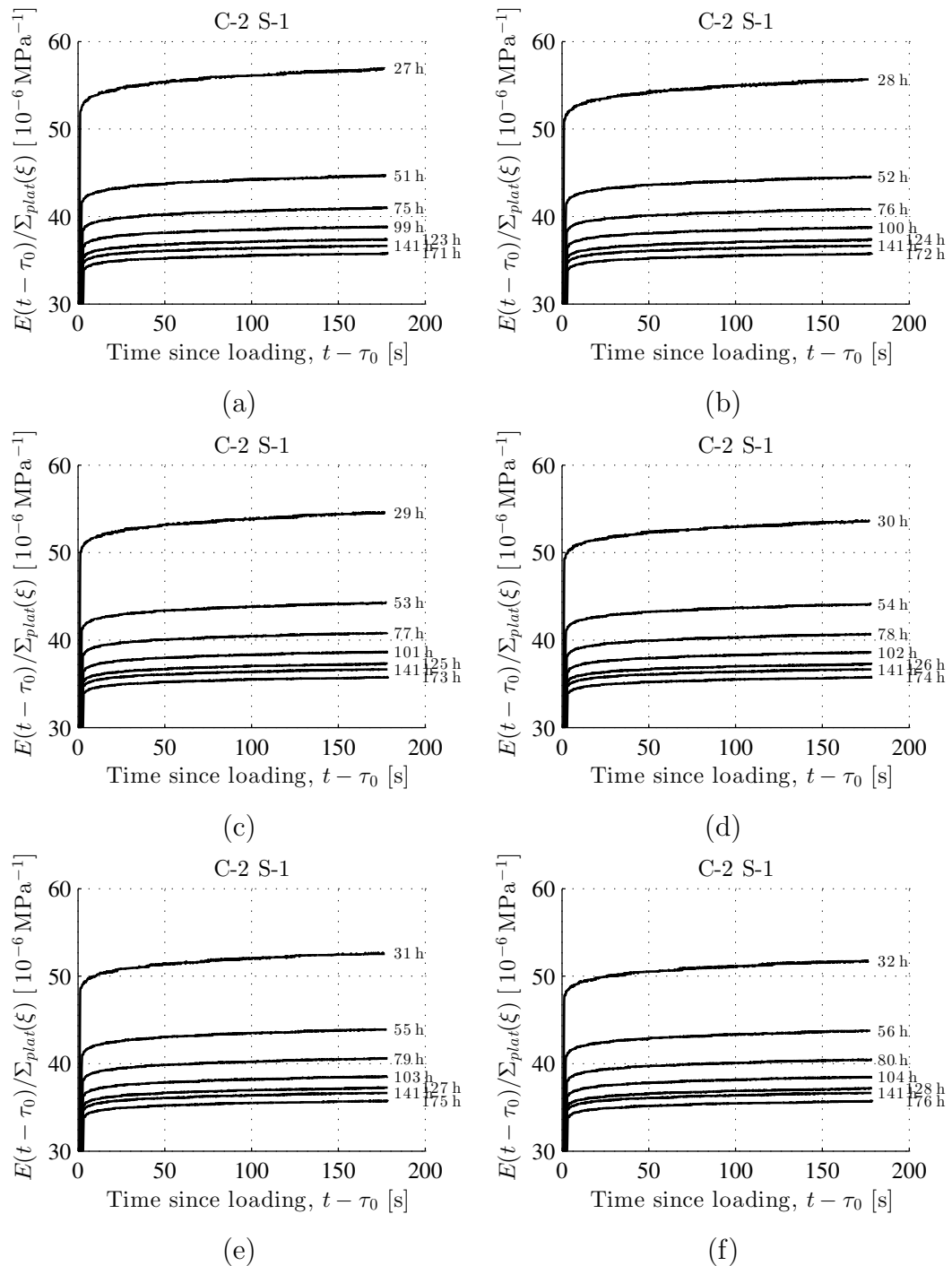


Figure 5.97: Measured strain evolution normalized with respect to the plateau stress as a function of the time since start of loading: concrete with $w/c = 0.50$, $a/c = 3.0$; ambient air temperature = 20°C ; ID = “C-2 S-1”, see Table 5.1; as for load levels, see Fig. 5.2

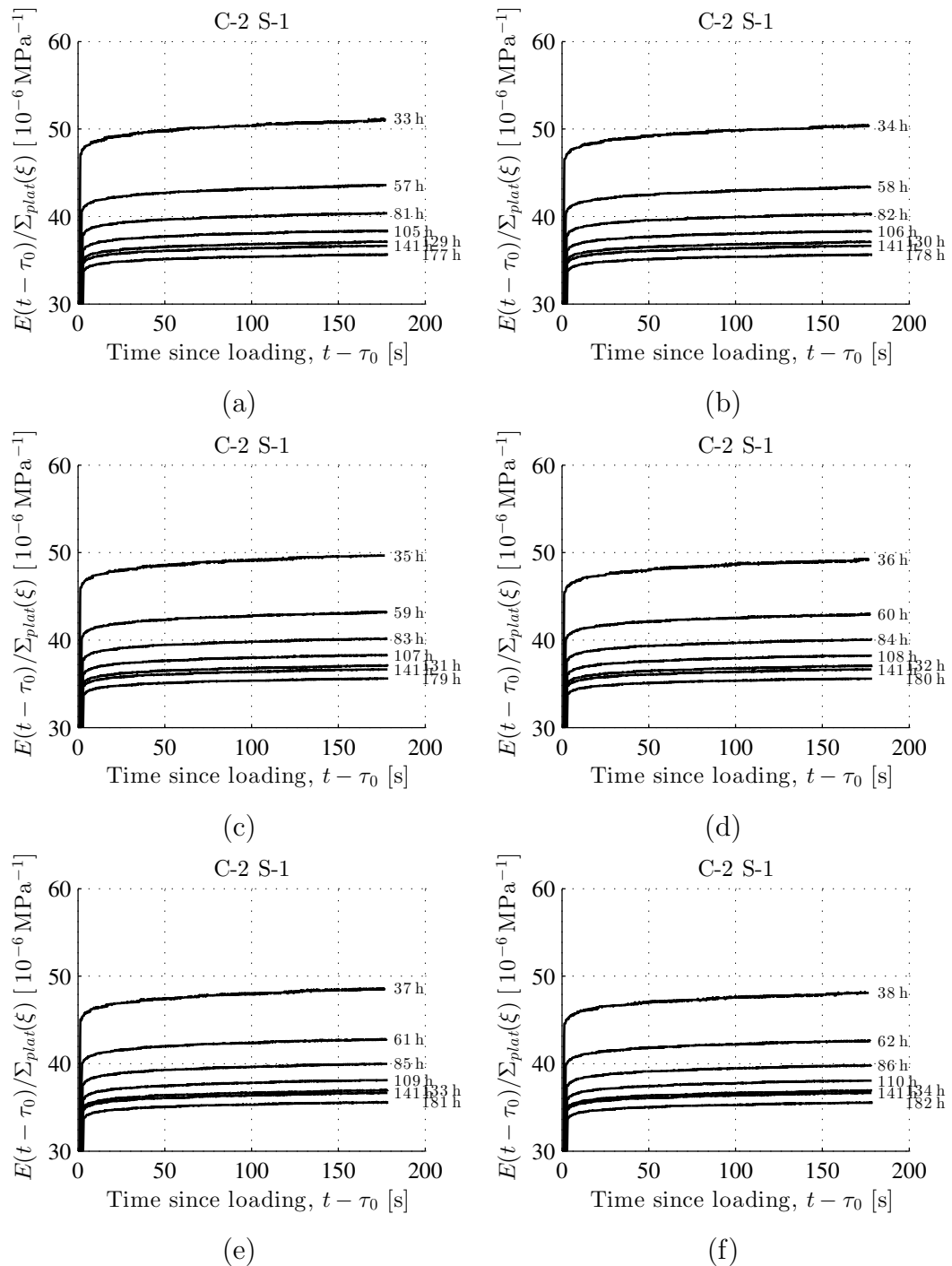


Figure 5.98: Measured strain evolution normalized with respect to the plateau stress as a function of the time since start of loading: concrete with $w/c = 0.50$, $a/c = 3.0$; ambient air temperature = 20°C ; ID = "C-2 S-1", see Table 5.1; as for load levels, see Fig. 5.2

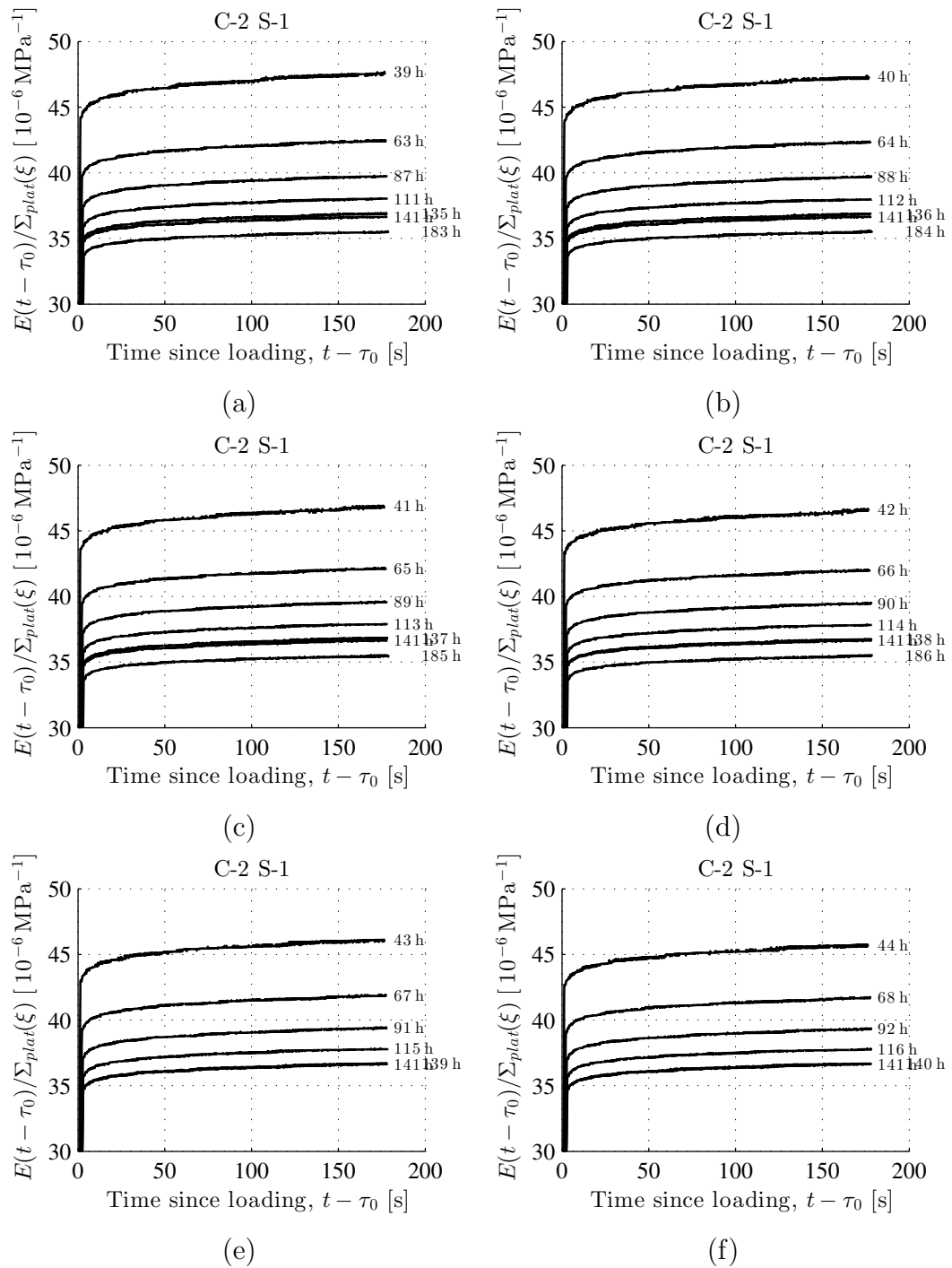


Figure 5.99: Measured strain evolution normalized with respect to the plateau stress as a function of the time since start of loading: concrete with $w/c = 0.50$, $a/c = 3.0$; ambient air temperature = 20°C ; ID = "C-2 S-1", see Table 5.1; as for load levels, see Fig. 5.2

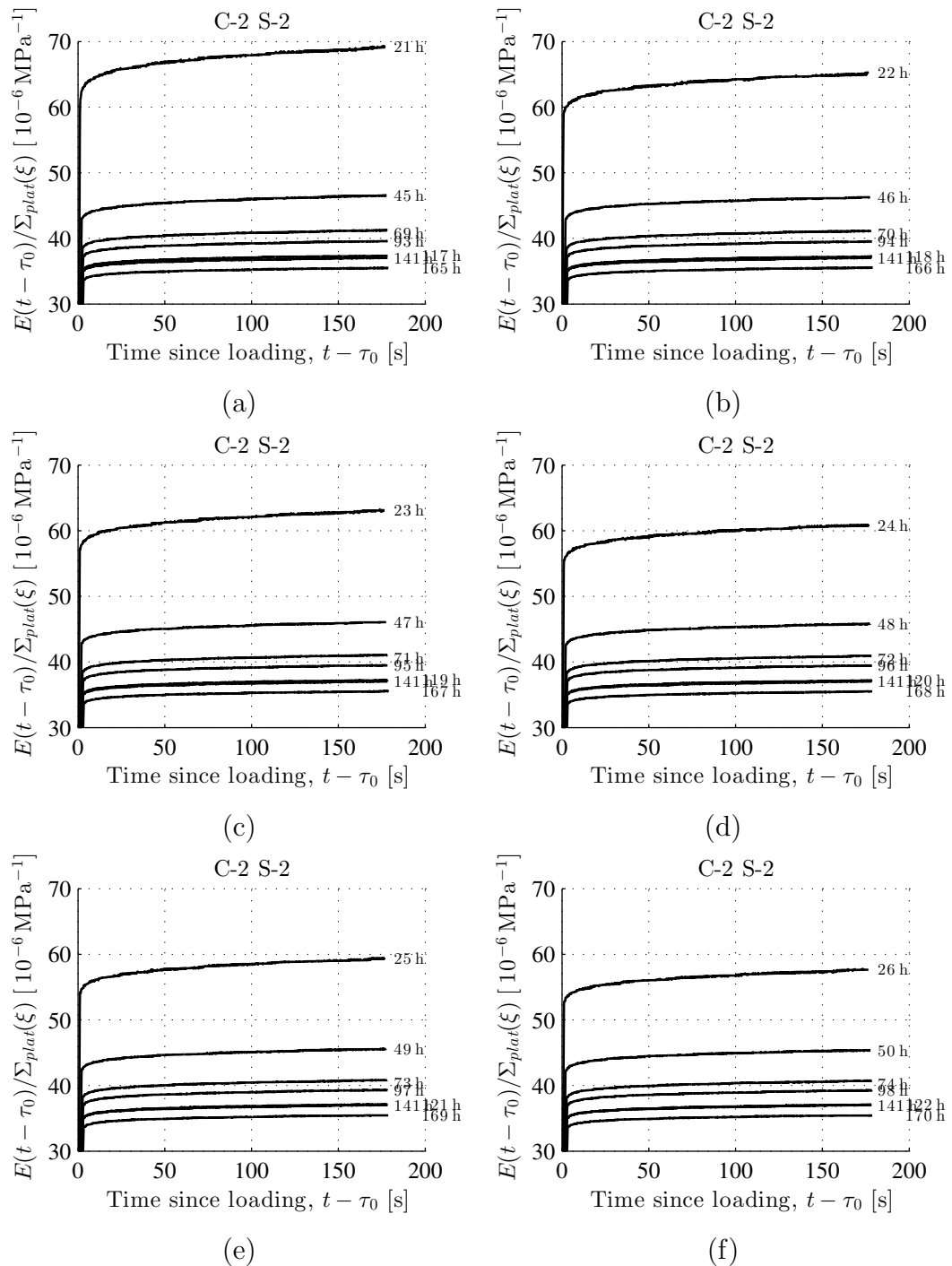


Figure 5.100: Measured strain evolution normalized with respect to the plateau stress as a function of the time since start of loading: concrete with $w/c = 0.50$, $a/c = 3.0$; ambient air temperature = 20°C ; ID = “C-2 S-2”, see Table 5.1; as for load levels, see Fig. 5.2

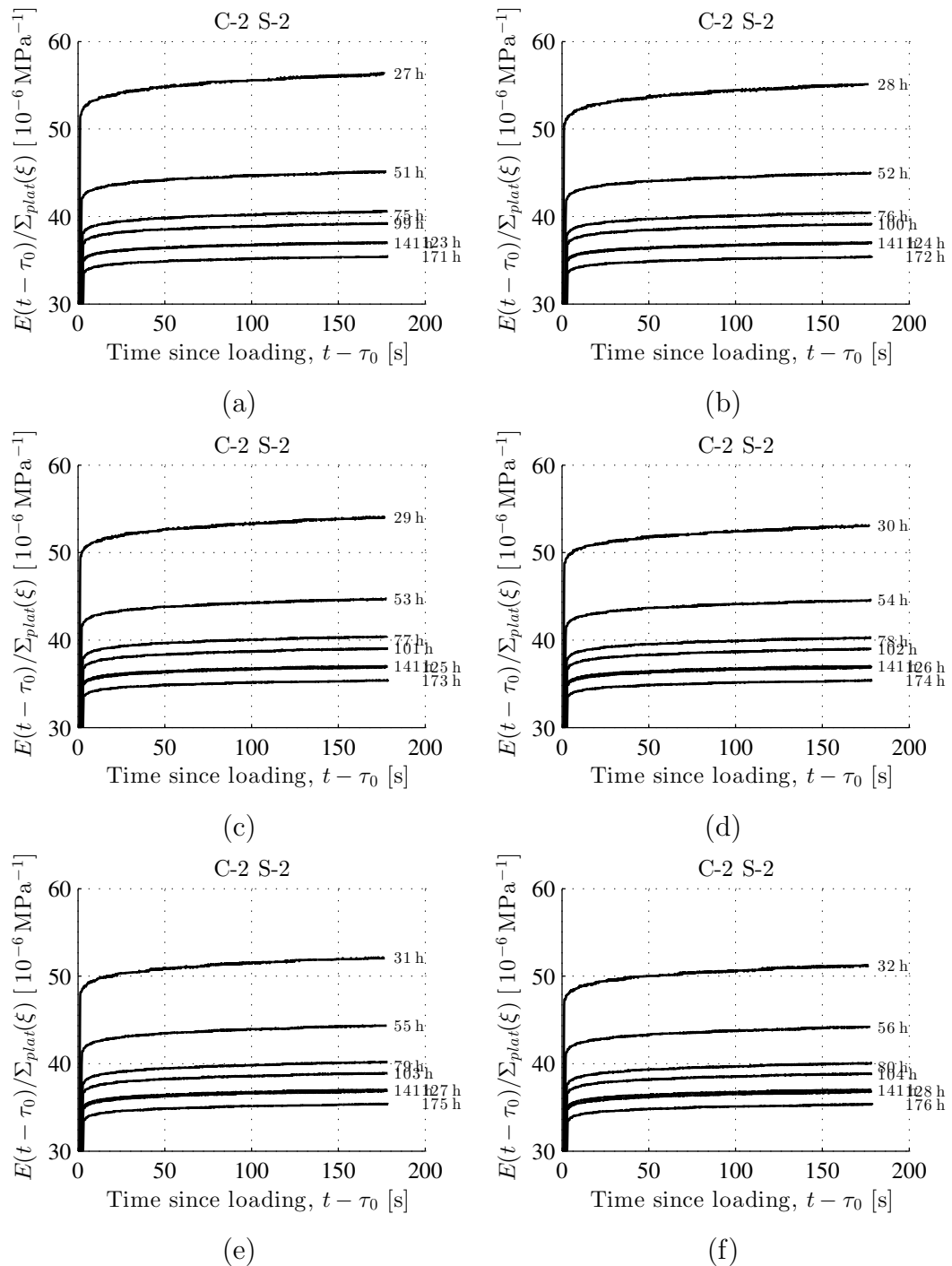


Figure 5.101: Measured strain evolution normalized with respect to the plateau stress as a function of the time since start of loading: concrete with $w/c = 0.50$, $a/c = 3.0$; ambient air temperature = 20°C ; ID = "C-2 S-2", see Table 5.1; as for load levels, see Fig. 5.2

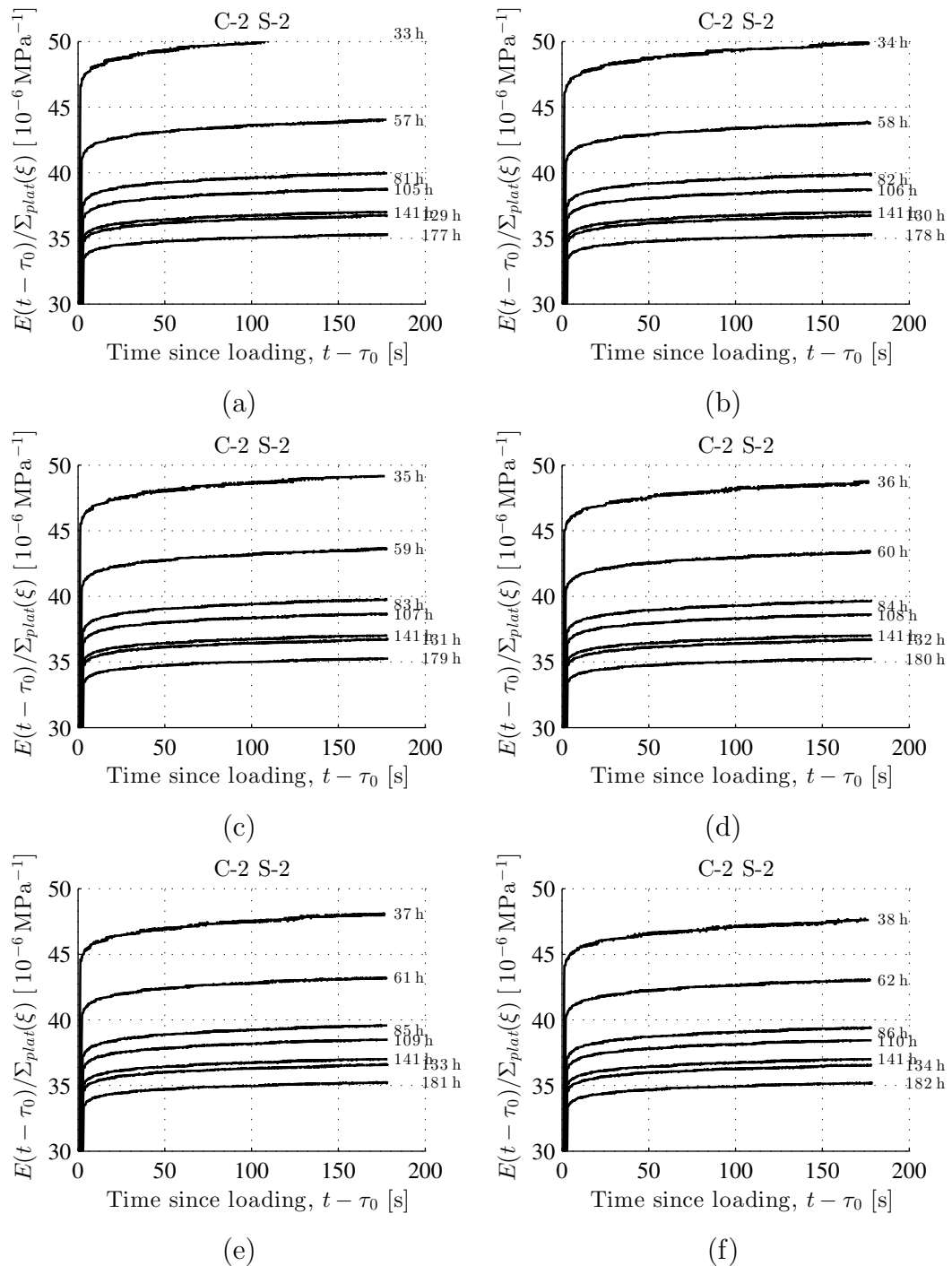


Figure 5.102: Measured strain evolution normalized with respect to the plateau stress as a function of the time since start of loading: concrete with $w/c = 0.50$, $a/c = 3.0$; ambient air temperature = 20°C ; ID = “C-2 S-2”, see Table 5.1; as for load levels, see Fig. 5.2

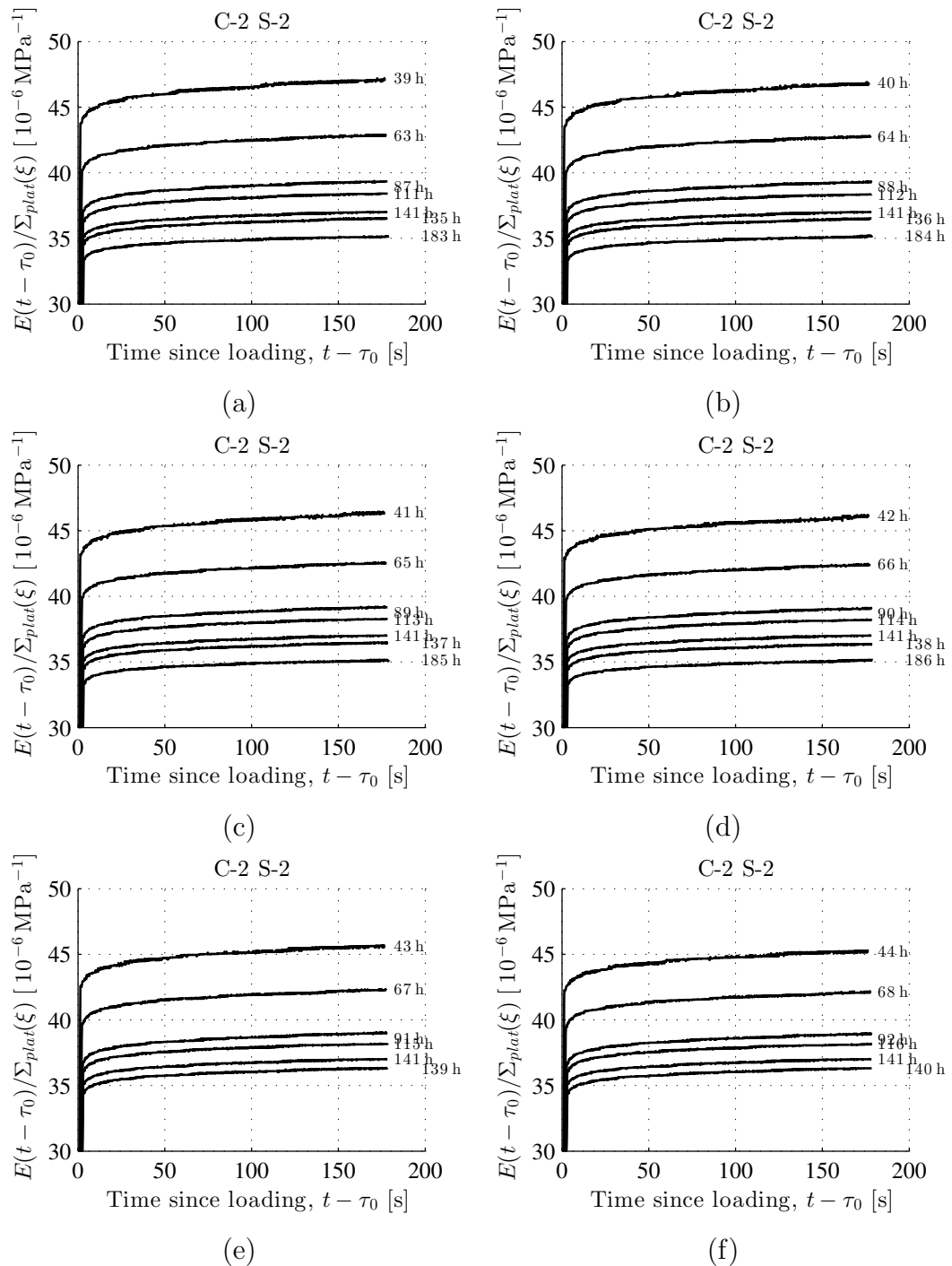


Figure 5.103: Measured strain evolution normalized with respect to the plateau stress as a function of the time since start of loading: concrete with $w/c = 0.50$, $a/c = 3.0$; ambient air temperature = $20\text{ }^{\circ}\text{C}$; ID = “C2 S-2”, see Table 5.1; as for load levels, see Fig. 5.2

Chapter 6

Conclusions

As for decoupling the time-dependent phenomena of creep and hydration as well as for carefully subdividing total deformation measurements into an instantaneous elastic part and a time-dependent creep contribution, the following conclusions are drawn:

- Decoupling the time-dependent phenomena of creep and hydration is possible by performing ultra short creep tests. Their duration must be so short that the ongoing chemical hydration reaction does *not* make a significant progress. This implies that the microstructure of the tested cementitious materials is virtually constant throughout the creep test. Therefore, ultra short creep experiments qualify as non-aging tests.
- The *elastic* Young's modulus is accessible by considering that creep strains are compressive throughout a compressive creep test – and this includes also the very initial phase of loading.
- The statically determined elastic Young's modulus is equal to the dynamically determined elastic Young's modulus, whereby the latter is, e.g., accessible by means of ultrasound characterization. This implies that the thermodynamic definition of elasticity applies also to cementitious materials, i.e. that elastic stiffness is independent of the loading rate.
- Secant Young's moduli, loading Young's moduli, and unloading Young's moduli shall not be misinterpreted as *elastic* Young's moduli, because

cementitious materials exhibit ultra fast creep. Deformation measurements exhibiting a strain rate-dependency must be expected to contain also contributions from dissipative phenomena, i.e. they shall not be treated as being purely elastic.

- The elastic Young's modulus allows for extracting time-dependent strains from total strains developing during a creep test.
- Significant creep strains develop already during the loading phase of a quasi-static test, and they need to be considered when it comes to reliable identification of creep functions of cementitious materials.
- The initial part of creep functions of hydrating cementitious materials, covering the first few minutes after sudden loading, can be described reliably by means of power laws.
- Early-age *evolutions* of elastic stiffness and of *non-aging* creep properties can be characterized by performing ultra short creep experiments once every hour, e.g. starting 21 hours after production and continuing up to material ages of eight days.

As for the microscopic origin of macroscopically observed creep, the microstructure of cementitious materials was resolved down to (sub)micron-sized needle-shaped hydrates; and this has delivered the following conclusions:

- Universal creep properties of (sub)micron-sized, needle-shaped, and well-saturated cement hydrates allow for explaining the deformation histories measured in more than 500 ultra short creep test on cement pastes, carried out during the first week after their production.
- The same creep properties of cement hydrates also allow for predicting the creep performance of a cement paste which was cured for 30 years under water, and which was subjected thereafter to a 30 days long creep test.
- This underlines that non-aging creep of well-saturated cement pastes can be predicted as a function of material composition (in terms of the initial water-to-cement mass ratio) and maturity (in terms of the hydration degree).

- It was also found that the macroscopic uniaxial creep functions of cement pastes are practically independent of the Poisson's ratio of the creeping hydrate needles.

As for predicting creep of mortars and concretes, the following conclusions are drawn:

- Creep prediction of mortars and concretes produced with oven-dried regular aggregates requires consideration of "internal curing", reminiscent of the situation encountered with lightweight aggregates.
- Aggregates with an open surface porosity may take up a significant mass of water during mixing of raw materials, and this water mass is later soaked "back" into the hydrating cement paste.
- Suction of water – from the open porosity of aggregates into the surrounding cement paste matrix – is driven by autogeneous shrinkage. 60 percent of shrinkage-induced voids were found to be filled by water coming from the open porosity of aggregates.
- Reliable prediction of creep of mortars and concretes requires the introduction of a new hydration model, envisioning that hydrating cement paste is a thermodynamically open system to the surface porosity of the aggregates. This requires introduction of a hydration-effective water-to-cement mass ratio of the cement paste matrix, and this effective w/c ratio is linearly increasing with increasing hydration degree.

Future outlook

The achieved research results motivate the following future outlook:

- It will be interesting to compare the herein described creep testing results with corresponding measurements from creep tests on "microstructurally designed" cement pastes, such as studied by [Termkhajornkit et al. \(2015\)](#) and by [Di Bella et al. \(2015\)](#). As for their production, a certain part of the clinker is replaced by chemically inert particles of similar size and stiffness. Complete hydration results in a material which is representative of an early-age microstructure, because the inert particles take over the role of unhydrated clinker.

- The identified non-aging creep properties will serve as the logic basis for developing multiscale *aging* creep models, because (i) the very first phase of an aging creep test is clearly of non-aging nature, and (ii) hydrate needles produced after the time instant of loading do also exhibit the same universal creep behavior as the hydrate needles which exist already at the time of loading. Existing non-aging creep formulations represent an interesting basis for these future developments, see the models by [Scheiner and Hellmich \(2009\)](#) and by [Sanahuja \(2013b\)](#).
- It will be also interesting to further resolve the microstructure of needle-shaped cement hydrates down to the even finer scales of calcium-silicate-hydrates and gel pores, where creep may origin from shear dislocations of interfaces which are filled by adsorbed water layers ([Pellenq et al. 2009](#); [Sanahuja and Dormieux 2010](#); [Shahidi et al. 2014, 2015a](#); [Vandamme et al. 2015](#); [Shahidi et al. 2016](#)).
- Finally, it will be interesting to apply the herein developed research methodologies also to blended cementitious materials, where part of cement clinker is replaced by locally available replacement materials, i.e. either by supplementary cementitious materials such as the waste products fly ash and slag, or by very fine-ground inert particles such as quartz or limestone fillers.

Appendix-A

Analytical expressions facilitating upscaling in LC space

Upscaling of the hydrate creep behavior, up to the larger scales of the hydrate foam and of the cement paste, respectively, is performed in the LC space, according to the analytical formulae described next. Thereby, we consider that an isotropic fourth-order tensor, \mathbb{G} , can be decomposed into a volumetric part and a deviatoric part as $\mathbb{G} = G^{vol}\mathbb{I}^{vol} + G^{dev}\mathbb{I}^{dev}$, where G^{vol} and G^{dev} , respectively, are the (scalar) volumetric and deviatoric components of the fourth-order tensor \mathbb{G} , and where \mathbb{I}^{vol} and \mathbb{I}^{dev} are the volumetric and deviatoric parts of the symmetric fourth-order identity tensor. They satisfy $\mathbb{I}^{vol} : \mathbb{I}^{vol} = \mathbb{I}^{vol}$, $\mathbb{I}^{dev} : \mathbb{I}^{dev} = \mathbb{I}^{dev}$, and $\mathbb{I}^{vol} : \mathbb{I}^{dev} = \mathbb{I}^{dev} : \mathbb{I}^{vol} = O$. In addition, the isotropic average of a transversally isotropic tensor \mathbb{F} can be written as (Torquato 2013; Sadowski et al. 2015)

$$\int_0^{2\pi} \int_0^\pi \mathbb{F}(\varphi, \vartheta) \frac{\sin \vartheta}{4\pi} d\vartheta d\varphi = \sum_{i=1}^3 \sum_{j=1}^3 \left[\frac{1}{3} F_{iijj} \mathbb{I}^{vol} + \frac{1}{5} \left(F_{ijij} - \frac{1}{3} F_{iijj} \right) \mathbb{I}^{dev} \right], \quad (1)$$

provided that the tensor \mathbb{F} exhibits the symmetries $F_{ijkl} = F_{jikl} = F_{ijlk}$.

We start our collection of analytical formulae with the LC-transformed Hill tensors occurring in concentration and stiffness expressions of Eqs. (54)-(3.26). Given the organization of cement paste according to Fig. 3.2, the inclusions in the corresponding Eshelby problems are all embedded in an infinite hydrate foam matrix with quasi-elastic ‘‘stiffness’’ \mathbb{R}_{hf}^* . For material phases with spherical shape ($j = sph$), i.e. for air, water, and cement clinker, and for cylindrical hydrates ($j = cyl$) the Hill tensor reads as

$$\mathbb{P}_j^{hf,*}(p) = \mathbb{S}_j^{hf,*}(p) : [\mathbb{R}_{hf}^*(p)]^{-1} \quad \forall j \in \{sph, cyl\}, \quad (2)$$

whereby $\mathbb{S}_j^{hf,*}$ denotes the LC-transformed Eshelby tensor. As for a spherical inclusion embedded in an infinite hydrate foam matrix, the LC-transformed Eshelby tensor $\mathbb{S}_{sph}^{hf,*}$ is isotropic, and its volumetric and deviatoric components read as (Zaoui 2002)

$$S_{sph}^{hf,*,vol}(p) = \frac{3 k_{hf}^*(p)}{3 k_{hf}^*(p) + 4 \mu_{hf}^*(p)}, \quad S_{sph}^{hf,*,dev}(p) = \frac{6 k_{hf}^*(p) + 2 \mu_{hf}^*(p)}{5 \cdot 3 k_{hf}^*(p) + 4 \mu_{hf}^*(p)}. \quad (3)$$

As for a cylindrical hydrate orientated in e_3 -direction and embedded in an infinite hydrate foam matrix, the non-zero components of the LC-transformed Eshelby tensor $\mathbb{S}_{cyl}^{hf,*}$ read as (Eshelby 1957; Hellmich et al. 2004)

$$\begin{aligned}
S_{cyl,1111}^{hf,*}(p) &= S_{cyl,2222}^{hf,*}(p) = \frac{9}{4} \frac{k_{hf}^*(p) + \mu_{hf}^*(p)}{3k_{hf}^*(p) + 4\mu_{hf}^*(p)}, \\
S_{cyl,1122}^{hf,*}(p) &= S_{cyl,2211}^{hf,*}(p) = \frac{1}{4} \frac{3k_{hf}^*(p) - 5\mu_{hf}^*(p)}{3k_{hf}^*(p) + 4\mu_{hf}^*(p)}, \\
S_{cyl,1133}^{hf,*}(p) &= S_{cyl,2233}^{hf,*}(p) = \frac{1}{2} \frac{3k_{hf}^*(p) - 2\mu_{hf}^*(p)}{3k_{hf}^*(p) + 4\mu_{hf}^*(p)}, \\
S_{cyl,1212}^{hf,*}(p) &= \frac{1}{4} \frac{3k_{hf}^*(p) + 7\mu_{hf}^*(p)}{3k_{hf}^*(p) + 4\mu_{hf}^*(p)}, \\
S_{cyl,1313}^{hf,*} &= S_{cyl,2323}^{hf,*} = \frac{1}{4},
\end{aligned} \tag{4}$$

whereby $\mathbb{S}_{cyl}^{hf,*}$ exhibits symmetries $S_{cyl,ijkl}^{hf,*} = S_{cyl,jikl}^{hf,*} = S_{cyl,jilk}^{hf,*}$.

Next, we discuss the expressions for the homogenized quasi-elastic “stiffness” tensor \mathbb{R}_{hf}^* , see Section “Homogenization of cement paste properties”. As for hydrate foam, insertion of the LC-transformed Eshelby tensor expressions (57) and (4) into (56), and further insertion of the thus obtained Hill tensors, together with the vanishing quasi-elastic “stiffnesses” of air and water (see Table 3.1) and the quasi-elastic “stiffness” of hydrates (50), into the expression for the quasi-elastic “stiffness” of the homogenized hydrate foam (55), yields scalar expressions for the LC-transformed bulk and shear moduli, reading as

$$\begin{aligned}
k_{hf}^*(p) &= f_{hyd}^{hf} k_{hyd} A_{\infty,hyd}^{*,vol}(p) \left[\left(f_{air}^{hf} + f_{H_2O}^{hf} \right) A_{\infty,pore}^{*,vol}(p) + f_{hyd}^{hf} A_{\infty,hyd}^{*,vol}(p) \right]^{-1}, \\
\mu_{hf}^*(p) &= f_{hyd}^{hf} \mu_{hyd}^*(p) A_{\infty,hyd}^{*,dev}(p) \left[\left(f_{air}^{hf} + f_{H_2O}^{hf} \right) A_{\infty,pore}^{*,dev}(p) + f_{hyd}^{hf} A_{\infty,dev}^{*,vol}(p) \right]^{-1},
\end{aligned} \tag{5}$$

with $A_{\infty,pore}^{*,vol}$, $A_{\infty,pore}^{*,dev}$, $A_{\infty,hyd}^{*,vol}$, and $A_{\infty,hyd}^{*,dev}$ denoting the LC-transformed volumetric and deviatoric components of the Eshelby problem-related strain concentration tensors for the pores (air and water) and for the hydrates, reading as

$$\begin{aligned}
A_{\infty,pore}^{*,vol}(p) &= \left[1 - S_{sph}^{hf,*,vol}(p) \right]^{-1}, \\
A_{\infty,pore}^{*,dev}(p) &= \left[1 - S_{sph}^{hf,*,dev}(p) \right]^{-1},
\end{aligned} \tag{6}$$

so that, according to (1), we finally have

$$\begin{aligned}
A_{\infty,hyd}^{*,vol}(p) &= \frac{3k_{hf}^*(p) + \mu_{hyd}^*(p) + 3\mu_{hf}^*(p)}{3k_{hyd} + \mu_{hyd}^*(p) + 3\mu_{hf}^*(p)}, \\
A_{\infty,hyd}^{*,dev}(p) &= \left\{ 9k_{hyd} [\mu_{hyd}^*(p)]^2 k_{hf}^*(p) + 64 [\mu_{hf}^*(p)]^4 + \right. \\
&\quad \left[63k_{hyd} + 84k_{hf}^*(p) + 184\mu_{hyd}^*(p) \right] [\mu_{hf}^*(p)]^3 + \\
&\quad \left[156k_{hyd}\mu_{hyd}^*(p) + 120k_{hf}^*(p)\mu_{hyd} + 72 [\mu_{hyd}^*(p)]^2 + 81k_{hyd}k_{hf}^*(p) \right] [\mu_{hf}^*(p)]^2 + \\
&\quad \left[36k_{hf}^*(p) [\mu_{hyd}^*(p)]^2 + 21k_{hyd} [\mu_{hyd}^*(p)]^2 + 90k_{hf}^*(p)k_{hyd}\mu_{hyd}^*(p) \right] \mu_{hf}^*(p) \left. \right\} \\
&\quad \left(5 \left\{ [\mu_{hf}^*(p)]^2 + [(7\mu_{hyd}^*(p) + 3k_{hf}^*(p))] \mu_{hf}^*(p) + 3k_{hf}^*(p)\mu_{hyd}^*(p) \right\} \right. \\
&\quad \left. [\mu_{hf}^*(p) + \mu_{hyd}^*(p)] [3k_{hyd} + \mu_{hyd}^*(p) + 3\mu_{hf}^*(p)] \right)^{-1}.
\end{aligned} \tag{7}$$

As for cement paste, insertion of LC-transformed Eshelby tensor expression (57) into (56), and further insertion of the thus obtained Hill tensor, together with the quasi-elastic “stiffnesses” of cement clinker (see Table 3.1) and of hydrate foam (58), into the expression for the quasi-elastic “stiffness” of the homogenized cement paste (3.26), yields scalar expressions for the LC-transformed bulk and shear moduli, reading as

$$\begin{aligned}
k_{cp}^*(p) &= \left[f_{hf}^{cp} k_{hf}^*(p) + f_{clin}^{cp} k_{clin} A_{\infty,clin}^{*,vol}(p) \right] \left[f_{hf}^{cp} + f_{clin}^{cp} A_{\infty,clin}^{*,vol}(p) \right]^{-1}, \\
\mu_{cp}^*(p) &= \left[f_{hf}^{cp} \mu_{hf}^*(p) + f_{clin}^{cp} \mu_{clin} A_{\infty,clin}^{*,dev}(p) \right] \left[f_{hf}^{cp} + f_{clin}^{cp} A_{\infty,clin}^{*,dev}(p) \right]^{-1},
\end{aligned} \tag{8}$$

with $A_{\infty,clin}^{*,vol}$, $A_{\infty,clin}^{*,dev}$ denoting the LC-transformed volumetric and deviatoric components of the Eshelby problem-related strain concentration tensor for clinker inclusions, reading as

$$\begin{aligned}
A_{\infty,clin}^{*,vol}(p) &= \left[1 + S_{sph}^{hf,*,vol}(p) \frac{k_{clin} - k_{hf}^*(p)}{k_{hf}^*(p)} \right]^{-1}, \\
A_{\infty,clin}^{*,dev}(p) &= \left[1 + S_{sph}^{hf,*,dev}(p) \frac{\mu_{clin} - \mu_{hf}^*(p)}{\mu_{hf}^*(p)} \right]^{-1}.
\end{aligned} \tag{9}$$

Appendix-B1

Multiscale material modeling: Elasticity Homogenization

Consider a representative volume element (RVE) of mortar or concrete (Fig. 4.2) to be subjected spatially homogeneous (“macroscopic”) stress $\underline{\Sigma}$, imposed at the boundary of the material in terms of “microscopic” traction vectors $\underline{T}(\underline{x})$ fulfilling Cauchy’s formula

$$\underline{T}(\underline{x}) = \underline{\Sigma} \cdot \underline{n}(\underline{x}) \quad (10)$$

with \underline{x} as the position vector and \underline{n} as the unit normal vector to the surface of the RVE. Boundary condition (10) together with equilibrium of the microscopic stress field i.e.

$$\operatorname{div} \underline{\sigma}(\underline{x}) = 0 \quad (11)$$

implies the so-called stress average rule (Hashin 1983; Zaoui 2002)

$$\underline{\Sigma} = \frac{1}{V} \int_V \underline{\sigma}(\underline{x}) \, dV, \quad (12)$$

with V as the volume of the RVE. Moreover, stresses $\underline{\sigma}(\underline{x})$ provoke strains $\underline{\varepsilon}(\underline{x})$ which are geometrically compatible with micro-displacements $\underline{\xi}(\underline{x})$ i.e. they satisfy the definition of the linearized strain tensor

$$\underline{\varepsilon}(\underline{x}) = \frac{1}{2} \left[\underline{\nabla} \underline{\xi}(\underline{x}) + {}^t \underline{\nabla} \underline{\xi}(\underline{x}) \right] \quad (13)$$

The external work density done by the traction vectors in (10) along the displacement $\underline{\xi}$ in (13) reads as (Germain et al. 1983)

$$\begin{aligned} W^{ext} &= \frac{1}{V} \int_{\partial V} \underline{T}(\underline{x}) \cdot \underline{\xi}(\underline{x}) \, dS \\ &= \frac{1}{V} \int_{\partial V} [\underline{\Sigma}(\underline{x}) \cdot \underline{n}(\underline{x})] \cdot [\underline{\varepsilon}(\underline{x}) \cdot \underline{x}] \, dS = \underline{\Sigma} : \left[\frac{1}{V} \int_V \underline{\varepsilon}(\underline{x}) \, dV \right] \end{aligned} \quad (14)$$

Eq. (14) clarifies that the macroscopic stress $\underline{\Sigma}$ does work on the spatial average over the microscopic strain. Thus, this average qualifies as the macroscopic strain tensor \underline{E} related to mortar or concrete (Hashin 1983),

$$\underline{E} = \frac{1}{V} \int_V \underline{\varepsilon}(\underline{x}) \, dV. \quad (15)$$

Considering linear elastic material behavior

$$\boldsymbol{\sigma}(\underline{x}) = \mathbf{C}(\underline{x}) : \boldsymbol{\varepsilon}(\underline{x}) \quad (16)$$

and exploiting that the field equations are linear delivered the strain concentration rule

$$\boldsymbol{\varepsilon}(\underline{x}) = \mathbf{A}(\underline{x}) : \mathbf{E} \quad (17)$$

where $\mathbf{A}(\underline{x})$ denotes the strain concentration tensor field. Introducing the phase strain average

$$\boldsymbol{\varepsilon}_i = \frac{1}{V_i} \int_{V_i} \boldsymbol{\varepsilon}(\underline{x}) dV \quad (18)$$

and considering the strain concentration rule (17) delivers

$$\begin{aligned} \boldsymbol{\varepsilon}_i &= \frac{1}{V_i} \int_{V_i} \mathbf{A}(\underline{x}) : \mathbf{E} dV \\ &= \frac{1}{V_i} \int_{V_i} \mathbf{A}(\underline{x}) dV : \mathbf{E} \\ \boldsymbol{\varepsilon}_i &= \mathbf{A}_i : \mathbf{E} \end{aligned} \quad (19)$$

where \mathbf{A}_i is the strain concentration tensor

$$\mathbf{A}_i = \frac{1}{V_i} \int_{V_i} \mathbf{A}(\underline{x}) dV \quad (20)$$

Combination of (18) with phase elasticity law $\boldsymbol{\sigma}_i = \mathbf{C}_i : \boldsymbol{\varepsilon}_i$ and the stress average rule formulated in average phase stresses $\boldsymbol{\sigma}_i$

$$\boldsymbol{\Sigma} = \sum_{i=1}^n f_i \boldsymbol{\sigma}_i \quad (21)$$

where f_i denotes the phase volume fraction, delivers

$$\boldsymbol{\Sigma} = \sum_{i=1}^n f_i \mathbf{C}_i : \mathbf{A}_i : \mathbf{E}$$

such that the homogenized elastic stiffness follows as

$$\mathbf{C}_{hom} = \sum_{i=1}^n f_i \mathbf{C}_i : \mathbf{A}_i. \quad (22)$$

Eq.(22) represents the homogenized stiffness of the microheterogeneous material. Clarifying that knowledge of phase strain concentration tensor, allows

for elasticity upscaling. Also the knowledge of the phase concentration tensors \mathbb{A}_i with $i = 1, 2, \dots, n$) allows for the scale transition from the macrostrain to microstrain as

$$\boldsymbol{\varepsilon}_i = \mathbb{A}_i : \mathbf{E}(t)$$

Consideration of the strain average rule formulated in average phase strains

$$\mathbf{E} = \sum_{i=1}^n f_i \boldsymbol{\varepsilon}_i \quad (23)$$

delivers

$$\mathbf{E} = \left[\sum_{i=1}^n f_i \mathbb{A}_i \right] : \mathbf{E} \quad (24)$$

such that $\mathbb{I} = \sum_{i=1}^n f_i \mathbb{A}_i$ with \mathbb{I} as a symmetric fourth order identity tensor, defined as

$$\mathbb{I}_{ijkl} = \frac{1}{2}(\delta_{ih}\delta_{jl} + \delta_{il}\delta_{jh}). \quad (25)$$

To estimate the phase strain concentration tensors, which are functions of volume fractions of material phases, phase stiffnesses, phase shapes, and interaction of material phases, we use here concept of Zaoui (Zaoui 2002) which is based on matrix-inclusion problems studied by Eshelby (Eshelby 1957). Consider an infinite three dimensional solid with one single ellipsoidal inclusion with uniform strain boundary conditions $\underline{\xi} = \mathbf{E}_\infty : \underline{x}$. The strain inside the inclusion is spatially constant

$$\boldsymbol{\varepsilon}_{inc} = [\mathbb{I} + \mathbb{P}_{inc} : (\mathbf{C}_{inc} - \mathbf{C}_\infty)]^{-1} : \mathbf{E}_\infty \quad (26)$$

here tensor \mathbb{P}_{inc} accounts for the shape of the inclusion, spherical for aggregates and air while needle shaped for the hydrates.

Lets us apply this approach to concrete comprised of two material phases, namely, cement paste and aggregates, in this case the strain average rule read as

$$\mathbf{E} = f_{cp} \boldsymbol{\varepsilon}_{cp} + f_{agg} \boldsymbol{\varepsilon}_{agg} \quad (27)$$

The microstress in the both phases can be written as

$$\begin{aligned} \boldsymbol{\varepsilon}_{cp} &= \mathbb{A}_{cp} : \mathbf{E} \\ \boldsymbol{\varepsilon}_{agg} &= \mathbb{A}_{agg} : \mathbf{E} \end{aligned} \quad (28)$$

where \mathbb{A}_{cp} and \mathbb{A}_{agg} are sought strain concentration tensors. Formation of two Eshelby problems are for cement pastes, and for aggregates, delivers

$$\begin{aligned}\boldsymbol{\varepsilon}_{cp} &= [\mathbb{I} + \mathbb{P}_{cp} : (\mathbb{C}_{cp} - \mathbb{C}_{\infty})^{-1} : \mathbf{E}_{\infty} \\ \boldsymbol{\varepsilon}_{agg} &= [\mathbb{I} + \mathbb{P}_{agg} : (\mathbb{C}_{agg} - \mathbb{C}_{\infty})^{-1} : \mathbf{E}_{\infty}.\end{aligned}\tag{29}$$

We assume that $\boldsymbol{\varepsilon}_{cp}$ and $\boldsymbol{\varepsilon}_{agg}$ in (29) are estimates for average phase strain in the real material, we are left with establishing reasonable links between

- \mathbb{C}_{∞} and stiffness property of the real material
- \mathbf{E}_{∞} and \mathbf{E}

As for the link between \mathbf{E}_{∞} to $\mathbf{E}(t)$, we rewrite (29) in the form

$$\begin{aligned}\boldsymbol{\varepsilon}_{cp} &= \mathbb{A}_{cp\infty} : \mathbf{E}_{\infty} \\ \boldsymbol{\varepsilon}_{agg} &= \mathbb{A}_{agg\infty} : \mathbf{E}_{\infty}\end{aligned}\tag{30}$$

and we insert these equations into the strain average rule (27)

$$\mathbf{E} = f_{cp}\boldsymbol{\varepsilon}_{cp} + f_{agg}\boldsymbol{\varepsilon}_{agg}$$

This delivers

$$\mathbf{E} = [f_{cp}\mathbb{A}_{cp\infty} + f_{agg}\mathbb{A}_{agg\infty}] : \mathbf{E}_{\infty}\tag{31}$$

$$\mathbf{E}_{\infty} = [f_{cp}\mathbb{A}_{cp\infty} + f_{agg}\mathbb{A}_{agg\infty}]^{-1} : \mathbf{E}\tag{32}$$

Insertion of (32) into (30) finally delivers

$$\begin{aligned}\mathbb{A}_{cp} &= \mathbb{A}_{cp\infty} : [f_{cp}\mathbb{A}_{cp\infty} + f_{agg}\mathbb{A}_{agg\infty}]^{-1} \\ \mathbb{A}_{agg} &= \mathbb{A}_{agg\infty} : [f_{cp}\mathbb{A}_{cp\infty} + f_{agg}\mathbb{A}_{agg\infty}]^{-1}\end{aligned}\tag{33}$$

For general n phase composites, the concentration tensors read as (Zaoui 2002)

$$\mathbb{A}_i = [\mathbb{I} + \mathbb{P}_i : (\mathbb{C}_i - \mathbb{C}_{\infty})^{-1} : \left[\sum_{j=1}^n f_j [\mathbb{I} + \mathbb{P}_j : (\mathbb{C}_j - \mathbb{C}_{\infty})^{-1} \right]^{-1}].\tag{34}$$

Inserting (34) into the definition of the homogenized stiffness

$$\mathbb{C}_{hom} = \sum_{i=1}^n f_i \mathbb{C}_i : \mathbb{A}_i$$

delivers

$$\mathbf{C}_{hom} = \sum_{i=1}^n f_i \mathbf{C}_i [\mathbb{I} + \mathbf{P}_i : (\mathbf{C}_i - \mathbf{C}_\infty)^{-1}] : \left[\sum_{j=1}^n f_j [\mathbb{I} + \mathbf{P}_j : (\mathbf{C}_j - \mathbf{C}_\infty)^{-1}] \right]^{-1} \quad (35)$$

As for the link between \mathbf{C}_∞ and a stiffness quantity of the material, there are two possibilities

- $\mathbf{C}_\infty = \mathbf{C}_{hom}$ in case of a polycrystalline arrangement of material phase, delivering a self consistent scheme.
- $\mathbf{C}_\infty = \mathbf{C}_{matrix}^{RVE}$ in case of a matrix inclusion morphology (like concrete), delivering Mori-Tanaka scheme ([Mori and Tanaka 1973](#))

In the present work, all considered phases exhibit isotropic elastic properties, such that their stiffness tensor can be expressed by a superposition of a volumetric and deviatoric part

$$\mathbf{C}_i = 3k_i \mathbb{I}_{vol} + 2\mu_i \mathbb{I}_{dev} \quad (36)$$

$$\mathbf{C}_i^{-1} = \frac{1}{3k_i} \mathbb{I}_{vol} + \frac{1}{2\mu_i} \mathbb{I}_{dev} \quad (37)$$

where $\mathbb{I}_{vol} + \mathbb{I}_{dev} = \mathbb{I}$, and where k_i and μ_i denote the bulk modulus and shear modulus of the phase i . Bulk and shear moduli can also be expressed as functions of elastic Young's modulus E_i : and Poisson's ratio ν_i :

$$k_i = \frac{E_i}{3(1 - 2\nu_i)} \quad \mu_i = \frac{E_i}{2(1 + \nu_i)} \quad (38)$$

Finally the Hill tensors \mathbf{P} ([Hill 1965](#)) for inclusions with spherical shapes reads as

$$\mathbf{P}_{sph} = \mathbf{S}_{sph}(\nu_\infty) : \mathbf{C}_\infty^{-1} \quad (39)$$

where Eshelby tensors \mathbf{S}_{sph} can be expressed as

$$\mathbf{S}_{sph} = \alpha_{sph}(\nu_\infty) \mathbb{I}_{vol} + \beta_{sph}(\nu_\infty) \mathbb{I}_{dev} \quad (40)$$

where α_{sph} and β_{sph} are functions of Poisson's ratio ν_∞ of the infinite matrix: In (40)

$$\alpha_{sph} = \frac{3k_\infty}{3k_\infty + 4\mu_\infty} = \frac{1 + \nu_\infty}{3(1 - \nu_\infty)}$$

$$\beta_{sph} = \frac{6(k_\infty + 2\mu_\infty)}{5(3k_\infty + 4\mu_\infty)} = \frac{2(4 - 5\nu_\infty)}{15(1 - \nu_\infty)} \quad (41)$$

Appendix-B2

Micromechanics involved in creep homogenization for upscaling from Cement paste to Concrete level

Cement pastes exhibit viscoelastic material behavior (Irfan-ul-Hassan et al. 2016),

$$\boldsymbol{\sigma}_{cp}(t) = \int_{-\infty}^t \mathbb{R}_{cp}(t-\tau) : \frac{\partial \boldsymbol{\varepsilon}_{cp}(\tau)}{\partial \tau} d\tau, \quad \boldsymbol{\varepsilon}_{cp}(t) = \int_{-\infty}^t \mathbb{J}_{cp}(t-\tau) : \frac{\partial \boldsymbol{\sigma}_{cp}(\tau)}{\partial \tau} d\tau, \quad (42)$$

where the creep and relaxation tensor functions, \mathbb{J}_{cp} and \mathbb{R}_{cp} , fulfill the convolution condition (Schwarzl and Struik 1968)

$$\int_{-\infty}^t \mathbb{J}_{cp}(t-\tau) : \mathbb{R}_{cp}(\tau) d\tau = \int_{-\infty}^t \mathbb{R}_{cp}(t-\tau) : \mathbb{J}_{cp}(\tau) d\tau = t \mathbb{I}, \quad (43)$$

and where the cement paste creep function has following format

$$\begin{aligned} \mathbb{J}_{cp}(\xi, t-\tau) = & \left[\frac{1-2\nu_{cp}(\xi)}{E_{cp}(\xi)} + \frac{1-2\nu_{cp}(\xi)}{E_{c,cp}(\xi)} \left(\frac{t-\tau}{t_{ref}} \right)^{\beta_{cp}(\xi)} \right] \mathbb{I}_{vol} \\ & + \left[\frac{1+\nu_{cp}(\xi)}{E_{cp}(\xi)} + \frac{1+\nu_{cp}(\xi)}{E_{c,cp}(\xi)} \left(\frac{t-\tau}{t_{ref}} \right)^{\beta_{cp}(\xi)} \right] \mathbb{I}_{dev} \end{aligned} \quad (44)$$

On the other hand, the quartz aggregates and air phases exhibit elastic material behavior,

$$\boldsymbol{\sigma}_j(t) = \mathbb{C}_j : \boldsymbol{\varepsilon}_j(t) \quad \forall j \in \{q, air\}, \quad (45)$$

see Eqs. (4.17) to (4.18), which refer to elastic properties of quartz aggregates and air, respectively. In Eq. (45) the stiffness tensors \mathbb{C}_j play the role of time-invariant (constant) relaxation “functions”,

$$\mathbb{C}_j = \mathbb{R}_j(t-\tau) = 3k_j \mathbb{I}_{vol} + 2\mu_j \mathbb{I}_{dev} \quad \forall j \in \{q, air\}, \quad (46)$$

whereby k_j and μ_j denote the (elastic) bulk and shear modulus of phase j .

Upscaling of this material behavior, up to the level of mortar and concrete, is particularly easily done in the Laplace-Carson (rather than the time) domain.

The Laplace-Carson (LC) transform $f^*(p)$ of any time-dependent function $f(t)$ is defined as

$$f^*(p) = p\hat{f}(p) = p \int_0^{\infty} f(t)e^{-pt} dt, \quad (47)$$

where p is the complex variable in the Laplace-Carson domain, and $\hat{f}(p)$ is the Laplace transform of $f(t)$. Applying the transformation rule (47) to the viscoelastic behavior of the cement paste (42) as well as to the elastic behavior of quartz aggregates and air (46) yields algebraic constitutive equations in the LC space, reading as (Gurtin and Sternberg 1962)

$$\boldsymbol{\varepsilon}_j^*(p) = \mathbb{J}_j^*(p) : \boldsymbol{\sigma}_j^*(p), \quad \boldsymbol{\sigma}_j^*(p) = \mathbb{R}_j^*(p) : \boldsymbol{\varepsilon}_j^*(p) \quad \forall j \in \{cp, q, air\}, \quad (48)$$

whereby the convolution condition (43) is transformed into a simple inversion rule,

$$\mathbb{R}_j^*(p) = [\mathbb{J}_j^*(p)]^{-1}. \quad (49)$$

Hence, LC transformation (47) of the cement paste creep function (44), followed by insertion of the respective result for $\mathbb{J}_{cp}^*(p)$ into (49), yields the LC-transformed relaxation function of cement paste as

$$\begin{aligned} \mathbb{R}_{cp}^*(p) &= 3k_{cp}^*(p)\mathbb{I}_{vol} + 2\mu_{cp}^*(p)\mathbb{I}_{dev} \\ &= \left[\frac{1-2\nu_{cp}}{E_{cp}} + \frac{1-2\nu_{cp}}{E_{c,cp}} \left(\frac{1}{t_{ref}} \right)^{\beta_{cp}} \Gamma(\beta_{cp}+1) p^{-\beta_{cp}} \right]^{-1} \mathbb{I}_{vol} \\ &\quad + \left[\frac{1+\nu_{cp}}{E_{cp}} + \frac{1+\nu_{cp}}{E_{c,cp}} \left(\frac{1}{t_{ref}} \right)^{\beta_{cp}} \Gamma(\beta_{cp}+1) p^{-\beta_{cp}} \right]^{-1} \mathbb{I}_{dev}. \end{aligned} \quad (50)$$

Because Eqs. (48) are formally identical to the relations encountered with linear elasticity homogenization, upscaling of viscoelastic properties to mortar or concrete can be done as quasi-elastic homogenization in the LC space. This is referred to as the correspondence principle (Read 1950, 1951; Laws and McLaughlin 1978; Beurthey and Zaoui 2000; Scheiner and Hellmich 2009). Upscaling is based on the LC-transformed average rules ("the strain average rule $\mathbf{E}(t) = f_{cp} \boldsymbol{\varepsilon}_{cp}(t) + f_q \boldsymbol{\varepsilon}_q(t) + f_{air} \boldsymbol{\varepsilon}_{air}(t)$ ") and ("stress average rule as $\boldsymbol{\Sigma}(t) = f_{cp} \boldsymbol{\sigma}_{cp}(t) + f_q \boldsymbol{\sigma}_q(t) + f_{air} \boldsymbol{\sigma}_{air}(t)$ ") which takes the form in this case as

$$\mathbf{E}^*(p) = f_{cp} \boldsymbol{\varepsilon}_{cp}^*(p) + f_q \boldsymbol{\varepsilon}_q^*(p) + f_{air} \boldsymbol{\varepsilon}_{air}^*(p) \quad (51)$$

$$\boldsymbol{\Sigma}^*(p) = f_{cp} \boldsymbol{\sigma}_{cp}^*(p) + f_q \boldsymbol{\sigma}_q^*(p) + f_{air} \boldsymbol{\sigma}_{air}^*(p) \quad (52)$$

Linearity of the problem defined by (11), (13), and (48) implies a *linear* strain concentration rule from the LC-transformed macrostrains to the LC-transformed microstrains in phase j , reading as

$$\boldsymbol{\varepsilon}_j^*(p) = \mathbb{A}_j^*(p) : \mathbf{E}^*(p) \quad \forall j \in \{cp, q, air\}, \quad (53)$$

where \mathbb{A}_j^* denotes the LC-transformed phase strain concentration tensor, which can be accessed from classical Eshelby-type matrix inclusion problems (Eshelby 1957; Laws and McLaughlin 1978; Benveniste 1987; Zaoui 2002), while considering the matrix-inclusion morphology of mortar and concrete by means of the Mori-Tanaka scheme (Mori and Tanaka 1973; Benveniste 1987). This results in

$$\begin{aligned} \mathbb{A}_j^*(p) = & \left\{ \mathbb{I} + \mathbb{P}_{sph}^*(p) : [\mathbb{R}_j^*(p) - \mathbb{R}_{cp}^*(p)] \right\}^{-1} : \\ & \left(f_{cp} \mathbb{I} + f_q \left\{ \mathbb{I} + \mathbb{P}_{sph}^*(p) : [\mathbb{R}_q^*(p) - \mathbb{R}_{cp}^*(p)] \right\}^{-1} \right. \\ & \left. + f_{air} \left\{ \mathbb{I} + \mathbb{P}_{sph}^*(p) : [\mathbb{R}_{air}^*(p) - \mathbb{R}_{cp}^*(p)] \right\}^{-1} \right)^{-1} \quad \forall j \in \{cp, q, air\} \end{aligned} \quad (54)$$

In Eq. (54), \mathbb{P}_{sph}^* denotes the LC transform of the fourth-order Hill tensor which accounts for the spherical shape of the inclusion phases j embedded in the matrix with “stiffness” \mathbb{R}_{cp}^* , see the Appendix for corresponding mathematical details. Insertion of the macro-to-micro strain concentration relation (53) and of the constitutive behavior (48)₂, into the LC-transformed stress average rule (52) leads, after comparison to the LC-transformed constitutive law at mortar and concrete level, $\boldsymbol{\Sigma}^*(p) = \mathbb{R}_{hom}^*(p) : \mathbf{E}^*(p)$, to the following expression for the LC-transformed homogenized relaxation tensor of mortar and concrete, \mathbb{R}_{hom}^* , reading as

$$\begin{aligned} \mathbb{R}_{hom}^*(p) = & \sum_j f_j \mathbb{R}_j^*(p) : \mathbb{A}_j^*(p) \\ = & \left(f_{cp} \mathbb{R}_{cp}^* + f_q \mathbb{R}_q^*(p) : \left\{ \mathbb{I} + \mathbb{P}_{sph}^*(p) : [\mathbb{R}_q^*(p) - \mathbb{R}_{cp}^*(p)] \right\}^{-1} \right. \\ & \left. + f_{air} \mathbb{R}_{air}^*(p) : \left\{ \mathbb{I} + \mathbb{P}_{sph}^*(p) : [\mathbb{R}_{air}^*(p) - \mathbb{R}_{cp}^*(p)] \right\}^{-1} \right) \\ & : \left(f_{cp} \mathbb{I} + f_q \left\{ \mathbb{I} + \mathbb{P}_{sph}^*(p) : [\mathbb{R}_q^*(p) - \mathbb{R}_{cp}^*(p)] \right\}^{-1} \right. \\ & \left. + f_{air} \left\{ \mathbb{I} + \mathbb{P}_{sph}^*(p) : [\mathbb{R}_{air}^*(p) - \mathbb{R}_{cp}^*(p)] \right\}^{-1} \right)^{-1}. \end{aligned} \quad (55)$$

Back transformation to time domain is done numerically, by means of the Gaver-Wynn-Rho algorithm (Scheiner and Hellmich 2009; Gaver 1966).

Analytical expressions facilitating upscaling in LC space

Upscaling of the creep behavior, up to the larger scales of mortar or concrete, is performed in the LC space, according to the analytical formulae described next. Thereby, we consider that an isotropic fourth-order tensor, \mathbb{G} , can be decomposed into a volumetric part and a deviatoric part as $\mathbb{G} = G^{vol}\mathbb{I}^{vol} + G^{dev}\mathbb{I}^{dev}$, where G^{vol} and G^{dev} , respectively, are the (scalar) volumetric and deviatoric components of the tensor. \mathbb{I}_{vol} and \mathbb{I}_{dev} are the volumetric and deviatoric parts of the fourth-order identity tensor \mathbb{I} , defined as $I_{ijkl} = 1/2(\delta_{ik}\delta_{jl} + \delta_{il}\delta_{jk})$, $\mathbb{I}_{vol} = 1/3(\mathbf{1} \otimes \mathbf{1})$, and $\mathbb{I}_{dev} = \mathbb{I} - \mathbb{I}_{vol}$, respectively, whereby $\mathbf{1}$ denotes the second-order identity tensor with components equal to the Kronecker delta δ_{ij} , namely $\delta_{ij} = 1$ for $i = j$, and 0 otherwise. They satisfy $\mathbb{I}^{vol} : \mathbb{I}^{vol} = \mathbb{I}^{vol}$, $\mathbb{I}^{dev} : \mathbb{I}^{dev} = \mathbb{I}^{dev}$, and $\mathbb{I}^{vol} : \mathbb{I}^{dev} = \mathbb{I}^{dev} : \mathbb{I}^{vol} = 0$.

We start our collection of analytical formulae with the LC-transformed Hill tensors for spherical inclusions embedded in an infinite cement matrix with quasi-elastic “stiffness” \mathbb{R}_{cp}^* , occurring in concentration and stiffness expressions of (55). The Hill tensor reads as

$$\mathbb{P}_{sph}^*(p) = \mathbb{S}_{sph}^*(p) : [\mathbb{R}_{cp}^*(p)]^{-1} \quad (56)$$

In Eq. (56), \mathbb{S}_{sph}^* denotes the LC-transformed Eshelby tensor of a spherical inclusion embedded in an infinite cement paste matrix. The LC-transformed Eshelby tensor \mathbb{S}_{sph}^* is isotropic, and its volumetric and deviatoric components read as (Zaoui 2002; Hellmich et al. 2004)

$$S_{sph}^{*,vol}(p) = \frac{3k_{cp}^*(p)}{3k_{cp}^*(p) + 4\mu_{cp}^*(p)}, \quad S_{sph}^{*,dev}(p) = \frac{6}{5} \frac{k_{cp}^*(p) + 2\mu_{cp}^*(p)}{3k_{cp}^*(p) + 4\mu_{cp}^*(p)}. \quad (57)$$

Next, we discuss the expressions for the homogenized quasi-elastic “stiffness” tensor \mathbb{R}_{hom}^* . As for mortar or concrete, insertion of the LC-transformed Eshelby tensor expressions (57) into (56), and further insertion of the obtained Hill tensor, together with the vanishing quasi-elastic “stiffnesses” of air and the available quasi-elastic “stiffness” of quartz (50), into the expression for the quasi-elastic “stiffness” of the homogenized mortar or concrete (55), yields

scalar expressions for the LC-transformed bulk and shear moduli, reading as

$$\begin{aligned} k_{hom}^*(p) &= [f_{cp}k_{cp}^*(p) + f_{agg}A_{\infty,agg}^{*,vol}(p)] \left[f_{cp}\mathbb{I} + f_{agg}A_{\infty,agg}^{*,vol}(p) + f_{air}A_{\infty,air}^{*,vol}(p) \right]^{-1}, \\ \mu_{hom}^*(p) &= [f_{cp}\mu_{cp}^*(p) + f_{agg}\mu_{agg}A_{\infty,agg}^{*,dev}(p)] \left[f_{cp}\mathbb{I} + f_{agg}A_{\infty,agg}^{*,dev}(p) + f_{air}A_{\infty,air}^{*,dev}(p) \right]^{-1}, \end{aligned} \quad (58)$$

with $A_{\infty,agg}^{*,vol}$, $A_{\infty,agg}^{*,dev}$, $A_{\infty,air}^{*,vol}$, and $A_{\infty,air}^{*,dev}$ denoting the LC-transformed volumetric and deviatoric components of the Eshelby problem-related strain concentration tensors for quartz aggregates and air. As for air, the volumetric and deviatoric components of the strain concentration tensor can be written as

$$\begin{aligned} A_{\infty,air}^{*,vol}(p) &= \left[1 - S_{sph}^{*,vol}(p) \right]^{-1}, \\ A_{\infty,air}^{*,dev}(p) &= \left[1 - S_{sph}^{*,dev}(p) \right]^{-1}, \end{aligned} \quad (59)$$

As for quartz, they read as

$$\begin{aligned} A_{\infty,agg}^{*,vol}(p) &= \left[1 + S_{sph}^{*,vol}(p) \frac{k_{agg} - k_{cp}^*(p)}{k_{cp}^*(p)} \right]^{-1}, \\ A_{\infty,agg}^{*,dev}(p) &= \left[1 + S_{sph}^{*,dev}(p) \frac{\mu_{agg} - \mu_{cp}^*(p)}{\mu_{cp}^*(p)} \right]^{-1}. \end{aligned} \quad (60)$$

PROCEEDINGS OF CONCREEP 10 PUBLISHED BY ASCE:
Mechanics and Physics of Creep, Shrinkage, and Durability of Concrete and Concrete Structures

Minutes-long creep tests on young cement pastes provide access to creep properties relevant for ageing creep with a duration of 2 days

ABSTRACT

Cementitious materials are particularly creep active at early ages. We here perform an ageing creep test on a cement paste sample exhibiting an initial water-to-cement mass ratio amounting to $w/c = 0.50$. The sample is conditioned to 20°C. The creep test is started 24 hours after production and runs for 48 hours. The loading amounts to 15% of the uniaxial compressive strength of the material at the time instant of loading. Inspired by a recently developed new testing protocol consisting of hourly-repeated three-minutes long creep tests [Irfan-ul Hassan et al. \(2015\)](#), we exploit force and deformation readings recorded during the *first three minutes* of our 2-days creep test, i.e. we identify Young's modulus and power-law creep properties. Given that the chemical hydration process does not progress significantly during the analyzed three minutes, the identified creep properties refer to *non-ageing* creep. The identified properties are combined with measurements of autogenous shrinkage, in order to predict the strain evolution over the entire 2-days runtime of our ageing creep test. When fitting of the creep function targets, through an appropriately chosen weight functions, the end of three minutes creep interval, in terms of both absolute creep strain and creep strain rate, then the resulting creep function remarkably well predicts creep up to a time period of 2 days.

INTRODUCTION

Cementitious materials are known to be creep active [Jones and Grasley \(2011\)](#); [Tamtsia and Beaudoin \(2000\)](#); [Briffaut et al. \(2012\)](#); [Zhang et al. \(2014\)](#); [Rossi et al. \(1994\)](#); [Bažant et al. \(2011, 2012\)](#), in particular at early ages [Tamtsia et al. \(2004\)](#); [Bažant et al. \(1976\)](#). In order to study early-age basic creep

of cement pastes, mortars, and concretes, we have developed a new testing protocol involving nondestructive, hourly repeated, three minutes long creep tests [Irfan-ul Hassan et al. \(2015\)](#). Three minutes are so short that the ongoing hydration process does not make a significant progress, i.e. our individual creep tests provide quantitative insight into the creep properties of specific (non-ageing) microstructures of cementitious materials. This raises the question, whether or not it is possible to extrapolate, based on observations carried out during three-minutes creep tests, the strain evolution of the material in much longer creep tests, say with a duration of two days. Herein, this question is exemplary answered based on creep test data obtained from cement paste testing. At first, we describe the tested material and the used test method. Then, characteristic results are presented, followed by identification of Young's modulus and creep properties, based on the measurements obtained during the first three minutes, and the assessment of the extrapolation capabilities. The paper closes with a discussion and conclusions.

MATERIALS AND METHODS

Materials

Raw materials used for production of cement paste are a commercial cement of type CEM I 42.5 N and distilled water. The investigated cement paste exhibits an initial water-to-cement mass ratio amounting to $w/c = 0.50$. We cast cylindrical specimens with a diameter of 70 mm and a height of 300 mm. Right after production, the specimens are sealed against the ambient environment, in order to prevent them from drying. The specimens are stored in a climate chamber conditioned to 20 °C.

Methods

The compression tests are carried out using an electromechanical universal testing machine of type Walter and Bai LFM 150. The used test setup is strongly inspired by the one recently developed for early-age stiffness characterization of cement pastes, see [Karte et al. \(2015\)](#). In more detail, the tested specimen is covered with several layers of a food preservation foil, in order to avoid significant drying. The entire test setup is placed inside an insulated temperature chamber conditioned to 20 °C, see Fig. [A.1 a](#). The specimen is

the central part of a serial arrangement described next. Bottlenecked steel

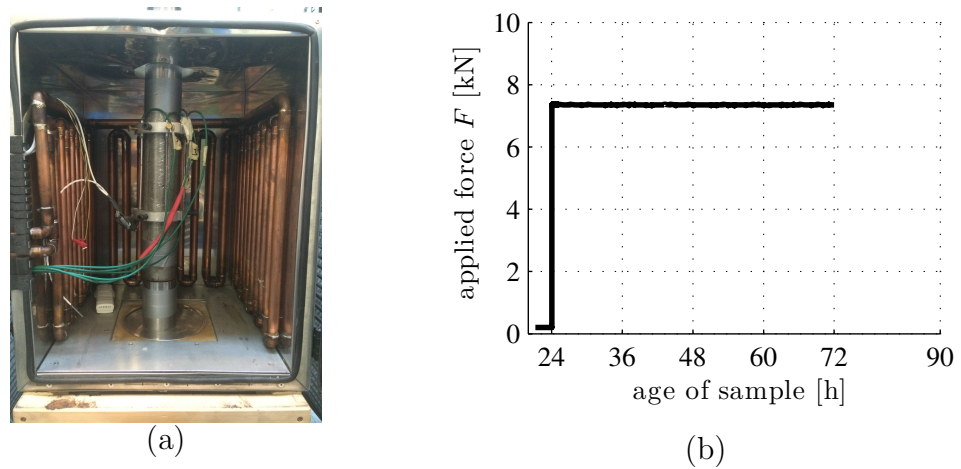


Figure A.1: (a) Test setup consisting of the cement paste specimen, metal cylinders with bottlenecks, two aluminum rings holding five Linear Variable Differential Transducers (LVDTs): view into a climate chamber conditioned to 20 degrees Centigrade, and (b) force history prescribed during the 2-days creep test

cylinders are attached to the top and to the bottom of the specimens, respectively, in order to facilitate a central load application. The force acting on the serial arrangement is measured by means of a force sensor integrated into the testing machine. Deformations of the specimen are measured with five Linear Variable Differential Transducers (LVDTs). To this end, two aluminum rings are attached to the central part of the specimen, by means of three screws per ring. The distance between the two rings amounts to 164 mm. The LVDTs are equally distributed around the specimen, i.e. the spacing amounts to 72° . This setting allows for realization of virtually purely uniaxial stress states in the monitored central part of the specimen - as undesired shear stresses which result from unavoidable friction in the interfaces between steel cylinders and specimen, have decayed to a negligible amount towards this central part [Karte et al. \(2015\)](#).

The 2-days creep tests was started 24 hours after the production of the specimen. Using a loading speed of 7.697 kN/s, corresponding to a specimen-related stress-rate amounting to 2 MPa/s, the loading of the specimen was increased up to 7.15 kN, corresponding to a compressive stress of 1.81 MPa. This amounts to 15% of the uniaxial compressive strength of the material, predicted by a validated multiscale model for uniaxial compressive strength of cement pastes [Pichler and Hellmich \(2011\)](#); [Pichler et al. \(2013\)](#) combined with the hydration

degree evolution determined by quasi-isothermal calorimetry. The force was held constant for 48 hours, such that the test ended once the specimen had reached at an age of three days, see Fig. A.1 b.

RESULTS

The five individual LVDT readings are averaged in order to compute the mean change of length between the two aluminum rings. Specimen strains are computed by dividing the mean change of length between the two aluminum rings by the distance of the two aluminum rings, amounting to 164 mm, see Fig. A.2 a.

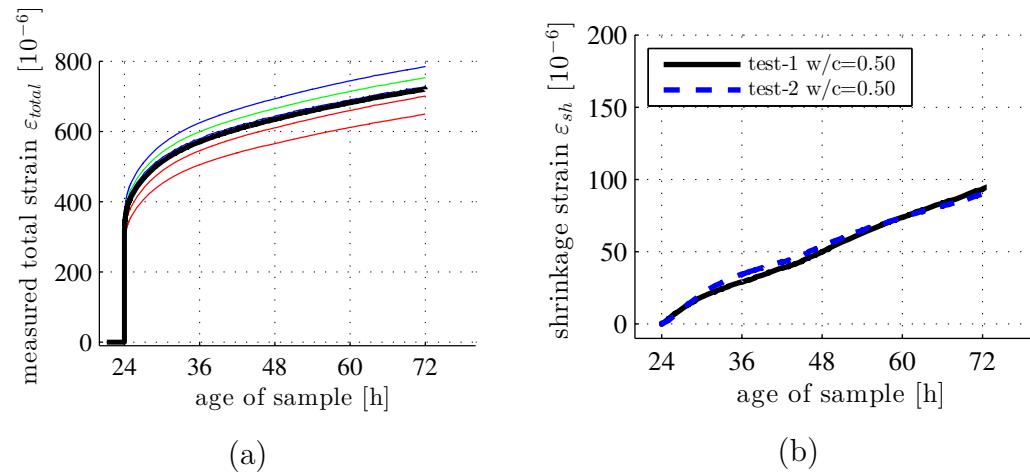


Figure A.2: (a) Strains measured during the 2-days creep test on cement paste with $w/c = 0.50$, subjected at an age of 24 h to a force amounting to 7.15 kN, and (b) shrinkage strain evolution, measured on independent specimens

During the second and third day after production, the chemical hydration reaction progresses significantly, such that significant autogenous shrinkage strains are expected to develop. They were measured in parallel to the 3-minutes creep testing activities described in [Irfan-ul Hassan et al. \(2015\)](#), see Fig. A.2 b.

IDENTIFICATION OF YOUNG'S MODULUS AND CREEP PROPERTIES DURING THE FIRST 3-MINUTES

Following the procedure for Young's modulus identification given in [Irfan-ul Hassan et al. \(2015\)](#), the Young's modulus is determined from the 3 minutes creep test as

$$E = 6.3 \text{ GPa} \quad (61)$$

Based on the identified Young's modulus, and considering that no significant shrinkage happens within three minutes, it is straightforward to extract from the total strain evolution, see Fig. [A.2 a](#), the creep strain evolution:

$$\varepsilon_{creep}(t) = \varepsilon_{total}(t) - \varepsilon_{elastic}(t) = \varepsilon_{total}(t) - \frac{F(t)}{EA} \quad (62)$$

where $F(t)$ is the measured force history, see Fig. [A.1 b](#) and $A = 3848.50 \text{ mm}^2$ stands for the cross-sectional area of the tested specimen, see also Fig. [A.3](#).

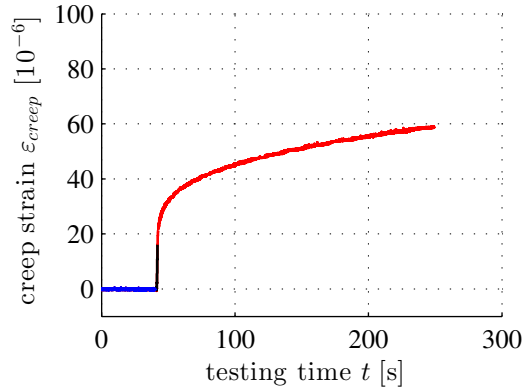


Figure A.3: Creep strains developing during the first three minutes of the 2-days creep test

Power-law creep model

As for identification of creep properties, we follow Tamtsia and Beaudoin [Tamtsia et al. \(2004\)](#) who introduced a power-law model for the creep compliance rate:

$$\frac{dJ(t)}{dt} = C \left(\frac{t - t_0}{t_{ref}} \right)^\gamma \quad (63)$$

Considering a theoretical creep test, where the loading is (i) suddenly increased, at time t_0 , to the the stress level σ_0 , and (ii) held constant thereafter,

the creep strain evolution reads as [Irfan-ul Hassan et al. \(2015\)](#)

$$\varepsilon_{creep}^{mod}(t) = \frac{\sigma_0}{E_c} \left(\frac{t - t_0}{t_{ref}} \right)^\beta \quad t \geq t_0 \quad (64)$$

where $E_c = (\gamma + 1)/(C t_{ref})$ denotes the creep modulus at time $t = t_0 + t_{ref}$ and $\beta = \gamma + 1$ stands, by analogy to γ in Eq. (63), for a dimensionless power-law exponent.

The creep strain evolution derived from our experiments indicates a significant development of creep strains already during the loading phase. This is the motivation to model the force history as a superposition of many small load increments, and to consider Eq. (4) in the framework of Boltzmann's superposition principle [Boltzmann \(1878\)](#).

$$\varepsilon_{creep}^{mod}(t) = \sum_{i=1}^n \frac{F(t_i) - F(t_{i-1})}{A} \left[\frac{1}{E_c} \left(\frac{t - t_i}{t_{ref}} \right)^\beta \right] \quad t_n \leq t \leq t_{n+1} \quad (65)$$

FITTING OF CREEP EVOLUTION OVER 3-MINUTES - AND EXTRAPOLATION CAPABILITIES TO 2-DAYS

Creep modulus E_c and power-law exponent β are identified such that the square root of sum of squares error, \mathcal{E}_{SRSS} , attains a minimum. It quantifies the difference between creep strains evolution $\varepsilon_{creep}(t)$ derived from the experiments, see Fig. A.3, and modeled creep strains evolution $\varepsilon_{creep}^{mod}(t)$, see Eq. (65),

$$\mathcal{E}_{SRSS}(E_c, \beta) = \sqrt{\frac{1}{N} \sum_{i=1}^N \left[\varepsilon_{creep}(t_i) - \varepsilon_{creep}^{mod}(t_i) \right]^2} \rightarrow \min \quad (66)$$

where $N = 5400$ is the total number of experimental readings collected during the first three minutes of the creep test. Optimization problem (66) is solved numerically. At first, intervals are defined for the creep modulus E_c and power-law exponent β . These intervals are subdivided into 7 equidistant values. For all $7 \times 7 = 49$ combinations, error function (66) is evaluated. The parameter combination associated with the smallest error value is treated as a close-to-optimum solution and serves as the basis for the definition of refined

search intervals for the next iteration step [Irfan-ul Hassan et al. \(2015\)](#). This procedure converges towards the following solution,

$$E_c = 9.72 \text{ GPa} \quad \text{and} \quad \beta = 0.23 \quad (67)$$

see also Fig. A.6 for the comparison of measured and model-predicted creep strain evolutions as well as for a contour plot of error function (66).

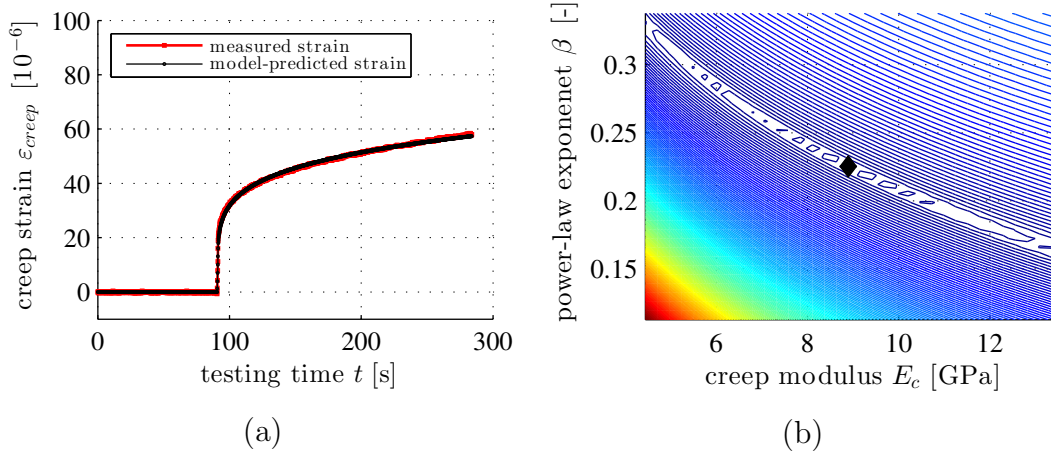


Figure A.4: Illustration of creep property identification: (a) comparison of measured and modeled creep strain evolution, and (b) contour plot of error function (66) as a function of creep modulus and power-law exponent; the marked point refers to the optimal solution (67)

Young's modulus, see (61), and creep properties (67), which were identified from measurements captured during the first three minutes of the 2-days creep test, together with the measured shrinkage strain evolution ε_{sh} , see Fig. A.2 b, are now used to predict the total strain evolution for a 2-days creep test

$$\varepsilon_{total}^{mod}(t) = \frac{F(t)}{EA} + \sum_{i=1}^n \frac{F(t_i) - F(t_{i-1})}{A} \left[\frac{1}{E_c} \left(\frac{t - t_i}{t_{ref}} \right)^\beta \right] + \varepsilon_{sh}(t) \quad (68)$$

$$t_n \leq t \leq t_{n+1}$$

The predicted strain evolution is of the same order of magnitude as the actually measured strain evolution. Typical prediction errors amount to 14%, see Fig. A.7. The reason for this difference is twofold

1. *Non-ageing* creep properties, valid for the microstructure formed 24 hours after production, are used for predicting the *ageing* creep strain evolution measured during the second and third day after production.

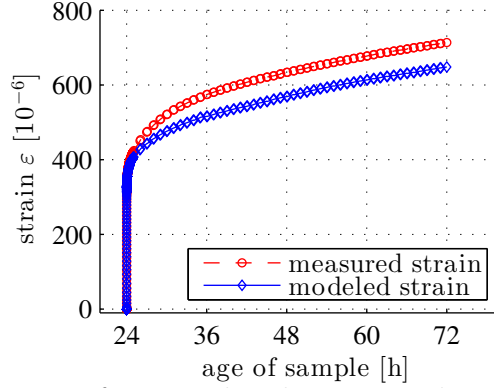


Figure A.5: Comparison of extrapolated strain evolution, see (68) as well as (61) and (67), with measured strain evolution, see Fig. A.3 b

2. Error function (66) is designed to identify a creep modulus and a power-law exponent which explain the measured creep strain evolution in an *overall* optimal fashion, i.e. emphasis is neither layed on the absolute strain values nor on the creep strain rate at the end of the 3-minutes interval.

FITTING OF CREEP EVOLUTION TARGETING THE END OF THE 3-MINUTES PERIOD - AND EXTRAPOLATION CAPABILITIES TO 2-DAYS

In order to improve the quality of extrapolation, we now re-formulate the error function (66) such that the optimization process puts emphasis on the absolute strain values and on the creep strain rate at the end of the 3-minutes interval. To this end, we introduce a weight function $w(t)$ which monotonously increases from the beginning to the end of the three minutes time interval

$$\mathcal{E}_{SRSS}(E_c, \beta, w) = \sqrt{\frac{\sum_{i=1}^N \left[\varepsilon_{creep}(t_i) - \varepsilon_{creep}^{mod}(t_i) \right]^2 w(t_i)}{\sum_{i=1}^N w(t_i)}} \rightarrow \min \quad (69)$$

Herein, we use an exponential for the weight function $w(t_i)$

$$w(t_i) = \exp \left[\ln(\max w) \frac{t_i - t_1}{t_N - t_1} \right] \in [1; \max w] \quad (70)$$

The optimization problem (69) is solved for increasing values of $\max w$, starting with $\max w = 1$. With increasing value of $\max w$, the optimal value of the creep modulus is decreasing, and the optimal value of the power-law exponent is increasing, until $\max w$ amount to one million:

$$\max w = 10^6 \quad (71)$$

Further increase of $\max w$ has no influence on the optimal values of creep modulus and power-law exponent, i.e. a stationary solution is reached:

$$\max w \geq 10^6 : \quad E_c = 7.36 \text{ GPa} \quad \text{and} \quad \beta = 0.25 \quad (72)$$

see also Fig. A.6 for the comparison of measured and model-predicted creep strain evolutions as well as for a contour plot of error function (69) with weight function $w(t_i)$ according to (70) and (71).

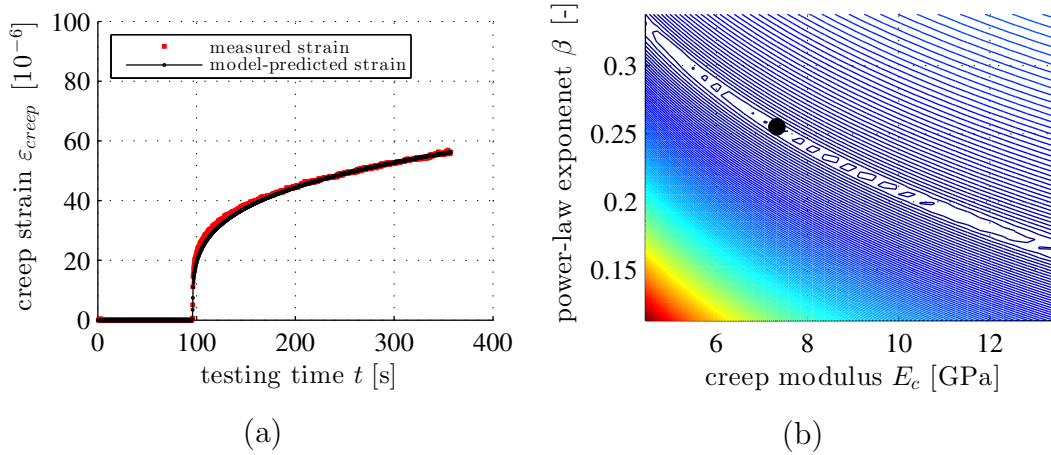


Figure A.6: Illustration of creep property identification (a) comparison of measured and modeled creep strain evolution, and (b) contour plot of error function (69), see also (70) and (71), as a function of creep modulus and power-law exponent; the marked point refers to the optimal solution (72)

Young's modulus, see (61), and creep properties (72), which were identified from measurements captured during the first three minutes of the 2-days creep test, together with the measured shrinkage strain evolution, see Fig. A.2 b, are now used to predict the total strain evolution for a 2-days creep test according to Eq. (68). The predicted strain evolution is closer to the measured strain evolution than before, as quantified by the typical prediction errors which is reduced to 4.5%, see Fig. A.7.

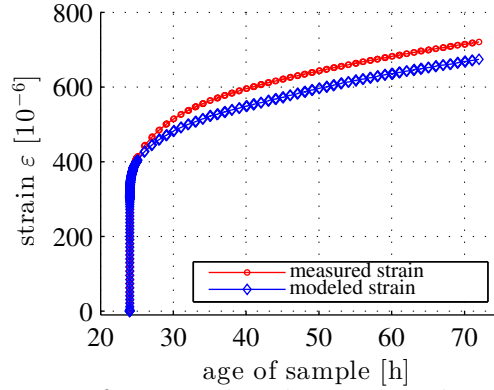


Figure A.7: Comparison of extrapolated strain evolution, see (68) as well as (61) and (72), with measured strain evolution, see Fig. A.2 a

DISCUSSION AND CONCLUSIONS

Herein, we have identified non-ageing creep properties of cement paste with $w/c = 0.50$ which cured at 20°C for 24 hours. To this end, we have exploited measurements taken in the first three minutes of a 2-days creep test. Together with independent shrinkage measurements, we have used the *non-ageing* creep properties for predicting the strain that evolves during the entire duration of the 2-days *ageing* creep test. Extrapolation quality is satisfactory, and this is very remarkable, because three minutes are by a factor of 960 shorter than two days, i.e. the extrapolation distance is very large.

Contour plots of the here-studied error functions (66) and (69), exhibit a valley-shaped structure, see Fig. A.4 b and Fig. A.6 b, respectively. Pairs of values of the creep modulus and the power-law exponent referring to the bottom of the valleys allow for an overall reliable explanation of the creep strain evolution measured in the first three minutes. In order to achieve an optimal extrapolation quality, it is of great importance to identify – among all the parameter combinations referring to the aforementioned valleys – the one parameter combination which explains the absolute strain values and the creep strain rate *at the end* of the three-minutes interval as good as possible.

The satisfactory extrapolation quality underlines that the microstructure formed at the time instant of loading plays an important role for ageing creep tests. In the future, it will be interesting to confront available multiscale models for ageing creep of cement paste Scheiner and Hellmich (2009); Sanahuja (2013b,c) with the experimental data reported herein, and with similar data stemming from tests on cement pastes with different compositions.

Bibliography

- Abate, J. and Valkó, P. (2004). Multi-precision Laplace transform inversion. *International Journal for Numerical Methods in Engineering*, 60(5):979 – 993.
- ACI, . (1992). Report on factors affecting shrinkage and creep of hardened concrete. Technical report, ACI, Farmington Hills, MI, USA.
- Acker, P. (2001). Micromechanical analysis of creep and shrinkage mechanisms. In Ulm, F.-J., Z.P., B., and (Eds.), W. F., editors, *Creep, Shrinkage and Durability Mechanics of Concrete and Other Quasi-brittle Materials*, pages 15 – 26, Amsterdam. 6th International Conference CONCREEP@MIT, Elsevier.
- Acker, P. and Ulm, F.-J. (2001). Creep and shrinkage of concrete: physical origins and practical measurements. *Nuclear Engineering and Design*, 203(2 – 3):143 – 158.
- Atrushi, D. (2003). *Tensile and compressive creep of early age concrete: testing and modelling*. PhD thesis, Norwegian Univ. of Science and Technology, Trondheim, Norway.
- Barthélémy, J.-F. and Dormieux, L. (2003). Détermination du critère de rupture macroscopique d’un milieu poreux par homogénéisation non linéaire [Determination of a macroscopic failure criterion for porous materials using nonlinear homogenization]. *Comptes Rendus Mécanique*, 331(4):271 – 276.
- Bass, J. (2013). *Elasticity of Minerals, Glasses, and Melts*. American Geophysical Union.
- Bazant, Z. (2001). Prediction of concrete creep and shrinkage: past, present and future. *Nuclear Engineering and Design*, 203(1):27 – 38.

- Bažant, Z., Asghari, A., and Schmidt, J. (1976). Experimental study of creep of hardened Portland cement paste at variable water content. *Matériaux et Constructions*, 9(4):279 – 290.
- Bažant, Z. and Chern, J. (1985). Concrete creep at variable humidity: constitutive law and mechanism. *Materials and Structures*, 18(1):1 – 20.
- Bažant, Z. and Prasannan, S. (1989a). Solidification theory for concrete creep. I: Formulation. *Journal of Engineering Mechanics (ASCE)*, 115(8):1691 – 1703.
- Bažant, Z. and Prasannan, S. (1989b). Solidification theory for concrete creep. II: Verification and application. *Journal of Engineering Mechanics (ASCE)*, 115(8):1704 – 1725.
- Bažant, Z., Yu, Q., and Li, G. (2012). Excessive long-time deflections of prestressed box girders. I: Record-span bridge in Palau and other paradigms. *Journal of Structural Engineering*, 138(6):676 – 686.
- Bažant, Z. P., Hubler, M. H., and Yu, Q. (2011). Pervasiveness of excessive segmental bridge deflections: Wake-up call for creep. *ACI Structural Journal*, 108(6):766 – 774.
- Bažant, Z. P. and L’Hermite, R. (1988). *Mathematical modeling of creep and shrinkage of concrete*. Wiley Chichester.
- Baweja, S., G.J., D., and Z.P., B. (1998). Triaxial composite model for basic creep of concrete. *Journal of Engineering Mechanics*, 124(9):959 – 965.
- Bazant, Z. and Li, G.-H. (2008). Comprehensive database on concrete creep and shrinkage. *ACI Materials Journal*, 105(6):635 – 637.
- Bažant, Z. P. and Panula, L. (1978). Practical prediction of time-dependent deformations of concrete. *Matériaux et Construction*, 11(5):307 – 316.
- Bentz, D., Lura, P., and Roberts, J. (2005). Mixture proportioning for internal curing. *Concrete International*, 27(2):35 – 40.
- Benveniste, Y. (1987). A new approach to the application of Mori-Tanaka’s theory in composite materials. *Mechanics of Materials*, 6(2):147 – 157.
- Bernard, O., Ulm, F.-J., and Germaine, J. (2003a). Volume and deviator creep of calcium-leached cement-based materials. *Cement and Concrete Research*, 33(8):1127 – 1136.

- Bernard, O., Ulm, F.-J., and Lemarchand, E. (2003b). A multiscale micromechanics-hydration model for the early-age elastic properties of cement-based materials. *Cement and Concrete Research*, 33(9):1293 – 1309.
- Beurthey, S. and Zaoui, A. (2000). Structural morphology and relaxation spectra of viscoelastic heterogeneous materials. *European Journal of Mechanics-A/Solids*, 19(1):1 – 16.
- Binda, L., Gatti, G., Mangano, G., Poggi, C., and Landriani, G. (1992). Collapse of the civic tower of pavia: a survey of the materials and structure. *Masonry International*, 6(1):11 – 20.
- Boltzmann, L. (1878). Zur Theorie der elastischen Nachwirkung. *Annalen Der Physik - Ann Phys-Berlin*, 241(11):430 – 432.
- Boulay, C., Crespini, M., Delsaute, B., and Staquet, S. (2012). Monitoring of the creep and the relaxation behaviour of concrete since setting time, part 1: compression. In *Strategies for Sustainable Concrete Structures*, pages 1 – 10, France. International Conference on Numerical Modeling Strategies for Sustainable Concrete Structures (SSCS).
- Boulay, C., Staquet, S., Delsaute, B., Carette, J., Crespini, M., Yazoghli-Marzouk, O., Merliot, E., and Ramanich, S. (2014). How to monitor the modulus of elasticity of concrete, automatically since the earliest age? *Materials and structures*, 47(1-2):141 – 155.
- Boumiz, A., Vernet, C., and Cohen Tenoudji, F. (1996). Mechanical properties of cement pastes and mortars at early ages. *Advanced Cement Based Materials*, 3(3-4):94 – 106.
- Briffaut, M., Benboudjema, F., Torrenti, J.-M., and Nahas, G. (2012). Concrete early age basic creep: Experiments and test of rheological modelling approaches. *Construction and Building Materials*, 36:373 – 380.
- Brooks, J. and Neville, A. (1975). Estimating long-term creep and shrinkage from short-term tests. *Magazine of Concrete Research*, 27(90):3–12.
- Carrier, B., Vandamme, M., Pellenq, R.-M., Bornert, M., Ferrage, E., Hubert, F., and Van Damme, H. (2016). Effect of water on elastic and creep properties of self-standing clay films. *Langmuir*. doi: 10.1021/acs.langmuir.5b03431.

- Chen, H., Wyrzykowski, M., Scrivener, K., and Lura, P. (2013). Prediction of self-desiccation in low water-to-cement ratio pastes based on pore structure evolution. *Cement and Concrete Research*, 49:38 – 47.
- Coussy, O. (2004). *Poromechanics*. John Wiley & Sons, England.
- Delsaute, B., Boulay, C., Granja, J., Carette, J., Azenha, M., Dumoulin, C., Karaiskos, G., Deraemaeker, A., and Staquet, S. (2016). Testing concrete E-modulus at very early ages through several techniques: An inter-laboratory comparison. *Strain*, 52(2):91 – 109.
- Delsaute, B., Carette, J., and Staquet, S. (2011). Monitoring of the creep and the relaxation behaviour of concrete at very early age: complementary results on the ceos concrete. In *Proceedings*, pages 1 – 6, Toledo, Spain. 8th International Conference on Fracture Mechanics of Concrete and Concrete Structures (Framcos VIII).
- Delsaute, B. and Staquet, S. (2011). Monitoring of the creep and the relaxation modelling of concrete under tension and compression. In *Proceedings*, pages 168 – 175, Beijing, China. RILEM International Symposium on Concrete Modelling(CONMOD).
- Delsaute, B., Staquet, S., and Boulay, C. (2012). Monitoring of the creep and the relaxation behaviour of concrete since setting time, part 2: tension. In *Strategies for Sustainable Concrete Structures*, pages 1 – 11, France. International Conference on Numerical Modeling Strategies for Sustainable Concrete Structures (SSCS).
- Di Bella, C., Wyrzykowski, M., Griffa, M., Termkhajornkit, P., Chanvilard, G., Stang, H., Eberhardt, A., and Lura, P. (2015). Application of microstructurally-designed mortars for studying early-age properties: Microstructure and mechanical properties. *Cement and Concrete Research*, 78:234 – 244.
- Dilger, W. and Wang, C. (1995). Shrinkage and creep of high performance concrete (hpc)—a critical review. In *Adam Neville Symposium on Concrete Technology, Las Vegas, NV*, pages 59 – 84.
- Dormieux, L., Kondo, D., and Ulm, F.-J. (2006). *Microporomechanics*. John Wiley & Sons, England.

- Erpicum, S., Laugier, F., Pfister, M., Piroton, M., Cicero, G.-M., and Schleiss, A. (2013). *Labyrinth and Piano Key Weirs II*. CRC Press.
- Eshelby, J. (1957). The determination of the elastic field of an ellipsoidal inclusion, and related problems. *Proceedings of the Royal Society of London A: Mathematical, Physical and Engineering Sciences*, 241(1226):376 – 396.
- Feng, G. and Ngan, A. (2002). Effects of creep and thermal drift on modulus measurement using depth-sensing indentation. *Journal of Materials Research*, 17(3):660 – 668.
- Fischer, I., Pichler, B., Lach, E., Turner, C., Barraud, E., and Britz, F. (2014). Compressive strength of cement paste as a function of loading rate: Experiments and engineering mechanics analysis. *Cement and Concrete Research*, 58(0):186 – 200.
- Freyssinet, E. (1933). Idées et voies nouvelles [Ideas and new ways]. *Science et Industrie, Edition mensuelle, Construction travaux publics*, 1:3 – 17. In French.
- Fritsch, A., Dormieux, L., and Hellmich, C. (2006). Porous polycrystals built up by uniformly and axisymmetrically oriented needles: homogenization of elastic properties. *Comptes Rendus Mécanique*, 334(3):151 – 157.
- Fritsch, A., Hellmich, C., and Young, P. (2013). Micromechanics-derived scaling relations for poroelasticity and strength of brittle porous polycrystals. *Journal of Applied Mechanics (ASME)*, 80(2):020905.
- Gaver, D. (1966). Observing stochastic processes, and approximate transform inversion. *Operations Research*, 14(3):444 – 459.
- Germain, P., Nguyen, S., and Suquet, P. (1983). Continuum thermodynamics. *Journal of Applied Mechanics*, 50:1010 – 1020.
- Ghabezloo, S. (2010). Association of macroscopic laboratory testing and micromechanics modelling for the evaluation of the poroelastic parameters of a hardened cement paste. *Cement and Concrete Research*, 40(8):1197 – 1210.
- Ghali, A., Favre, R., and Elbadry, M. (2006). *Concrete structures: Stresses and deformations: Analysis and design for serviceability*. CRC Press.

- Gu, H., Song, G., Dhonde, H., Mo, Y., and Yan, S. (2006). Concrete early-age strength monitoring using embedded piezoelectric transducers. *Smart materials and structures*, 15(6):1837.
- Gurtin, M. and Sternberg, E. (1962). On the linear theory of viscoelasticity. *Archive for Rational Mechanics and Analysis*, 11(1):291 – 356.
- Hachem, F. and Schleiss, A. (2011). Detection of local wall stiffness drop in steel-lined pressure tunnels and shafts of hydroelectric power plants using steep pressure wave excitation and wavelet decomposition. *Journal of Hydraulic Engineering*, 138(1):35 – 45.
- Hanson, J. and Laboratories, B. R. (1953). *A 10-year Study of Creep Properties of Concrete*. Denver: Engineering Laboratories Branch, Design and Construction Division, United States.
- Hashin, Z. (1983). Analysis of composite materials – a survey. *Journal of Applied Mechanics*, 50(3):481 – 505.
- Hatt, W. (1907). Notes on the effect of time element in loading reinforced concrete beams. *In Proceedings: American Society for Testing Materials*, 7:421 – 433.
- Havláek, P. and Jirásek, M. (2012). Modeling of concrete creep based on microprestress-solidification theory. *Acta Polytechnica*, 52(2):34 – 42.
- Hellmich, C., Barthélémy, J.-F., and Dormieux, L. (2004). Mineral–collagen interactions in elasticity of bone ultrastructure—a continuum micromechanics approach. *European Journal of Mechanics-A/Solids*, 23(5):783 – 810.
- Hellmich, C., Lechner, M., Lackner, R., Macht, J., and Mang, H. A. (2001). *Creep in Shotcrete Tunnel Shells*, pages 217 – 229. Springer Netherlands, Dordrecht.
- Hellmich, C. and Mang, H. (2005). Shotcrete elasticity revisited in the framework of continuum micromechanics: from submicron to meter level. *Journal of Materials in Civil Engineering*, 17(3):246 – 256.
- Hellmich, C., Sercombe, J., Ulm, F.-J., and Mang, H. (2000). Modeling of early-age creep of shotcrete. ii: Application to tunneling. *Journal of Engineering Mechanics*, 126(3):292–299.

- Hershey, A. (1954). The elasticity of an isotropic aggregate of anisotropic cubic crystals. *Journal of Applied Mechanics - Transactions of the ASME*, 21(3):236 – 240.
- Hilaire, A., Benboudjema, F., Darquennes, A., Berthaud, Y., and Nahas, G. (2014). Modeling basic creep in concrete at early-age under compressive and tensile loading. *Nuclear Engineering and Design*, 269(0):222 – 230. Special Issue - The International Conference on Structural Mechanics in Reactor Technology (SMiRT21), New Delhi India, Nov 06-11, 2011.
- Hill, R. (1965). Continuum micro-mechanics of elastoplastic polycrystals. *Journal of the Mechanics and Physics of Solids*, 13(2):89 – 101.
- Ioannidou, K., Krakowiak, K., Bauchy, M., Hoover, C., Masoero, E., Yip, S., Ulm, F.-J., Levitz, P., Pellenq, R.-M., and Del Gado, E. (2016). Mesoscale texture of cement hydrates. *Proceedings of the National Academy of Sciences*, 113(8):2029 – 2034.
- Irfan-ul Hassan, M., Pichler, B., Reihnsner, R., and Hellmich, C. (2015). Minutes-long creep tests on young cement pastes provide access to creep properties relevant for ageing creep with a duration of 2 days. In *10th International Conference on Mechanics and Physics of Creep, Shrinkage, and Durability of Concrete and Concrete Structures*. ASCE.
- Irfan-ul-Hassan, M., Pichler, B., Reihnsner, R., and Hellmich, C. (2016). Elastic and creep properties of young cement paste, as determined from hourly repeated minute-long quasi-static tests. *Cement and Concrete Research*, 82:36 – 49.
- Jensen, O. and Lura, P. (2006). Techniques and materials for internal water curing of concrete. *Materials and Structures*, 39(9):817 – 825.
- Jiang, W., De-Schutter, G., and Yuan, Y. (2014). Degree of hydration based prediction of early age basic creep and creep recovery of blended concrete. *Cement and Concrete Composites*, 48:83 – 90.
- Jones, C. and Grasley, Z. (2011). Short-term creep of cement paste during nanoindentation. *Cement and Concrete Composites*, 33(1):12 – 18.
- JSCE, . (2000). Creep and shrinkage of concrete. Technical report, JSCE, Tokyo.

- Justs, J., Wyrzykowski, M., Bajare, D., and Lura, P. (2015). Internal curing by superabsorbent polymers in ultra-high performance concrete. *Cement and Concrete Research*, 76:82 – 90.
- Karte, P., Hlobil, M., Reihnsner, R., Dörner, W., Lahayne, O., Eberhardsteiner, J., and Pichler, B. (2015). Unloading-based stiffness characterization of cement pastes during the second, third, and fourth day after production. *Strain*, 51(2):156 – 169.
- Keeton, J. R. (1965). Study of creep in concrete. Technical report, US Naval civil engineering laboratory, port Hueneme.
- Kolias, S. and Williams, R. (1980). Relationships between the static and the dynamic moduli of elasticity in cement stabilised materials. *Materiaux et Construction*, 13(2):99–107.
- Königsberger, M., Irfan-ul Hassan, M., Pichler, B., and Hellmich, C. (2016). Downscaling-based identification of non-aging power-law creep of cement hydrates. *Journal of Engineering Mechanics*. Accepted for publication.
- Kovler, K. (1994). Testing system for determining the mechanical behaviour of early age concrete under restrained and free uniaxial shrinkage. *Materials and Structures*, 27(6):324 – 330.
- Kröner, E. (1958). Berechnung der elastischen Konstanten des Vielkristalls aus den Konstanten des Einkristalls(calculation of elastic constants of much crystal from the constants of single crystal). *Zeitschrift für Physik*, 151(4):504 – 518.
- Laplante, P. (2003). *Propriétés mécaniques de bétons durcissants: Analyse comparée des bétons classique et à très hautes performances [Mechanical properties of hardening concrete: A comparative analysis of ordinary and high performance concretes]*. PhD thesis, Ecole Nationale des Ponts et Chaussées, Paris.
- Laws, N. (1977). The determination of stress and strain concentrations at an ellipsoidal inclusion in an anisotropic material. *Journal of Elasticity*, 7(1):91–97.
- Laws, N. and McLaughlin, R. (1978). Self-consistent estimates for the viscoelastic creep compliances of composite materials. *Proceedings of the Royal*

- Society of London A: Mathematical, Physical and Engineering Sciences*, 359(1697):251 – 273.
- Le Roy, R., De Larrard, F., and Pons, G. (1996). Calcul des déformations instantanées et différées des bétons à hautes performances. *Extension du domaine d'application des règlements de calcul BAEL/BPEL aux bétons à*, 80:63 – 84.
- Lin, F. and Meyer, C. (2009). Hydration kinetics modeling of Portland cement considering the effects of curing temperature and applied pressure. *Cement and Concrete Research*, 39(4):255–265.
- Luczynski, K., Brynk, T., Ostrowska, B., Swieszkowski, W., Reihsner, R., and Hellmich, C. (2013). Consistent quasistatic and acoustic elasticity determination of poly-l-lactide-based rapid-prototyped tissue engineering scaffolds. *Journal of Biomedical Materials Research Part A*, 101(1):138 – 144.
- Luczynski, K., Thirsfeld, A., Bernardi, J., Eberhardsteiner, J., and Hellmich, C. (2015). Extracellular bone matrix exhibits hardening elastoplasticity and more than double cortical strength: Evidence from homogeneous compression of non-tapered single micron-sized pillars welded to a rigid substrate. *Journal of the Mechanical Behavior of Biomedical Materials*.
- Manzano, H., Masoero, E., Lopez-Arbeloa, I., and Jennings, H. (2013). Shear deformations in calcium silicate hydrates. *Soft Matter*, 9(30):7333 – 7341.
- Manzano, H., Moeini, S., Marinelli, F., Van Duin, A., Ulm, F.-J., and Pellenq, R.-M. (2012). Confined water dissociation in microporous defective silicates: Mechanism, dipole distribution, and impact on substrate properties. *Journal of the American Chemical Society*, 134(4):2208 – 2215.
- MATLAB (2013). *Version R2013(b) including MATLAB Optimization Toolbox Version 6.4*. The MathWorks Inc., Natick, Massachusetts.
- Mazloom, M. (2008). Estimating long-term creep and shrinkage of high-strength concrete. *Cement and Concrete Composites*, 30(4):316 – 326.
- Mori, T. and Tanaka, K. (1973). Average stress in matrix and average elastic energy of materials with misfitting inclusions. *Acta Metallurgica*, 21(5):571 – 574.

- Nehdi, M. and Soliman, A. (2011). Early-age properties of concrete: Overview of fundamental concepts and state-of-the-art research. *Proceedings of Institution of Civil Engineers: Construction Materials*, 164(2):57 – 77.
- Neville, A. (1964). Creep of concrete as a function of its cement paste content. *Magazine of Concrete Research*, 16(46):21 – 30.
- Neville, A. (1971). *Creep of concrete: plain, reinforced, and prestressed*. Elsevier Science, Amsterdam Netherlands.
- Nguyen, D.-T., Alizadeh, R., Beaudoin, J., Pourbeik, P., and Raki, L. (2014). Microindentation creep of monophasic calciumsilicatehydrates. *Cement and Concrete Composites*, 48:118 – 126.
- Němeček, J. (2009). Creep effects in nanoindentation of hydrated phases of cement pastes. *Materials Characterization*, 60(9):1028 – 1034.
- Pellenq, R.-M., Kushima, A., Shahsavari, R., Van Vliet, K., Buehler, M., Yip, S., and Ulm, F.-J. (2009). A realistic molecular model of cement hydrates. *Proceedings of the National Academy of Sciences*, 106(38):16102 – 16107.
- Pichler, B., Fischer, I., Lach, E., Terner, C., Barraud, E., and Britz, F. (2014). The influence of loading rate on the compressive strength of cementitious materials: Experiments and “separation of time scales”-based analysis. In Bicanic, N., de Borst, R., Mang, H., and Meschke, G., editors, *Computational Modelling of Concrete Structures - Proceedings of EURO-C 2014*, volume 2, pages 731 – 739.
- Pichler, B. and Hellmich, C. (2011). Upscaling quasi-brittle strength of cement paste and mortar: A multi-scale engineering mechanics model. *Cement and Concrete Research*, 41(5):467 – 476.
- Pichler, B., Hellmich, C., Eberhardsteiner, J., Wasserbauer, J., Termkhajornkit, P., Barbarulo, R., and Chanvillard, G. (2013). Effect of gel-space ratio and microstructure on strength of hydrating cementitious materials: An engineering micromechanics approach. *Cement and Concrete Research*, 45(0):55 – 68.
- Pichler, B., Hellmich, C., and Mang, H. (2005). Impact of rocks onto gravel design and evaluation of experiments. *International Journal of Impact Engineering*, 31(5):559 – 578.

- Pichler, C. and Lackner, R. (2008). A multiscale creep model as basis for simulation of early-age concrete behavior. *Computers and Concrete*, 5(5):295 – 328.
- Pichler, C. and Lackner, R. (2009). Identification of logarithmic-type creep of calcium-silicate-hydrates by means of nanoindentation. *Strain*, 45(1):17 – 25. cited By 11.
- Powers, T. (1958). Structure and physical properties of hardened Portland cement paste. *Journal of the American Ceramic Society*, 41(1):1 – 6.
- Powers, T. and Brownyard, T. (1946 – 1947). Studies of the physical properties of hardened Portland cement paste. *American Concrete Institute Journal Proceedings*, 18(2 – 8):101–992.
- Powers, T. and Brownyard, T. (1946). Studies of the physical properties of hardened Portland cement paste. *American Concrete Institute*, 18:101 – 132.
- Read, W. (1950). Stress analysis for compressible viscoelastic media. *Journal of Applied Physics*, 21(7):671 – 674.
- Read, W. (1951). General theory of deformation of viscoelastic substances. *Journal of Polymer Sciences*, 7(2-3):191 – 205.
- RILEM, D. L. C. T. (1995). Guidelines for characterizing concrete creep and shrinkage in structural design codes or recommendations. Technical report, RILEM.
- Rossi, P., Godart, N., Robert, J., Gervais, J., and Bruhat, D. (1994). Investigation of the basic creep of concrete by acoustic emission. *Materials and Structures*, 27(113):510 – 514.
- Rossi, P., Tailhan, J.-L., Le Maou, F., Gaillet, L., and Martin, E. (2011). Basic creep behavior of concretes investigation of the physical mechanisms by using acoustic emission. *Cement and Concrete Research*, 42(1):61 – 73.
- Ruiz, M. F., Muttoni, A., and Gambarova, P. (2007). Relationship between non-linear creep and cracking of concrete under uniaxial compression. *Journal of Advanced Concrete Technology*, 5(3):383 – 393.

- Sadowski, P., Kowalczyk-Gajewska, K., and Stupkiewicz, S. (2015). Classical estimates of the effective thermoelastic properties of copper–graphene composites. *Composites Part B: Engineering*, 80:278 – 290.
- Sakata, K. and Shimomura, T. (2004). Recent progress in research on and code evaluation of concrete creep and shrinkage in japan. *Journal of Advanced Concrete Technology*, 2(2):133 – 140.
- Salençon, J. (2001). *Handbook of Continuum Mechanics*. Springer Berlin Heidelberg.
- Sanahuja, J. (2013a). Effective ageing viscoelastic behaviour of solidifying materials : estimations from homogenization of random media. In *Poromechanics V@ sProceedings of the Fifth Biot Conference on Poromechanics*, volume 1-Poromechanics V: Fifth Biot Conference on Poromechanics, pages 1715 – 1724.
- Sanahuja, J. (2013b). Effective behaviour of ageing linear viscoelastic composites: Homogenization approach. *International Journal of Solids and Structures*, 50(19):2846 – 2856.
- Sanahuja, J. (2013c). *Efficient Homogenization of Ageing Creep of Random Media: Application to Solidifying Cementitious Materials*, chapter 23, pages 201 – 210. American Society of Civil Engineers.
- Sanahuja, J. and Dormieux, L. (2010). Creep of a C-S-H gel: a micromechanical approach. *Anais da Academia Brasileira de Ciências (Annals of the Brazilian Academy of Science)*, 82(1):25 – 41.
- Sanahuja, J., Dormieux, L., and Chanvillard, G. (2007). Modelling elasticity of a hydrating cement paste. *Cement and Concrete Research*, 37(10):1427 – 1439.
- Sanahuja, J., Dormieux, L., Meille, S., Hellmich, C., and Fritsch, A. (2010). Micromechanical explanation of elasticity and strength of gypsum: from elongated anisotropic crystals to isotropic porous polycrystals. *Journal of Engineering Mechanics (ASCE)*, 136(2):239 – 253.
- Scheiner, S. and Hellmich, C. (2009). Continuum microviscoelasticity model for ageing basic creep of early-age concrete. *Journal of Engineering Mechanics*, 135(4):307 – 323.

- Schutter, G. and Taerwe, L. (1996). Degree of hydration-based description of mechanical properties of early age concrete. *Materials and Structures*, 29(6):335 – 344.
- Schwarzl, F. and Struik, L. (1968). Analysis of relaxation measurements. *Advances in Molecular Relaxation Processes*, 1(3):201 – 255.
- Sellier, A., Multon, S., Buffo-Lacarrère, L., Vidal, T., Bourbon, X., and Camps, G. (2016). Concrete creep modelling for structural applications: non-linearity, multi-axiality, hydration, temperature and drying effects. *Cement and Concrete Research*, 79:301 – 315.
- Shahidi, M., Pichler, B., and Hellmich, C. (2014). Viscous interfaces as source for material creep: A continuum micromechanics approach. *European Journal of Mechanics - A/Solids*, 45:41 – 58.
- Shahidi, M., Pichler, B., and Hellmich, C. (2015a). Interfacial micromechanics assessment of classical rheological models. I: Single interface size and viscosity. *Journal of Engineering Mechanics*, 142(3):04015092.
- Shahidi, M., Pichler, B., and Hellmich, C. (2016). Interfacial micromechanics assessment of classical rheological models. II: Multiple interface sizes and viscosities. *Journal of Engineering Mechanics*, 142(3):04015093.
- Shahidi, M., Pichler, B., Wendner, R., Scheiner, S., and Hellmich, C. (2015b). Interfacial micromechanics assessment of rheological chain models and their application to early-age creep of concrete. In *10th International Conference on Mechanics and Physics of Creep, Shrinkage, and Durability of Concrete and Concrete Structures (CONCREEP-10)*, pages 260 – 269.
- Shariq, M., Prasad, J., and Abbas, H. (2016). Creep and drying shrinkage of concrete containing {GGBFS}. *Cement and Concrete Composites*, 68:35 – 45.
- Shrive, G., Masia, M., and Lissel, S. (2001). Strengthening and rehabilitation of masonry using fibre reinforced polymers. *Universidad de Calgary, Departamento de Ingeniería Civil, Calgary, Alberta, Canadá*.
- Smith, D. M. (1991). Mechanical properties of mass concrete at early ages. Technical report, DTIC Document, Washington, NY.

- Tamtsia, B. and Beaudoin, J. (2000). Basic creep of hardened cement paste. A re-examination of the role of water. *Cement and Concrete Research*, 30(9):1465 – 1475.
- Tamtsia, B., Beaudoin, J., and Marchand, J. (2004). The early age short-term creep of hardening cement paste: Load-induced hydration effects. *Cement and Concrete Composites*, 26(5):481 – 489.
- Termkhajornkit, P., Barbarulo, R., and Chanvillard, G. (2015). Microstructurally-designed cement pastes: A mimic strategy to determine the relationships between microstructure and properties at any hydration degree. *Cement and Concrete Research*, 71:66 – 77.
- Thomas, J. and Jennings, H. (2006). A colloidal interpretation of chemical aging of the C-S-H gel and its effects on the properties of cement paste. *Cement and Concrete Research*, 36(1):30 – 38.
- Torquato, S. (2013). *Random Heterogeneous Materials: Microstructure and Macroscopic Properties*, volume 16. Springer, New York.
- Ullah, S., Pichler, B., and Hellmich, C. (2013). Modeling ground-shell contact forces in natm tunneling based on three-dimensional displacement measurements. *Journal of Geotechnical and Geoenvironmental Engineering*, 139(3):444–457.
- Ullah, S., Pichler, B., Scheiner, S., and Hellmich, C. (2010). Shell-specific interpolation of measured 3d displacements, for micromechanics-based rapid safety assessment of shotcrete tunnels. *Computer Modeling in Engineering and Sciences (CMES)*, 57(3):279.
- Ullah, S., Pichler, B., Scheiner, S., and Hellmich, C. (2012). Influence of shotcrete composition on load-level estimation in natm-tunnel shells: Micromechanics-based sensitivity analyses. *International Journal for Numerical and Analytical Methods in Geomechanics*, 36(9):1151–1180.
- Ulm, F.-J. and Coussy, O. (1995). Modeling of thermochemomechanical couplings of concrete at early ages. *Journal of Engineering Mechanics*, 121(7):785 – 794.
- Ulm, F. J. and Constantinides, G. and Heukamp, F. H. (2004). Is concrete a poromechanics materials? – a multiscale investigation of poroelastic properties. *Materials and Structures*, 37(1):43 – 58.

- Valkó, P. and Abate, J. (2004). Comparison of sequence accelerators for the Gaver method of numerical Laplace transform inversion. *Computers & Mathematics with Applications*, 48(3):629 – 636.
- Vandamme, M., Bažant, Z., and Keten, S. (2015). Creep of lubricated layered nano-porous solids and application to cementitious materials. *Journal of Nanomechanics and Micromechanics*, 5(4):04015002.
- Vandamme, M. and Ulm, F.-J. (2009). Nanogranular origin of concrete creep. *Proceedings of the National Academy of Sciences of the United States of America*, 106(26):10552 – 10557.
- Vandamme, M. and Ulm, F.-J. (2013). Nanoindentation investigation of creep properties of calcium silicate hydrates. *Cement and Concrete Research*, 52:38 – 52.
- Voigt, T., Akkaya, Y., and Shah, S. (2003). Determination of early age mortar and concrete strength by ultrasonic wave reflections. *Journal of Materials in Civil Engineering*, 15(3):247–254.
- WBCSD (2013). World business council for sustainable development. sustainability benefits of concrete. *WBCSD*.
- Wyrzykowski, M. and Lura, P. (2014). The effect of external load on internal relative humidity in concrete. *Cement and Concrete Research*, 65:58 – 63.
- Wyrzykowski, M., Lura, P., Pesavento, F., and Gawin, D. (2011). Modeling of internal curing in maturing mortar. *Cement and Concrete Research*, 41(12):1349 – 1356.
- Youakim, S. (2006). A simplified method for prediction of long term prestress loss in post tensioned concrete bridges. Technical report, California Department of Transportation, University of California, San Diego, California.
- Yuan, Y. and Wan, Z. (2002). Prediction of cracking within early-age concrete due to thermal, drying and creep behavior. *Cement and Concrete Research*, 32(7):1053 – 1059.
- Zaoui, A. (2002). Continuum micromechanics: Survey. *Journal of Engineering Mechanics*, 128(8):808 – 816.

-
- Zhang, Q. (2014). *Creep properties of cementitious materials effect of water and microstructure. An approach by microindentation*. PhD thesis, Laboratoire Navier, Ecole des Ponts ParisTech, Champs-sur-Marne.
- Zhang, Q., Roy, R., Vandamme, M., and Zuber, B. (2014). Long-term creep properties of cementitious materials: Comparing microindentation testing with macroscopic uniaxial compressive testing. *Cement and Concrete Research*, 58:89 – 98.
- Zhao, J. (1990). *Mechanical properties of concrete at early ages*. University of Ottawa (Canada).
- Zhutovsky, S. and Kovler, K. (2012). Effect of internal curing on durability-related properties of high performance concrete. *Cement and Concrete Research*, 42(1):20 – 26.

List of Figures

2.1	Test setup consisting of the cement paste specimen, metal cylinders with bottleneck, and two aluminum rings holding five LVDTs (a) schematic illustration of symmetric upper half of the test setup, (b) actual test setup inside climate chamber containing two temperature sensors and copper pipes filled with conditioning fluid	13
2.2	Typical force readings captured during a three-minutes creep test	14
2.3	(a) Prediction of compressive strength based on validated multiscale model (Pichler and Hellmich 2011; Pichler et al. 2013) as a function of hydration degree, (b) evolution of hydration degree as a function of material age, derived from quasi-isothermal calorimetry at 20 degrees Celsius	15
2.4	Load plateau values prescribed during creep testing of cement pastes with (a) $w/c = 0.42$, (b) $w/c = 0.45$, and (c) $w/c = 0.50$	15
2.5	Length-changes measured during a creep test on a cement paste specimen with $w/c = 0.42$, subjected at an age of 70 h to a force amounting to 22.79 kN: (a) five individual LVDT readings, (b) mean of five LVDT readings	16
2.6	Stress-strain diagrams referring to unloading at the end of three-minutes creep test: the slope of best linear fit represents the sought unloading modulus E_u	17

2.7	Creep strains evolutions computed according to Eq. (1) for cement paste with $w/c = 0.42$ subjected at an age of 70 h to a force amounting to 22.79 kN: (a) unloading modulus (13.633 GPa) results in nonphysical tensile undershooting, (b) improved estimate of Young's modulus (13.995 GPa) delivers a qualitatively plausible creep strain evolution without tensile undershooting, and (c) overall creep strain evolution obtained with the improved estimate of the (elastic) Young's modulus	18
2.8	Contour plot of the error function (2.6) showing shifting and refinement of search intervals: (a) "old" testing grid with corresponding estimate for optimum solution, in terms of variable combination for E_c and power-law exponent β ; and (b) "new" testing grid for the next iteration of the optimization procedure	21
2.9	Evolution of elastic Young's modulus for cement paste with (a) $w/c = 0.42$, (b) $w/c = 0.45$, and (c) $w/c = 0.50$	22
2.10	Evolution of unloading modulus for cement paste with (a) $w/c = 0.42$, (b) $w/c = 0.45$, and (c) $w/c = 0.50$	22
2.11	Comparison of model predicted strain evolution, see Eq. (66), and measured strain evolution for cement paste with $w/c = 0.42$ subjected at an age of 70 h to a force amounting to 22.79 kN: (a) comparison of total strains, (b) comparison of creep strains; optimal values of E_c and β read as $E_c = 29.94$ GPa and $\beta = 0.22$	23
2.12	Computed error between measured and modeled strain for $w/c = 0.42$: (a) absolute error \mathcal{E}_{SRSS} according to Eq. (2.6), (b) relative error \mathcal{E}_{rel} according to Eq. (2.7)	24
2.13	Evolution of creep modulus E_c for cement paste with (a) $w/c = 0.42$, (b) $w/c = 0.45$, and (c) $w/c = 0.50$	24
2.14	Evolution of power-law exponent β in standard optimization over Tamtsia model for cement paste with (a) $w/c = 0.42$, (b) $w/c = 0.45$, and (c) $w/c = 0.50$	25
2.15	Elastic Young's modulus E as a function of hydration degree, for cement paste with (a) $w/c = 0.42$, (b) $w/c = 0.45$, and (c) $w/c = 0.50$	25

2.16	Creep modulus E_c as a function of hydration degree, for cement paste with (a) $w/c = 0.42$, (b) $w/c = 0.45$, and (c) $w/c = 0.50$	26
2.17	Power law exponent β as a function of hydration degree, for cement paste with (a) $w/c = 0.42$, (b) $w/c = 0.45$, and (c) $w/c = 0.50$	26
2.18	Strain evolution of a specimen loaded, at an age of 70 h, to a force of 22.79 kN for three minutes; and being without load thereafter: measurements and predictions according to Eq. (66)	28
2.19	Creep compliance $\frac{1}{E_c}$ as a function of gel space ratio γ_g for cement pastes with different w/c ratios	29
2.20	Comparison between the static Young's modulus identified herein, with the dynamic Young's modulus reported by Karte et al. (Karte et al. 2015). Very remarkably they turn out to be essentially the same, (a) $w/c = 0.42$, and (b) $w/c = 0.50$	32
2.21	Transition from power law-type to logarithmic creep behavior, shown by example of creep experiments reported by Zhang et al. (Zhang et al. 2014) for mature cement pastes which were tested longer than 75 days: creep functions plotted over (a) linear and (b) logarithmic time scale	33
2.22	Extrapolation from three-minutes non-aging creep tests to two-days aging creep tests of cement paste with $w/c = 0.42$: measured creep strains during two-days creep tests starting at 24 hours age, see dashed curves; and 99% confidence interval of extrapolated creep strain evolution, see shaded domain; corresponding material properties are collected in Table 2.1	34
2.23	Shrinkage strain evolution quantified as the difference of absolute strains measured right <i>before</i> two successive creep tests, for $w/c = 0.42$	35
3.1	Experimentally measured temporal evolutions of viscous creep strains (divided by the applied stress at the loading plateau) and corresponding power-law fits according to Eq. (3.1) for 35 h old cement paste with $w/c \in \{0.42, 0.45, 0.50\}$; quadratic correlation coefficients amount to $R^2 = \{99.7\%, 99.6\%, 99.5\%\}$; see (Irfan-ul-Hassan et al. 2016) for details	40

3.2	Micromechanical representation of cement paste by means of the two-step homogenization scheme of Pichler and Hellmich (2011): (a) RVE of matrix-inclusion composite “cement paste” where a spherical clinker phase is embedded in a hydrate foam matrix [modeled by means of a Mori-Tanaka scheme (Mori and Tanaka 1973; Benveniste 1987; Bernard et al. 2003b)]; (b) polycrystalline RVE of “hydrate foam” built up of spherical capillary porosity (water and air phases), as well as of needle-shaped hydrate phases oriented uniformly in all space directions [modeled by means of a self-consistent scheme (Hershey 1954; Hill 1965; Fritsch et al. 2006)]; all schematic 2D sketches refer to 3D volume elements	42
3.3	Comparison of the experimentally determined and model-predicted viscous strains of cement pastes aged 30, 40, 60, and 144 hours, respectively; the relation between material age and hydration degree is taken from Irfan-ul-Hassan et al. (2016)	50
3.4	Comparison of experimental data (Tamtsia and Beaudoin 2000) for (total) creep functions of 30 year-old cement paste samples with $w/c=0.5$, with corresponding model predictions	51
3.5	Viscous part of the uniaxial creep function of 40 h old cement paste with $w/c \in \{0.42, 0.45, 0.50\}$: point-wisely obtained model predictions and corresponding power-law fits according to Eq. (3.27), with quadratic correlations coefficients $R^2 > 99.9\%$	52
3.6	Model-predicted elastic and creep properties for hydrating cement pastes with hydration degrees $\xi \in [0, 1]$ and exhibiting water-to-cement mass ratios $w/c \in [0.2, 1]$: (a) Young’s elastic modulus, (b) Young’s creep modulus, (c) dimensionless creep exponent	53

- 3.7 Nanoscopic downscaling from hydrate foam microstructure introduced in Fig. 3.2(b): (a) Hybrid Molecular Dynamics - Grand Canonical Monte Carlo simulations suggest emergence of elongated morphological features at the level of the hydrate foam (a); these needles, represented by the needle-shaped hydrate phases shown in Fig. 3.2(b), are made up of hydrate gel (b), consisting itself of gel pores and solid hydrates (c); the latter are built from calcium silicate layers separated or covered by films of confined water 55
- 4.1 Hydration-driven evolution of volume fractions of cement paste constituents (cement, water, hydrates, and voids) according to Powers-Acker's hydration model: (a) complete phase volume evolution diagram according to (Powers and Brownyard 1946; Acker and Ulm 2001); (b) detail illustrating void filling extent α , concerning partial void filling by water that is soaked from the open porosity of quartz into the cement paste matrix 62
- 4.2 Micromechanical representation of mortar and concrete: 2D sketch of 3D matrix-inclusion composites comprising a continuous cement paste matrix with embedded spherical inclusions representing quartz aggregates and air pores 66
- 4.3 Results from hourly-repeated three-minute creep testing on cement pastes with initial water-to-cement mass ratios amounting to 0.42, 0.45, and 0.50, respectively: (a) elastic modulus E_{cp} , (b) creep modulus $E_{c,cp}$, and (c) creep exponent β_{cp} ; as functions of hydration degree, see (Irfan-ul-Hassan et al. 2016) 67
- 4.4 Quantification of effective viscoelastic properties of the cement paste matrix as a function of the effective water-to-cement mass fraction w_{cp}/c , by means of quadratic interpolation between creep test results on plain cement pastes with $w/c \in [0.42, 0.45, 0.50]$: (a) elastic modulus E_{cp} , (b) creep modulus $E_{c,cp}$, and (c) creep exponent β_{cp} ; at degree of hydration $\xi = 0.40$ 68
- 4.5 Relation between elastic modulus and Poisson's ratio of cement pastes with initial water-to-cement mass ratios amounting to 0.42, 0.45, and 0.50, respectively; predictions of the validated multiscale model of Pichler and Lackner (2009) and Pichler and Hellmich (2011) 68

-
- 4.6 Three-minute creep tests on mortars and concretes: (a) force history during creep testing carried out at an age of 100 h on Mortar #1; and (b) prescribed load levels chosen to be smaller than or equal to 15 % of the expected compressive strength 70
- 4.7 Plateau stress-normalized strains obtained from three minute-long creep tests on mortars and concretes, at the hydration degrees given in Eq. (4.19), and the corresponding load plateaus according to Eq. (4.20): (a) Mortar #1: $w/c = 0.50$, $a/c = 3.00$, (b) Mortar #2: $w/c = 0.42$, $a/c = 2.70$, (c) Concrete #1: $w/c = 0.50$, $a/c = 3.00$, (d) Concrete #2: $w/c = 0.42$, $a/c = 2.70$ 71
- 4.8 Application of the water migration model according to Eq. (4.10) to Mortar #1, with a mix-related (nominal) composition given through $w/c = 0.50$ and $a/c = 3.0$, as well as water uptake capacity of quartz and void water-filling extent according to Eq. (4.25): (a) Comparison of experimentally-determined and model-predicted plateau stress-normalized strains, at the hydration degrees given in Eq. (4.19) and the corresponding load plateaus according to Eq. (4.20); (b) evolution of the effective water-to-cement mass fraction of the cement paste matrix, as a function of degree of hydration; for the complete set of material properties of cement paste, see Table 4.3 74
- 4.9 Application of the water migration model according to Eq. (4.10) to Mortar #2, with a mix-related (nominal) composition given through $w/c = 0.42$ and $a/c = 2.7$, as well as water uptake capacity of quartz and void water-filling extent according to Eq. (4.25): (a) Comparison of experimentally-determined and model-predicted plateau stress-normalized strains, at the hydration degrees given in Eq. (4.19) and the corresponding load plateaus according to Eq. (4.20); (b) evolution of effective water-to-cement mass fraction of the cement paste matrix, as a function of degree of hydration; for the complete set of material properties of cement paste, see Table 4.4 76

- 4.10 Application of the water migration model according to Eq. (4.10) to Concrete #1, with a mix-related (nominal) composition given through $w/c = 0.50$ and $a/c = 3.0$, with void water-filling extent according to Eqs. (4.25), as well as with water uptake capacity of quartz and entrapped air volume fraction according to Eq. (4.33): (a) Comparison of experimentally-determined and model-predicted plateau stress-normalized strains, at the hydration degrees given in Eq. (4.19) and the corresponding load plateaus according to Eq. (4.20); (b) evolution of effective water-to-cement mass fraction of the cement paste matrix, as a function of degree of hydration; for the complete set of material properties of cement paste, see Table 4.5 78
- 4.11 Application of the water migration model according to Eq. (4.10) to Concrete #2, with a mix-related (nominal) composition given through $w/c = 0.42$ and $a/c = 2.7$, with void water-filling extent according to Eq. (4.25), with water uptake capacity of quartz according to Eqs. (4.33) and with entrapped air volume fraction according to Eq. (4.37): (a) Comparison of experimentally-determined and model-predicted plateau stress-normalized strains, at the hydration degrees given in Eq. (4.19) and the corresponding load plateaus according to Eq. (4.20); (b) evolution of effective water-to-cement mass fraction of the cement paste matrix, as a function of degree of hydration; for the complete set of material properties of cement paste, see Table 4.6 80
- 4.12 Comparison of experimentally-determined and model-predicted plateau stress-normalized strains, using nominal compositions as input, see Table 4.1, at the hydration degrees given in Eq. (4.19) and the corresponding load plateaus according to Eq. (4.20); For (a) Mortar #1, (b) Mortar #2, (c) Concrete #1, and (d) Concrete #2: Model predicted strains overestimate the experimentally measured strains; see also Table 4.2 82
- 5.1 Force and stress values prescribed during loading plateau for creep testing of cement pastes; (a) CP-1, $w/c = 0.42$, (b) CP-2, $w/c = 0.45$, and (c) CP-3, $w/c = 0.50$ 89
- 5.2 Force and stress values prescribed during loading plateau for creep testing of mortars and concretes 89

-
- 5.3 Measured strain evolution normalized with respect to the plateau stress as a function of the time since start of loading: cement paste with $w/c = 0.42$; ambient air temperature = 20 °C; ID = “CP-1 S-1”, see Table 5.1; as for load levels, see Fig. 5.1(a) 90
- 5.4 Measured strain evolution normalized with respect to the plateau stress as a function of the time since start of loading: cement paste with $w/c = 0.42$; ambient air temperature = 20 °C; ID = “CP-1 S-1”, see Table 5.1; as for load levels, see Fig. 5.1(a) 91
- 5.5 Measured strain evolution normalized with respect to the plateau stress as a function of the time since start of loading: cement paste with $w/c = 0.42$; ambient air temperature = 20 °C; ID = “CP-1 S-1”, see Table 5.1; as for load levels, see Fig. 5.1(a) 92
- 5.6 Measured strain evolution normalized with respect to the plateau stress as a function of the time since start of loading: cement paste with $w/c = 0.42$; ambient air temperature = 20 °C; ID = “CP-1 S-1”, see Table 5.1; as for load levels, see Fig. 5.1(a) 93
- 5.7 Measured strain evolution normalized with respect to the plateau stress as a function of the time since start of loading: cement paste with $w/c = 0.42$; ambient air temperature = 20 °C; ID = “CP-1 S-2”, see Table 5.1; as for load levels, see Fig. 5.1(a) 94
- 5.8 Measured strain evolution normalized with respect to the plateau stress as a function of the time since start of loading: cement paste with $w/c = 0.42$; ambient air temperature = 20 °C; ID = “CP-1 S-2”, see Table 5.1; as for load levels, see Fig. 5.1(a) 95
- 5.9 Measured strain evolution normalized with respect to the plateau stress as a function of the time since start of loading: cement paste with $w/c = 0.42$; ambient air temperature = 20 °C; ID = “CP-1 S-2”, see Table 5.1; as for load levels, see Fig. 5.1(a) 96
- 5.10 Measured strain evolution normalized with respect to the plateau stress as a function of the time since start of loading: cement paste with $w/c = 0.42$; ambient air temperature = 20 °C; ID = “CP-1 S-2”, see Table 5.1; as for load levels, see Fig. 5.1(a) 97
- 5.11 Measured strain evolution normalized with respect to the plateau stress as a function of the time since start of loading: cement paste with $w/c = 0.45$; ambient air temperature = 20 °C; ID = “CP-2 S-1”, see Table 5.1; as for load levels, see Fig. 5.1(b) 98

-
- 5.12 Measured strain evolution normalized with respect to the plateau stress as a function of the time since start of loading: cement paste with $w/c = 0.45$; ambient air temperature = 20°C ; ID = “CP-2 S-1”, see Table 5.1; as for load levels, see Fig. 5.1(b) 99
- 5.13 Measured strain evolution normalized with respect to the plateau stress as a function of the time since start of loading: cement paste with $w/c = 0.45$; ambient air temperature = 20°C ; ID = “CP-2 S-1”, see Table 5.1; as for load levels, see Fig. 5.1(b) 100
- 5.14 Measured strain evolution normalized with respect to the plateau stress as a function of the time since start of loading: cement paste with $w/c = 0.45$; ambient air temperature = 20°C ; ID = “CP-2 S-1”, see Table 5.1; as for load levels, see Fig. 5.1(b) 101
- 5.15 Measured strain evolution normalized with respect to the plateau stress as a function of the time since start of loading: cement paste with $w/c = 0.45$; ambient air temperature = 20°C ; ID = “CP-2 S-2”, see Table 5.1; as for load levels, see Fig. 5.1(b) 102
- 5.16 Measured strain evolution normalized with respect to the plateau stress as a function of the time since start of loading: cement paste with $w/c = 0.45$; ambient air temperature = 20°C ; ID = “CP-2 S-2”, see Table 5.1; as for load levels, see Fig. 5.1(b) 103
- 5.17 Measured strain evolution normalized with respect to the plateau stress as a function of the time since start of loading: cement paste with $w/c = 0.45$; ambient air temperature = 20°C ; ID = “CP-2 S-2”, see Table 5.1; as for load levels, see Fig. 5.1(b) 104
- 5.18 Measured strain evolution normalized with respect to the plateau stress as a function of the time since start of loading: cement paste with $w/c = 0.45$; ambient air temperature = 20°C ; ID = “CP-2 S-2”, see Table 5.1; as for load levels, see Fig. 5.1(b) 105
- 5.19 Measured strain evolution normalized with respect to the plateau stress as a function of the time since start of loading: cement paste with $w/c = 0.50$; ambient air temperature = 20°C ; ID = “CP-3 S-1”, see Table 5.1; as for load levels, see Fig. 5.1(c) 106
- 5.20 Measured strain evolution normalized with respect to the plateau stress as a function of the time since start of loading: cement paste with $w/c = 0.50$; ambient air temperature = 20°C ; ID = “CP-3 S-1”, see Table 5.1; as for load levels, see Fig. 5.1(c) 107

-
- 5.21 Measured strain evolution normalized with respect to the plateau stress as a function of the time since start of loading: cement paste with $w/c = 0.50$; ambient air temperature = 20°C ; ID = “CP-3 S-1”, see Table 5.1; as for load levels, see Fig. 5.1(c) 108
- 5.22 Measured strain evolution normalized with respect to the plateau stress as a function of the time since start of loading: cement paste with $w/c = 0.50$; ambient air temperature = 20°C ; ID = “CP-3 S-1”, see Table 5.1; as for load levels, see Fig. 5.1(c) 109
- 5.23 Measured strain evolution normalized with respect to the plateau stress as a function of the time since start of loading: cement paste with $w/c = 0.50$; ambient air temperature = 20°C ; ID = “CP-3 S-2”, see Table 5.1; as for load levels, see Fig. 5.1(c) 110
- 5.24 Measured strain evolution normalized with respect to the plateau stress as a function of the time since start of loading: cement paste with $w/c = 0.50$; ambient air temperature = 20°C ; ID = “CP-3 S-2”, see Table 5.1; as for load levels, see Fig. 5.1(c) 111
- 5.25 Measured strain evolution normalized with respect to the plateau stress as a function of the time since start of loading: cement paste with $w/c = 0.50$; ambient air temperature = 20°C ; ID = “CP-3 S-2”, see Table 5.1; as for load levels, see Fig. 5.1(c) 112
- 5.26 Measured strain evolution normalized with respect to the plateau stress as a function of the time since start of loading: cement paste with $w/c = 0.50$; ambient air temperature = 20°C ; ID = “CP-3 S-2”, see Table 5.1; as for load levels, see Fig. 5.1(c) 113
- 5.27 Measured strain evolution normalized with respect to the plateau stress as a function of the time since start of loading: cement paste with $w/c = 0.42$; ambient air temperature = 30°C ; ID = “CP-4 S-1”, see Table 5.1; as for load levels, see Fig. 5.1(a) 114
- 5.28 Measured strain evolution normalized with respect to the plateau stress as a function of the time since start of loading: cement paste with $w/c = 0.42$; ambient air temperature = 30°C ; ID = “CP-4 S-1”, see Table 5.1; as for load levels, see Fig. 5.1(a) 115
- 5.29 Measured strain evolution normalized with respect to the plateau stress as a function of the time since start of loading: cement paste with $w/c = 0.42$; ambient air temperature = 30°C ; ID = “CP-4 S-1”, see Table 5.1; as for load levels, see Fig. 5.1(a) 116

-
- 5.30 Measured strain evolution normalized with respect to the plateau stress as a function of the time since start of loading: cement paste with $w/c = 0.42$; ambient air temperature = $30\text{ }^{\circ}\text{C}$; ID = “CP-4 S-1”, see Table 5.1; as for load levels, see Fig. 5.1(a) 117
- 5.31 Measured strain evolution normalized with respect to the plateau stress as a function of the time since start of loading: cement paste with $w/c = 0.42$; ambient air temperature = $30\text{ }^{\circ}\text{C}$; ID = “CP-4 S-2”, see Table 5.1; as for load levels, see Fig. 5.1(a) 118
- 5.32 Measured strain evolution normalized with respect to the plateau stress as a function of the time since start of loading: cement paste with $w/c = 0.42$; ambient air temperature = $30\text{ }^{\circ}\text{C}$; ID = “CP-4 S-2”, see Table 5.1; as for load levels, see Fig. 5.1(a) 119
- 5.33 Measured strain evolution normalized with respect to the plateau stress as a function of the time since start of loading: cement paste with $w/c = 0.42$; ambient air temperature = $30\text{ }^{\circ}\text{C}$; ID = “CP-4 S-2”, see Table 5.1; as for load levels, see Fig. 5.1(a) 120
- 5.34 Measured strain evolution normalized with respect to the plateau stress as a function of the time since start of loading: cement paste with $w/c = 0.50$; ambient air temperature = $30\text{ }^{\circ}\text{C}$; ID = “CP-4 S-2”, see Table 5.1; as for load levels, see Fig. 5.1(a) 121
- 5.35 Measured strain evolution normalized with respect to the plateau stress as a function of the time since start of loading: cement paste with $w/c = 0.42$; ambient air temperature = $10\text{ }^{\circ}\text{C}$; ID = “CP-5 S-1”, see Table 5.1; as for load levels, see Fig. 5.1(a) 122
- 5.36 Measured strain evolution normalized with respect to the plateau stress as a function of the time since start of loading: cement paste with $w/c = 0.42$; ambient air temperature = $10\text{ }^{\circ}\text{C}$; ID = “CP-5 S-1”, see Table 5.1; as for load levels, see Fig. 5.1(a) 123
- 5.37 Measured strain evolution normalized with respect to the plateau stress as a function of the time since start of loading: cement paste with $w/c = 0.42$; ambient air temperature = $10\text{ }^{\circ}\text{C}$; ID = “CP-5 S-1”, see Table 5.1; as for load levels, see Fig. 5.1(a) 124
- 5.38 Measured strain evolution normalized with respect to the plateau stress as a function of the time since start of loading: cement paste with $w/c = 0.42$; ambient air temperature = $10\text{ }^{\circ}\text{C}$; ID = “CP-5 S-1”, see Table 5.1; as for load levels, see Fig. 5.1(a) 125

5.39	Measured strain evolution normalized with respect to the plateau stress as a function of the time since start of loading: cement paste with $w/c = 0.42$; ambient air temperature = 10°C ; ID = “CP-5 S-2”, see Table 5.1; as for load levels, see Fig. 5.1(a)	126
5.40	Measured strain evolution normalized with respect to the plateau stress as a function of the time since start of loading: cement paste with $w/c = 0.42$; ambient air temperature = 10°C ; ID = “CP-5 S-2”, see Table 5.1; as for load levels, see Fig. 5.1(a)	127
5.41	Measured strain evolution normalized with respect to the plateau stress as a function of the time since start of loading: cement paste with $w/c = 0.42$; ambient air temperature = 10°C ; ID = “CP-5 S-2”, see Table 5.1; as for load levels, see Fig. 5.1(a)	128
5.42	Measured strain evolution normalized with respect to the plateau stress as a function of the time since start of loading: cement paste with $w/c = 0.42$; ambient air temperature = 10°C ; ID = “CP-5 S-2”, see Table 5.1; as for load levels, see Fig. 5.1(a)	129
5.43	Evolution of (a) elastic Young’s modulus E_{cp} (b) creep modulus $E_{c,cp}$ (c) power-law exponent β_{cp} , for cement paste CP-1	130
5.44	Evolution of (a) elastic Young’s modulus E_{cp} (b) creep modulus $E_{c,cp}$ (c) power-law exponent β_{cp} , for cement paste CP-2	130
5.45	Evolution of (a) elastic Young’s modulus E_{cp} (b) creep modulus $E_{c,cp}$ (c) power-law exponent β_{cp} , for cement paste CP-3	130
5.46	Evolution of (a) elastic Young’s modulus E_{cp} (b) creep modulus $E_{c,cp}$ (c) power-law exponent β_{cp} , for cement paste CP-4	131
5.47	Evolution of (a) elastic Young’s modulus E_{cp} (b) creep modulus $E_{c,cp}$ (c) power-law exponent β_{cp} , for cement paste CP-5	131
5.48	Measured strain evolution normalized with respect to the plateau stress as a function of the time since start of loading: mortar with $w/c = 0.42$, $a/c = 2.70$; ambient air temperature = 20°C ; ID = “M-1 S-1”, see Table 5.1; as for load levels, see Fig. 5.2	132

5.49 Measured strain evolution normalized with respect to the plateau stress as a function of the time since start of loading: mortar with $w/c = 0.42$, $a/c = 2.70$; ambient air temperature = 20°C ; ID = “M-1 S-1”, see Table 5.1; as for load levels, see Fig. 5.2	133
5.50 Measured strain evolution normalized with respect to the plateau stress as a function of the time since start of loading: cement paste with $w/c = 0.42$, $a/c = 2.70$; ambient air temperature = 20°C ; ID = “M-1 S-1”, see Table 5.1; as for load levels, see Fig. 5.2	134
5.51 Measured strain evolution normalized with respect to the plateau stress as a function of the time since start of loading: mortar with $w/c = 0.42$, $a/c = 2.70$; ambient air temperature = 20°C ; ID = “M-1 S-1”, see Table 5.1; as for load levels, see Fig. 5.2	135
5.52 Measured strain evolution normalized with respect to the plateau stress as a function of the time since start of loading: mortar with $w/c = 0.42$, $a/c = 2.70$; ambient air temperature = 20°C ; ID = “M-1 S-2”, see Table 5.1; as for load levels, see Fig. 5.2	136
5.53 Measured strain evolution normalized with respect to the plateau stress as a function of the time since start of loading: mortar with $w/c = 0.42$, $a/c = 2.70$; ambient air temperature = 20°C ; ID = “M-1 S-2”, see Table 5.1; as for load levels, see Fig. 5.2	137
5.54 Measured strain evolution normalized with respect to the plateau stress as a function of the time since start of loading: mortar with $w/c = 0.42$, $a/c = 2.70$; ambient air temperature = 20°C ; ID = “M-1 S-2”, see Table 5.1; as for load levels, see Fig. 5.2	138
5.55 Measured strain evolution normalized with respect to the plateau stress as a function of the time since start of loading: mortar with $w/c = 0.42$, $a/c = 2.70$; ambient air temperature = 20°C ; ID = “M-1 S-2”, see Table 5.1; as for load levels, see Fig. 5.2	139

5.56 Measured strain evolution normalized with respect to the plateau stress as a function of the time since start of loading: mortar with $w/c = 0.45$, $a/c = 2.80$; ambient air temperature = 20°C ; ID = “M-2 S-1”, see Table 5.1; as for load levels, see Fig. 5.2	140
5.57 Measured strain evolution normalized with respect to the plateau stress as a function of the time since start of loading: mortar with $w/c = 0.45$, $a/c = 2.80$; ambient air temperature = 20°C ; ID = “M-2 S-1”, see Table 5.1; as for load levels, see Fig. 5.2	141
5.58 Measured strain evolution normalized with respect to the plateau stress as a function of the time since start of loading: mortar with $w/c = 0.45$, $a/c = 2.80$; ambient air temperature = 20°C ; ID = “M-2 S-1”, see Table 5.1; as for load levels, see Fig. 5.2	142
5.59 Measured strain evolution normalized with respect to the plateau stress as a function of the time since start of loading: mortar with $w/c = 0.45$, $a/c = 2.80$; ambient air temperature = 20°C ; ID = “M-2 S-1”, see Table 5.1; as for load levels, see Fig. 5.2	143
5.60 Measured strain evolution normalized with respect to the plateau stress as a function of the time since start of loading: mortar with $w/c = 0.45$, $a/c = 2.80$; ambient air temperature = 20°C ; ID = “M-2 S-2”, see Table 5.1; as for load levels, see Fig. 5.2	144
5.61 Measured strain evolution normalized with respect to the plateau stress as a function of the time since start of loading: mortar with $w/c = 0.45$, $a/c = 2.80$; ambient air temperature = 20°C ; ID = “M-2 S-2”, see Table 5.1; as for load levels, see Fig. 5.2	145
5.62 Measured strain evolution normalized with respect to the plateau stress as a function of the time since start of loading: mortar with $w/c = 0.45$, $a/c = 2.80$; ambient air temperature = 20°C ; ID = “M-2 S-2”, see Table 5.1; as for load levels, see Fig. 5.2	146

5.63 Measured strain evolution normalized with respect to the plateau stress as a function of the time since start of loading: mortar with $w/c = 0.45$, $a/c = 2.80$; ambient air temperature = 20 °C; ID = “M-2 S-2”, see Table 5.1; as for load levels, see Fig. 5.2	147
5.64 Measured strain evolution normalized with respect to the plateau stress as a function of the time since start of loading: mortar with $w/c = 0.50$, $a/c = 3.0$; ambient air temperature = 20 °C; ID = “M-3 S-1”, see Table 5.1; as for load levels, see Fig. 5.2	148
5.65 Measured strain evolution normalized with respect to the plateau stress as a function of the time since start of loading: mortar with $w/c = 0.50$, $a/c = 3.0$; ambient air temperature = 20 °C; ID = “M-3 S-1”, see Table 5.1; as for load levels, see Fig. 5.2	149
5.66 Measured strain evolution normalized with respect to the plateau stress as a function of the time since start of loading: mortar with $w/c = 0.50$, $a/c = 3.0$; ambient air temperature = 20 °C; ID = “M-3 S-1”, see Table 5.1; as for load levels, see Fig. 5.2	150
5.67 Measured strain evolution normalized with respect to the plateau stress as a function of the time since start of loading: mortar with $w/c = 0.50$, $a/c = 3.0$; ambient air temperature = 20 °C; ID = “M-3 S-1”, see Table 5.1; as for load levels, see Fig. 5.2	151
5.68 Measured strain evolution normalized with respect to the plateau stress as a function of the time since start of loading: mortar with $w/c = 0.50$, $a/c = 3.0$; ambient air temperature = 20 °C; ID = “M-3 S-2”, see Table 5.1; as for load levels, see Fig. 5.2	152
5.69 Measured strain evolution normalized with respect to the plateau stress as a function of the time since start of loading: mortar with $w/c = 0.50$, $a/c = 3.0$; ambient air temperature = 20 °C; ID = “M-3 S-2”, see Table 5.1; as for load levels, see Fig. 5.2	153

5.70 Measured strain evolution normalized with respect to the plateau stress as a function of the time since start of loading: mortar with $w/c = 0.50$, $a/c = 3.0$; ambient air temperature = 20°C ; ID = “M-3 S-2”, see Table 5.1; as for load levels, see Fig. 5.2	154
5.71 Measured strain evolution normalized with respect to the plateau stress as a function of the time since start of loading: mortar with $w/c = 0.50$, $a/c = 3.0$; ambient air temperature = 20°C ; ID = “M-3 S-2”, see Table 5.1; as for load levels, see Fig. 5.2	155
5.72 Measured strain evolution normalized with respect to the plateau stress as a function of the time since start of loading: mortar with $w/c = 0.42$, $a/c = 1.35$; ambient air temperature = 20°C ; ID = “M-4 S-1”, see Table 5.1; as for load levels, see Fig. 5.2	156
5.73 Measured strain evolution normalized with respect to the plateau stress as a function of the time since start of loading: mortar with $w/c = 0.42$, $a/c = 1.35$; ambient air temperature = 20°C ; ID = “M-4 S-1”, see Table 5.1; as for load levels, see Fig. 5.2	157
5.74 Measured strain evolution normalized with respect to the plateau stress as a function of the time since start of loading: mortar with $w/c = 0.42$, $a/c = 1.35$; ambient air temperature = 20°C ; ID = “M-4 S-1”, see Table 5.1; as for load levels, see Fig. 5.2	158
5.75 Measured strain evolution normalized with respect to the plateau stress as a function of the time since start of loading: mortar with $w/c = 0.42$, $a/c = 1.35$; ambient air temperature = 20°C ; ID = “M-4 S-1”, see Table 5.1; as for load levels, see Fig. 5.2	159
5.76 Measured strain evolution normalized with respect to the plateau stress as a function of the time since start of loading: mortar with $w/c = 0.42$, $a/c = 1.35$; ambient air temperature = 20°C ; ID = “M-4 S-2”, see Table 5.1; as for load levels, see Fig. 5.2	160

5.77 Measured strain evolution normalized with respect to the plateau stress as a function of the time since start of loading: mortar with $w/c = 0.42$, $a/c = 1.35$; ambient air temperature = 20°C ; ID = “M-4 S-2”, see Table 5.1; as for load levels, see Fig. 5.2	161
5.78 Measured strain evolution normalized with respect to the plateau stress as a function of the time since start of loading: mortar with $w/c = 0.42$, $a/c = 1.35$; ambient air temperature = 20°C ; ID = “M-4 S-2”, see Table 5.1; as for load levels, see Fig. 5.2	162
5.79 Measured strain evolution normalized with respect to the plateau stress as a function of the time since start of loading: mortar with $w/c = 0.42$, $a/c = 1.35$; ambient air temperature = 20°C ; ID = “M-4 S-2”, see Table 5.1; as for load levels, see Fig. 5.2	163
5.80 Measured strain evolution normalized with respect to the plateau stress as a function of the time since start of loading: mortar with $w/c = 0.50$, $a/c = 1.50$; ambient air temperature = 20°C ; ID = “M-5 S-1”, see Table 5.1; as for load levels, see Fig. 5.2	164
5.81 Measured strain evolution normalized with respect to the plateau stress as a function of the time since start of loading: mortar with $w/c = 0.50$, $a/c = 1.50$; ambient air temperature = 20°C ; ID = “M-5 S-1”, see Table 5.1; as for load levels, see Fig. 5.2	165
5.82 Measured strain evolution normalized with respect to the plateau stress as a function of the time since start of loading: mortar with $w/c = 0.50$, $a/c = 1.50$; ambient air temperature = 20°C ; ID = “M-5 S-1”, see Table 5.1; as for load levels, see Fig. 5.2	166
5.83 Measured strain evolution normalized with respect to the plateau stress as a function of the time since start of loading: mortar with $w/c = 0.50$, $a/c = 1.50$; ambient air temperature = 20°C ; ID = “M-5 S-1”, see Table 5.1; as for load levels, see Fig. 5.2	167

5.84 Measured strain evolution normalized with respect to the plateau stress as a function of the time since start of loading: mortar with $w/c = 0.50$, $a/c = 1.50$; ambient air temperature = 20°C ; ID = “M-5 S-2”, see Table 5.1; as for load levels, see Fig. 5.2	168
5.85 Measured strain evolution normalized with respect to the plateau stress as a function of the time since start of loading: mortar with $w/c = 0.50$, $a/c = 1.50$; ambient air temperature = 20°C ; ID = “M-5 S-2”, see Table 5.1; as for load levels, see Fig. 5.2	169
5.86 Measured strain evolution normalized with respect to the plateau stress as a function of the time since start of loading: mortar with $w/c = 0.50$, $a/c = 1.50$; ambient air temperature = 20°C ; ID = “M-5 S-2”, see Table 5.1; as for load levels, see Fig. 5.2	170
5.87 Measured strain evolution normalized with respect to the plateau stress as a function of the time since start of loading: mortar with $w/c = 0.50$, $a/c = 1.50$; ambient air temperature = 20°C ; ID = “M-5 S-2”, see Table 5.1; as for load levels, see Fig. 5.2	171
5.88 Measured strain evolution normalized with respect to the plateau stress as a function of the time since start of loading: concrete with $w/c = 0.42$, $a/c = 2.70$; ambient air temperature = 20°C ; ID = “C-1 S-1”, see Table 5.1; as for load levels, see Fig. 5.2	172
5.89 Measured strain evolution normalized with respect to the plateau stress as a function of the time since start of loading: concrete with $w/c = 0.42$, $a/c = 2.70$; ambient air temperature = 20°C ; ID = “C-1 S-1”, see Table 5.1; as for load levels, see Fig. 5.2	173
5.90 Measured strain evolution normalized with respect to the plateau stress as a function of the time since start of loading: concrete with $w/c = 0.42$, $a/c = 2.70$; ambient air temperature = 20°C ; ID = “C-1 S-1”, see Table 5.1; as for load levels, see Fig. 5.2	174

5.91 Measured strain evolution normalized with respect to the plateau stress as a function of the time since start of loading: concrete with $w/c = 0.42$, $a/c = 2.70$; ambient air temperature = 20 °C; ID = “C-1 S-1”, see Table 5.1; as for load levels, see Fig. 5.2	175
5.92 Measured strain evolution normalized with respect to the plateau stress as a function of the time since start of loading: concrete with $w/c = 0.42$, $a/c = 2.70$; ambient air temperature = 20 °C; ID = “C-1 S-2”, see Table 5.1; as for load levels, see Fig. 5.2	176
5.93 Measured strain evolution normalized with respect to the plateau stress as a function of the time since start of loading: concrete with $w/c = 0.42$, $a/c = 2.70$; ambient air temperature = 20 °C; ID = “C-1 S-2”, see Table 5.1; as for load levels, see Fig. 5.2	177
5.94 Measured strain evolution normalized with respect to the plateau stress as a function of the time since start of loading: concrete with $w/c = 0.42$, $a/c = 2.70$; ambient air temperature = 20 °C; ID = “C-1 S-2”, see Table 5.1; as for load levels, see Fig. 5.2	178
5.95 Measured strain evolution normalized with respect to the plateau stress as a function of the time since start of loading: concrete with $w/c = 0.42$, $a/c = 2.70$; ambient air temperature = 20 °C; ID = “C1 S-2”, see Table 5.1; as for load levels, see Fig. 5.2	179
5.96 Measured strain evolution normalized with respect to the plateau stress as a function of the time since start of loading: concrete with $w/c = 0.50$, $a/c = 3.0$; ambient air temperature = 20 °C; ID = “C-2 S-1”, see Table 5.1; as for load levels, see Fig. 5.2	180
5.97 Measured strain evolution normalized with respect to the plateau stress as a function of the time since start of loading: concrete with $w/c = 0.50$, $a/c = 3.0$; ambient air temperature = 20 °C; ID = “C-2 S-1”, see Table 5.1; as for load levels, see Fig. 5.2	181

5.98	Measured strain evolution normalized with respect to the plateau stress as a function of the time since start of loading: concrete with $w/c = 0.50$, $a/c = 3.0$; ambient air temperature = 20 °C; ID = “C-2 S-1”, see Table 5.1; as for load levels, see Fig. 5.2	182
5.99	Measured strain evolution normalized with respect to the plateau stress as a function of the time since start of loading: concrete with $w/c = 0.50$, $a/c = 3.0$; ambient air temperature = 20 °C; ID = “C-2 S-1”, see Table 5.1; as for load levels, see Fig. 5.2	183
5.100	Measured strain evolution normalized with respect to the plateau stress as a function of the time since start of loading: concrete with $w/c = 0.50$, $a/c = 3.0$; ambient air temperature = 20 °C; ID = “C-2 S-2”, see Table 5.1; as for load levels, see Fig. 5.2	184
5.101	Measured strain evolution normalized with respect to the plateau stress as a function of the time since start of loading: concrete with $w/c = 0.50$, $a/c = 3.0$; ambient air temperature = 20 °C; ID = “C-2 S-2”, see Table 5.1; as for load levels, see Fig. 5.2	185
5.102	Measured strain evolution normalized with respect to the plateau stress as a function of the time since start of loading: concrete with $w/c = 0.50$, $a/c = 3.0$; ambient air temperature = 20 °C; ID = “C-2 S-2”, see Table 5.1; as for load levels, see Fig. 5.2	186
5.103	Measured strain evolution normalized with respect to the plateau stress as a function of the time since start of loading: concrete with $w/c = 0.50$, $a/c = 3.0$; ambient air temperature = 20 °C; ID = “C2 S-2”, see Table 5.1; as for load levels, see Fig. 5.2	187
A.1	(a) Test setup consisting of the cement paste specimen, metal cylinders with bottlenecks, two aluminum rings holding five Linear Variable Differential Transducers (LVDTs): view into a climate chamber conditioned to 20 degrees Centigrade, and (b) force history prescribed during the 2-days creep test	207

A.2	(a) Strains measured during the 2-days creep test on cement paste with $w/c=0.50$, subjected at an age of 24 h to a force amounting to 7.15 kN, and (b) shrinkage strain evolution, measured on independent specimens	208
A.3	Creep strains developing during the first three minutes of the 2-days creep test	209
A.4	Illustration of creep property identification: (a) comparison of measured and modeled creep strain evolution, and (b) contour plot of error function (66) as a function of creep modulus and power-law exponent; the marked point refers to the optimal solution (67)	211
A.5	Comparison of extrapolated strain evolution, see (68) as well as (61) and (67), with measured strain evolution, see Fig. A.3 b .	212
A.6	Illustration of creep property identification (a) comparison of measured and modeled creep strain evolution, and (b) contour plot of error function (69), see also (70) and (71), as a function of creep modulus and power-law exponent; the marked point refers to the optimal solution (72)	213
A.7	Comparison of extrapolated strain evolution, see (68) as well as (61) and (72), with measured strain evolution, see Fig. A.2 a .	214

List of Tables

2.1	(Elastic) Young’s modulus, creep modulus, and power-law exponent of four samples with $w/c = 0.42$, subjected to three-minutes creep tests, 24 hours after their production; and 99 % confidence intervals of expected values of lognormal distributions	36
3.1	Isotropic elastic phase properties from Pichler and Hellmich (2011); corresponding phase stiffness tensors read as $\mathbb{C}_j = 3k_j\mathbb{I}^{vol} + 2\mu_j\mathbb{I}^{dev}$	48
3.2	Comparison of hydrate creep properties of Eq. (3.2) and (3.35), identified by means of downscaling 500 macroscopic creep tests on cement pastes: isochoric creep vs. creep at constant Poisson’s ratio; prediction error ϵ according to Eq. (3.33)	56
4.1	Nominal composition of tested mortars and concretes	69
4.2	Prediction Errors \mathcal{E} (MPa^{-1}) according to Eq. (4.24)	72
4.3	Input quantities for creep homogenization of Mortar #1 with mix-related (nominal) composition quantified through $w/c = 0.50$ and $a/c = 3.0$: effective water-to-cement mass fractions of the cement paste matrix according to Eqs. (4.10) and (4.25), as well as corresponding viscoelastic properties of the cement paste matrix found by means of interpolation (see Fig. 4.4), for hydration degrees listed in Eq. (4.19)	74

4.4	Input quantities for creep homogenization of Mortar #2 with mix-related (nominal) composition quantified through $w/c = 0.42$ and $a/c = 2.7$: effective water-to-cement mass fractions of the cement paste matrix according to Eqs. (4.10) and (4.25), as well as corresponding viscoelastic properties of the cement paste matrix found by means of interpolation (see Fig. 4.4), for hydration degrees listed in Eq. (4.19)	76
4.5	Input quantities for creep homogenization of Concrete #1 with mix-related (nominal) composition quantified through $w/c = 0.50$ and $a/c = 3.0$: effective water-to-cement mass fractions of the cement paste matrix according to Eqs. (4.10), with void water-filling extent according to Eq. (4.25), and with water uptake capacity of quartz and entrapped air volume fraction according to Eq. (4.33), as well as corresponding viscoelastic properties of the cement paste matrix found by means of interpolation (see Fig. 4.4), for hydration degrees listed in Eq. (4.19)	79
4.6	Input quantities for creep homogenization of Concrete #2 with mix-related (nominal) composition quantified through $w/c = 0.42$ and $a/c = 2.7$: effective water-to-cement mass fractions of the cement paste matrix according to Eq. (4.10), with void water-filling extent according to Eq. (4.25), with water uptake capacity of quartz according to Eqs. (4.33), and with entrapped air volume fraction according to Eq. (4.37), as well as corresponding viscoelastic properties of the cement paste matrix found by means of interpolation (see Fig. 4.4), for hydration degrees listed in Eq. (4.19)	81
5.1	Mix composition and testing temperature of characterized cement pastes, mortars, and concretes	88

Curriculum Vitae

Engr. MUHAMMAD IRFAN-UL-HASSAN

M.SC. STRUCTURAL ENGINEERING

B.SC. CIVIL ENGINEERING

Ph.D. Researcher

Institute for Mechanics of Materials and Structures (IMWS)

Vienna University of Technology, Vienna, Austria

Designation: Assistant Professor, Civil Engineering. Department,
University of Engineering and Technology (UET), Lahore-Pakistan

Professional Affiliations:

Member Pakistan Engineering Council, Member Pakistan Engineering Congress

Member IEP [Institution of Engineers Pakistan]

Member ACI

Ex. Member Technical Committee for Lahore College for Women University-Pakistan

Cell Number: +43-688-60075558 Office: +43-1-58801-20235

Address Pakistan: Assistant Professor, Civil Engg. Dept. U.E.T. Lahore 54890. Pakistan

Email: Muhammad.irfan-ul-hassan@tuwien.ac.at
mihassan786@gmail.com

Qualification

Degree	Name of Institution	Specialization
PhD (Candidate)	Vienna University of Technology, Austria	Civil Engineering/Cement and Concrete Research
M.Sc. Engineering	University of Engineering and Technology (UET) Lahore, Pakistan	Structural Engineering
B.Sc. Engineering	UET Lahore	Civil Engineering
F.Sc. (Intermediate)	Govt. College Sargodha-Pakistan	Pre-Engineering
SSC (School)	Govt. High School , Naushera, Khushab-Pakistan	Science

EXPERIENCE

Teaching, research and Design Experience

10 Years total experience includes teaching, research, designing structures, vetting projects, report writing, Lab testing, Earthquake rehabilitation, Coordinator Studies dept. and Publication of papers.

Name of Employer	Designation	Period served		Job details (Teaching, R&D, , Technical,
University of Engineering and Technology, (UET) Lahore	Assistant Professor [BPS-19]	25-06-2007	To date	Teaching/Research
UET Lahore	Lecturer [BPS-17]	06-02-2006	24-06-2007	Lecturer
General	Visiting supervisory Consultant	2002	2006	Structural Design supervision
Gandhara Consultant	Consulting Engineer	Jul-2001	Dec-2001	Structural Design Consultancy

Research Experience and Projects

Selected Publications

- 1- ***Elsevier Journal of Cement and Concrete Research (CCR)***: "*Elastic and Creep Properties of Young Cement Paste, as Determined from Hourly Repeated Minute-Long Quasi-Static Tests*"; M. Irfan-ul-Hassan, B. Pichler, R. Reihnsner, Ch.Hellmich: , vol. 82 (2016), 36 – 49.
- 2- ***ASCE Journal of Engineering Mechanics (JEM)*** , Downscaling-based identification of non-aging power-law creep of cement hydrate, M. Königsberger, M. Irfan-ul-Hassan, B. Pichler, Ch. Hellmich, Accepted for publication,, 2016.
- 3- ***ASCE Journal of nanomechanics and micromechanics, (NMENG)***: How water-aggregate interactions affect concrete creep: a multiscale analysis, M. Irfan-ul-

Hassan , M. Königsberger , R. Reihnsner, Ch. Hellmich, and B. Pichler, submitted for publication, 2016.

- 4- **Research Journal of Engineering and Technology Mehran University**: Critical Traffic Loading for the Design of Prestressed Concrete Bridge, M. I. Hassan, Z. A. Siddiqi & M. Ashraf, Vol. 28, Number-3, July-2009.
- 5- **Journal of Science International, Lahore** : Design comparison of slab system using EFM and DDM, M.I. Hassan & M. Ali, vol. 1, Number. 2 , 2009.
- 6- **M.Sc. Thesis**: Critical Traffic Loading for the Design of Prestressed Concrete Bridge superstructure, M.I. Hassan M.Sc. Thesis, Civil Engg. Dept., University of Engineering & Tech. Lahore, Pakistan. Published in 2005.

Contribution towards Conferences, Workshops, Symposiums, and Seminars

1. **Concreep-10, Proceeding of the 10th International Conference published by American Society of Civil Engineers (ASCE), 2015 on Mechanics and Physics of Creep, Shrinkage, and Durability of Concrete and Concrete Structures**", M. Irfan-Ul-Hassan, B. Pichler, R. Reihnsner, Ch. Hellmich: "*Minutes-long Creep Tests on Young Cement Pastes Provide Access to Creep Properties Relevant for Aging Creep with a Duration of 2 Days*"; in: ", Paper-Nr. 348, 10 S.
2. **Danubia-Adria Symposium on Advances in Experimental Mechanics (DAS 2016)**": M. Königsberger, M. Irfan-Ul-Hassan, R. Reihnsner, Ch. Hellmich, B. Pichler: "*Innovative Creep Testing on Cement Pastes Allows for Deciphering Creep of Concrete at Early Ages*"; in: "*Proceedings of the 33rd , Slovenian Society of Experimental Mechanics, 2016.*
3. **Proceedings of the 2015 Conference of the ASCE Engineering Mechanics Institute, Stanford University, USA (EMI 2015)**", American Society of Civil Engineers (ASCE), 2015 : M. Irfan-Ul-Hassan, B. Pichler, R. Reihnsner, Ch. Hellmich: "*Early-Age Short-Term Creep Characterization of Cement Pastes and Mortars*". 1 S.
4. **"Book of Abstracts of the 20th Inter-Institute Seminar for Young Researchers"**, Cracow University of Technology, 2015, B. Pichler, M. Irfan-Ul-Hassan, R. Reihnsner, M. Königsberger, Ch. Hellmich, H.A. Mang: "*Multiscale Structural Analysis*"; in: , ISBN: 978-83-7242-684-0, S. 15.

5. ***Proceedings of the 5th International Workshop of Young Doctors in Geomechanics (W(H)YDOC 15)***", Ecole des Ponts ParisTech, 2015. M. Irfan-Ul-Hassan, B. Pichler, Ch. Hellmich: "*Early-Age Non-Aging Viscoelastic Properties of Cement Paste: Lessons Learned from Macroscopic Testing*".
6. ***Proceedings of the 2015 Conference of the ASCE Engineering Mechanics Institute, Stanford University, USA (EMI 2016)*** "Isochoric Creep of Hydrate Gel Needles Explains Macroscopic Creep of Cementitious Materials" ,M. Königsberger, M. Irfan-ul-Hassan, Ch. Hellmich, B. Pichler.
7. ***The Concrete Convention and Exposition of the American Concrete Institute (ACI), Kansas City, USA:***
"*Macroscopic Short-Term Creep Testing of Hydrating Cementitious Materials*";
Lecture; 12.04.2015 – 16.04.2015.
8. ***Pre-Framcos Workshop May-29,2016, Berkeley*** : Ultrashort-term creep of concrete: Experiments and multiscale modeling,. B. Pichler, M. Irfan-Ul-Hassan, R. Reihnsner, M. Königsberger, Ch. Hellmich.
9. ***ECCOMAS Congress 2016: Jun 5-10, Crete, Greece:*** CREEP HOMOGENIZATION OF CEMENTITIOUS MATERIALS M. Königsberger, M. Irfan-ul-Hassan, B. Pichler, Ch. Hellmich

Undergraduate Subjects Taught

- 1- Design of Structures
- 2- Plain and Reinforced Concrete
- 3- Structural Analysis
- 4- Engineering Mechanics
- 5- Computer programming
- 6- Civil Engg. Drawing

Post Graduate Subjects taught

- 1- Advanced Reinforced Concrete Design [In Dept. of Arch. Engg. and Design in M.Sc. Building Engg.]

Research Interests

- 1- Properties of structural concrete material
- 2- Concrete Mechanics
- 3- Structural Performance studies of high rise buildings in seismic regions.

Undergraduate Projects Supervised

1. Design comparison of buildings using computer aided and manual design
2. Report writing on load testing, strengthening of different projects.
3. Design of Telecommunication towers
4. Design of Medical complex
5. Design of Academic building
6. Design of Auditorium Building
7. Slab design Comparison using EFM and DDM

Post Graduate Research projects

- 1- Detailed study on performance based seismic design of RC buildings structural system

Practical Experience as Structural Designer and Consultant Specialist for different Civil Engg. Projects

- 2- Design of schools in seismic zone Kashmir and Mozaffarabad, Pakistan.
- 3- Design of First INMOL cyclotron complex in Lahore
- 4- Design of Ibne Sina medical college and medical complex in Multan
- 5- Design of theater BZU Multan
- 6- Design of HEC library Islamabad and Training center Ayubia, Pakistan
- 7- Design of physics dept, hostel, and Over head tank of GCU Sargodha
- 8- Design of IT Center, special education dept, PU, Lahore
- 9- Design of Lecture Hall, Hostel for University of Lahore
- 10- Report writing on load testing, strengthening of many projects.
- 11- Design Review of High Rise Building [Novotel Hotel] Lahore Cantt.
- 12- Structural design of University of Lahore Pharmacy Block, Lecture Theater, Guest House

Computer Skills

- 1- MATLAB
- 2- Visual BASIC
- 3- MS-Office
- 4- SAP 2000
- 5- EATBS
- 6- SAFE
- 7- MAPLE
- 8- TeX